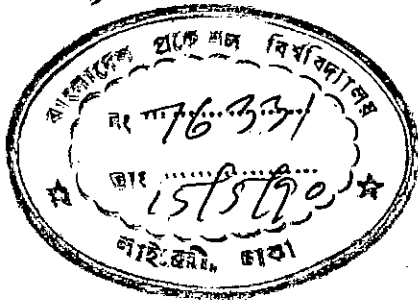


693.5
1990
KHA

3

NONLINEAR BEHAVIOUR OF SLABS IN COUPLED SHEAR WALL STRUCTURES

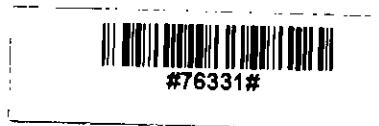


A THESIS

BY

KHANDAKER MUHAMMED ANWAR HOSSAIN

Submitted to the Department of Civil Engineering,
Bangladesh University of Engineering and Technology, Dhaka
in partial fulfilment of the requirement for the degree
of
MASTER OF SCIENCE IN CIVIL ENGINEERING



January, 1990

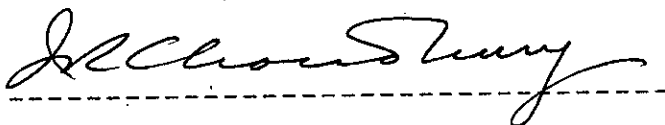
NONLINEAR BEHAVIOUR OF SLABS IN COUPLED SHEAR WALL STRUCTURES

A Thesis

by

Khandaker Muhammed Anwar Hossain

Approved as to style and content by:



(Dr. J.R. Choudhury)

: Supervisor

Professor of Civil Engg.,

BUET, Dhaka.

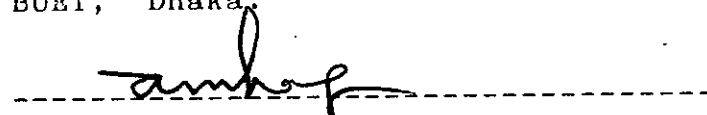


(Dr. Md. Shafiul Bari)

: Co-Supervisor

Assistant Professor of Civil Engg.

BUET, Dhaka.



(Dr. Alamgir Mojibul Hoque)

: Member

Professor and Head

Department of Civil Engg.

BUET , Dhaka.

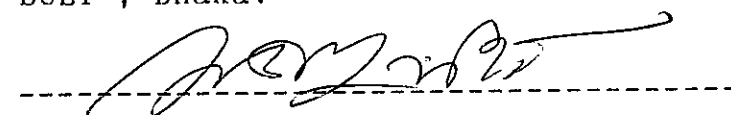


(Dr. Sohrabuddin Ahmad)

: Member

Professor of Civil Engg.,

BUET , Dhaka.



(Dr. Md. Mizanul Huq)

: Member

Managing Director

Engineering Consulting Services (Pvt.) Ltd.

Dhanmondi, Dhaka.

ACKNOWLEDGEMENTS

The author wishes to express his sincerest debt of gratitude to Dr. Jamilur Reza Choudhury , Professor of Civil Engineering , BUET for his guidance and valuable suggestions and affectionate encouragement at all stages of this study .

Thanks are also extended to him for making necessary facilities available for the successful accomplishment of this job in his capacity as Director , Computer Centre , BUET .

The author is grateful to Dr. Md. Shafiul Bari , Assistant Professor , Department of Civil Engineering , BUET for his kind supervision and valuable suggestions during the progress of this work .

Particular appreciation is expressed also to all the staffs of the BUET Computer Centre , for their support.

Sincere thanks are expressed to Mr. M. A. Malek of Civil Engineering Department , BUET for his services in typing the thesis.

ABSTRACT

This thesis deals with the behaviour of slabs in coupled shear wall structures considering the nonlinear behaviour of reinforced concrete.

Nonlinear behaviour of reinforced concrete is introduced through modelling of concrete in its precracking, cracking and post cracking (with yielding of steel) stages. A nonlinear 3-D finite element programme using 20-noded brick element is used. Design of slabs for gravity and lateral load is done by direct design approach using a linear 2-D finite element programme with plate bending element.

Overall flexural behaviour of slab is studied by determining the resistance of slab against wall rotation. In this work, wall rotation is applied incrementally until failure of slab-wall junction, the equivalent wall moment transferred from wall to slab being determined in each increment. From moment-rotation relationship, the variation of bending stiffness of floor slabs with the increase in load is calculated.

Effect of amount of reinforcement on flexural behaviour of slab is also studied. The relative influences of a range of structural parameters on the stiffness and effective slab width are evaluated and design curves are presented to facilitate their determination.

The variation of stresses and strain in slab and crack propagation in slabs are also studied and presented. Flexural stiffness and effective width are found to be influenced by physical dimensions of shearwall slab structure. It is also found that the effective slab width gradually decreases with increase in load. Several graphs and charts relating stiffness and effective width of slab to various geometrical dimensions of slab-shear wall structure are presented to facilitate their determination.

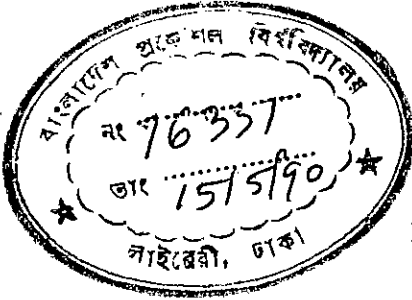


TABLE OF CONTENTS

	Page No.
	i
ABSTRACT	ii
NOTATIONS	iii
CHAPTER 1 INTRODUCTION	1
1.1 General	1
1.2 Choice of Structural System	2
1.3 Slab- Shear Wall System	4
1.4 Structural Actions of Shear Wall-Slab Structure Subjected to Lateral Load	6
1.5 Purpose of this Study	8
CHAPTER 2 LITERATURE REVIEW	10
2.1 General	10
2.2 Analysis of Shear Wall	10
2.3 Effective Width of Floor Slab	12
2.4 Behaviour of Slab in Coupled Shear Wall Structures	15
2.5 Nonlinear Analysis of Reinforced Concrete Structures	18
2.6 Conclusion	20
CHAPTER 3 DESIGN OF REINFORCED CONCRETE SLABS	21
3.1 Introduction	21
3.2 Theory of Elasticity in Slab Design	21
3.3 Theory of Plasticity in Slab Design	23
3.4 The Yield Condition	23
3.5 Direct Design Method	26
3.5.1 The Equilibrium Condition	27
3.5.2 The Yield Condition	27
3.5.3 Rules for Placing Orthogonal Reinforcement	29
3.5.4 The Mechanism Condition	32

3.6	Procedure Adopted for the Design of a Typical Model	34
3.6.1	General	34
3.6.2	Design for Gravity Loads	34
3.6.3	Design for Wind Loads	36
3.6.4	Determination of Combined Effect	36
CHAPTER 4	MODELLING OF NONLINEAR BEHAVIOUR OF REINFORCED CONCRETE USING FINITE ELEMENT TECHNIQUE	38
4.1	Introduction	38
4.2	Finite Element Formulation	38
4.2.1	Discretization by Finite Element	38
4.2.2	Element Type	42
4.2.3	Shape Functions	42
4.2.4	Strain Matrix	45
4.2.5	Stress Strain Relationship	48
4.2.6	Numerical Integration	50
4.3	Simulation of Steel Reinforcement	50
4.4	Mathematical Modelling of Concrete	52
4.4.1	Introduction	52
4.4.2	Kotsovos Constitutive Laws for Concrete	53
4.4.3	Failure Criteria of Concrete	60
4.4.4	Modelling of Concrete Cracking	61
4.4.5	Shear Retention Factor Used in this Work	69
4.5	Nonlinear Methods Used in this Work	70
4.5.1	General	70
4.5.2	Convergence Criteria Used in this Work	73
4.5.3	Analysis Termination Criteria	74
4.5.4	Procedure Adopted for Nonlinear Analysis	74
4.5.5	Nonlinear 3-D Finite Element Program	78
4.5.5.1	List of Subroutines with their brief description	80

CHAPTER 5	THEORETICAL NONLINEAR STUDY	88
5.1	General	88
5.2	Procedure Adopted for Nonlinear Study	88
5.2.1	Finite Element Discretization of Models	88
5.2.2	Investigations on Boundary Conditions	90
5.2.3	Determination of M- θ from Finite Element Solution	92
5.3	Idealization of M- θ Curves	92
5.4	Material Properties of Models	94
5.5	Geometric Dimensions of Models	95
5.6	Parameter Study	99
5.7	Model Investigations on Effect of Reinforcement	103
5.8	Model Investigations to Study the Effect of Geometric Parameters	110
5.8.1	Description of Behaviour of Slabs in Theoretical Studies	115
5.8.2	Study on Behaviour of Steel in Slab	151
5.8.2.1	Model Descriptions	151
5.8.2.2	Yielding Pattern of Steel for the Models	168
5.8.2.3	Discussion on Behaviour of Steel	168
5.8.3	Interpretation of Results	172
5.8.4	Analytical Interpretation of Nonlinear Results	183
CHAPTER 6	CONCLUSIONS AND SUGGESTIONS FOR FURTHER STUDY	188
6.1	Conclusions	188
6.2	Suggestions for Further Study	189
REFERENCES		190
APPENDIX		193



NOTATIONS

L	Corridor width
X	Length of the slab
Y	Bay width of the slab
W	Width of the shearwall
t	Thickness of the slab
Y_e	Effective width of the slab
M	Equivalent wall moment
Q	Total shear force
θ	Wall rotation
q	Shear force per unit length of the wall
T	Axial force in the wall
D	Flexural rigidity of the slab
δ	Imposed nodal displacement
E	Modulus of elasticity of the slab material
ν	Poisson's ratio
I	Second moment of area of the effective beam
K	Nondimensional parameter to express stiffness of slab
M_x, M_y, M_{xy}	Applied moment field on the slab
M_n	Normal moment
M^*_n	Moment of resistance in normal direction (n)
M^*_x	Moment of resistance in X-direction
M^*_y	Moment of resistance in Y-direction
π	Total potential energy
$[\sigma]$	Stress vector
$[\epsilon]$	Strain vector
V	Volume of the structure
S	Loaded surface area
[N]	Shape function
[B]	Strain matrix
[D]	Elasticity matrix

ξ, η, ζ	Local co-ordinate system
[J]	Jacobian matrix
q, r, θ	Cylindrical co-ordinate system
$\sigma_1, \sigma_2, \sigma_3$	Three principal stresses
σ_{oct}	Normal octahedral stress
ϵ_{oct}	Normal octahedral strain
τ_{oct}	Shear octahedral stress
γ_{oct}	Shear octahedral strain
$\epsilon_1, \epsilon_2, \epsilon_3$	Three principal strain
K_s	Secant bulk modulus
G_s	Secant shear modulus
f'_c	Cylinder compressive strength
x, y, z	Global co-ordinate system
G	Reduced shear modulus
β	Shear retention factor
[T]	Transformation matrix for strain matrix
l, m, n	Direction cosines of principal stresses
ϵ_m	Average of the three principal strains at a cracked point
$\epsilon_{t.o}$	Cracking tensile strain
[R]	External load vector
[F _u]	Residual forces
N	Total number of nodal points
r	Denotes the iteration number
[P _i]	Total equivalent nodal forces of the element
u, v, w	Nodal displacements in x, y, z directions respectively
f_{cu}	Cube crushing strength of concrete
f_r	Modulus of rupture of concrete
E_c	Modulus of elasticity of concrete
f_y	Yield strength of steel
E_s	Modulus of elasticity of steel
ϵ_y	Yield strain of steel
K_o	Precracking stiffness
K_{cr}	Cracking stiffness

K_p	Post cracking stiffness
$M_{c r}$	Cracking moment
M_y	Yield moment
M_u	Ultimate moment
$Y_{e o}$	Precracking effective width
$Y_{e c r}$	Cracking effective width
$Y_{e p}$	Post cracking effective width
d	Effective depth of the slab
$M_{c r a}$	Analytical cracked moment
$M_{u a}$	Analytical ultimate moment
S.P.	Sampling point

CHAPTER 1

INTRODUCTION

1.1. General

Recent years have seen a rapid increase in the number of tall buildings, for commercial and residential purposes throughout the world. This increase has highlighted the necessity for a greater knowledge of the behaviour of these structures, and, in particular, the necessity for producing methods of analysis capable of giving rapid and accurate assessments of their overall strength and stiffness as well as detailed information about any local stress concentrations.

As buildings increase in height, it becomes more important to ensure adequate lateral stiffness to resist loads which may arise due to wind, seismic or perhaps even blast effects. This stiffness may be achieved in various ways. In framed structures it may be obtained by bracing members, by the rigidity of the joints, by complete shear truss assemblies acting in conjunction with the frame or by infilling the frame with shear resistant panels. An obvious simplification of the latter is shear wall construction, in which the relatively high in-plane stiffness of the walls both external and internal, is employed to resist lateral forces. The floor slabs which are extremely stiff in their own plane, serve not only to collect and distribute the lateral forces to the walls, but, by a complex structural interaction with the walls, increase the lateral stiffness of the buildings.

In principle, in any structural system, all of the load resisting systems and components should be equally active and ideally should work together under all types and combinations of design loads. In other words, the parts of the structural system that primarily resist horizontal loads should be able to contribute to the resistance to vertical loads as well. The most

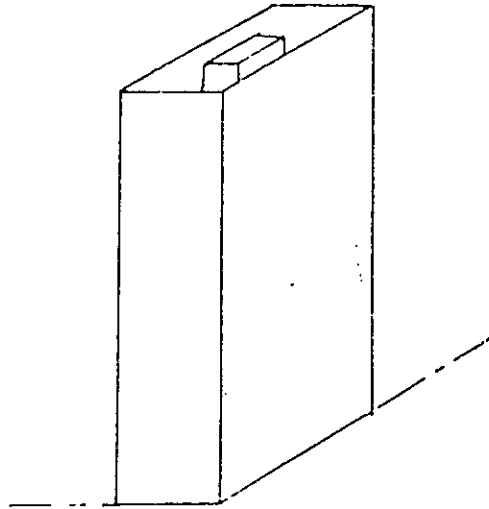
efficient structural system is the one that manages to combine all the structural subsystems or components into a completely integrated system in which most of the elements take part in resisting the loads. However, this ideal case is unlikely to be fully achieved in practice, due to constraints such as efficiency and ease of assembly and construction, manufacturing of joints, economic considerations and other requirements.

1.2. Choice of Structural Systems

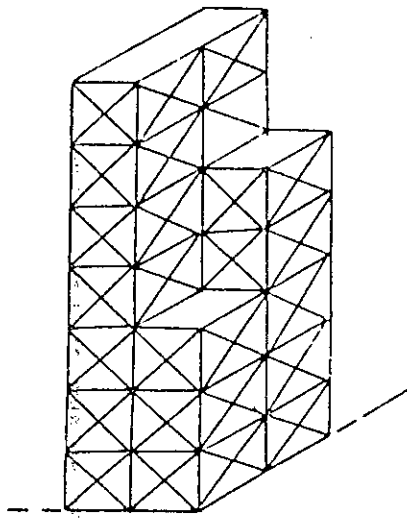
From a structural engineering standpoint, one of the major distinguishing characteristics of a tall building is the need to resist large lateral forces due to wind or earthquake. The lateral load resisting system must do this, and at the same time must prevent excessive deflections or accelerations and must help to provide stability. A lateral system is generally considered to be efficient if the provision of the lateral load resistance does not increase floor and column sizes beyond those required for gravity loads.

When high-rise buildings are designed using conventional beam-column frame the effect of the lateral forces on the column is very pronounced. The economic use of this type of structural system can be made up to a building height of about 20 stories. Moreover, as it is simply impossible to make a truly rigid beam column joint, the amount of sway produced due to lateral loads is also a limiting factor.

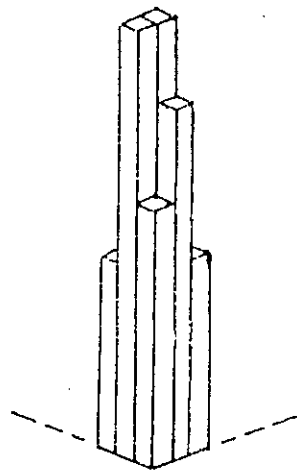
Designers are always in search of new structural systems which shall be capable of resisting lateral loads more economically without endangering safety of the occupants. Shear walls become natural choice for the buildings rising higher than 20 stories. By definition the shear wall is a "structural system providing strength, stiffness and stability against lateral forces deriving its stiffness from inherent structural form". For higher



Schematic sketch of tube - in - tube system



Column diagonal truss tube



Bundled tube

Fig. 1.1: Structural Systems

structural efficiency rigidly jointed frames interconnected with shear walls are also used.

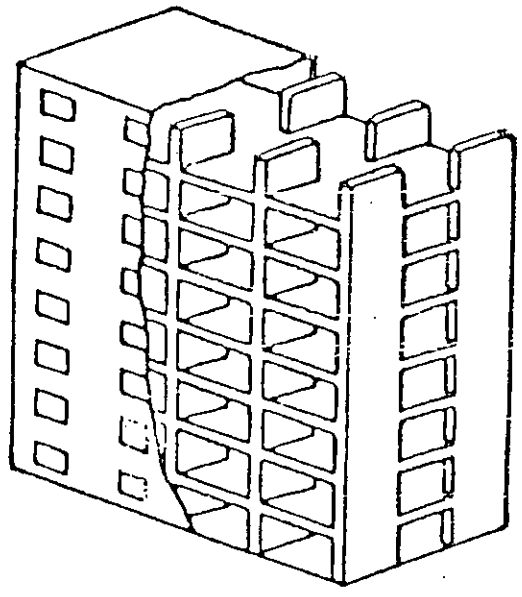
For buildings rising above 30 stories, perimeter walls are used as a structural member. The walls behave as a tube stiffened by the floor slabs which have very high inplane stiffness. Since a solid tube is not possible, they may be considered as a perforated tube, a framed tube or a latticed tube as shown in Fig.1.1. To have a perfect tubular effect the central core is also treated as a structural member. Sometimes the shear walls are also used to act as stiffeners inside the tubes. For higher buildings, tubes are grouped together as "bundled tube" (Fig.1.1) and it is more efficient than the previous one.

In short, the most efficient structural system for any proposed high-rise building should be selected from those mentioned above taking into consideration the expected behaviour of the building under lateral load. The efficiency is being judged by the fact that the structure, though designed for gravity loads only, the internal stresses remains well within allowable over stresses when subjected to lateral loads.

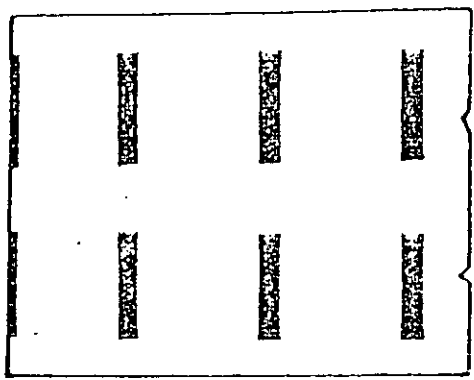
1.3. Shear Wall-Slab System

A popular form of high rise structure, is a slab-coupled shear wall structure. The reason is that the height of majority of the high rise buildings fall within the limit upto which the shear walls are economic. From the constructional and architectural view point, it is relatively easy to make the final structure aesthetically pleasing.

Fig.1.2(a) shows a perspective view of a shearwall structure with a typical floor plan. The special features of this type of building are that the two rows of apartments are connected by a common corridor and the partition walls are treated as shear walls. As no projecting stems of beams run across the corridor,



(a) Perspective view of a shear wall building.



(b) Plan of a typical shear wall building.

Fig. 1.2

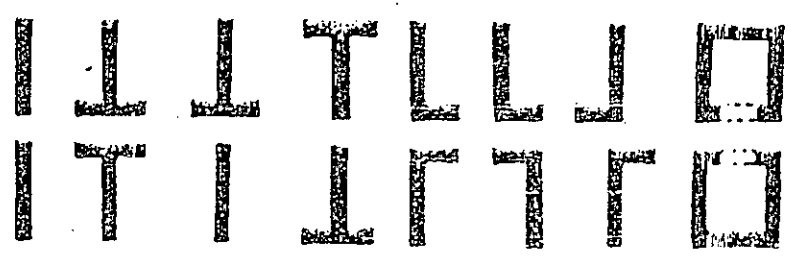


Fig. 1.3 : Different wall configurations.

there is no need for false ceilings and the height of the building is appreciably reduced thus acomodating more floors in the same height.

Shear walls may be defined as planar vertical elements distinguished by their relative thinness and substantial length. As it is not always possible to construct solid shear walls, pierced walls adopted to make room for corridors and other service facilities. Therefore the shear walls are further identified as having few openings or penetrations such that they have little or no flexibility due to the flexure of individual pieces of the wall. Their flexibility is generally limited to the sum of overall shear deformation and overturning flexural deformation. Shear walls are also used to enclose lift shafts and stair walls to form partially open box structures which act as strong points in the building. Thus, in practice, shear walls of various shapes such as planar, flanged or box-shaped, may be coupled together in shear wall-slab structures. The different types and layouts of shear wall are shown in Fig. 1.3.

1.4. Structural Actions of Shear Wall-Slab Structure subjected to Lateral load

In practical structures, the walls are interconnected through floor slabs and resist both lateral and gravity loads. Special considerations must be given to provide sufficient stiffness in all directions against lateral loads. When subjected to lateral forces, the shear wall is dominated by its flexural behaviour and shear effects are insignificant.

The shear walls resist the lateral loads on the structure by cantilever bending action, which results in rotation of the wall crosssections. The free bending of a pair of shear wall is resisted by the floor slabs, which are forced to rotate and bend out of plane where they are connected rigidly to the walls (Fig. 1.4(b)). Due to the large width of the wall, considerable

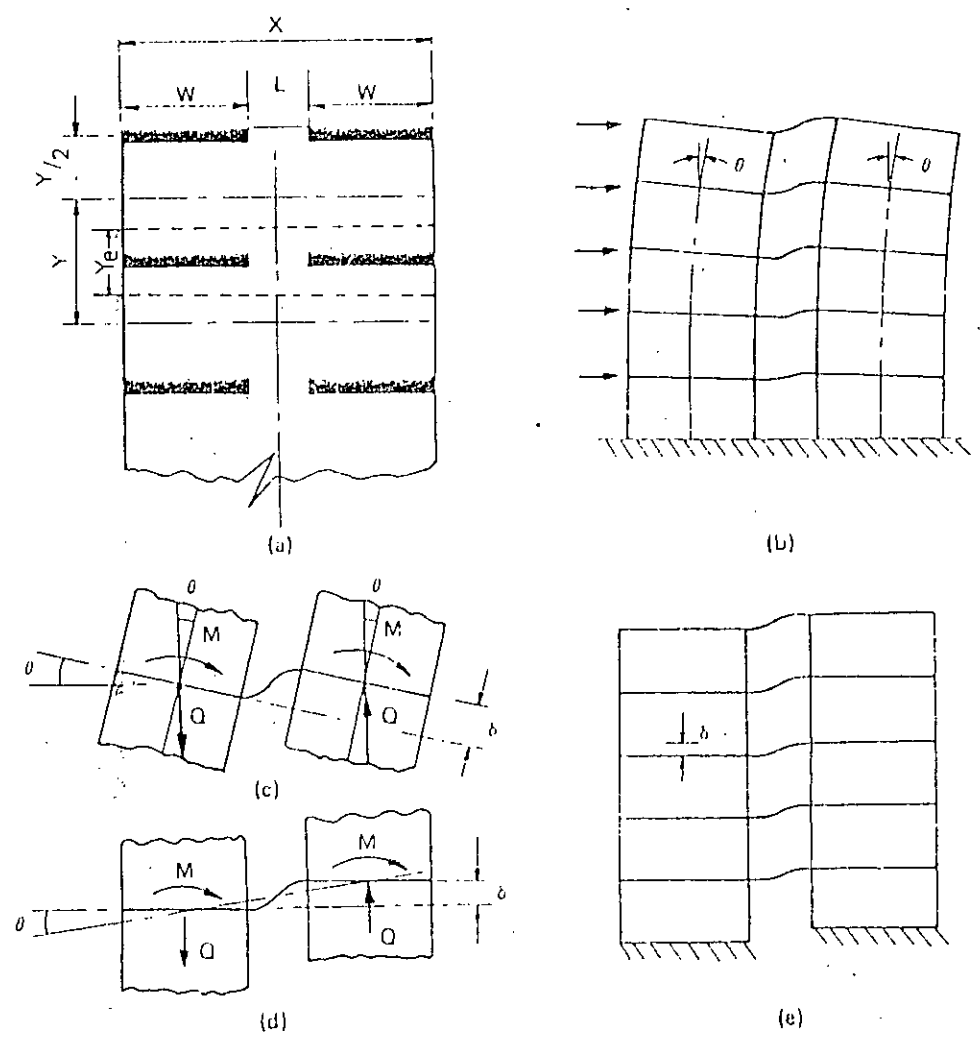


Fig. 1.4 : Structural Actions of Coupled Shear Wall-Slab Structure Subjected to Lateral Loads or Differential Movement

differential shearing action is imposed on the connecting slab, which develops transverse reactions to resist the wall deformations (Fig. 1.4(c)), and induces tensile and compressive axial forces into the walls. As a result of the large lever arm involved, relatively small axial forces can give rise to substantial moment of resistance, thereby reducing greatly the wind moments in the walls and resulting tensile stresses at the windward edges. The lateral stiffness of the structure is also considerably increased.

A similar situation arises if relative vertical deformation of the wall occurs, due to unequal vertical loading on the walls or due to differential foundation settlements. The effect on the slab is similar to that produced by parallel wall rotations caused by bending (Figs. 1.4(d) & 1.4(e)).

1.5 Purpose of this study

The structural analysis and design of slab-coupled shear wall structure can be performed if the behaviour of slab in the system is adequately known. As we know that the shear walls are provided to give lateral rigidity to the structure and connecting slabs play a significant role in resisting lateral load, the lateral stiffness of the walls cannot be calculated unless the stiffness against wall rotation is known. The stiffness of the slabs is dependent upon a number of parameters such as corridor width, the thickness and width of the shear walls, the span of the slab and the shape of the shear walls. Again, to have a complete idea of the behaviour of the slab, overall study which includes cracking of slab concrete, crack propagation in slab and behaviour of steel in slab is to be performed. Previous work as discussed in Chapter 2 has been concerned with the determination of bending stiffness and effective width of slab considering the linear behaviour of reinforced concrete. A survey of the available literature revealed that very little information is available on the behaviour of slab-coupled shear wall structure

at the onset of cracking, yielding of steel and crushing of concrete which cause nonlinear behaviour of the system .

The objects of the work reported in this thesis are:

(a) To develop a nonlinear 3-D finite element programme for analysis of coupled shear wall structures, based on available finite element programs.

(b) To study the behaviour of slab in coupled shear wall structure considering nonlinear behaviour of reinforced concrete

(c) To investigate the variation of equivalent wall moment (M) with change in wall rotation(θ), until failure of the slab.

(d) To evaluate the variation of stiffness from M/ θ graphs and hence the variation of effective width of slab for different wall slab configuration using planar walls.

(e) To investigate the effect of slab reinforcements on the behaviour of slab.

CHAPTER 2

LITERATURE REVIEW

2.1 General

The structural analysis and design of slab-coupled shear wall system can be conveniently performed using the technique developed for beam-coupled shear wall system provided the effective width of the slab can be established. In a coupled wall system, the stresses are not uniform across the width of the slab. In order to design the slab safely, it is necessary to know the magnitude and distribution of stresses developed through the coupling action. It is also essential to determine accurately the interactive forces developed at the slab-wall junction. In this chapter, a brief critical review of previous experimental and analytical research work done in the following fields is given:

- a) Analysis of shear wall structures to determine the stresses due to lateral loads.
- b) Effective stiffness of slabs coupling shear walls.

2.2 Analysis of Shear Wall

The analysis of shear walls pierced with regular sets of similar openings, i.e., coupled shear walls, has attracted several investigators. A simplified analysis has been produced by assuming that the discrete system of connections, formed by lintel beams or floor slabs as shown in Fig. 2.1, may be replaced by an equivalent continuous medium, as shown in Fig 2.2. By assuming that the axially rigid lintel beams have a point of contraflexure at midspan, the behaviour of the system can be defined by a single second order differential equation. A general closed form solution of the problem can be obtained.

Using the above simplified approach, Rossman (1) first derived solutions for a wall with one or two symmetric bands of openings, with various conditions of support at the lower end.

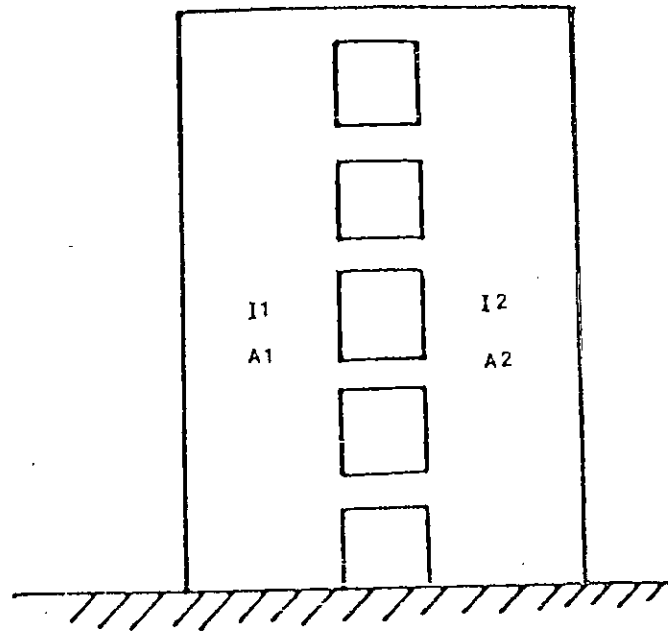


Fig. 2.1 : A typical shear wall with openings.

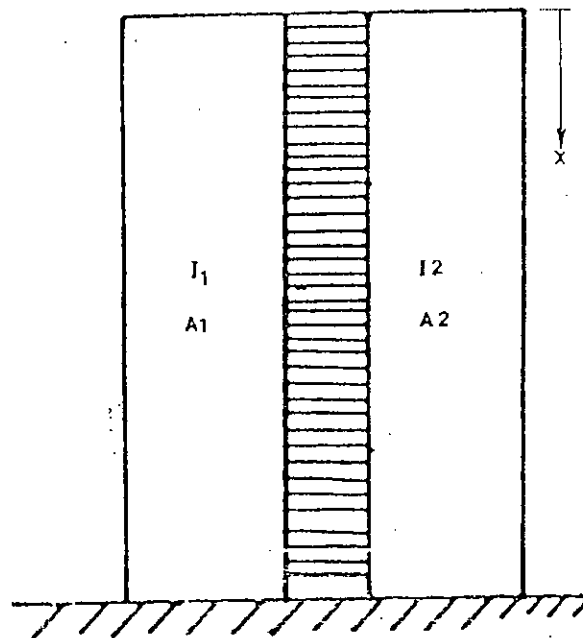


Fig. 2.2 : Shear wall with idealized continuous connection of laminae.

Deformations due to bending moment and normal forces on the walls and flexural and shear deformations in the connecting beam were also taken into account. The axial force in the walls was chosen as the statically redundant function. So, if q is the shear force related to the unit length, the axial force in the wall is

$$T = \int_0^x q \cdot dx \quad (2.1)$$

where x is the distance, measured from the top of the wall as shown in Fig.2.2. Making use of certain simplifying assumptions, the governing differential equation takes the form

$$d^2 T / dx^2 - \alpha^2 T = - X \quad (2.2)$$

A direct mathematical solution of the above equation can be obtained for any loading case. Equations (2.3) and (2.4) show the general solutions of above differential equation for the case of concentrated lateral load at the top and uniformly distributed lateral load respectively.

$$T = C_1 \sinh \alpha x - (Y/\alpha^2) x \quad (2.3)$$

$$T = C_1 \sinh \alpha x - (2\beta/\alpha^4)(\cosh \alpha x - 1) + (\beta/\alpha^2) x \quad (2.4)$$

The co-efficients α , β and Y depend on the load and the geometrical properties of the shear wall. Once the value of T is known, the shear force and bending moment in the connecting beams can be easily calculated using equilibrium conditions. This is also known as continuous medium method.

2.3 Effective Width of floor slab

The shear wall-slab structures subjected to lateral loads deflect and the rotation of the walls generate moments in the slabs as shown in Fig.2.3. The portion of the slab which acts as a beam connecting the walls and is active in resisting the moment

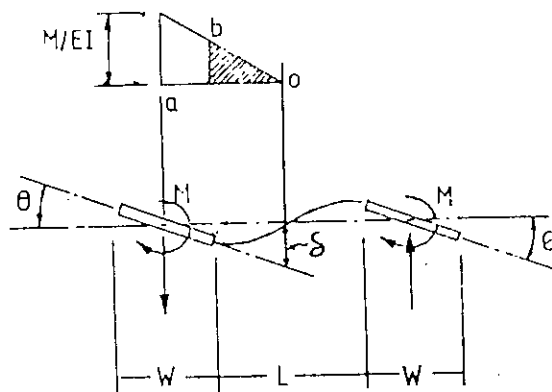


Fig.2.3 : Slab deformation due to wall rotation

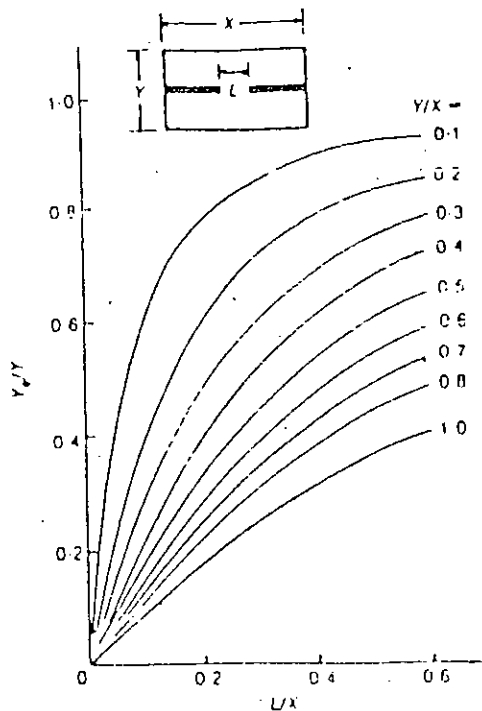


Fig. 2.4 : Design curves for effective width of slab (planar walls).

is called effective width of the slab (Fig.1.4(a)).

The resistance of the floor slab against the displacements imposed by the shear walls is a measure of its coupling stiffness, which can be defined in terms of the displacements at its ends and the forces producing them. Thus referring to Fig.2.3, the stiffness of the slab may be defined as rotational stiffness, M/θ . The relationship between M/θ , EI and the effective width is as follows:

Referring to Fig.2.3 and using the moment area diagram to determine the relation between M and θ . Let the deflection equal the moment of area abo about o . Then:

$$\delta = (M/12EI) (L^3 / (L+W))$$

$$\text{and } \theta = 2. \delta / (L+W)$$

$$\text{Therefore, } M/\theta = 6EI(L+W)^2 / L^3$$

where EI is the "equivalent beam stiffness" of the connecting slab. Using a nondimensional parameter K to express the stiffness of the slab:

$$K = M / D \theta \quad (2.5)$$

where D is the flexural rigidity of the slab, W is the width of the wall I is the second moment of area of the beam of effective width Y_e and slab thickness is t .

$$D = E t^3 / 12(1 - \nu^2)$$

$$I = Y_e \cdot t^3 / 12$$

The effective width can then be expressed in terms of the rotational stiffness factor, in non-dimensional form, as,

$$Y_e/Y = \left(\frac{K}{6(1-\nu)} \right) \left(\frac{L}{Y} \right) \left(\frac{L}{L+W} \right) \quad (2.6)$$

where Y is the bay width or longitudinal spacing and ν is the poisson's ratio of the slab material.

This theoretical basis for calculating the flexural stiffness and effective width of the slab was used by several investigators ; Coull & Wong (12), Qadeer & Stafford Smith (7), Huq (11), has also been used in this thesis.

2.4 Behaviour of Slab in Coupled Shear Wall Structures

The aforementioned theory in section 2.2 is concerned with shear walls interconnected by beams only. The structural analysis and design of a slab-coupled shear wall system may be readily performed using existing techniques of beam coupled shear wall structures , provided that the width of the slab which acts effectively as wide coupling beam or its corresponding structural stiffness , can be assessed. So previous investigations were restricted in finding the effective width of the slab.

Barnard and Schwaighofer (2) used Rossman theory with simplification to solve for stresses in shear walls connected solely through slabs. They assumed the entire width of the slab to be effective and verified the theoretical analysis by model tests of shear walls connected by slabs of various widths. The discussion of the same paper by Choudhury (3), Qadeer (4) and Michael (5) revealed that taking the entire slab width as effective may lead to a serious error in the calculation of stresses . It has also been discussed that the simplified Rossman theory can not be put into general use.

Choudhury (6) tested an asbestos cement model and found out that only 25% of the total width was effective. He came to similar conclusions through an analysis of floor slabs by finite

element method.

Qadeer and Stafford Smith (7) analyzed the slab by finite difference method and through experiments which gave results very close to those from theoretical studies. They produced a set of curves with slab width, cantilever width, corridor width and the width of the shear walls as variables for effective width. From those curves it is seen that effective width is a function of all these parameters, while a close inspection reveals that the slab width and corridor width have the most significant effect on the effective width. Michael (8) showed that a single curve, can be drawn with all the data presented by Qadeer and Smith. He also tried to fit into it another curve, having equation

$$(L/Y + 0.8)(1 - Y_e/Y) = 0.9, \text{ where}$$

L is the corridor width, Y is the slab width and Y_e is the effective width of the slab.

Coull (9) tested a perspex model with closer transverse spacing of orthogonal system of walls and found that the stiffening effect of the close-spaced walls upon the floor slab is a major factor in calculating the effective width of the coupling floor slab. He also used Rossman's theory in calculating the resulting stresses which compared favourably with those obtained experimentally. He is of the opinion that in the particular type of cases the value of effective width is greater than the full width of the slab.

The influence of orthogonal walls acting as flanges has been examined theoretically using the finite element method by Tso and Mahmoud (10). They used finite element technique to obtain the stiffness of slab-coupled shear wall system. The configurations of the wall systems included slab coupled planar walls, T-section walls and box core walls. Their final aim was to prepare design curves in terms of the effective width of the slab between shear walls. They pointed out the fact that the additional stiffening effect from the coupling slab is significant only when the wall

opening is small.

Huq (11) tested a number of steel models . He attempted to prepare a set of suitable design curves for effective width of slab in flate plate structures.He evaluated the effective width for different shapes of shear walls.He also evaluated effective width as a function of corridor width and width of the slab itself.According to his investigation effective width increases with increasing corridor width / slab width ratio.

Huq also tested a micro concrete model to find the variation of effective width of the slab with increase in load. Although no definite conclusions could be drawn from a single test ,he found that the strain and consequently stress across the slab is not uniform ,when it is subjected to lateral loads . The model failed along a transverse section passing through the interior edges of a wall. Also the effective width decreases with the increase in load .

Coull & Wong (12) analysed coupled shear walls with different shear wall configuration by finite element method and prepared a set of design curves .They investigated theoretically the variation of effective width of slab or stiffness with different geometrical layout parameters.The effective slab widths as a function of wall length, slab width,wall opening width for a pair of inline plane coupled shear wall configuration were evaluated .They concluded from the curves of Y_e/Y vs. W/L for the two raatios of $L/Y - 0.5$ and 1.5 that the effect of variation in wall length may be disregarded in the evaluation of effective width if the ratio of the shorter wall length to the wall opening is greater than 0.5 . It was also concluded that the influence of slab width is strong when Y/X is smaller than L/X ,but when Y/X is larger than L/X the influences of slab width diminishes rapidly. The influence of L/X on Y_e/X for a particular value of Y/X is almost identical to the influence of Y/X on Y_e/X for the same value of L/X . A generalized curve $Y_e/Y = L/Y(1-0.4L/Y)$ was also formulated to relate effective width with L/Y . The effective slab

widths were evaluated for flanged shear wall configuration and found that the presence of external wall flanges increases the effective width of the slab by less than 4% for the extreme case considered. It was concluded that the influence of external wall flanges may be safely disregarded. Typical non dimensional design curves for effective width of slab are shown in Fig. 2.4.

2.5. Nonlinear Analysis of Reinforced Concrete Structures

Nonlinear analysis of reinforced concrete needs suitable modelling of its behaviour, that is, modelling of concrete in its precracking and cracking stages and modelling of reinforcement. Although the steel behaviour is better defined and generally agreed upon, concrete behaviour shows considerable statistical scatter. A reinforced concrete model should handle suitably the cracking of concrete, crack propagation and yielding of steel.

Kotsovos (13,14,15,16) provided mathematical expressions for deformational as well as strength properties of concrete suitable for use in nonlinear computer based methods to analyze concrete structures after doing comprehensive investigations. Detailed description is given in chapter 4.

The parameters which have an effect on the numerical solution of nonlinear analysis are - mesh size, tension stiffening, tensile strength of concrete, angle of crack, shear retention factor of cracked concrete and the norm of convergence tolerance. The influences of the some of the above parameters were thoroughly investigated by Elnouno (17). Nonlinear analysis was also carried out by Bari (18) who found that the mesh size has insignificant effect on the strains upto the yield point, but it has a considerable effect on the failure load. For the slab model analyzed by him, it was found that the failure load decreases about 20% when mesh is refined from six to twelve elements.

The high convergence tolerance with no tension stiffening

model has a considerable advantage over the tension stiffening model in that it requires a smaller number of iterations to keep the residual forces within tolerance and hence less computer time. From previous study by Bari (18), it was found that the strains are not affected by the value of shear retention factor () upto yield point of steel but the ultimate failure load is affected.

Numerical treatment of postcracking behaviour of concrete was studied by Kabir (19). He proposed that after the formation of the numerical crack, the stress normal to the crack should be reduced gradually to account for the tension stiffening effect. Reducing the crack normal stress to zero soon after the formation of crack may significantly underestimate the actual behaviour. Treating concrete as a no tension material is perhaps not numerically desirable specially in the context of smeared cracking model (discussed in chapter 4). The conventional tension stiffening schemes are based on uniaxial stress relaxation procedures which depend on strains normal to crack. The adoption of a biaxial stress criterion for cracking and uniaxial stress decay for tension stiffening may lead to a mathematically inadmissible state of stress at a cracked point. To overcome such difficulty, an alternative simple scheme had been postulated by Kabir (19) which performed quite well. It should be noted that while this alternative scheme continuously decreases the crack normal stress in every subsequent iteration, it fails to correlate the strain normal to crack with the corresponding stress. Considering the complex nature of the crack propagation, such co-relation is not essential.

The nonlinear scheme was employed by Bari (18) to study the behaviour of shear wall slab junction. The wall was assumed to have zero thickness. To study the effect of wall thickness on the behaviour of slab, a nonlinear analysis was carried by him, which showed that the ultimate strength of the structure was slightly lower and stiffness was slightly higher considering the thickness of shear wall.

Bari (18) tested several models of shear wall floor slab junction to establish suitable design method for shear wall slab structure using shear reinforcement and verified the results by nonlinear 3-D finite element analysis. He considered the effect of lateral load as a concentrated load applied at the point of contraflexure of slab. He treated the slab as a cantilever extended from shear wall. Lateral load effect was applied as vertical load at the tip of the slab at point of contraflexure. From load deflection curve he tried to find the stiffness of the slab. He found that the stiffness of the slab gradually decreases as the load increases. This stiffness may not be considered as flexural stiffness of the slab because the wall does not rotate and slab deflect as a true cantilever from shear wall.

2.5. Conclusions

Reviewing the previous works, it is clear that all the investigator's doing research on bending stiffness of floor slab in shear wall structures perform their investigations considering the linear behaviour of slab material. Most of the Researcher's try to present suitable design curves and equations for calculating the effective width and stiffness of slab with respect to geometrical parameters such as Y/X , L/X or L/Y and effect of reinforcement is not considered. But reinforced concrete is a composite material which exhibit nonlinear response to progressive loading. Hence the behaviour of slab will be influenced by the factors responsible for nonlinear response with those of geometrical parameters.

CHAPTER 3

DESIGN OF REINFORCED CONCRETE SLABS

3.1 Introduction

There are a number of possible approaches to the analysis and design of reinforced concrete slab systems. The various approaches available are elastic theory, limit analysis theory and modifications to them. Such methods can be used to analyze a given slab system to determine either the stresses in the slabs and the supporting system or the load-carrying capacity. The methods can also be used to determine the distribution of moments and shears to allow the reinforcing steel and concrete sections to be designed.

3.2 Theory of Elasticity in Slab Design

Classical elastic theory of analysis applies to slabs which are sufficiently thin for shear deformations to be insignificant and sufficiently thick for in-plane forces to be unimportant. The distribution of moments and shears found by elastic theory is such that :

- (1) The equilibrium conditions are satisfied at every point in the slab.
- (2) The boundary conditions are complied with, and
- (3) Stress is proportional to strain; that is, bending moments are proportional to curvature.

The governing equation is a fourth-order partial differential equation in terms of the deflection of the slab at general point (x,y) on the slab, the loading on the slab, and the flexural rigidities of the slab section. The solution of the equation gives the distributions of bending and torsional moments and shear forces through the slab.

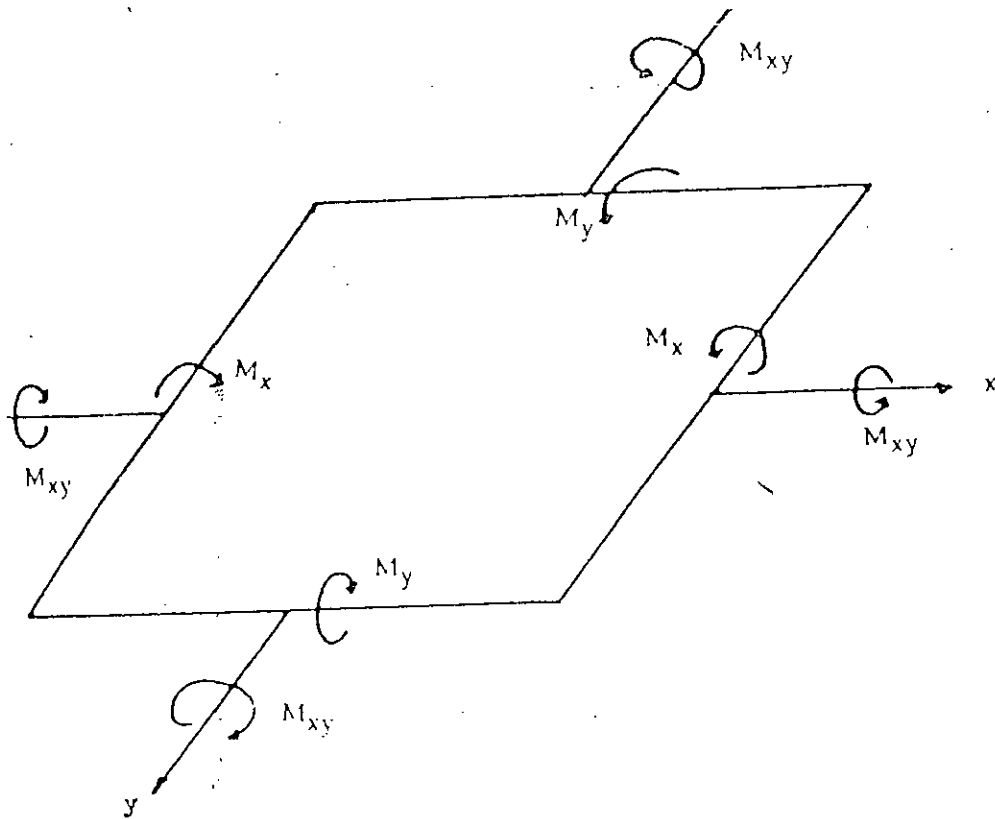


Fig. 3.1 : A typical slab under moment field.

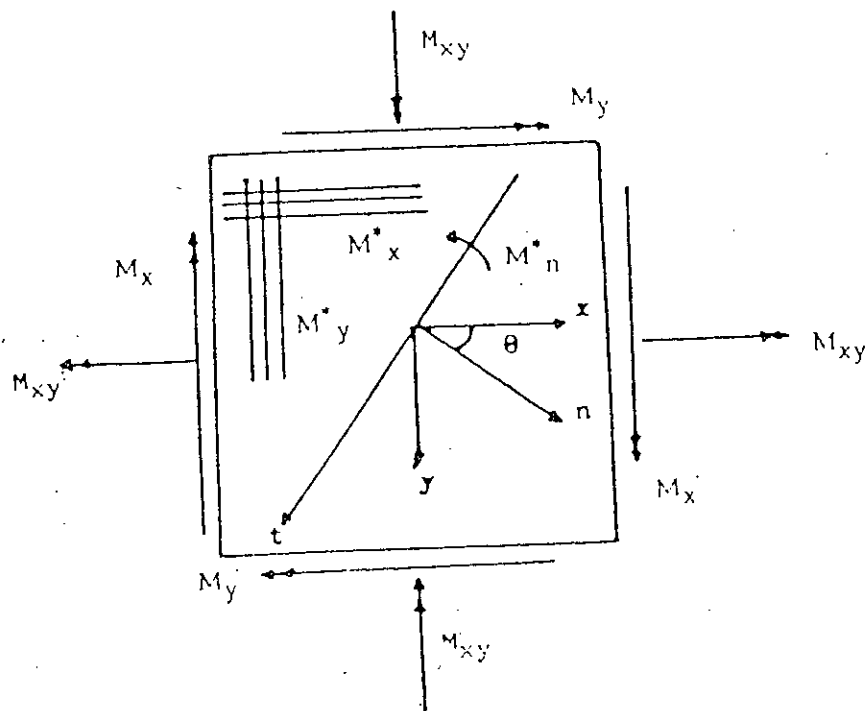


Fig. 3.2 : A typical slab element with orthogonal reinforcement.

3.3 Theory of Plasticity in Slab Design

This theory recognizes that because of plasticity, redistribution of moments and shears away from the elastic distribution can occur before the ultimate load is reached. Any solution to the ultimate load has to satisfy the following conditions of classical plasticity which assumes unlimited ductility :

a) The Equilibrium Condition : The internal stresses must be in equilibrium with the externally applied loads

b) The Yield Condition : The yield criteria defining the strength of the slab sections must nowhere be exceeded.

c) The Mechanism Condition : Under the ultimate load, sufficient plastic regions must exist to transform the structure into a mechanism.

If conditions (a) and (b) are satisfied we get a lower-bound solution. While on the other hand, if condition (c) is used in conjunction with virtual work, then we get an upper-bound solution.

3.4 The Yield Condition

The yield condition defines the combination of stresses necessary to cause plastic flow at a point. Let us Consider the slab element shown in Fig.3.1 under the moment field M_x , M_y and M_{xy} . The sign convention adopted here is such that all moments acting on the element are positive as shown in the Figure. The following simplifying assumptions are made in order to derive the yield criterion in terms of three moment components :

1. The concrete is assumed to have a zero tensile strength.
2. Bar diameters are small in comparison with slab depth, and that they can carry stresses only in their original direction. Accordingly, kinking of bars across a yield line is not considered.
3. The slab element is lightly reinforced, so that compression failure is not permissible and only ductile failures are allowed. This is necessary for moment redistribution, so

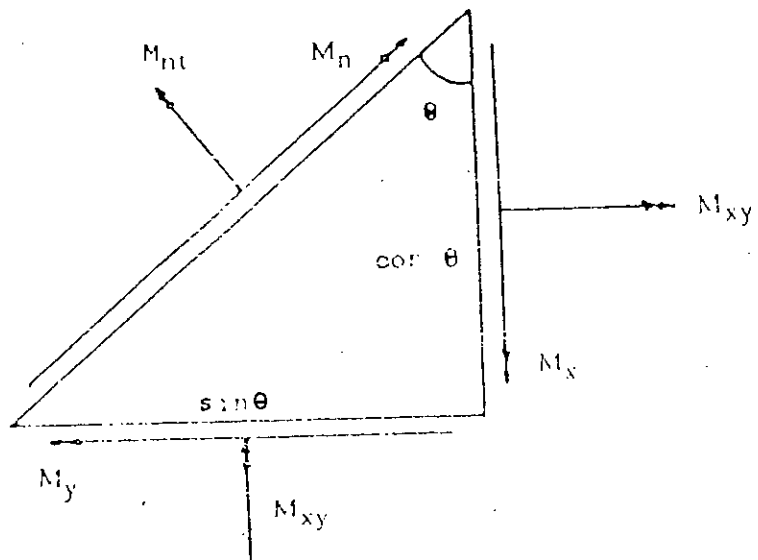


Fig. 3.3 : Equilibrium of a slab element under applied moment field.

that the slab elements can reach their ultimate strength at sufficient number of sections, to convert the slab into a mechanism.

4. Membrane forces do not exist. It is acknowledged that the coexistence of such forces with flexural fields on the slab elements, will considerably effect the resisting moment of the slab element depending on whether they are compressive or tensile and the restraint existing at the boundary of the slab.

For simplicity, the reinforcement in the element is assumed to lie parallel to the element sides as shown in Fig. 3.2. The element may be reinforced on the top and bottom surfaces. The basic idea is that, if at any point in the slab element (Fig. 3.2), a line with a normal n and direction t is examined, then the normal moment M_n , must not exceed the value M^*_n , where M^*_n is the moment of resistance that the reinforcement in the slab could develop in direction n . This is therefore a normal moment criterion.

Taking the normal to the yield line at an angle θ to the x -axis and considering the equilibrium of the element shown in Fig. 3.3, we shall have

$$M_n = M_x \cos^2 \theta + M_y \sin^2 \theta - M_{xy} \sin 2\theta \quad (3.1)$$

$$M_t = M_x \sin^2 \theta + M_y \cos^2 \theta - M_{xy} \sin 2\theta \quad (3.2)$$

$$M_{nt} = 1/2 (M_x - M_y) \sin 2\theta + M_{xy} \cos 2\theta \quad (3.3)$$

The normal moment M_n should be compared with the resisting moment M_n . This resisting moment at the yield line can be expressed assuming that both x and y steel are at yield, as follows :

$$M^*_n = M^*_x \cos^2 \theta + M^*_y \sin^2 \theta \quad (3.4)$$

where M^*_x = moment of resistance in x -direction.

M^*y = moment of resistance in y-direction.

The value of M^*n must always be greater than Mn , hence

$$(M^*n - Mn) = 0 \quad (3.5)$$

Substituting (3.1) and (3.4) in (3.5) we have

$$(M^*x - Mx)\cos^2\theta + (M^*y - My)\sin^2\theta + Mxy\sin 2\theta = 0 \quad (3.6)$$

dividing by $\cos\theta$

$$(M^*x - Mx) + (M^*y - My)\tan^2\theta + 2Mxy\tan\theta = 0 \quad (3.7)$$

At the yield line, the left hand side of equation (3.7) will be minimum. Differentiating with respect to $\tan\theta$, we have

$$2(M^*y - My)\tan\theta + 2Mxy = 0 \quad (3.8)$$

then

$$\tan\theta = -Mxy / (M^*y - My) \quad (3.9)$$

Substituting $\tan\theta$ in equation (3.7) and rearranging

$$(M^*x - Mx)(M^*y - My) = M^2_{xy} \quad (3.10)$$

This equation is the yield criterion for orthotropically reinforced concrete slabs. This is often called Wood-Armer (20,21) yield criterion.

3.5 Direct Design Method

With the widespread availability of finite element programs, it is possible to design slabs at ultimate load using elastic stress fields in conjunction with the Wood-Armer yield criteria for slabs (equation 3.10). This method called 'direct

design method' was suggested by Wood(20) and extended by Armer(21) and later applied and tested by Bari(18). The steps involved are as follows:

i) the elastic distribution of moments at ultimate load is determined by the finite element method.

ii) Using the moment triad (M_x, M_y, M_{xy}) thus obtained, the design moments are calculated so as to satisfy the yield criterion of equation (3.10).

iii) Flexural steel area is then calculated to resist the corresponding ultimate design moments M^*_x and M^*_y . The method satisfies the fundamental requirements of equilibrium, yield and mechanism conditions at ultimate collapse as dictated by classical plasticity theory as follows :

3.5.1 The Equilibrium Condition

To satisfy this condition, the elastic stresses must be in equilibrium with external loads. Since the distribution of stresses in this method is found using finite element method which is derived from equilibrium equations, this condition is automatically satisfied. Owing to its simplicity and versatility, the method can be applied to any type of slab problem with any edge condition.

3.5.2 The Yield Condition

Having obtained M_x, M_y, M_{xy} we have to derive M^*_x and M^*_y so as not to violate the yield condition as given by equation (3.10). This can be done as follows:

(i) if $M^*_y = 0$ then $M^*_x = M_x - M^2_{xy}/M_y$

ii) if $M^*_x = 0$ then $M^*_y = M_y - M^2_{xy}/M_x$

iii) if M^*_x and M^*_y not equal to zero;

We need to find minimum of $(M^*x + M^*y) = f$

From equation (3.10) : $M^*y = M^2_{xy}/(M^*x - Mx) + My$

$$f = [M^*x + (M^2_{xy}/(M^*x - Mx)) + My] \quad (3.11-a)$$

For minimum or maximum of 'f'; $\delta(f)/\delta M^*x = 0$

$$\text{i.e., } 1 - M^2_{xy}/(M^*x - Mx)^2 = 0$$

$$\text{or } (M^*x - Mx) = + |Mxy| \quad (3.11-b)$$

For minimum of 'f' ; $\delta^2 f / \delta M^*x^2 = +ve$

$$\text{or } M^2_{xy}/(M^*x - Mx)^3 > 0; \text{ or } (M^*x - Mx) > 0$$

Taking positive sign from equation (3.11-b), we have

$$M^*x - Mx = |Mxy|$$

$$M^*x = Mx + |Mxy| \quad (3.11-c)$$

From equation (3.10),

$$M^*y = My + |Mxy| \quad (3.12)$$

For positive moment fields;

$$M^*x = 0 \quad \text{when } Mx = - |Mxy|$$

$$M^*y = 0 \quad \text{when } My = - |Mxy|$$

Both M^*x and $M^*y = 0$ when $Mx, My = M^2_{xy}$

3.5.3 Rules for Placing Orthogonal Reinforcement

3.5.3.1 Bottom Steel

(a) Compute the normal design moments

$$M^*_x = M_x + |M_{xy}| \quad (3.13)$$

$$M^*_y = M_y + |M_x| \quad (3.14)$$

if $M^*_x < 0$ then

$$M^*_y = M_y - (M^2_{xy}/M_x) \text{ with } M^*_x = 0 \quad (3.15)$$

if $M^*_y < 0$ then

$$M^*_x = M_x - (M^2_{xy}/M_y) \text{ with } M^*_y = 0 \quad (3.16)$$

(b) If still in (3.15) and (3.16) one gets a negative sign, then put such normal moment equal to zero, i.e., no reinforcement is required.

(c) If both M^*_x and M^*_y are negative, then no bottom steel is required.

3.5.3.2 Top Steel

(a) Compute the normal moments

$$M^*_x = M_x - |M_x| \quad (3.17)$$

$$M^*_y = M_y - |M_{xy}| \quad (3.18)$$

if $M^*_x > 0$ then

$$M^*_y = M_y - (M^2_{xy}/M_x) \text{ with } M^*_x = 0 \quad (3.19)$$

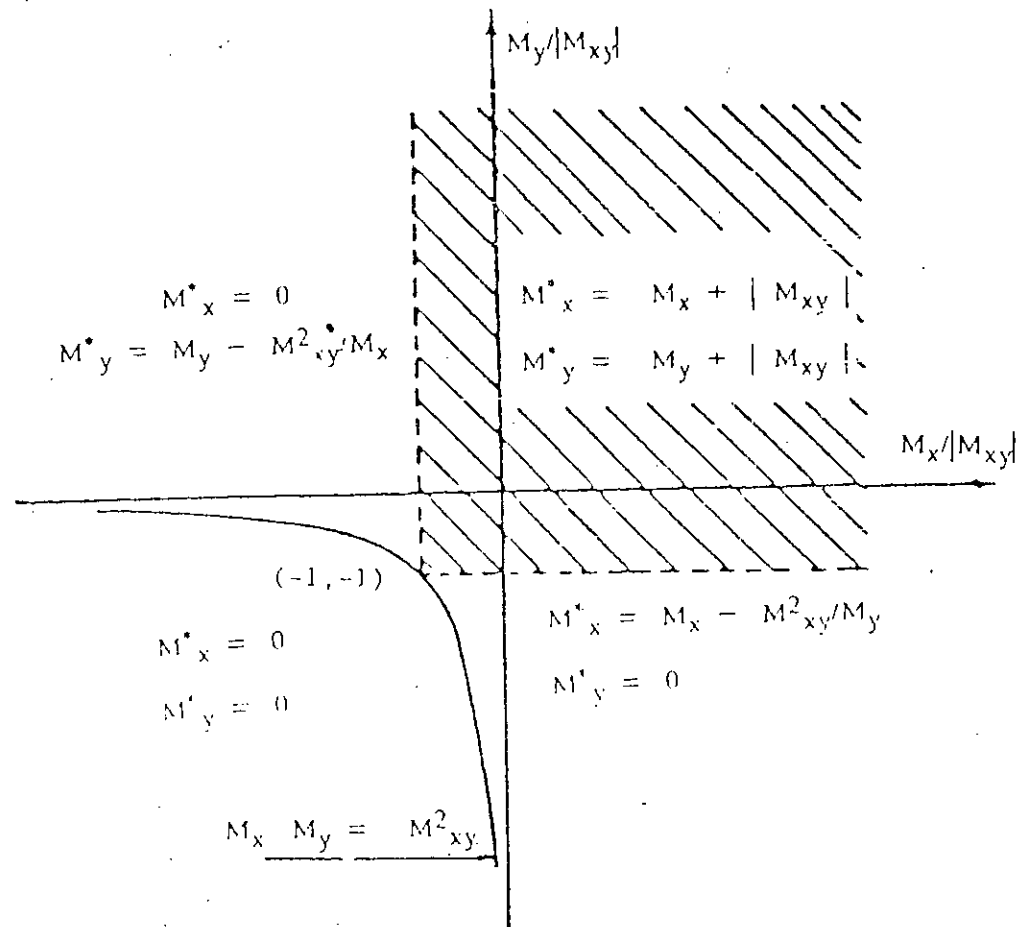


Fig. 3.4 : Design equations for bottom steel.

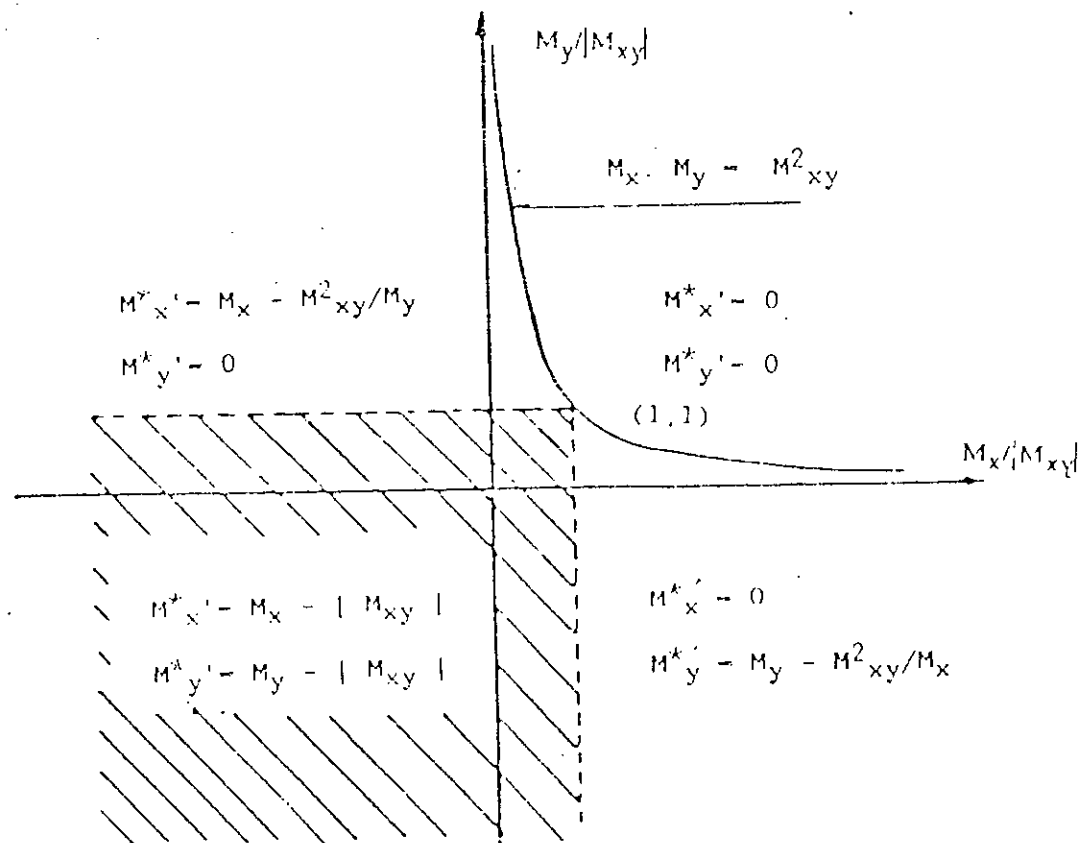


Fig. 3.5 : Design equations for top steel.

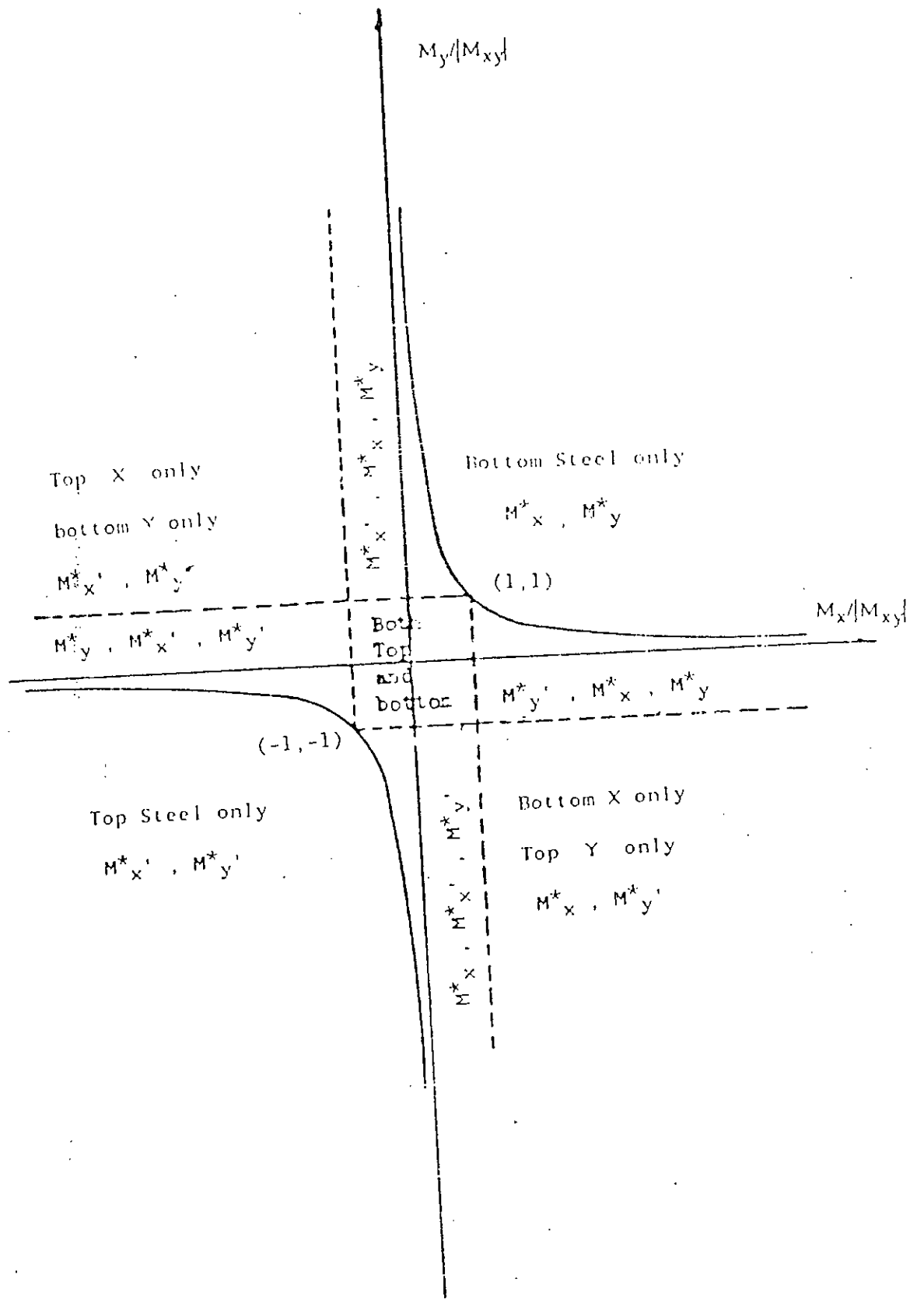


Fig. 3.6 : Reinforcement required for a given moment triad.

if $M^*y > 0$ then

$$M^*x = Mx - (M^2_{xy}/My) \quad \text{with} \quad M^*y = 0 \quad (3.20)$$

(b) If still in (3.19) and (3.20) one gets a positive sign, then put such normal moment equal to zero, i.e., no reinforcement is required.

(c) If both M^*x and M^*y are positive, then no top steel is required.

Figs.3.4 to 3.6 give a detailed picture of these rules. For general use, the diagrams are sketched in a nondimensional form. The designer, after establishing the point $(Mx/|M_{xy}|, My/|M_{xy}|)$ on the diagram, can easily know which equation to use to get the required design normal moments. Bottom steel equations are given in Fig.3.4, while those for top steel in Fig.3.5. Fig. 3.6 shows the two branches of the yield hyperbola and indicates the directions of the steel to be provided at any point. (Primed moments refer to top steel).

A two dimensional finite element computer programme based on this direct design approach was used to calculate the flexural reinforcement needed in the slab. The flow chart is shown in Fig. 3.7.

3.5.4 The Mechanism Condition

Because the necessary resistance is made equal to the calculated stress at every point in the slab, it is anticipated that all slab parts will attain their ultimate strength under the design load. Accordingly with minimum amount of redistribution, every point will yield at the design load, thus converting the slab into mechanism. Because of the fact that minimum redistribution is needed to achieve collapse by this method, the demand for ductility which depends on the difference between the first and last yield in the structure as normally emphasized by the theory of plasticity will obviously drop.

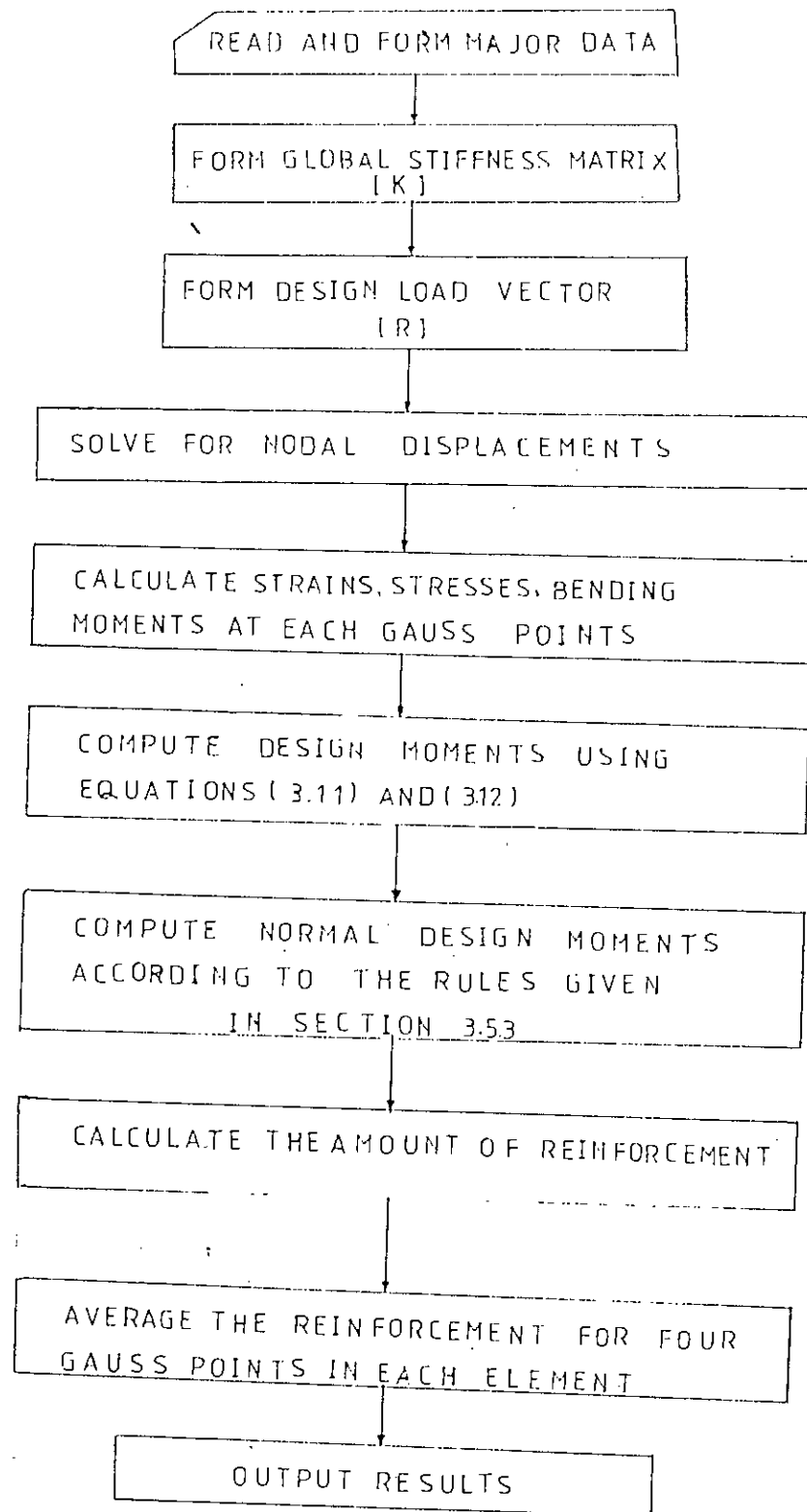


Fig. 3.7: FLOW CHART OF THE PROGRAMME

3.6. Procedure Adopted for the design of a typical model

3.6.1. General

In this article a general procedure of designing slab reinforcements will be discussed which was followed. A linear 2-D finite element computer programme based on direct design approach was used to calculate the flexural reinforcements for gravity and lateral loads. The slabs were divided into an assembly of plate bending elements having three degrees of freedom at each node and advantages of symmetry were used in analyzing the slabs. A floor plane of a typical shear wall structure is shown in Fig. 1.4(a).

3.6.2. Design for gravity loads

Gravity loads include selfweight of slab and live load. A live load of 40 psf was used in design. Finite element mesh used in gravity load design is shown in Fig. 3.8. A complete panel was used by divided it into 24 elements. The boundary conditions used are as follows:

If w = translation in z -direction (normal to paper)

$$\delta w / \delta x = \text{rotation about } y\text{-axis;}$$

$$\delta w / \delta y = \text{rotation about } x\text{-axis;}$$

then all the nodes along line ab, cd, ef and gh will have

$w = \delta w / \delta x = \delta w / \delta y = 0$; and all nodes along line bc and fg will have $\delta w / \delta x = 0$.

Gravity load per node was calculated from the area of slabs surrounding that node. By applying loads per each node we had the reinforcements required for the slab were determined. A slab of 200 mm thickness was used for all the models.

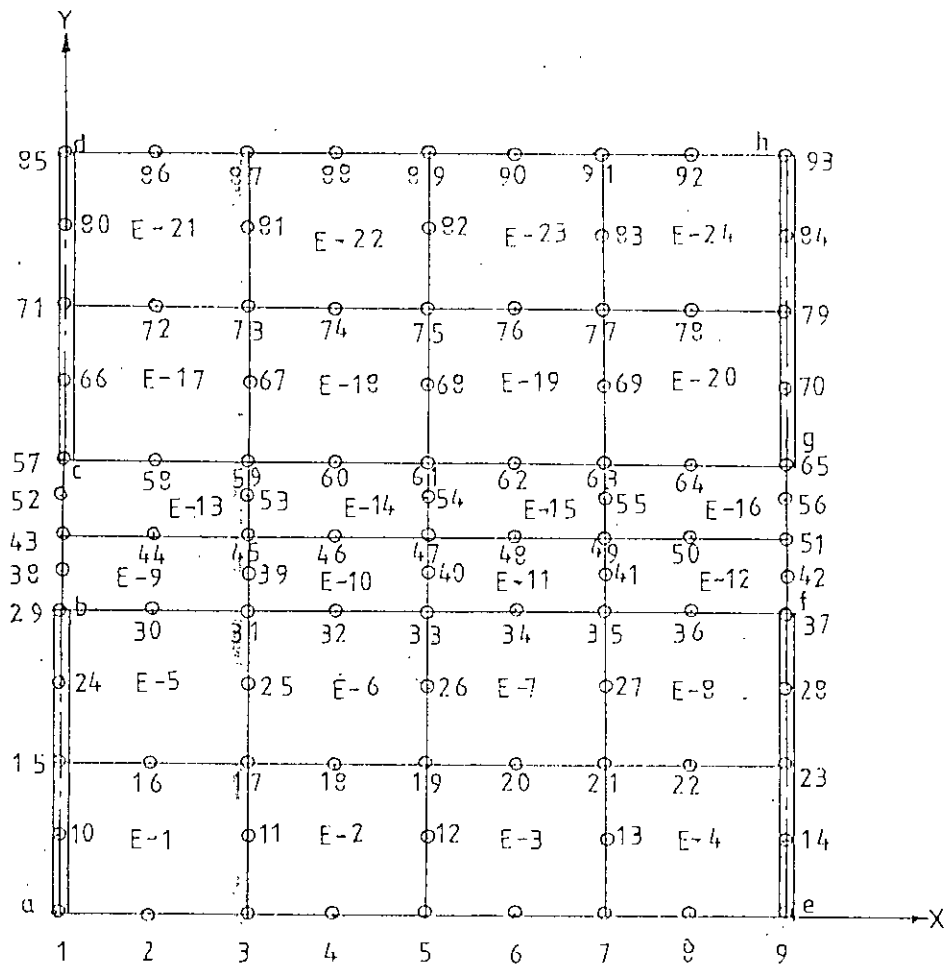


Fig. 3.8 : Finite Element Mesh for Gravity Load

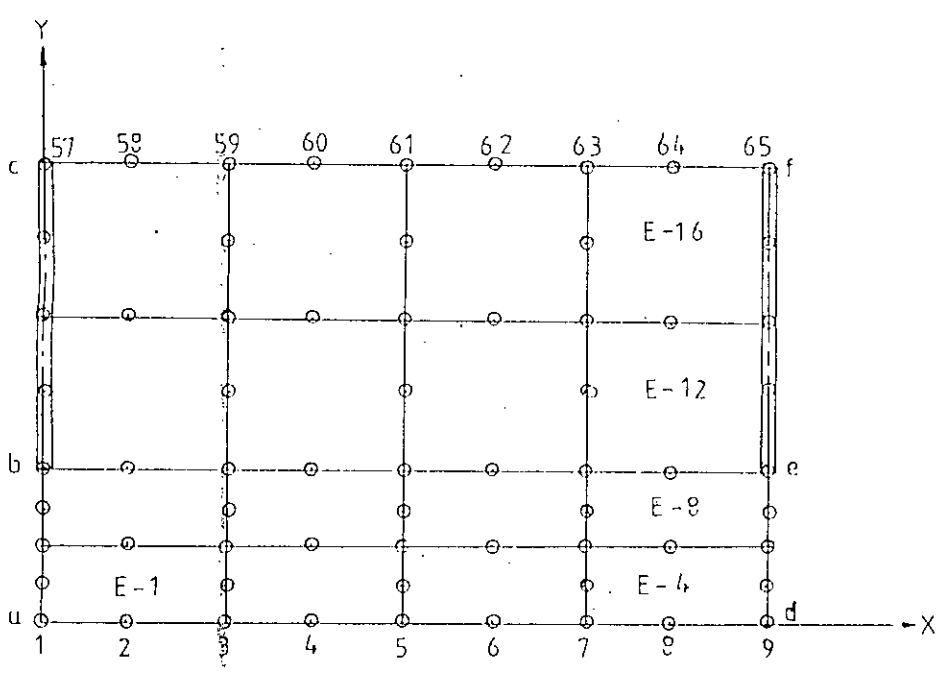


Fig. 3.9: Finite Element Mesh for Wind Load

3.6.3. Design for lateral load

An equivalent static wind load of 0.6 kip/feet was used. Assuming the wind pressure to be constant with height, the maximum wind shear V_w , induced in most highly stressed slab was calculated by continuous medium method making use of the recommendations of Coull and Wong for the effective width (see Figs. 2.4). A slab thickness of 200 mm and a floor to floor height of 3m were adopted to analyze all the structures having 20 storeys with rectangular shear walls. Fig. 3.9 shows the finite element mesh for wind load design where use of symmetry was made. The boundary conditions used are as follows: all nodes along line bc and ef will have $w = \delta w / \delta x = \delta w / \delta y = 0$; and all nodes along line ab, and de will have $\delta w / \delta x = 0$. The slab was then designed by applying the maximum wind shear V_w distributing it among the nodes along line ad. For two cases: applying V_w downward and upward, reinforcements in the slabs were found out.

3.6.4. Determination of combined effect

At the centre of each element, the computer programme gave the moment triad (M_x, M_y, M_{xy}) due to wind and gravity loadings. Using the moment triad, the values of design moments M^*_x, M^*_y were evaluated according to the design method. Flexural steel required to resist these design moments at ultimate conditions was calculated using the recommendations of BS 8110 with materials safety factors assumed to be unity. The finite element programme results in a variable reinforcement pattern and the amount of steel given were per element. For example, amount of steel in Model TMO1 for gravity and two cases of wind loading are shown in Fig. 3.10. Only quarter panel is shown because for nonlinear 3-D analysis only one quarter of a complete panel was used taking the advantage of symmetry and antisymmetry. To find the total steel in an element maximum of the two cases due to wind was added to that due to gravity. Now crossing suitable bars reinforcements were placed in the slab.

T=508 B=0	T=0 B=462
T=434 B=0	T=0 B=422
T=178 B=0	T=0 B=172

Flexural steel (in mm²)
due to gravity load

T=144 B=0	T=0 B=119
T=272 B=0	T=0 B=173
T=180 B=0	T=0 B=122

Flexural steel due to
downward wind shear

T=150 B=0	T=0 B=150
T=113 B=51	T=0 B=121
T=0 B=68	T=27 B=0

Flexural steel due to
upward wind shear

T=658 B=0	T=0 B=612
T=706 B=51	T=0 B=594
T=358 B=68	T=27 B=294

Total steel (in mm²)

T=562 B=562	T=562 B=562
T=562 B=562	T=562 B=562
T=258 B=258	T=258 B=258

Steel provided (in mm²)

Fig. 3.10: Reinforcement Calculation for Model TMOD1

CHAPTER 4

MODELLING OF NONLINEAR BEHAVIOUR OF REINFORCED
CONCRETE USING FINITE ELEMENT TECHNIQUE

4.1 Introduction

In recent years, the finite element method is firmly established as the most powerful general method for structural analysis and has provided engineers with a design tool of very wide applicability. In the case of reinforced concrete cracking, tension stiffening, nonlinear multiaxial material properties, complex interface behaviour, creep, shrinkage and other effects were previously ignored or treated in a very approximate manner. All those parameters can now be considered rationally by finite element method. The application of the finite element method to nonlinear problems is associated with a considerable increase in numerical work as compared with linear problems. However, development in the last two decades have ensured that high speed digital computers which meet this need are now available. In this chapter, an approach for three dimensional nonlinear finite element analysis of reinforced concrete is presented.

4.2. Finite Element Formulation

The finite element method is now well documented, no attempt will be made to describe it in detail. But in order to define terms for the sake of completeness a brief review of the method will be presented instead.

4.2.1 Discretisation by Finite Element

The finite element method started as an extension of the stiffness method of analysis of skeletal structures and was applied to two and three dimensional problems in structural

mechanics. However, unlike skeletal structures, there are no well-defined joints where equilibrium of forces can be established. So the continuum is divided into a series of elements of arbitrary shapes which are connected at a finite number of points known as nodal points. This process is known as discretisation.

For structural applications, one convenient method of obtaining the governing equilibrium equations is by minimizing the total potential energy of the system. The total potential energy, π , can be expressed as :

$$\pi = \int_V [\sigma]^T [\epsilon] dv - \int_V [\delta]^T [p] dv - \int_S [\delta]^T [q] ds \quad (4.1)$$

where $[\sigma]$ and $[\epsilon]$ are the stress and strain vectors respectively, $[\delta]$ the displacements at any point, $[p]$ the body force per unit volume and $[q]$ the applied surface tractions. Integrations are carried over the volume 'V' of the structure and loaded surface area 'S'. The first term on the right hand side of equation (4.1) represents the internal strain energy and the second and third terms are respectively the work contributions of the body forces and distributed surface loads. In the finite element displacement method, the displacement is assumed to have unknown values only at the nodal points so that the variation within any element is described in terms of the nodal values by means of interpolation functions.

$$\text{Thus} \quad [\delta] = [N] [\delta^e] \quad (4.2)$$

where $[N]$ is the set of interpolation functions termed as shape functions and $[\delta^e]$ the vector of nodal displacements of the element. The strains within the element can be expressed in terms of the element nodal displacements as

$$[\epsilon] = [B] [\delta^e] \quad (4.3)$$

where $[B]$ is the strain matrix generally composed of derivatives of shape functions. Finally, the stress may be related to the strains by use of an elasticity matrix $[D]$ as follows

$$[\sigma] = [D] \cdot [\epsilon] \quad (4.4)$$

Provided that no singularities exist in the integrands of the functional, the total potential energy of the continuum will be the sum of the energy contributions of the individual elements.

Thus

$$\pi = \sum \pi_e \quad (4.5)$$

where π_e represents the total potential of element 'e' which, using equation (4.1), can be written as

$$\begin{aligned} \pi_e = & \frac{1}{2} \int_{V_e} \{\delta^e\}^T [B]^T [D] [B] \{\delta^e\} dV - \\ & \int_{V_e} \{\delta^e\}^T [N]^T [p] dV - \int_{S_e} \{\delta^e\}^T [N]^T [q] ds \end{aligned} \quad (4.6)$$

where V_e is the element volume and S_e the loaded element surface area. Performance of minimisation for element 'e' with respect to the nodal displacement $\{\delta^e\}$ for the element results in

$$\begin{aligned} \frac{\partial \pi_e}{\partial \delta^e} = & \int_{V_e} ([B]^T [D] [B]) \{\delta^e\} dV - \int_{V_e} [N]^T [p] dV - \int_{S_e} [N]^T [q] ds \quad (4.7) \\ = & [K^e] \{\delta^e\} - [F^e] \end{aligned}$$

where

$$[F^e] = \int_{V_e} [N]^T [p] dV + \int_{S_e} [N]^T [q] ds \quad (4.8)$$

are the equivalent nodal forces, and

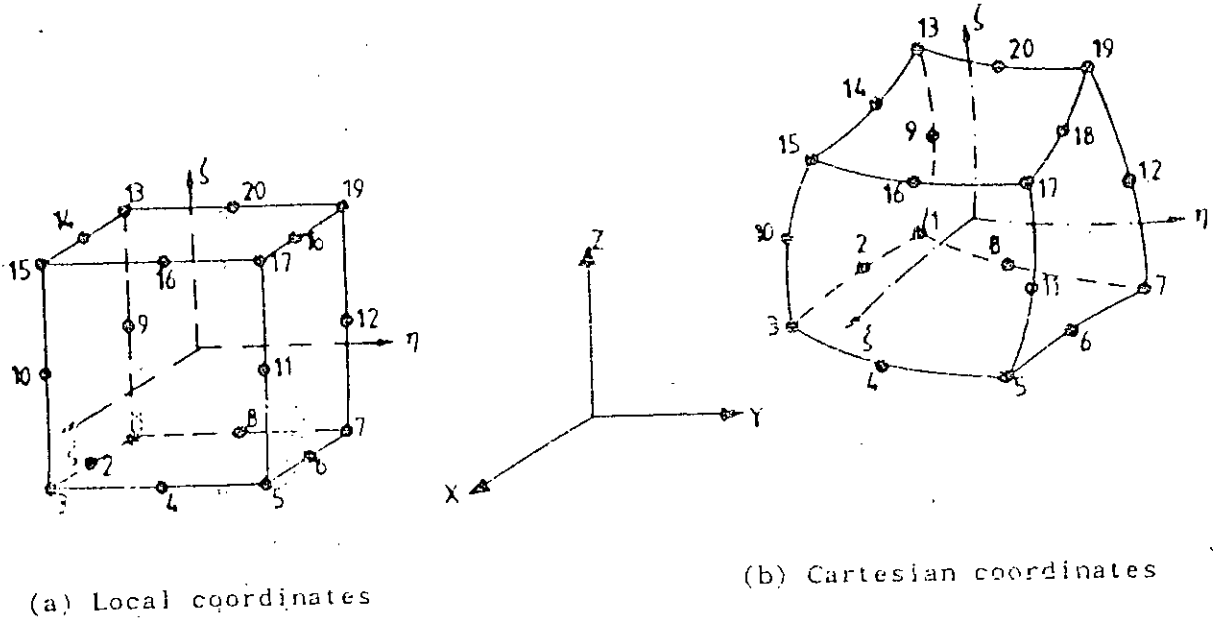


Fig. 4.1 : 20-Noded isoparametric brick element

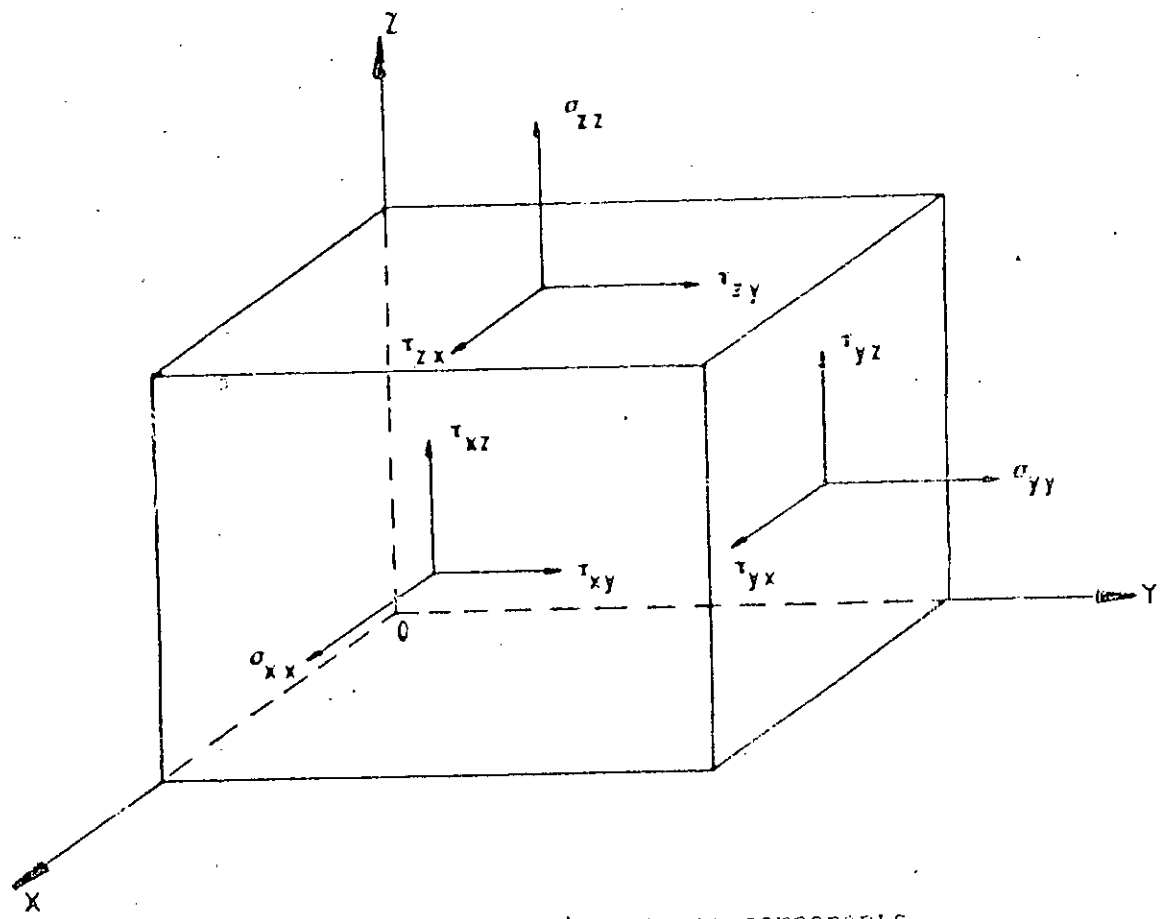


Fig. 4.2 : Cartesian stress components

$$[K^e] = \int_{V_c} [B]^T [D] [B] \quad (4.9)$$

is termed the 'element stiffness matrix'. The summation of the terms in equation (4.7) over all the elements, when equated to zero, results in a system of equilibrium equations for the complete continuum. These equations are then solved by any standard technique to yield the nodal displacements. The strains and therefore the stresses within each element can be calculated from the displacements using equations (4.3) and (4.4).

4.2.2 Element Type

The selection of the element type is always related to the type of problems to be solved. As three dimensional nonlinear analysis is the prime concern of the analytical portion of this study, the 20-noded isoparametric brick element as illustrated in Fig.4.1, is used throughout this work to represent concrete. Reinforcing steel is simulated by bars embedded inside the concrete element at their actual locations in the structure without imposing any restrictions on the mesh choice. The mathematical derivations of these bars can be found in Reference (17). This element was chosen to consider the effect of the six stress components σ_x , σ_y , σ_z , τ_{xy} , τ_{yz} , τ_{zx} (Fig. 4.2). Each nodal point has three degrees of freedom, viz., translation in x-direction = u, translation in y-direction = v, and translation in z-direction = w. Each element has its own local spatial coordinate system (ξ, η, ζ) (Fig. 4.1), with the origin at the centre of element such that each local coordinate ranges from -1 to +1 only.

4.2.3 Shape Functions

Shape functions are interpolation functions which describe the variation within the element of the displacement in terms of

the nodal displacement

$$[\delta] = \sum_{i=1}^n [N_i] [\delta_i] \quad (4.10)$$

where N_i is the shape function at the i -th node at which the nodal displacement is δ_i .

The efficiency of any particular element type will depend on how well the shape functions are capable of representing the true displacement field. The isoparametric family are a group of elements in which the shape functions are used to define the geometry as well as the displacement field. This leads to reduced computational effort and efficiency. The isoparametric elements are better known for their accuracy and versatility over simpler type of elements. Moreover a considerable saving of computer effort is obtained, even though a complex element requires more time to formulate. This is because it requires fewer elements compared with more simple elements.

For three dimensional applications, the displacements field at a particular local coordinate (ξ, η, ζ) are $u(\xi, \eta, \zeta)$, $v(\xi, \eta, \zeta)$,

$w(\xi, \eta, \zeta)$ and are defined using three displacements degrees of freedom u_i, v_i, w_i at each of the twenty nodes and a quadratic interpolation scheme. The coordinate values $x(\xi, \eta, \zeta)$, $y(\xi, \eta, \zeta)$ and $z(\xi, \eta, \zeta)$ at any point (ξ, η, ζ) within the element may be defined by the expressions :

$$\begin{aligned} x(\xi, \eta, \zeta) &= \sum_{i=1}^{20} N_i(\xi, \eta, \zeta) \cdot x_i \\ y(\xi, \eta, \zeta) &= \sum_{i=1}^{20} N_i(\xi, \eta, \zeta) \cdot y_i \\ z(\xi, \eta, \zeta) &= \sum_{i=1}^{20} N_i(\xi, \eta, \zeta) \cdot z_i \end{aligned} \quad (4.11)$$

and where (x_i, y_i, z_i) are the coordinates of node 'i' and $N_i(\xi, \eta, \zeta)$ are three dimensional quadratic shape functions. In the present work, such shape functions of each of the twenty nodes were obtained from reference(16) as follows :

For corner nodes $\xi_i = \pm 1$ $\eta_i = \pm 1$ $\zeta_i = \pm 1$

$$N_i(\xi, \eta, \zeta) = \frac{1}{8} (1 \pm \xi \xi_i)(1 \pm \eta \eta_i)(1 \pm \zeta \zeta_i) (\xi \xi_i + \eta \eta_i + \zeta \zeta_i - 2) \quad (4.12)$$

For mid-side node $\xi_i = \pm 0$ $\eta_i = \pm 1$ $\zeta_i = \pm 1$

$$N_i(\xi, \eta, \zeta) = \frac{1}{4} (1 - \xi^2)(1 + \eta \eta_i)(1 + \zeta \zeta_i) \quad (4.13)$$

For mid-side node $\xi_i = \pm 1$ $\eta_i = \pm 0$ $\zeta_i = \pm 1$

$$N_i(\xi, \eta, \zeta) = \frac{1}{4} (1 + \xi \xi_i)(1 - \eta^2)(1 + \zeta \zeta_i) \quad (4.14)$$

For mid-side node $\xi_i = \pm 1$ $\eta_i = \pm 1$ $\zeta_i = \pm 0$

$$N_i(\xi, \eta, \zeta) = \frac{1}{4} (1 + \xi \xi_i)(1 + \eta \eta_i)(1 - \zeta^2) \quad (4.15)$$

Each of the twenty shape function has a value of unity at the node to which it is related and zero at other nodes. To calculate the displacements $u(\xi, \eta, \zeta)$, $v(\xi, \eta, \zeta)$ and $w(\xi, \eta, \zeta)$ at any point within the element, expressions similar to (4.10) may be written as follows :

$$\begin{aligned} u(\xi, \eta, \zeta) &= \sum_{i=1}^{20} N_i(\xi, \eta, \zeta) \cdot u_i \\ v(\xi, \eta, \zeta) &= \sum_{i=1}^{20} N_i(\xi, \eta, \zeta) \cdot v_i \\ w(\xi, \eta, \zeta) &= \sum_{i=1}^{20} N_i(\xi, \eta, \zeta) \cdot w_i \end{aligned} \quad (4.16)$$

4.2.4 Strain Matrix

In three dimensional linear analysis, the strain - displacement relationship from theory of elasticity may be written as

$$\begin{aligned}
 \epsilon_x &= \partial u / \partial x \\
 \epsilon_y &= \partial v / \partial y \\
 \epsilon_z &= \partial w / \partial z \\
 \gamma_{xy} &= \partial u / \partial y + \partial v / \partial x \\
 \gamma_{yz} &= \partial v / \partial z + \partial w / \partial y \\
 \gamma_{zx} &= \partial w / \partial x + \partial u / \partial z
 \end{aligned}
 \tag{4.17}$$

in which $\epsilon_x, \epsilon_y, \epsilon_z$ are the normal strain components and $\gamma_{xy}, \gamma_{yz}, \gamma_{zx}$ are the shear strain components. Equations (4.17) may be written in matrix form as follows:

$$[\epsilon] = \begin{bmatrix} \epsilon_x \\ \epsilon_y \\ \epsilon_z \\ \gamma_{xy} \\ \gamma_{yz} \\ \gamma_{zx} \end{bmatrix} = \begin{bmatrix} \partial / \partial x & 0 & 0 \\ 0 & \partial / \partial y & 0 \\ 0 & 0 & \partial / \partial z \\ \partial / \partial y & \partial / \partial x & 0 \\ 0 & \partial / \partial z & \partial / \partial y \\ \partial / \partial z & 0 & \partial / \partial x \end{bmatrix} \begin{bmatrix} u \\ v \\ w \end{bmatrix}
 \tag{4.18}$$

using the finite element idealisation we can write

$$[\epsilon] = \sum_{i=1}^{20} \begin{bmatrix} \partial N_i / \partial x & 0 & 0 \\ 0 & \partial N_i / \partial y & 0 \\ 0 & 0 & \partial N_i / \partial z \\ \partial N_i / \partial y & \partial N_i / \partial x & 0 \\ 0 & \partial N_i / \partial z & \partial N_i / \partial y \\ \partial N_i / \partial z & 0 & \partial N_i / \partial x \end{bmatrix} \begin{bmatrix} u_i \\ v_i \\ w_i \end{bmatrix} \quad (4.19)$$

or simply

$$[\epsilon] = \sum_{i=1}^{20} [B_i] [\delta_i] \quad (4.20)$$

where $[B_i]$ is the 6×3 strain matrix in equation (4.19) which contains the cartesian derivatives of the shape functions. Since the shape functions N_i are defined in terms of the local coordinates of the element (ξ, η, t) a transformation from local to global coordinates is required to obtain the $[B]$ matrix in equation (4.19). This is done through the well known Jacobian matrix which is written as

$$[J] = \begin{bmatrix} \partial x / \partial \xi & \partial y / \partial \xi & \partial z / \partial \xi \\ \partial x / \partial \eta & \partial y / \partial \eta & \partial z / \partial \eta \\ \partial x / \partial t & \partial y / \partial t & \partial z / \partial t \end{bmatrix} \quad (4.21)$$

thus

$$[J] = \sum_{i=1}^{20} \begin{bmatrix} \frac{\partial N_i}{\partial \xi} \cdot x_i & \frac{\partial N_i}{\partial \xi} \cdot y_i & \frac{\partial N_i}{\partial \xi} \cdot z_i \\ \frac{\partial N_i}{\partial \eta} \cdot x_i & \frac{\partial N_i}{\partial \eta} \cdot y_i & \frac{\partial N_i}{\partial \eta} \cdot z_i \\ \frac{\partial N_i}{\partial \zeta} \cdot x_i & \frac{\partial N_i}{\partial \zeta} \cdot y_i & \frac{\partial N_i}{\partial \zeta} \cdot z_i \end{bmatrix} \quad (4.22)$$

The inverse of the jacobian matrix will be

$$[J]^{-1} = \begin{bmatrix} \frac{\partial \xi}{\partial x} & \frac{\partial \eta}{\partial x} & \frac{\partial \zeta}{\partial x} \\ \frac{\partial \xi}{\partial y} & \frac{\partial \eta}{\partial y} & \frac{\partial \zeta}{\partial y} \\ \frac{\partial \xi}{\partial z} & \frac{\partial \eta}{\partial z} & \frac{\partial \zeta}{\partial z} \end{bmatrix} \quad (4.23)$$

Therefore the cartesian derivatives are given by

$$\begin{bmatrix} \frac{\partial N_i}{\partial x} \\ \frac{\partial N_i}{\partial y} \\ \frac{\partial N_i}{\partial z} \end{bmatrix} = [J]^{-1} \begin{bmatrix} \frac{\partial N_i}{\partial \xi} \\ \frac{\partial N_i}{\partial \eta} \\ \frac{\partial N_i}{\partial \zeta} \end{bmatrix} \quad (4.24)$$

4.2.5 Stress - Strain Relationship

For linear analysis of uncracked concrete, and in the absence of initial stresses and strains, the stress-strain relationship may be written in the form

$$[\sigma] = [D] [\epsilon] \quad (4.25)$$

where [D] is the elasticity matrix which takes the form

$$[D] = \frac{E(1-\nu)}{(1+\nu)(1-2\nu)} \begin{bmatrix} 1 & \frac{\nu}{(1-\nu)} & \frac{\nu}{(1-\nu)} & 0 & 0 & 0 \\ & 1 & \frac{\nu}{(1-\nu)} & 0 & 0 & 0 \\ & & 1 & 0 & 0 & 0 \\ & & & \frac{(1-2\nu)}{2(1-\nu)} & 0 & 0 \\ \text{Symmetry} & & & & \frac{(1-2\nu)}{2(1-\nu)} & 0 \\ & & & & & \frac{(1-2\nu)}{2(1-\nu)} \end{bmatrix} \quad (4.26)$$

where 'E' is the Young's modulus of elasticity and ν is Poisson's ratio. The concrete nonlinearity as considered in this work is only the material nonlinearity and all changes in material properties enter through the changes in elasticity matrix [D].

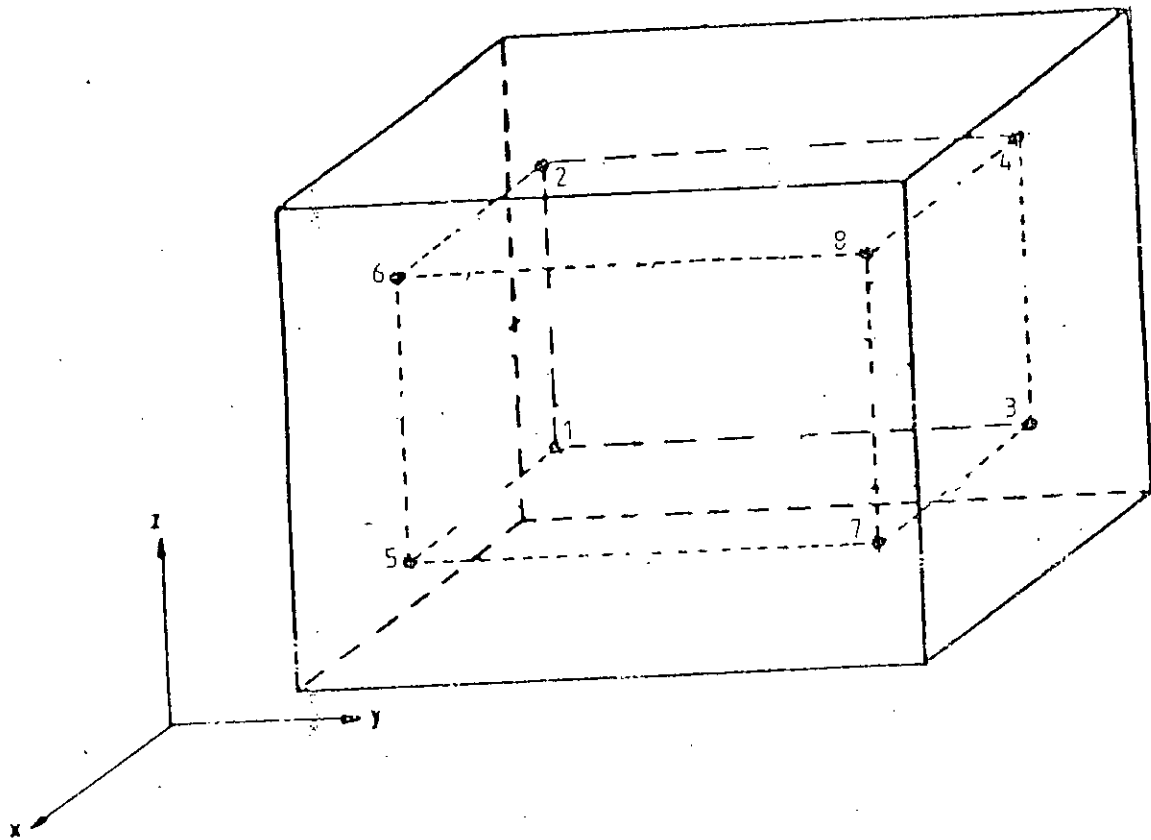


Fig. 4.3 : Location of Gauss points for the integration rule; those for the $4 \times 4 \times 4$ rules follow the same order and

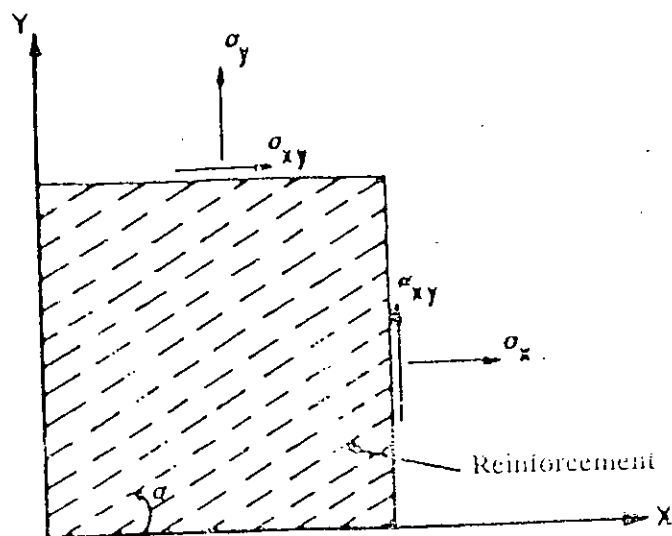


Fig. 4.4 (a) : Distributed representation of steel

4.2.6 Numerical Integration

Analytical integration of equation (4.9) is impossible. Therefore some form of numerical integration must be resorted to. In this study Gauss-Legendre quadrature rules have been used exclusively because of their higher efficiency over other forms of quadrature. For n sampling points they can integrate exactly a polynomial $f(\epsilon)$ of degree $(2n-1)$. Also they are suitable for isoparametric elements because the range of these integration rules are ± 1 on element boundaries. A $2 \times 2 \times 2$ Gauss rule was used for monitoring nonlinear behaviour especially cracking, as shown in Fig.4.3.

4.3 Simulation of Steel Reinforcement

In modelling reinforced concrete by finite element methods, at least the following three alternative representations of the reinforcement have been used: (a) distributed, (b) discrete and (c) embedded. For a distributed representation (Fig. 4.4(a)), the steel is assumed to be distributed over the concrete element, with a particular orientation angle. A composite concrete reinforcement constitutive relation need to be used in this case. To derive such a relation, perfect bond must be assumed between the concrete and steel. A discrete representation of the reinforcement, using one-dimensional elements (Fig. 4.4(b)), has been widely used. Axial force members are assumed to be pin connected with three degrees of freedom at the nodal points. The one-dimensional reinforcement element is superimposed on a three dimensional finite element mesh representing concrete. The approach is simple and it is possible to account for possible displacement of the reinforcement with respect to the surrounding concrete. A serious disadvantage, however, is that the location of steel often dictates the concrete mesh. This may result in slender elements, where the reinforcing bars are too close

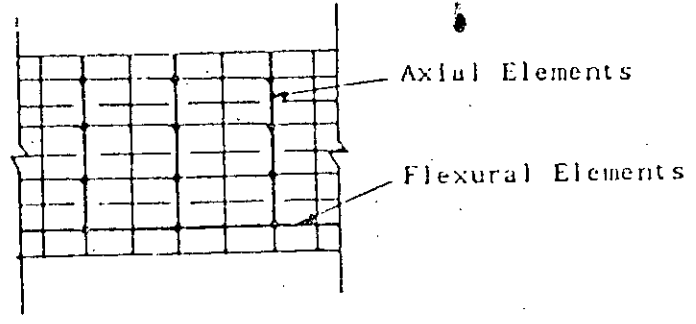


Fig. 4.4 (b) : Discrete representation of steel

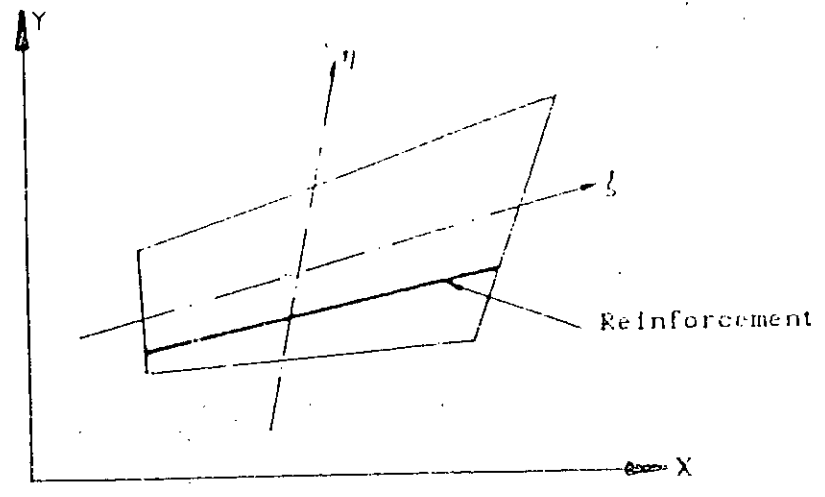


Fig. 4.4 (c) : Embedded representation of steel

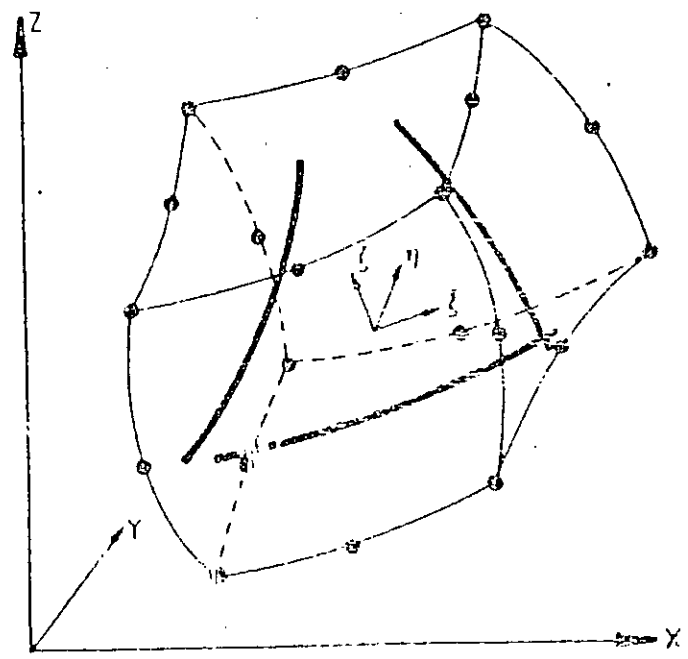


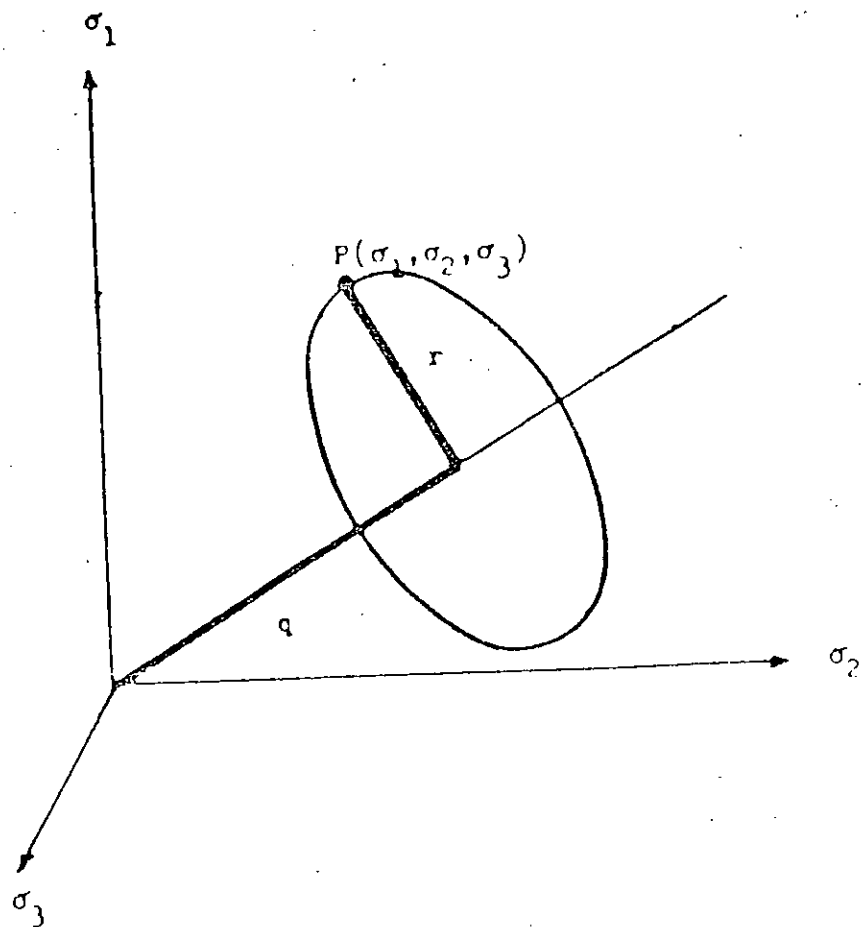
Fig. 4.5 : Embedded bars within the 20-noded isoparametric brick element

Having obtained such experimental data, it must be transformed into sets of mathematical formulae, adequately describing the basic characteristics to be of real use to reinforced concrete analysis. These mathematical formulae are normally called "constitutive equations" or sometimes, "constitutive models" for concrete. No one mathematical model can completely describe the complex behaviour of real materials under all conditions. Each material model is aimed at a certain class of phenomena and captures their essential features and disregards what is considered to be of minor importance in that class of applications. One such set of laws, used in this work to model concrete compressive triaxial behaviour, is due to Kotsovos et al (13,14,15,16). As cracking of concrete is probably the major cause of nonlinearity in most reinforced concrete structures, a separate three dimensional cracking model is developed and incorporated in the finite element programme. Particular attention is paid to proper modelling of shear transfer across a cracked concrete surface. A biaxial stress-strain law is used for reinforcing steel. Full bond is assumed between concrete and steel.

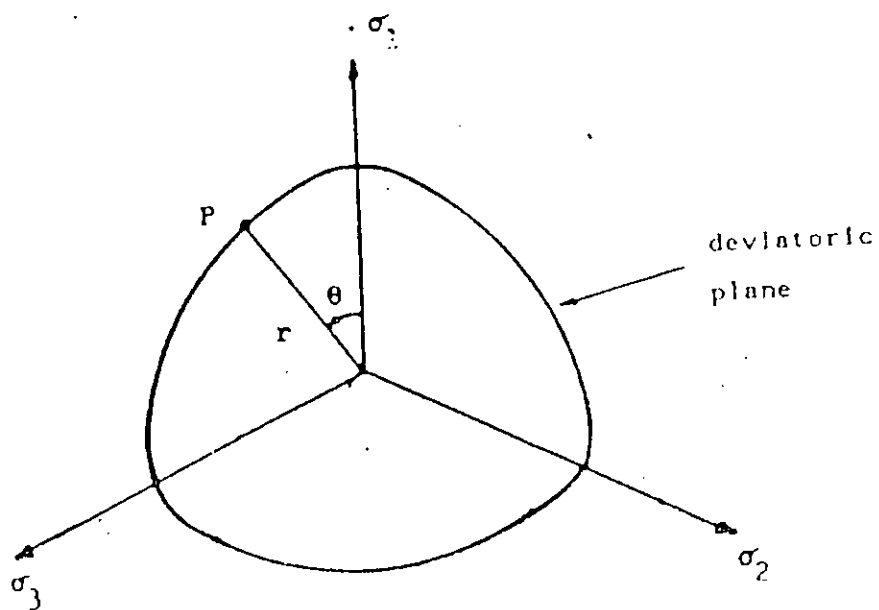
4.4. Kotsovos' Constitutive Laws for Concrete

A comprehensive programme(13,14,15,16) of investigation into the behaviour of concrete under complex states of stress was carried out at the Imperial College, London. After analysing the results, Kotsovos provided mathematical expressions for deformational as well as strength properties of concrete suitable for use in nonlinear computer based methods to analyze concrete structures. These expressions were successfully implemented in the computer program by Bari(18) and used in the present work.

For the construction of the constitutive equations for concrete, the geometrical representation of the stress state at a point is very useful. Since the stress tensor σ_{ij} has six independent components, it is of course possible to consider these components as positional co-ordinates in a six-dimensional



(a)



(b)

Fig. 4.6 : Cylindrical coordinate system

space. However it is too difficult to deal with. The simplest alternative is to take the three principal stresses σ_1 , σ_2 , σ_3 such that $\sigma_1 \geq \sigma_2 \geq \sigma_3$ as co-ordinates and represent the stress state at a point in the three-dimensional stress space. This orthogonal co-ordinate system σ_1 , σ_2 , σ_3 can be transformed into a cylindrical co-ordinate system q , r , θ and the two systems are related by the following equations:

$$q = (\sigma_1 + \sigma_2 + \sigma_3) / \sqrt{3}$$

$$r = [(\sigma_1 - \sigma_2)^2 + (\sigma_2 - \sigma_3)^2 + (\sigma_3 - \sigma_1)^2]^{0.5} / \sqrt{3}$$

$$\cos \theta = 1/6 [(\sigma_1 + \sigma_2 - 2\sigma_3) / r]$$

The variables 'q' and 'r' define the hydrostatic and deviatoric components respectively, of a stress state, whereas the variable 'θ' defines the direction of the deviatoric component on the octahedral plane as shown in Figure (4.6) and varies from

$$\theta = 0^\circ \text{ for } \sigma_1 = \sigma_2 > \sigma_3$$

$$\theta = 60^\circ \text{ for } \sigma_1 > \sigma_2 = \sigma_3$$

The hydrostatic and deviatoric components can also be expressed in terms of the normal (σ_{oct}) and shear (τ_{oct}) octahedral stresses which are defined as follows

$$\sigma_{\text{oct}} = (\sigma_1 + \sigma_2 + \sigma_3) / 3 = q / \sqrt{3}$$

$$\tau_{\text{oct}} = 1/3 \sqrt{(\sigma_1 - \sigma_2)^2 + (\sigma_2 - \sigma_3)^2 + (\sigma_3 - \sigma_1)^2} = r / \sqrt{3}$$

Similarly, the normal (ϵ_{oct}) and shear (γ_{oct}) octahedral strains are defined as follows:

$$\epsilon_{\text{oct}} = (\epsilon_1 + \epsilon_2 + \epsilon_3) / 3$$

$$\gamma_{\text{oct}} = [(\epsilon_1 - \epsilon_2)^2 + (\epsilon_2 - \epsilon_3)^2 + (\epsilon_3 - \epsilon_1)^2]^{0.5} / 3$$

where $\epsilon_1, \epsilon_2, \epsilon_3$ are the principal strains. The mathematical formulae reported here for the deformational and strength properties are applicable to a range of concretes with uniaxial, cylinder compressive strength (f'_c) varying from about 15 to 65 N/mm². For the deformational properties, use has been made of the secant bulk (K_s) and secant shear (G_s) moduli which are expressed as follows:

$$K_s = \frac{\sigma_{oct}}{3 \epsilon_{oct}}$$

$$G_s = \frac{\tau_{oct}}{2 \gamma_{oct}} \quad (4.30)$$

The deformational behaviour of concrete under increasing stress can be completely described by the relationships between: (a) hydrostatic stress, σ_{oct} and volumetric strain, ϵ_{oh} ; (b) deviatoric stress, τ_{oct} , and deviatoric strain, γ_{oct} ; and (c) deviatoric stress, τ_{oct} and volumetric strain, ϵ_{od} . The σ_{oct} - ϵ_{oh} and τ_{oct} - γ_{oct} relationships can be described by the mechanical properties of the model as follows:

$$\frac{K_s}{K_o} = \frac{1}{1 + A (\sigma_{oct}/f'_c)^{b-1}} \quad \text{for} \quad \frac{\sigma_{oct}}{f'_c} < 2.0$$

$$\frac{K_s}{K_o} = \frac{1}{1 + 2^{(b-1)} \cdot b \cdot A - 2^b (b-1) A (\sigma_{oct}/f'_c)^{-1}} \quad \text{for} \quad \sigma_{oct}/f'_c > 2.0 \quad (4.31)$$

$$\frac{G_s}{G_o} = \frac{1}{1 + C (\tau_{oct}/f'_c)^{d-1}} \quad (4.32)$$

K_0 and G_0 (in KN/mm) are the initial values of the moduli K_s and G_s ; and A , b , C , d are parameters which depend on the material properties such that

$$K_0 = 11.0 + 0.0032 f'_c{}^2$$

$$G_0 = 9.224 + 0.136 f'_c + 3.296 \times 10^{-15} f'_c (8.273)$$

$$A = 0.516 \quad \text{for } f'_c < 31.7 \text{ N/mm}^2, \text{ or}$$

$$= \frac{0.516}{1.0 + (0.0027)(f'_c - 31.7)^{2.397}} \quad \text{for } f'_c > 31.7 \text{ N/mm}^2$$

$$b = 2.0 + 1.81 \times 10^{-8} f'_c (4.461)$$

$$C = 3.573 \text{ for } f'_c < 31.7 \text{ N/mm}^2, \text{ or} \quad (4.33)$$

$$= \frac{3.573}{1.0 + 0.0134 (f'_c - 31.7)^{1.414}} \quad \text{for } f'_c > 31.7 \text{ N/mm}^2$$

$$d = 2.12 + 0.0183 f'_c \quad \text{for } f'_c > 31.7 \text{ N/mm}^2$$

$$= 2.7 \quad \text{for } f'_c < 31.7 \text{ N/mm}^2$$

In order to evaluate the effect of internal stresses on deformation, use is made of the artificial concept that the volume strain (i.e. ϵ_{od}) under deviatoric stress is due to the hydrostatic component of such stresses, σ_{int} . Since

$$\sigma_{int} = 3 K_s \cdot \epsilon_{od} \quad (4.34)$$

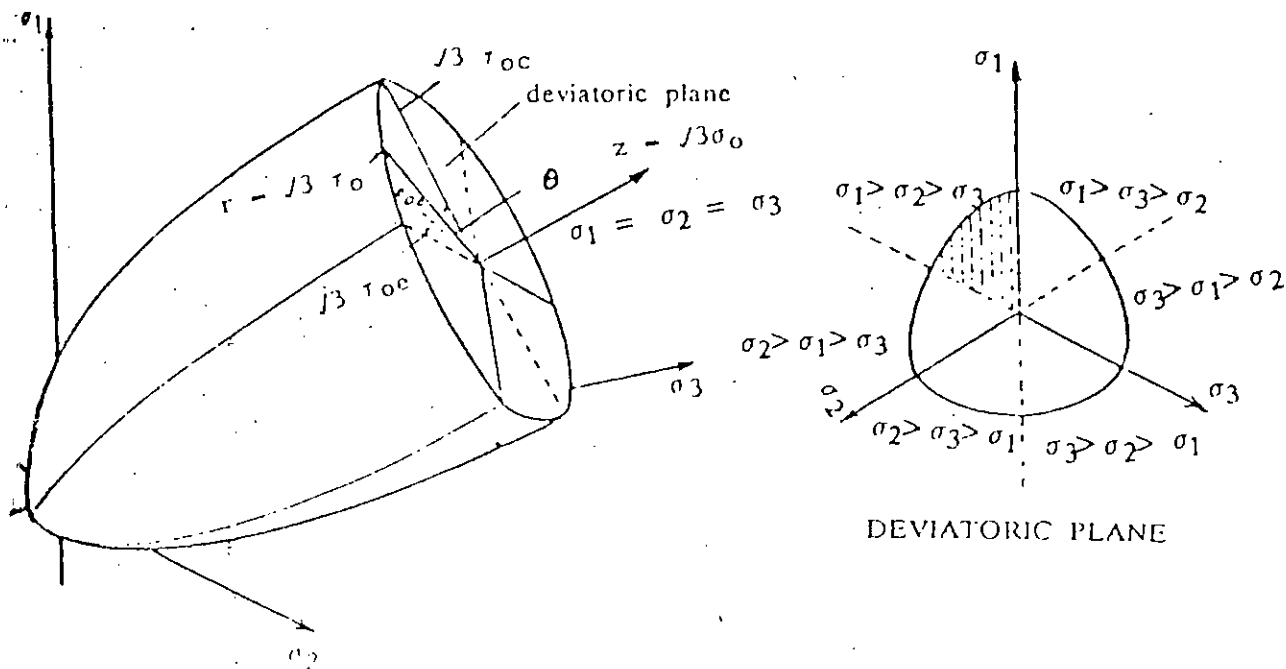


Fig. 4.7 : Schematic representation of the ultimate strength surface

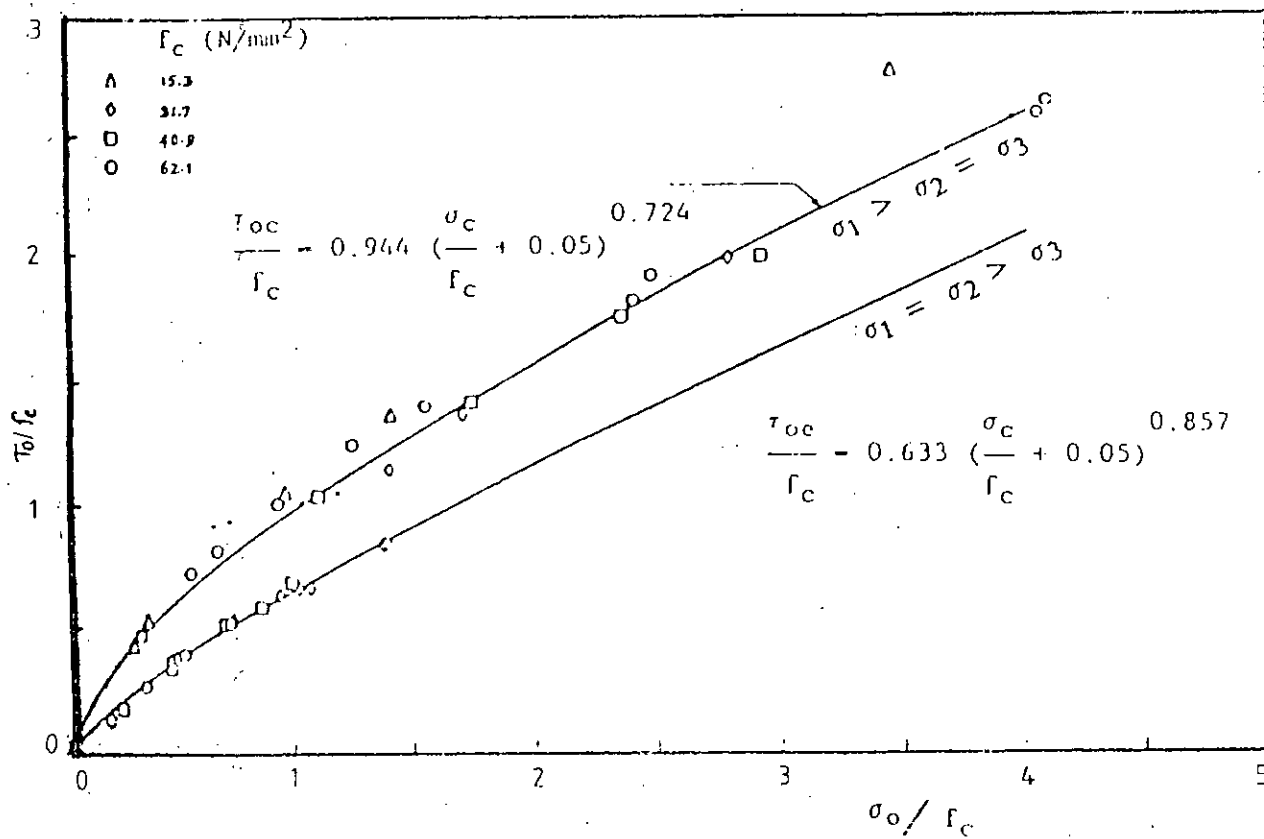


Fig. 4.8: Combinations of octahedral stresses at ultimate strength for concrete under the axisymmetric stress states $\sigma_1 > \sigma_2 = \sigma_3$ and $\sigma_1 = \sigma_2 > \sigma_3$

The hydrostatic component σ_{int} is equivalent to three principal stresses $\sigma_1 = \sigma_2 = \sigma_3 = \sigma_{int}$; and its effect on deformation, ϵ_{od} will be the deformational response of the model under these principal stresses. Equations (4.31) and (4.32) when used with equation (4.30), the resulting value of ϵ_{oct} (in 4.30) will be ϵ_{oh} , thus the total octahedral normal strain will be

$$\epsilon_{oct} = \epsilon_{oh} + \epsilon_{od} \quad (4.35)$$

The strength of concrete under multiaxial stresses is a function of the state of stress consisting of six components. Based on an analysis of strength data, Kotsovos derived mathematical expressions to describe the strength properties of concrete under biaxial or triaxial stress states which can be presented as follows:

T_{oe} is the value of T_{oct} at the ultimate strength level for $\theta = 0$ degree;

T_{oc} is the value of T_{oct} at the ultimate strength level for $\theta = 60$ degrees;

the value of T_{oct} at the ultimate strength level for any values of θ such that $0 < \theta < 60$ degrees may be given by the following expression:

$$T_{of} = \frac{2\tau_{oc}(\tau_{oc}^2 - \tau_{oe}^2)\cos\theta + \tau_{oc}(2\tau_{oe} - \tau_{oc})[4(\tau_{oc}^2 - \tau_{oe}^2)\cos^2\theta + 5\tau_{oc}^2 - 4\tau_{oc}\tau_{oe}]^{0.5}}{4(\tau_{oc}^2 - \tau_{oe}^2)\cos^2\theta + (\tau_{oc} - 2\tau_{oe})^2} \quad (4.36)$$

If isotropic material behaviour is assumed, equation (4.36) may be used to define a six-fold symmetric (about the space diagonal) ultimate strength surface, provided the variations of τ_{oc} and T_{oc} with T_{oct} are established (Fig.4.7). Fig.4.8 shows the normalized combinations of octahedral stresses at the ultimate strength level obtained from triaxial tests. The envelopes in this figure are considered to describe adequately the strength of most concretes likely to be encountered in practice. A mathematical description of the above strength envelopes was

obtained as follows

$$\begin{aligned}\tau_{oc}/f'c &= 0.944 [(a_{oct}/f'c) + 0.05]^{0.724} \\ \tau_{oc}/f'c &= 0.633 [(a_{oct}/f'c) + 0.05]^{0.857}\end{aligned}\tag{4.37}$$

These expressions are used in this work to define an ultimate strength surface.

4.4.3 Failure Criteria of Concrete

Criteria such as yielding, initiation of cracking, load carrying capacity, and extent of deformation are generally used to define failure. In general, concrete failures can be divided into two types: tensile type and compressive type. Tensile type and compressive type of failures are generally characterised by ductility and brittleness, respectively. With respect to the present definition of failure, tensile type of failure is defined by the formation of major cracks and the loss of the tensile strength normal to the crack direction. In the case of compressive type of failure, many small cracks develop and the concrete element loses its strength completely. In this work, it is assumed that concrete suffers a crushing type of failure if: (a) the failure surface presented in equation (4.36) is violated, or (b) the maximum principal compressive strain is greater than a specified value (which is taken as 0.0035 according to BS 8110)

Condition (a) holds for isotropic (uncracked) concrete material, and it is found that condition (b) will never be satisfied prior to condition (a) as long as the material is isotropic. But when a crack exists, condition (a) is not applicable; thus only condition (b) holds. After crushing, the current stresses drop abruptly to zero and the concrete is assumed to lose its resistance completely against further deformation. Therefore the rigidity matrix $[D]$ will be zero.

In this study it is assumed that concrete will suffer a

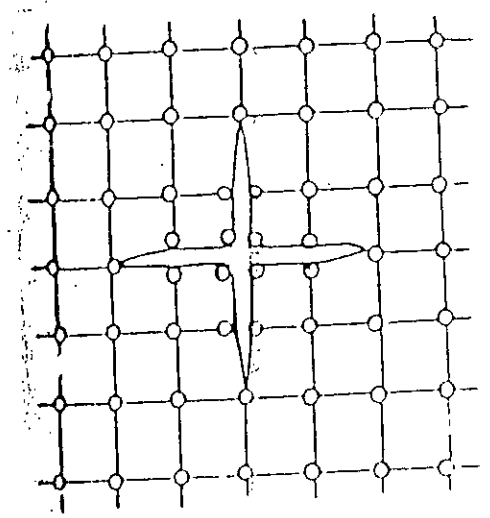
cracking type of failure if:

(a) the failure surface presented in equations(4.36 & 4.37) is violated, or (b) the maximum tensile principal stress exceeds a specified value. A value equals $f_t/2$, is approximately the value on the failure surface for uniaxial tensile stress state. Condition (a) holds for isotropic (uncracked) concrete material. Under multiaxial stress state, condition (b) will never be satisfied prior to condition (a) as long as the material is uncracked. When at least one crack exists at any point due to condition (a), only condition (b) is applicable to check against a second or a third crack. Once a crack has formed, the tensile stress across the crack drops abruptly to zero and the resistance of the material against further deformation normal to the crack direction is reduced to zero. However, material parallel to the crack is assumed to carry stress according to the uniaxial or biaxial conditions prevailing parallel to the crack.

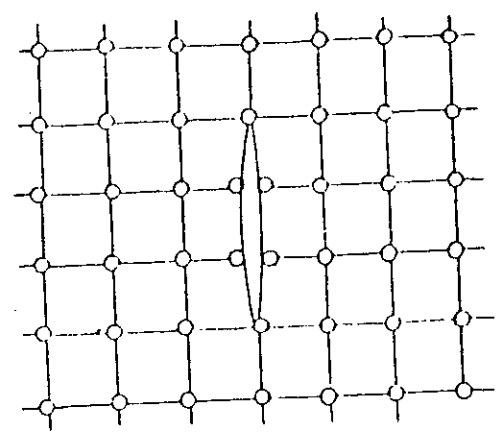
4.4.4 Modelling of Concrete Cracking

4.4.4.1 General

The tensile weakness of concrete results in cracking which is regarded as a major factor contributing to the nonlinear behaviour of reinforced concrete structures. Early studies on modelling of reinforced concrete nonlinear behaviour resulted in two methods of representing the cracking of concrete. The first approach, termed discrete crack representation (18,19) uses a redefined discrete crack system. The major drawbacks of this procedure, however, are that the topology of the structure has to be continuously altered as cracking progresses and that a previous knowledge of the crack pattern might be necessary. The second approach, known as the smeared crack model (18,19) assumes the cracked concrete remains a continuum. This implies that an infinite number of parallel cracks occur at a specific point if a certain cracking criterion is satisfied. By using the smeared cracking approach the problem of changing the topology of the

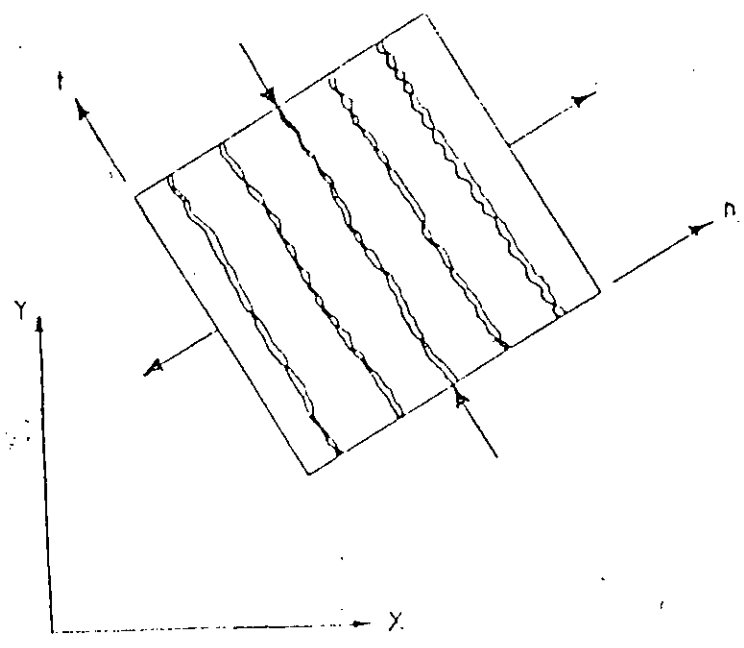


Two - directional cracking



(b) One - directional cracking

(i) Discrete cracking model



(ii) Sheared cracking model

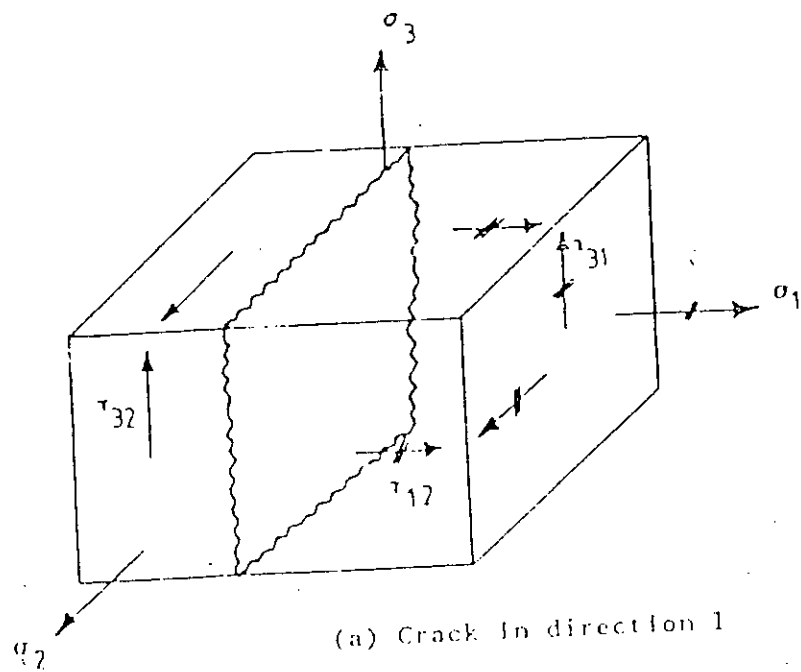
Fig. 4.9 - Discrete and sheared cracking models

13391

structure with crack propagation is overcome. Moreover the initiation, orientation and propagation of cracks at the sampling points are automatically generated resulting in complete generality. Fig.4.9 illustrates both cracking models as applied to two dimensional analysis. The selection of which cracking model to use depends largely upon the purpose of the finite element study undertaken and the nature of the output desired. Generally, if overall load-displacement behaviour, without regard to local stresses and 'realistic' crack patterns is desired, the smeared crack representation is probably the best choice. If, on the other hand, detailed local behaviour is of prime importance, adaptations of the discrete cracking model is useful. The element type, size and grid pattern have significant effects on both models. The smeared crack approach is the most commonly used because it is easy to implement. In this study the overall behaviour of the model is of particular importance is used to represent concrete with embedded bars to simulate the reinforcing steel at its exact location in the structure. Therefore, the smeared crack simulation is adopted. The main features of the smeared cracking model may be summarized as follows:

- i) cracking in one, two or three directions is allowed, known as fixed crack analysis.
- ii) cracks are allowed to open or close during the load increment
- iii) no tension stiffening but shear retention is allowed, known as no-tension analysis.

In the fixed crack direction analysis, (18) in the three dimensional stress spaces, σ_1 , σ_2 , σ_3 ; cracks might occur normal to any principal stresses (Fig.4.10). It is quite possible for any point to be cracked in more than one direction. Upto three cracks at a point are allowed in this analysis provided that they are orthogonal to one another. once a crack occurs its direction in the cartesian xyz space is fixed and retained as such in all subsequent loading. In this method, matrix [D] is modified such that the modulus of elasticity 'E' of the concrete is reduced to zero in the direction normal to the crack.



stress affected
by cracking.
(only normal stress
is set to zero).

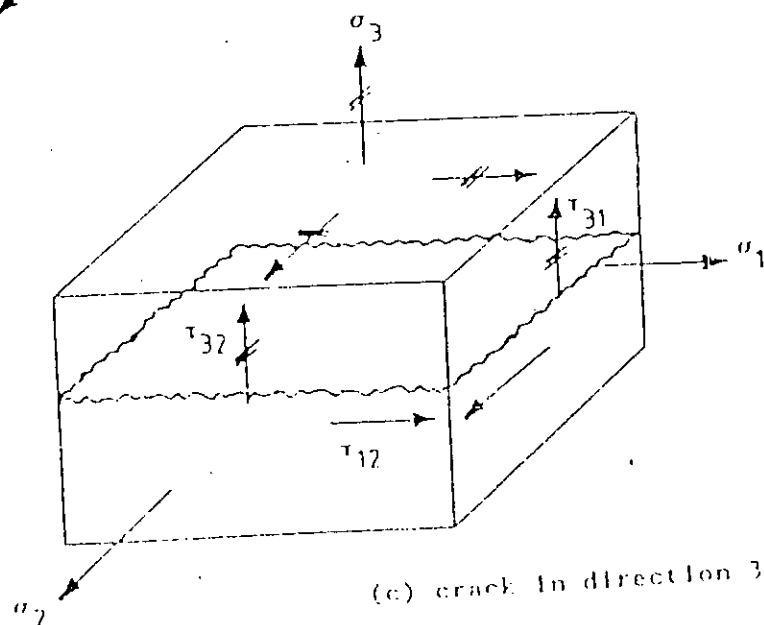
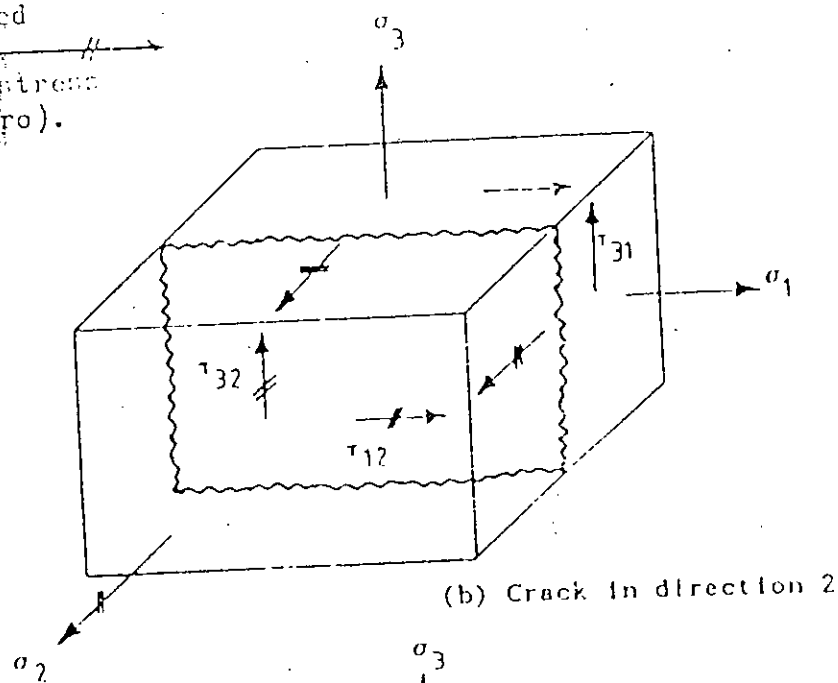


Fig. 6.10. : Types of cracks in concrete

Further a reduced shear modulus 'G' is assumed on the cracked plane to account for the aggregate interlocking .Because of the fact that shear stress is allowed to act at the cracked surfaces, this procedure allows tensile stress to built up on surface other than crack direction.

4.4.4.2 Determination of Rigidity Matrix for Fixed Crack Analysis

The traxial rigidity matrix for uncracked isotropic concrete is :

$$[D] = \frac{E(1-\nu)}{(1+\nu)(1-2\nu)} \begin{bmatrix} 1 & \frac{\nu}{(1-\nu)} & \frac{\nu}{(1-\nu)} & 0 & 0 & 0 \\ & 1 & \frac{\nu}{(1-\nu)} & 0 & 0 & 0 \\ & & 1 & 0 & 0 & 0 \\ & & & \frac{(1-2\nu)}{2(1-\nu)} & 0 & 0 \\ & \text{Symmetry} & & & \frac{(1-2\nu)}{2(1-\nu)} & 0 \\ & & & & & \frac{(1-2\nu)}{2(1-\nu)} \end{bmatrix} \quad (4.38)$$

In principal stress space, and with reference to the adopted cracking criterion, if the concrete is cracked in direction 1 (Fig.4.10(a)) the rigidity matrix will be

$$[D_c]_1 = \begin{bmatrix} 0 & 0 & 0 & 0 & 0 & 0 \\ & D_{22} & D_{23} & 0 & 0 & 0 \\ & & D_{33} & 0 & 0 & 0 \\ & & & \beta G & 0 & 0 \\ & \text{Symmetry} & & & D_{55} & 0 \\ & & & & & \beta G \end{bmatrix} \quad (4.39)$$

where D_{ij} are the corresponding values in the $[D]$ matrix and β is the shear retention factor, $0 \leq \beta \leq 1$. 'G' is the shear modulus of the material; its value will be the value obtained from the constitutive laws prior to cracking. If the concrete is said to be cracked in direction 2 (Fig. 4.10 (b)) the rigidity matrix will be

$$[D_c]_2 = \begin{bmatrix} D_{11} & 0 & D_{13} & 0 & 0 & 0 \\ & 0 & 0 & 0 & 0 & 0 \\ & & D_{33} & 0 & 0 & 0 \\ \text{Symmetry} & & & \beta G & 0 & 0 \\ & & & & \beta G & 0 \\ & & & & & D_{66} \end{bmatrix} \quad (4.40)$$

and if it is said to be cracked in direction 3 (Fig. 4.10(c)) the rigidity matrix will be

$$[D_c]_3 = \begin{bmatrix} D_{11} & D_{12} & 0 & 0 & 0 & 0 \\ & D_{22} & 0 & 0 & 0 & 0 \\ & & 0 & 0 & 0 & 0 \\ \text{Symmetry} & & & D_{44} & 0 & 0 \\ & & & & \beta G & 0 \\ & & & & & \beta G \end{bmatrix} \quad (4.41)$$

Depending on the stress situation, cracks may occur in more than one direction at a single Gauss point. In this case combinations between $[D_c]_1$, $[D_c]_2$, and $[D_c]_3$ may be necessary as follows: If cracked in direction 1 and direction 2, then D matrix is given by

$$[D_c]_{1,2} = \begin{bmatrix} 0 & 0 & 0 & 0 & 0 & 0 \\ & 0 & 0 & 0 & 0 & 0 \\ & & D_{11} & 0 & 0 & 0 \\ \text{Symmetry} & & & \beta G & 0 & 0 \\ & & & & \beta G & 0 \\ & & & & & \beta G \end{bmatrix} \quad (4.42)$$

if cracked in direction 2 and direction 3, then D matrix is given by

$$[D_c]_{2,3} = \begin{bmatrix} D_{11} & 0 & 0 & 0 & 0 & 0 \\ & 0 & 0 & 0 & 0 & 0 \\ & & 0 & 0 & 0 & 0 \\ \text{Symmetry} & & & \beta G & 0 & 0 \\ & & & & \beta G & 0 \\ & & & & & \beta G \end{bmatrix} \quad (4.43)$$

if cracked in direction 3 and direction 1, then D matrix is given by

$$[D_c]_{3,1} = \begin{bmatrix} 0 & 0 & 0 & 0 & 0 & 0 \\ & D_{22} & 0 & 0 & 0 & 0 \\ & & 0 & 0 & 0 & 0 \\ \text{Symmetry} & & & \beta G & 0 & 0 \\ & & & & \beta G & 0 \\ & & & & & \beta G \end{bmatrix} \quad (4.44)$$

and finally if cracked in all three principal directions it is assumed that this cracked point is incapable of resisting any stress. Therefore

$$[Dc]_{1,2,3} = \{0\} \tag{4.45}$$

Depending on the number of cracks which occur at a Gauss point at a particular level of loading, the appropriate rigidity matrix will be evaluated at that Gauss point and for simplifying the discussion it will be merely termed hereafter as [Dc] and used in the evaluation of the stiffness matrix. The rigidity matrix [Dc] is defined with respect to the directions of principal stresses at the Gauss point under consideration. To enable its use in the global x,y, z space, a process of transformation must be followed

$$[Dc]_{x,y,z} = [T_\epsilon]^T [Dc] [T_\epsilon]$$

where [T] is the transformation matrix for strain tensor which takes the following form:

$$[T_\epsilon] = \begin{bmatrix} \ell_1^2 & m_1^2 & n_1^2 & \ell_1 m_1 & m_1 n_1 & n_1 \ell_1 \\ \ell_2^2 & m_2^2 & n_2^2 & \ell_2 m_2 & m_2 n_2 & n_2 \ell_2 \\ \ell_3^2 & m_3^2 & n_3^2 & \ell_3 m_3 & m_3 n_3 & n_3 \ell_3 \\ 2\ell_1 \ell_2 & 2m_1 m_2 & 2n_1 n_2 & (\ell_1 m_2 + \ell_2 m_1) & (m_1 n_2 + m_2 n_1) & (n_1 \ell_2 + n_2 \ell_1) \\ 2\ell_1 \ell_3 & 2m_1 m_3 & 2n_1 n_3 & (\ell_1 m_3 + \ell_3 m_1) & (m_1 n_3 + m_3 n_1) & (n_1 \ell_3 + n_3 \ell_1) \\ 2\ell_2 \ell_3 & 2m_2 m_3 & 2n_2 n_3 & (\ell_2 m_3 + \ell_3 m_2) & (m_2 n_3 + m_3 n_2) & (n_2 \ell_3 + n_3 \ell_2) \end{bmatrix}$$

where ℓ_1, m_1, n_1 are the direction cosines of the first principal stress; ℓ_2, m_2, n_2 are those for the second principal stress; and

σ_3, m_3, n_3 are for the third principal stress. The three principal directions are orthogonal to each other. The three principal directions at a point can vary during loading before cracking is initiated, but they are fixed if at least two cracks exist at that point. One crack fixes only one principal direction but constraints the other two to be perpendicular to the crack. Once a crack occurs due to any principal stress, say σ_1 , this stress will be set to zero and the crack plane must be perpendicular to the direction of this principal stress. In subsequent load cycles, the direction of crack will be fixed and a two dimensional analysis on the crack plane will be followed to evaluate the values and directions of the other two principal stresses (in fact they will not be principal stresses due to the fact that shear stresses will exist also as in Fig. 4.10). If the material cracks in two directions, all the principal directions will be fixed, and the values of the 'offending' principal stresses will be set to zero.

4.4.5 Shear Retention Factor used in This Work

After cracking of concrete two main mechanisms develop through which shear is transferred from the weak cracked section to the surrounding sound concrete; namely (1) aggregate interlocking on the two adjacent surfaces and (2) dowel action of any reinforcing bars crossing these cracks. The two mechanisms are interrelated and several factors govern their relative contribution towards the total shear transferred. The main known factors are: (1) crack spacing, (2) presence or otherwise of reinforcement crossing the cracks, (3) bar size, (4) total number of bars crossing, (5) bar orientation relative to the crack direction, (6) aggregate size and roughness, (7) concrete strength, (8) crack width and (9) mode of failure. In the smeared cracking approach the shear transfer is modelled through the so-called "shear retention factor", β , which varies between 0 and 1 and is defined as:

$$\beta = G' / G \quad (4.46)$$

where G' is the reduced shear modulus for cracked concrete and G is the shear modulus for the uncracked concrete.

To achieve the aim of incorporating a realistic shear retention factor to model shear transfer across cracked concrete, the following nonlinear relationship based on the average of the three principal strains at any cracked point is used, Bari (18).

$$\beta = 1 \quad \text{for } \epsilon_m < \epsilon_{to} \text{ (for uncracked concrete)}$$

$$\beta = 0.25 \epsilon_{to} / \epsilon_m \quad \text{for } \epsilon_m \geq \epsilon_{to} \quad (4.47)$$

where β is the shear retention factor; ϵ_m is the average of the three principal strains at a cracked point; and ϵ_{to} is the cracking tensile strain which was taken as 0.0001. The above relationship seems more realistic than a constant factor because the physical contact between the two faces of the cracked planes weakens at larger crack widths, thus decreasing the aggregate interlocking forces. In the present work, irrespective of the number of cracks at a single Gauss point one shear retention factor is used for all the cracks at that point.

4.5 Nonlinear Method used in This Work

4.5.1 General

A nonlinear structural problem must obey the basic laws of continuum mechanics, i.e., equilibrium, compatibility, and the constitutive relations of the material. Displacement compatibility is automatically satisfied in the displacement finite element technique. Common nodes between elements ensure continuity and compatibility of displacements along element boundaries, and polynomial shape functions ensure continuity and single valued displacements internally. Therefore it becomes necessary only to enforce that the nonlinear constitutive relations are correctly satisfied whilst at the same time preserving the equilibrium of the structure. There can be several

causes of nonlinear behaviour in a structure, which can be divided into three categories: 1) Material nonlinearity, 2) Geometric nonlinearity and 3) Mixed material and geometric nonlinearity. Stress-strain relations are a major source of nonlinearity. Only nonlinearity caused by short-term nonlinear behaviour of concrete and steel is considered in this study. These include the tensile cracking of concrete, the nonlinear stress-strain relations of concrete, and the yielding and work-hardening of steel.

A nonlinear solution is obtained by solving a series of linear problems such that the appropriate nonlinear conditions are satisfied at any stage to a specified degree of accuracy. One way of achieving this goal is to ensure that at any loading stage, the solution results in stresses consistent with the displacement field and satisfying the given constitutive equations. These stresses will be statically equivalent to a set of internal nodal forces which should be in equilibrium with the externally applied loads. In general, these equivalent nodal forces are not equal and the differences between the external and internal forces are termed "residual forces". These residuals must be removed by repeatedly applying them on the structure until an acceptable tolerance is achieved. The solution of nonlinear problems by the finite element method are usually attempted by one of the following three basic techniques:

- a) Incremental (step-wise procedure)
- b) Iterative (Newton methods)
- c) Incremental-Iterative (mixed procedure)

where the nonlinearity occurs in the stiffness matrix $[K]$ which, in the case of short-term behaviour of reinforced concrete, is a function of nonlinear material properties. Details of the methods are given in reference (22).

A modified version of the mixed procedure is used in this work. The modified "Newton-Raphson" approach is used to evaluate the stiffnesses. The stiffnesses are evaluated using a second rigidity matrix; and it was found (18) that varying the stiffnesses at second iteration in each increment results in the cheapest solution. For the calculation of unbalanced nodal forces, a modification of the initial stress method is used, termed the method of "Residual Forces" (23). The basic technique is that, at any stage, a load system equivalent to the total stress level is evaluated and checked against the applied loading system. The difference between the two will result in a set of residuals that are a measure of lack of equilibrium. These residuals are then applied in the structure to restore equilibrium. The process is then repeatedly continued to dissipate the out-of-balance forces to a sufficiently small value. Thus for equilibrium it is required that

$$[F_u] = \int_v [B]^T [\sigma] dv - [R] = 0$$

where $[\sigma]$ are the actual stresses depending on the constitutive law being used, $[R]$ is external load vector, $[F_u]$ the residual forces.

In this work a version of frontal solution, originally introduced by Irons (24) and later modified by Hinton & Owen (25), is used. The main features of the frontal solution technique is that, it assembles the equations and eliminates the variables at the same time. This means that the total stiffness matrix of the structure is never formed as such the reduced equations corresponding to eliminated variables are stored in core in a temporary array called a buffer area. As soon as this array is full, the information is then transferred to disc. This saves the core storage and computer time through proper house keeping. Another important feature is that in frontal solver node numbering is irrelevant and it is the element numbering that matters for storage allocation.

4.5.2 Convergence Criteria Used in This Work

A reliable convergence criteria must be used to terminate the iteration process when the desired accuracy has been reached. The accuracy is specified by the user through what is called "convergence tolerances". These convergence tolerances are the quantitative values that determine the accuracy of equilibrium acceptable to the user and it must be realistic. Three types of convergence criteria have been in common use for structural analysis, namely, (a) Force convergence criteria, (b) Displacement convergence criteria and (c) Energy convergence criteria. Each of the three alternatives has its merits and the selection of a suitable one depends on many factors. The rate of convergence depends on the method used in the solution (constant or variable stiffness). It is also required to specify a maximum number of iterations, irrespective of the state of convergence. The maximum number of iterations may influence the predicted shape of the load-deflection curve, but it is an important safe guard against unlimited and often unnecessary cycles of full solution. However, whatever criterion is chosen, care must be taken to avoid spending much effort trying to obtain the unattainable and perhaps needless accuracy. Special attention must be given to the cracking stage when large forces are suddenly released into the system.

In this study force convergence criterion is used. Because it is a direct measure of equilibrium between the external and internal forces. A global approach is adopted, where convergence is monitored using norm as follows :

$$\frac{\left| \sum_{i=1}^N (F_{u,i}^r)^2 \right|^{0.5}}{\left| \sum_{i=1}^N (R_i)^2 \right|^{0.5}} \times 100 \leq \text{Toler}$$

where N is the total number of nodal points in the system, r denotes the iteration number, $F_{u,i}$ is the residual forces at node i and R_i is the total external applied load at node i . This

criteria states that the convergence occurs if the norm of the residual forces becomes less than a specified tolerance times the norm of the total applied forces.

4.5.3. Analysis Termination Criteria

The program must have some means of detecting the collapse of the structure. The failure of the structure takes place when no further loading can be sustained. A maximum deflection can be used as a criterion to stop the analysis. The maximum iterations can also be used. In this study, however, the growth of iterative displacements is used to detect failure. This is coupled with a search through the diagonal terms of the stiffness matrix to detect zero or negative values, in which case analysis is terminated. It was found that the negative or zero pivots were always associated with very large displacements at or immediately beyond the failure loads and always occurred after 2-3 unconverged (sometimes diverged) increments. This was also associated with severe cracking, yielding and crushing situations.

4.5.4. Procedure Adopted in the Program for Analysis

Consider the analysis at a particular iteration i . The displacements are calculated according to equation

$$[\delta] = [K (\sigma, \epsilon)]^{-1} [R]$$

which illustrates the basic nonlinear relationship between nodal displacements $[\delta]$ and external nodal forces $[R]$, due to the influence of the material laws on stiffness matrix $[K]$, using the appropriate rigidity matrix $[D]_{x, y, z}$.

(1) For every stress sampling point, evaluate incremental values of strains $[\Delta \epsilon_i]$ and stresses $[\Delta \sigma_i]$ using the appropriate rigidity matrix $[D]_{x,y,z}$.

(2) Check whether the sampling point under consideration has suffered from a compressive crushing situation in any of the previous load cycles, if so, step(8) will be executed.

(3) Check whether this stress sampling point has suffered from a tensile cracking situation in any of the previous load cycles, if so, step(7) will be executed.

(4) Using the stress-strain relationships described in the concrete material law, evaluate the total actual stresses in concrete $[\sigma_i]$ which correspond to the linearly calculated total strains.

$$[\epsilon_i] = [\epsilon_{i-1}] + [\Delta \epsilon_i]$$

$$[\sigma_i] = [\sigma_{i-1}] + [D]_{x,y,z} [\Delta \epsilon_i]$$

(5) Check for concrete compressive failure criteria violation. If violated, all the stress component at this gauss point will be set to zero in this iteration and in all subsequent load cycles: $[\sigma_i] = 0.0$; also the components of the rigidity matrix will be set to zero for stiffness calculations in all the subsequent load cycles.

$$[D]_{x,y,z} = 0.0$$

(6) Check for concrete tensile failure criteria. If violated a crack will occur, thus a new rigidity matrix $[D_c]_{x,y,z}$ will be formulated according to the number directions of the cracks.

(7) If previously cracked in one direction, it is required to check for further cracking as follows:

(a) for the previous load cycle, the principal stresses $\sigma_1, \sigma_2, \sigma_3$ had the direction cosines $(l_1, m_1, n_1); (l_2, m_2, n_2)$ and (l_3, m_3, n_3) . These directions are termed here as x', y', z' as

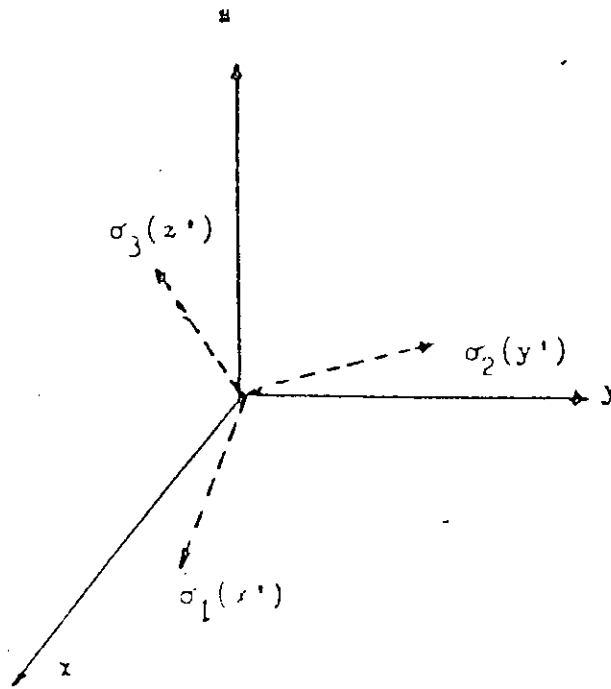


Fig. 4.11 : Principal stresses in global axes.

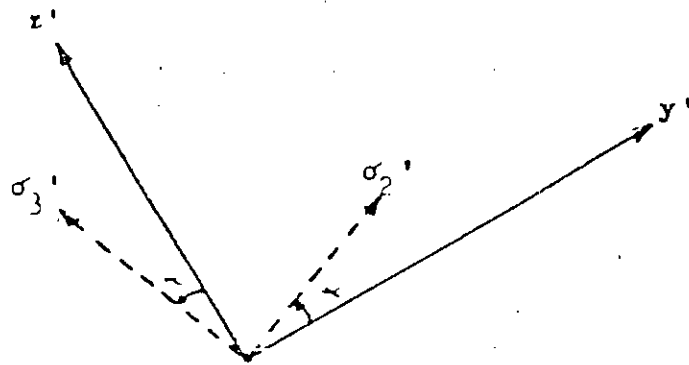


Fig. 4.12 : The angle of the new principal stress direction

shown in Fig.4.11.

(b) In the present load cycle, these direction cosines which were obtained from the previous load cycle were used in stiffness calculation to evaluate the new stress vector $[\sigma]$ with regard to the appropriate rigidity matrix $[D_c]$.

(c) Now for principal stress calculation in cracked material, the new stress vector $[\sigma]$ will be transformed from x, y, z space to $[\sigma']$ in x', y', z' space by

$$[\sigma'] = [T_\sigma] [\sigma]$$

where $[T]$ is the transformation matrix for stress vector.

The new transformed stress tensor, $[\sigma']$ will be (see Fig.4.11)

$$[\sigma'] = \begin{bmatrix} \sigma'_x & \sigma'_y & \sigma'_z & \tau'_{xy} & \tau'_{yz} & \tau'_{zx} \end{bmatrix}^T$$

and for the instance of a cracked caused by σ_1 , the value of σ'_x will be set to zero ($\sigma_1 = \sigma'_x$), and to evaluate the new values of σ'_2 and σ'_3 we are dealing with a two dimensional problem of which the active stress components are $\sigma'_y, \sigma'_z, \tau'_{yz}$. thus

$$\sigma'_2, \sigma'_3 = \frac{\sigma'_y + \sigma'_z}{2} \pm \sqrt{\left[\frac{\sigma'_y - \sigma'_z}{2} \right]^2 + (\tau'_{yz})^2}$$

$$\tan 2\alpha = \frac{2\tau'_{yz}}{\sigma'_y - \sigma'_z}$$

where α is the angle by which the directions of σ'_2, σ'_3 deviated from y', z' axes in the event of cracked caused by σ_1 (Fig.4.12).

(d) Having obtained the α , and knowing the direction cosines of x, y, z axes with respect to the global x, y, z space, we need to calculate the direction cosines of σ'_2, σ'_3 which are (l_2', m_2', n_2') , (l_3', m_3', n_3') , such that their plane remains perpendicular to the already fixed direction of σ_1 which caused the crack in our example. This can be done as follows:

$$\text{if } [\sigma'] = [A] [\sigma]$$

$$\text{and } [\sigma''] = [C] [\sigma']$$

$$\text{then } [\sigma''] = [C] [A] [\sigma]$$

where [A] and [C] are the appropriate transformation matrices. The product [C][A] will contain all the required direction cosines of the new principal stresses contained in [σ''].

(e) These nine values of direction cosines will be the ones to be used in the next load cycle for stiffness and new stress vector calculations; and the values of the principal stresses σ_2' , σ_3' will be used to check against the cracking criterion because σ_1 was set to zero (in this example). If the cracking criterion is violated further cracks will occur and the appropriate rigidity matrix [Dc] must be used.

(8) Evaluate the equivalent nodal forces contributed by concrete element

$$[P_i]_{\text{conc}} = \int_v [B]^T [\sigma_i] dv$$

(9) Add the equivalent nodal forces contributed by concrete element to those contributed by steel reinforcement to get the total equivalent nodal forces of the element, [Pi]

$$[P_i] = [P_i]_{\text{conc}} + [P_i]_{\text{steel}}$$

(10) Check for convergence

4.5.5. Nonlinear 3-D Finite Element Program

The program analyses nonlinear three dimensional stress problems using 20-noded isoparametric brick elements for concrete and embedded bars of reinforcing steel. The bars can be embedded anywhere within the elements, the only restriction being that

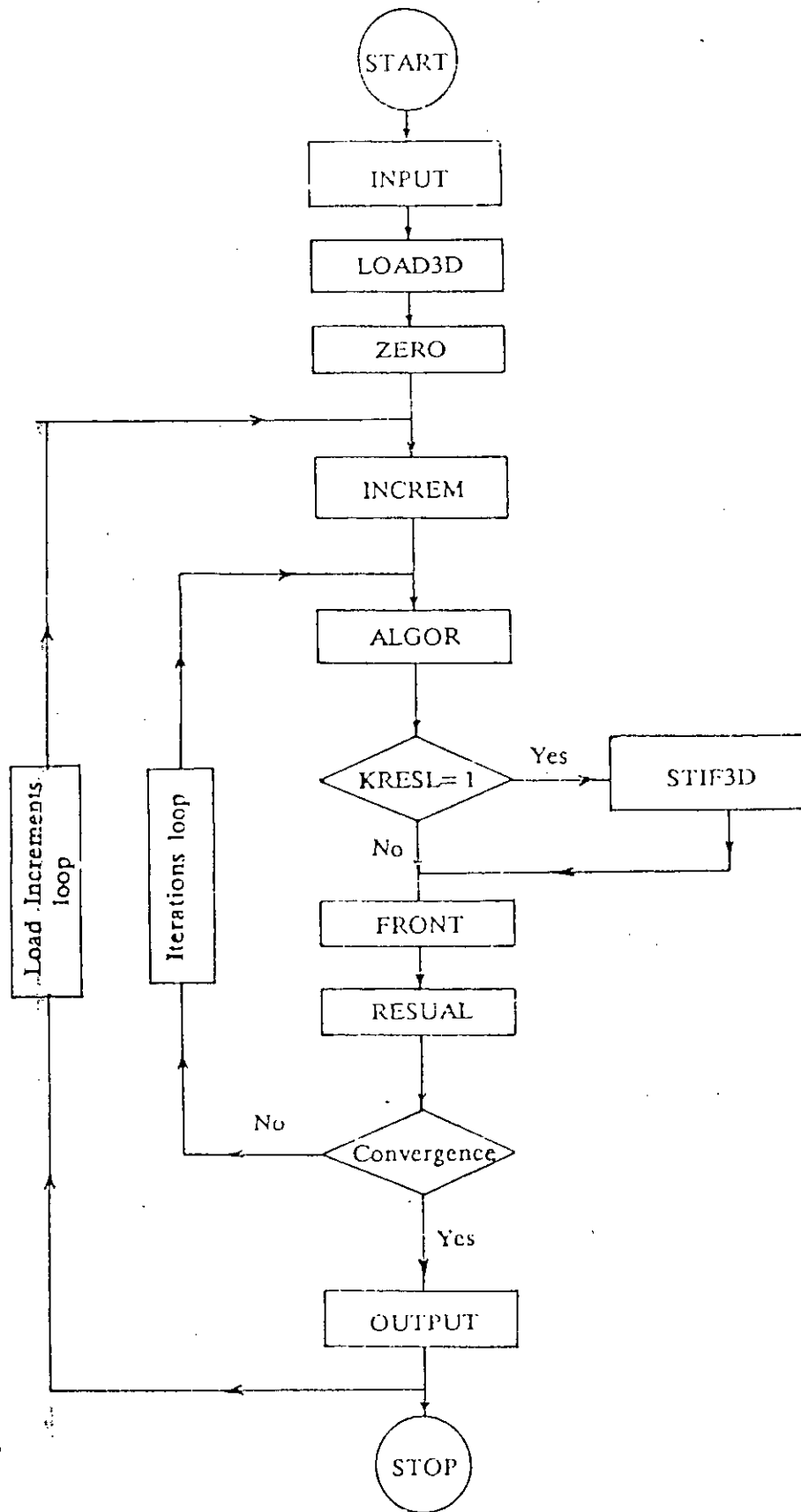


Fig.4.13 : Flowchart for 3-D finite element program

they must be parallel to the local coordinates (ξ, η, ζ) of the basic concrete element.

The incremental-iterative method is used to solve the nonlinear equations. The resulting equations are solved by Frontal Technique including buffer storage area in order to reduce the cost of the analysis. The program includes a triaxial short term constitutive equations for concrete, developed by Kotsovos, a three dimensional smeared cracking model and a bilinear stress-strain law for steel.

Automatic mesh generator is not included. Coordinates of midside nodes are always automatically generated. Because of the enormous amount of output, the control of the output is generally left to the user.

4.5.5.1 List of Subroutines with their brief description

1. Program MAIN

This is the master program from which all other subroutines are called. Flow chart is given in Fig. 4.13. (16)

2. Subroutine ZERO

This initializes various arrays to zero for accumulation of loads, reactions, displacements, stress etc.

3. Subroutine INPUT

This reads the required informations for geometry, boundary conditions, material properties for concrete and steel and calls the required subroutines for data checking.

4. Subroutine MIDSID

This computes the coordinates of the midside nodes for the 20 noded isoparametric brick elements.

5. Subroutine GAUSSQ

This sets up the sampling (Gauss) point positions and weighting factors for numerical integration.

6. Subroutine STIF3D

This computes the stiffness matrix for the brick element accounting for the cracking crushing and the material laws of concrete .

7. Subroutine BARSTF

This computes the stiffness of all the bars embeded within the basic concrete element and adds them into the appropriate places in the stiffness matrix .

8. Subroutine LOAD3D

This computes the equivalent nodal forces after reading the relevent data for any combination of load types.

9. Subroutine SFR3

This computes shape functions and their derrivatives .

10. Subroutine JACOB3

This calculates the coordinates of all Gauss points and Jacobian matrix , its inverse and determinant .

11. Subroutine BMAT3D

This calculates the strain matrix [B]

12. Subroutine MOD3D

This evaluates the material property matrix [D] accounting for the stress state prevailing at the Gauss point in question ready for stiffness calculation .

13. Subroutine DBE

This calculates the stress matrix [DB]

14. Subroutine ALGOR

This indicates by resolution index "KRESL" whether or not the system of equations is to be accompanied by a full reformulation of the element stiffnesses depending on the algorithm chosen , the current load increment and the current iteration .

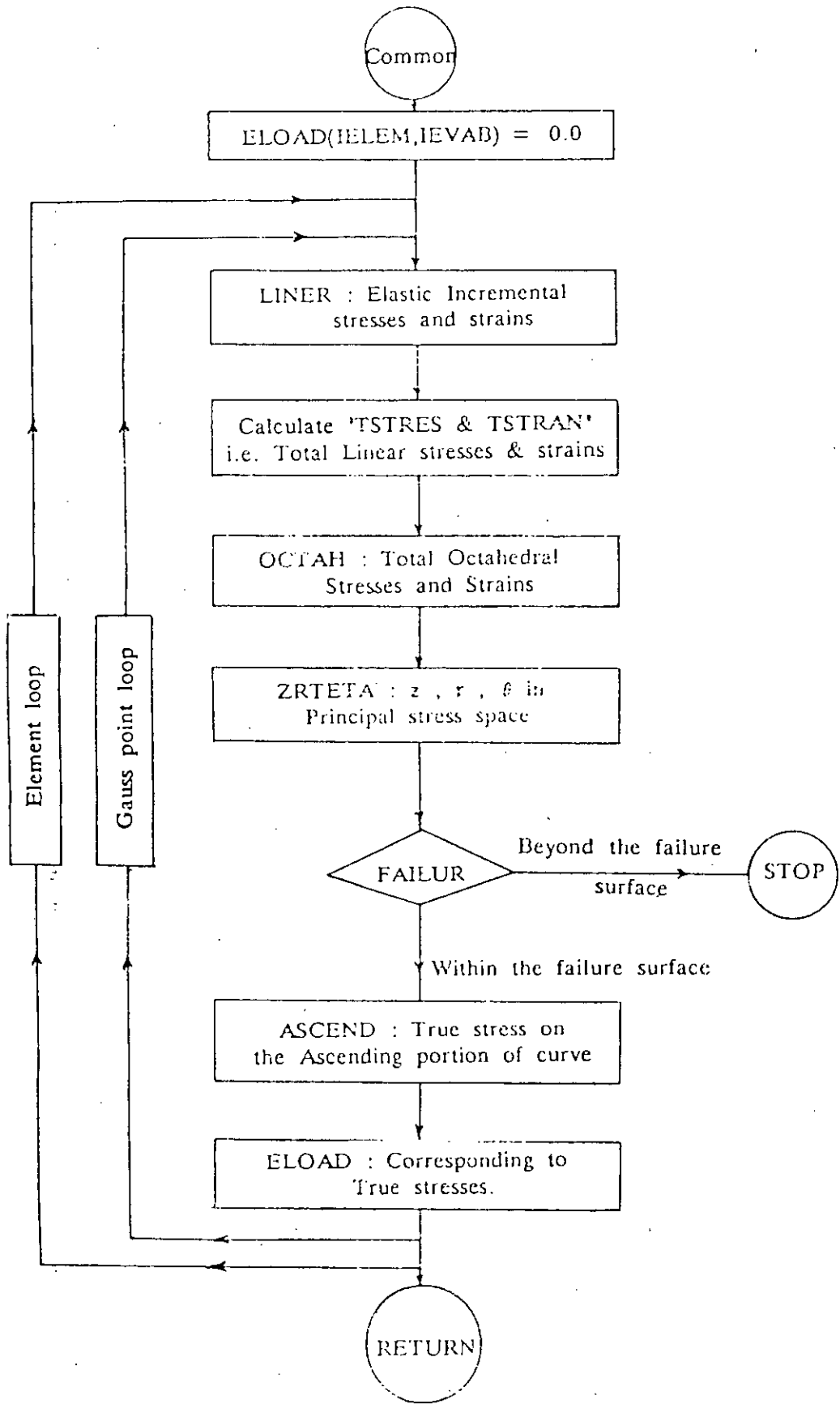


Fig.4.14 : Flowchart for Subroutine RESUAL (A,B,C,D)

15. Subroutine INCREM

This increments the load applied in subroutine LOAD3D .

16. Subroutine CONVER

This checks the convergence of the iteration process using residual force method .

17. Subroutine LINER

This evaluates incremental stresses and strains assuming linear elastic behaviour .

18. Subroutine FRONT

This calculates the deformations due to the incremental loads (in case of first iteration of every load increment) and due to the residual loads (in case of subsequent iterations) using Frontal Solution Technique.

19. Subroutine RESUAL

This computes the total stress tensor of the structure and calls the required subroutines to find the true stresses and evaluates the equivalent nodal forces . Fig.4.14 shows the flow chart of the subroutine .(16)

20. Subroutine PRNPAL

This calculates the principal stresses and strains and their directions at all gauss points in the element in x,y,z space .

21. Subroutine OCTAH

This calculates the octahedral stresses and strains .

22. Subroutine ZRTETA

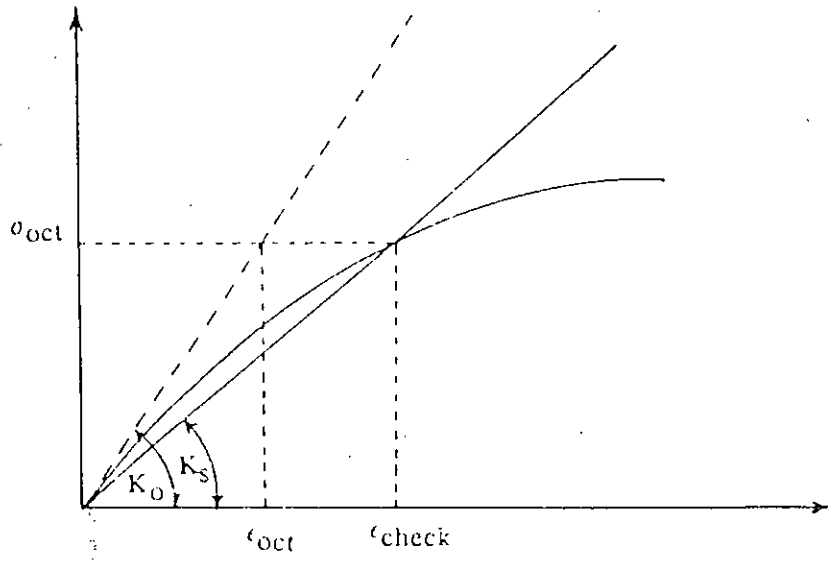
This calculates the coordinates z,r,e in the principal stress space to determine the failure surface as : (Fig. 4.7)(18)

z : hydrostatic axis in the principal stress space

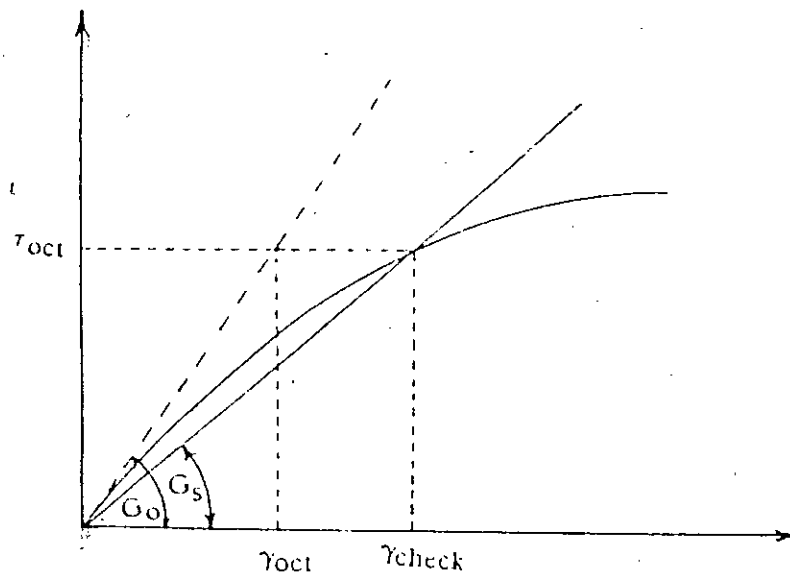
$$z = \sqrt{3} \sigma_{oct}$$

r : deviatoric axis

$$r = \sqrt{3} \tau_{oct}$$



(a) $\sigma_{oct} - \epsilon_{oct}$ curve



(b) $\tau_{oct} - \gamma_{oct}$ curve

Fig. 4.15

θ : the angle of similarity which specifies the deviation of r from σ_1 on the π plane, $0 \leq \theta \leq 60^\circ$

$$\cos \theta = \frac{1}{\sqrt{6}} (\sigma_1 + \sigma_2 - 2\sigma_3)$$

23. Subroutine FAILURE

This determines the failure surface envelope using Kotsovos failure criteria with equations 4.36 & 4.37 .

24. Subroutine EPSLN

This calculates the secant bulk modulus, K_s from its initial value K_0 using equations 4.31 & 4.33 . This also calculates the corresponding octahedral normal strain, ϵ_{check} on the normal stress strain curve (Fig.4.15) as follows:(16)

$$\epsilon_{check} = \frac{\sigma_{oct}}{3 K_s}$$

25. Subroutine GAMA

This calculates the shear modulus, G_s from initial value G_0 using equations 4.32 & 4.33 . This also calculates the octahedral shear strain, γ_{check} on the octahedral shear stress-strain curve as follows :(Fig.4.15)

$$\gamma_{check} = \frac{\tau_{oct}}{2 G_s}$$

26. Subroutine ASCEND

For the gauss point at which the state of stress is within the failure surface, this subroutine calculates the correct normal and shear stresses by direct internal iterations. ϵ_{check} obtained from subroutine EPSLN must equal to ϵ_{oct} obtained from subroutine OCTAH, otherwise σ_{oct} is increased or decreased (Fig. 4.15). Iterations are continued until ϵ_{check} is very close to ϵ_{oct} with acceptable tolerance of 1.0 E-10 . The same procedure is adopted for $\tau_{oct} - \gamma_{oct}$ curve. Having found the

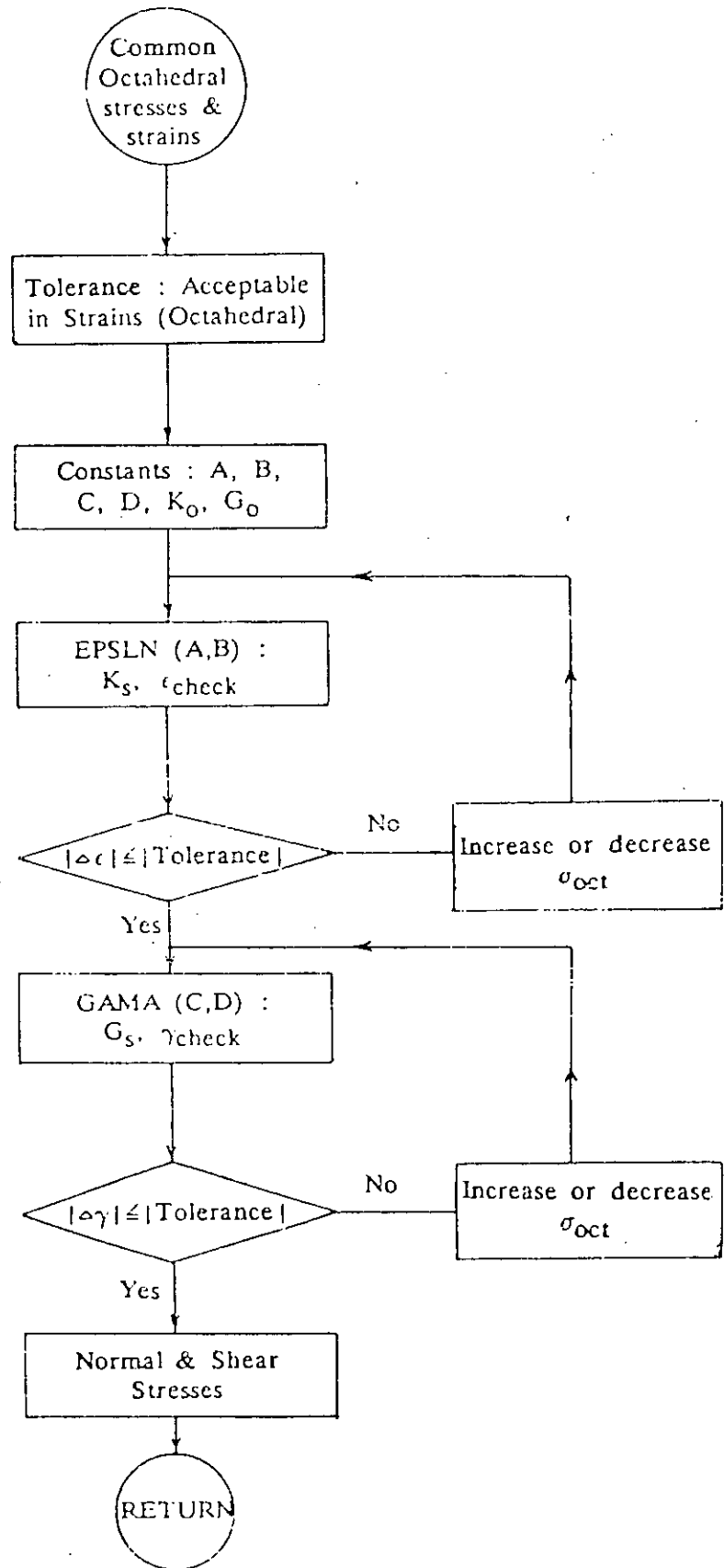


Fig .4.16 : Flowchart for Subroutine ASCEND (A,B,C,D)

correct values of σ_{oct} and τ_{oct} . the corresponding normal and shear stresses are then calculated from

$$\sigma_{ij} = 2 G_s \epsilon_{ij} + \delta_{ij} (3 K_s - 2G_s) \epsilon_{oct}$$

Flow chart is given in Fig.4.16 .(18)

27. Subroutine BARSTS

This subroutine evaluates reinforcing bar stresses and brings down the stresses to the yield value in case of yielding of steel

28. Subroutine CRKING

This deals with cracking and crushing of concrete using appropriate criteria . For cracking the offending principal stress is set to zero and the appropriate crack directions are fixed . For crushing ,all stresses are set to zero .

29. Subroutine TRNSF

This subroutine sets up the transformation matrices used to transform the stresses and strains to the required directions .

30. Subroutine OUTPUT

This gives the required output of the analysis.

31. Subroutine CHECK1

32. Subroutine ECHO

33. Subroutine CHECK2

Subroutines 31,32 and 33 detect the error in data supplied and gives the informations about type of error with termination of execution .

CHAPTER 5

THEORETICAL NONLINEAR STUDY

5.1 General

Nonlinear analysis of reinforced concrete structures by finite element analysis is centred around a suitable model for the description of its nonlinear material responses. The nonlinear stress-strain relationship of concrete is well known and form only a part of the total nonlinear behaviour of concrete. On the other hand, initiation of cracks in concrete in early stages of loading contributes significantly to the total nonlinear effects of concrete structures. The initiation of cracks at a sampling point in no way indicates a complete failure of that point. Rather it should be treated as a starting point of nonlinear behaviour of concrete. In the cracking environment of concrete, the overall load deflection response depend significantly on how well the post cracking behaviour is modelled in the numerical solution of such problem. The nonlinear 3-D program, discussed in Chapter 4 and used in this work, models suitably the nonlinear material responses of reinforced concrete. In this chapter, the findings of theoretical investigations have been discussed systematically.

5.2 Procedure Adopted for Nonlinear Study

5.2.1 Finite Element Discretization of Models

A typical floor plan of shear wall slab structure is presented in Fig. 1.4(a). For the models studied, the slab panel

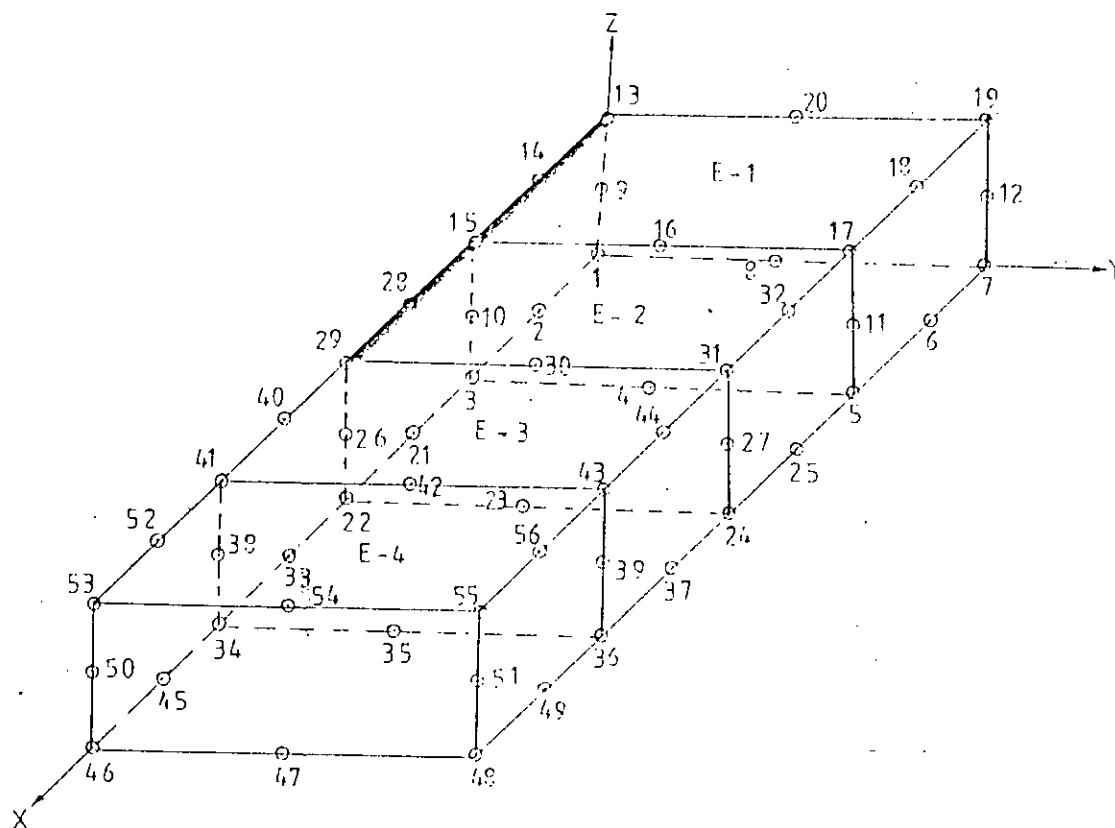
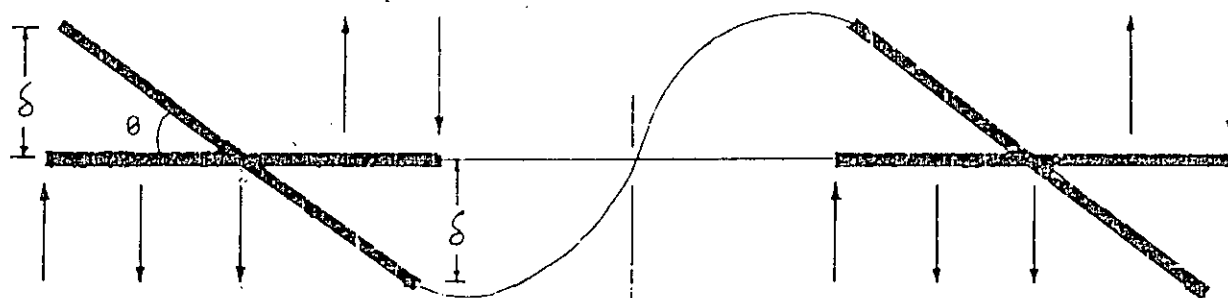


Fig. 5.1 : Typical finite element mesh with four elements

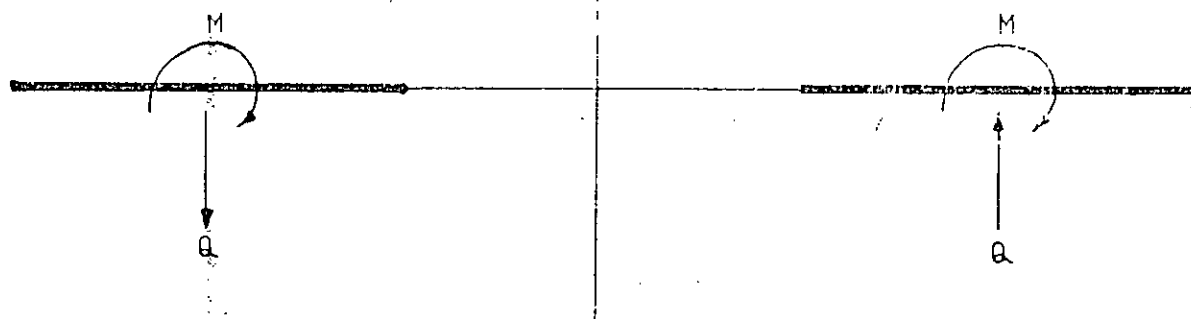
was divided into an assembly of 3-D, 20-noded brick elements having 3-degrees of freedom at each node. As a result of conditions of symmetry and antisymmetry in the slab, only one quadrant of the complete panel needs to be analyzed with appropriate boundary conditions. A typical finite element mesh having four elements with node numbering is shown in Fig. 5.1.

5.2.2 Investigation on Boundary Conditions

The purpose of the study was to investigate the behaviour of slabs in coupled shear wall structures. For this the flexural stiffness and effective width of floor slabs were studied following the procedure discussed in article 2.3. Therefore the behaviour of slab in resisting the rotation of the wall (θ) due to equivalent wall moment (M) resulting from structural actions of coupled shear wall structures as discussed in article 1.4 was studied. The rotation (θ) was applied incrementally and in each increment the behaviour of slab such as propagation of cracks and stresses and strains in steel and modes of failure were investigated through nonlinear analysis. Appropriate boundary conditions were imposed in finite element mesh to simulate the conditions described in article 2.3. Three cases of boundary conditions were imposed and the behaviour of the slab was studied and compared with each other to select the appropriate one. Detailed description of the investigations on different boundary conditions is provided in Appendix . Effect of boundary conditions on slab deformation , flexural stiffness of slab and crack propagation in slab was studied and compared with each other . After investigations CASE I was found to represent the structure adequately and was used throughout the study.



(a)



(b)



Fig. 5.2 : Determination of M and θ from analysis

5.2.3. Determination of M and θ from Finite Element Solution

Equal displacement (δ) were prescribed at wall nodes to produce rotation θ of wall as shown in Fig. 5.2(a). In each increment, the finite element solution furnished the displacements, stress resultant values at all nodes and also reactions at the restrained nodes as shown in Fig. 5.2(a). The reactions at the wall nodes provided the static equivalent wall moment M and the total shearforce, Q , transferred from the wall to the slab as shown in Fig. 5.2(b) when wall undergoes the imposed relative translation due to rotation θ .

Rotation (θ) of wall was increased at each increment by a factor until failure of the slab and in each increment wall moment was evaluated corresponding to wall rotation. In this way M - θ relationship throughout the entire stages of loading were evaluated. Hence using the equations 2.5 and 2.6, flexural stiffness K and effective width of the slabs and their variations throughout the entire loading history were evaluated.

5.3. Idealization of M - θ Curve

For discussion purposes and to analyze the M - θ curve critically, each curve is idealized in the manner as shown in Fig. 5.3(a). The slope of the initial linear part of the M - θ curve 'ab' is the precracking stiffness K_0 . The point 'b' on the curve is roughly an indication for the first appearance of the cracks. After cracking of concrete, the first part of the nonlinear curve is approximated by a straight line 'bc' and the slope of this part will be called 'cracked section stiffness K_{cr} '. The point 'c' on the curve is roughly an indication for the first yielding in flexural reinforcement. After yielding the second part of the nonlinear curve is approximated by a straight

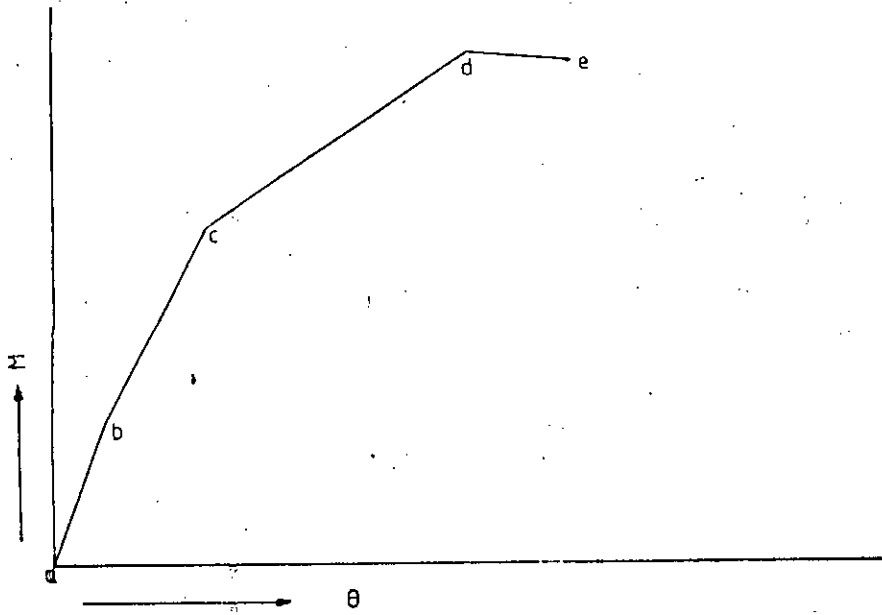


Fig. 5.3(a) : Idealized M - θ Curve

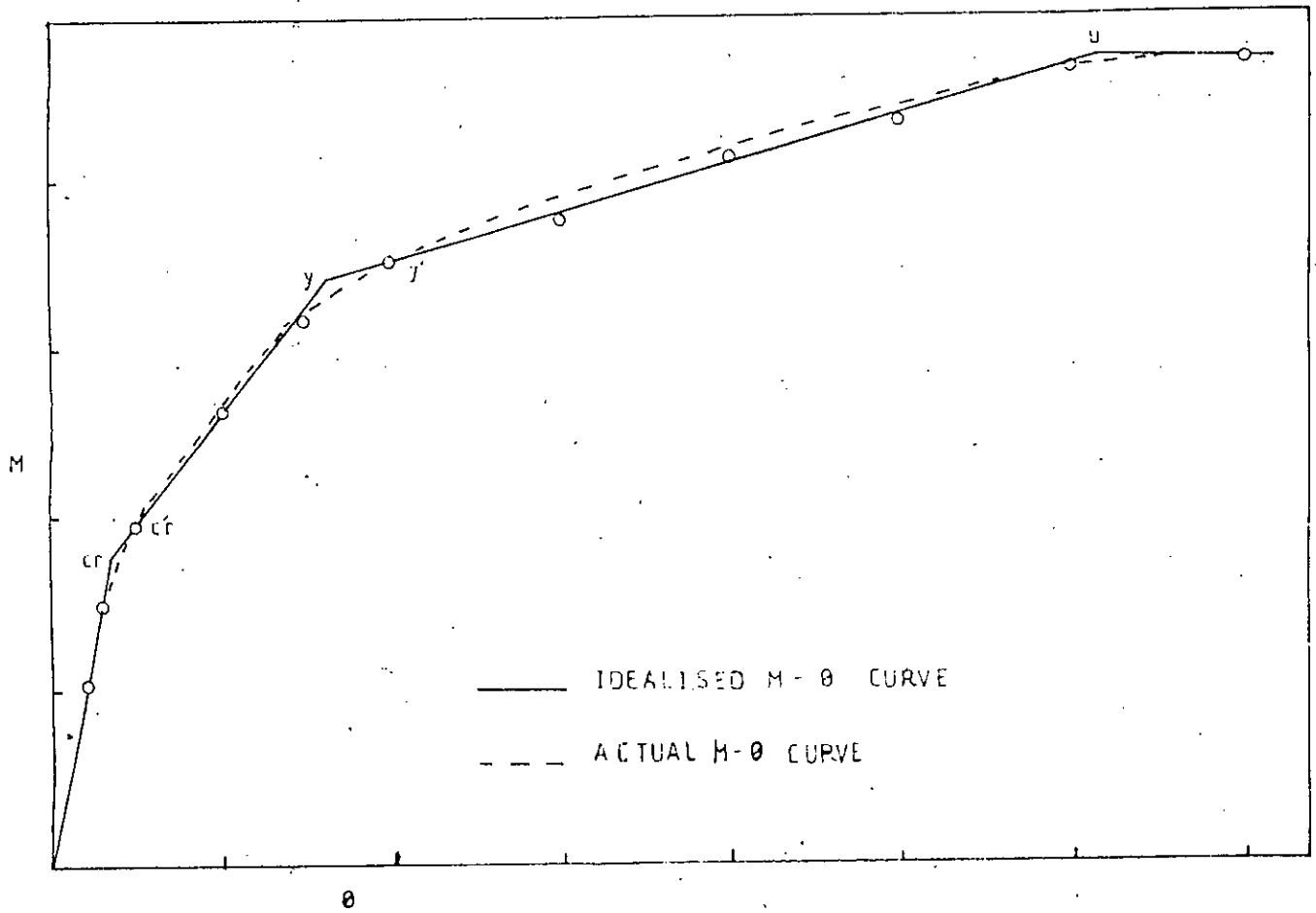


Fig. 5.3(b) : Typical Idealization of M - θ Curve

line 'cd' and the slope of this part will be called post cracking stiffness ' K_p '. The portion 'de' indicates the probable model failure.

A typical idealization of M- θ curve is shown in Fig.5.3(b). In this Fig. points C_r and y on idealized curve represent start of cracking and start of steel yielding respectively. Whereas in analysis, the points C_r' and y' represent the start of cracking and yielding of steel respectively. This is because, during analysis rotation was applied incrementally and it was not possible to find cracking and yielding points exactly. The moments at points C_r , y and U will be termed as cracking moment M_{cr} , yield moment M_y and ultimate moment M_u respectively.

For all the models investigated, idealized M- θ curves will be drawn showing the actual points on the graph. The stiffness K_0 , K_{cr} and K_p will be evaluated from idealized M- θ curve using equation 2.5. In calculating the value of stiffnesses (K_0, K_{cr}, K_p) using equation 2.5, precracking value of flexural rigidity (D) will be used. But after cracking of concrete, the value of D of the slab will be reduced. So calculated values of stiffnesses (K_{cr} , K_p) will be lower than the actual values.

5.4. Material Properties of Models

As reinforced concrete was the slab material, the concrete and steel properties were assumed and are presented in Table 5.3.

TABLE 5.1

Concrete Properties

Cube crushing strength, f_{cu}	= 27.6 N/mm ²
Modulus of rupture, f_r	= 2.76 N/mm ²
Modulus of elasticity, E_c	= 0.210E + 05 N/mm ²
Poisson's ratio of slab material, ν	= 0.15

Steel Properties

Yield strength, f_y	= 345 N/mm ²
Modulus of elasticity E_s	= .210 E + 06 N/mm ²
Yield strain, ϵ_y	= 0.001642

5.4. Geometric Dimensions of Models

The investigations have been carried out for a range of typical values of bay width (Y), corridor width (L) and length of slab panel (X) as shown in Fig. 5.4. Shaded area shows the one quadrant of the panel analyzed for each model. Table 5.2 shows the geometric dimensions of all the models investigated in this work.

Placing of Reinforcement in Models :

In all the models, reinforcements were provided according to the design as discussed in Chapter 3. Large diameter bars were used to minimize the number of bars in the slab. This was done to save the computer time during execution.

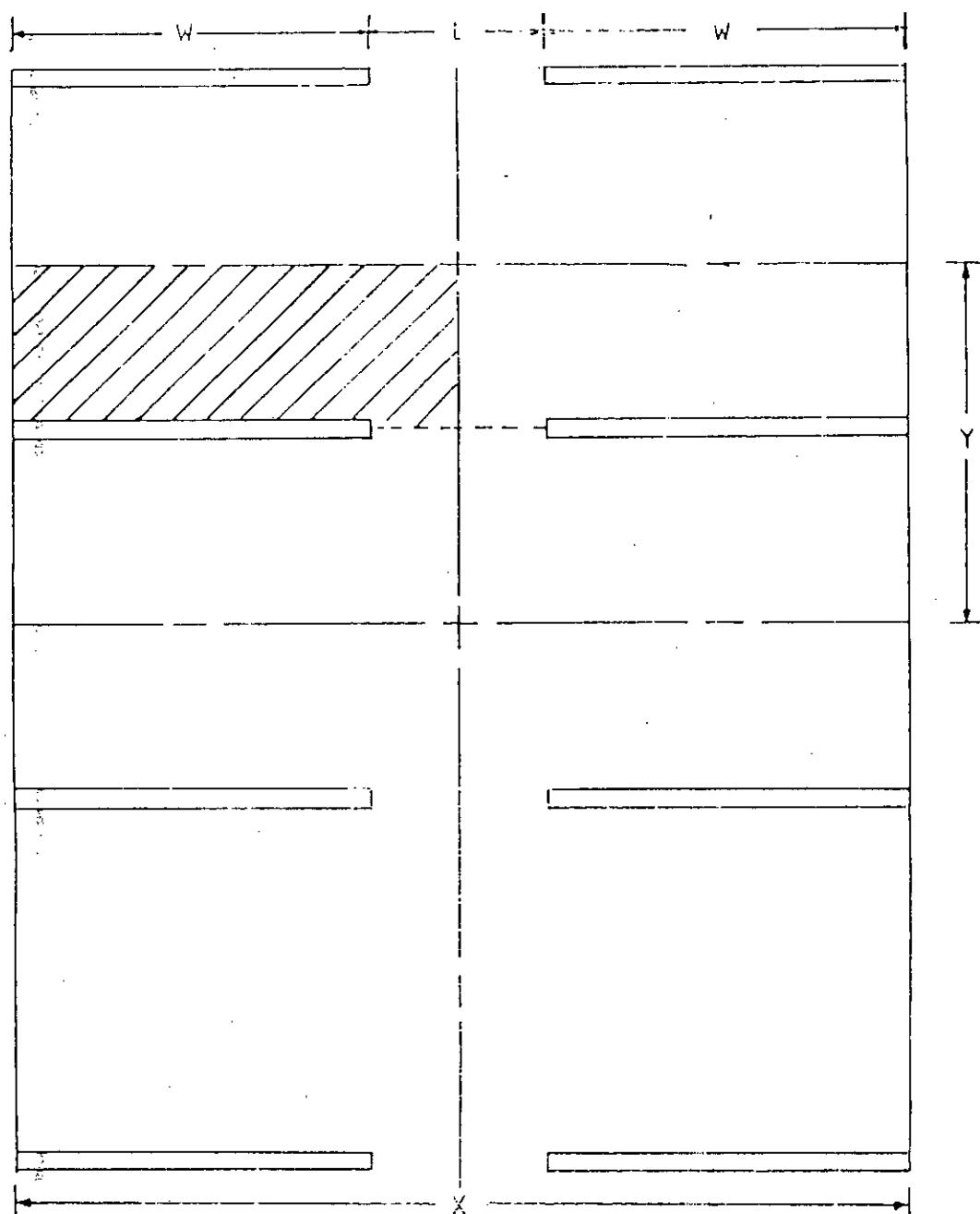


Fig. 5.4 : Geometric dimension of Models

TABLE 5.2

Model No.	Length of slab (X) in m	Corridor width(L) in m	Bay width (Y) in m	Width of wall (W) in m	slab thickness(t) in m
TMOD1	14.4	2.4	6.0	6.0	0.20
TMOD2	14.4	2.4	6.0	6.0	0.20
TMOD3	14.4	2.4	6.0	6.0	0.20
TMOD4	14.4	2.4	6.0	6.0	0.20
MOD61*	12.0	1.2	7.2	5.4	0.20
MOD62	12.0	2.4	7.2	4.8	0.20
MOD63	12.0	3.6	7.2	4.2	0.20
MOD64	12.0	4.8	7.2	3.6	0.20
MOD65	12.0	6.0	7.2	3.0	0.20
MOD66	12.0	7.2	7.2	2.4	0.20
MOD41	12.0	1.2	4.8	5.4	0.20
MOD42	12.0	2.4	4.8	4.8	0.20
MOD43	12.0	3.6	4.8	4.2	0.20
MOD44	12.0	4.8	4.8	3.6	0.20
MOD45	12.0	6.0	4.8	3.0	0.20
MOD46	12.0	7.2	4.8	2.4	0.20
MOD21	12.0	1.2	2.4	5.4	0.20
MOD22	12.0	2.4	2.4	4.8	0.20
MOD23	12.0	3.6	2.4	4.2	0.20
MOD24	12.0	4.8	2.4	3.6	0.20
MOD25	12.0	6.0	2.4	3.0	0.20
MOD26	12.0	7.2	2.4	2.4	0.20
MOD11	12.0	1.2	1.2	5.4	0.20
MOD12	12.0	2.4	1.2	4.8	0.20
MOD13	12.0	3.6	1.2	4.2	0.20
MOD14	12.0	4.8	1.2	3.6	0.20
MOD15	12.0	6.0	1.2	3.0	0.20
MOD16*	12.0	7.2	1.2	2.4	0.20

*Models are numbered in such a way that the 1st & 2nd numeric values in decimal represent the values of Y/X & L/X respectively

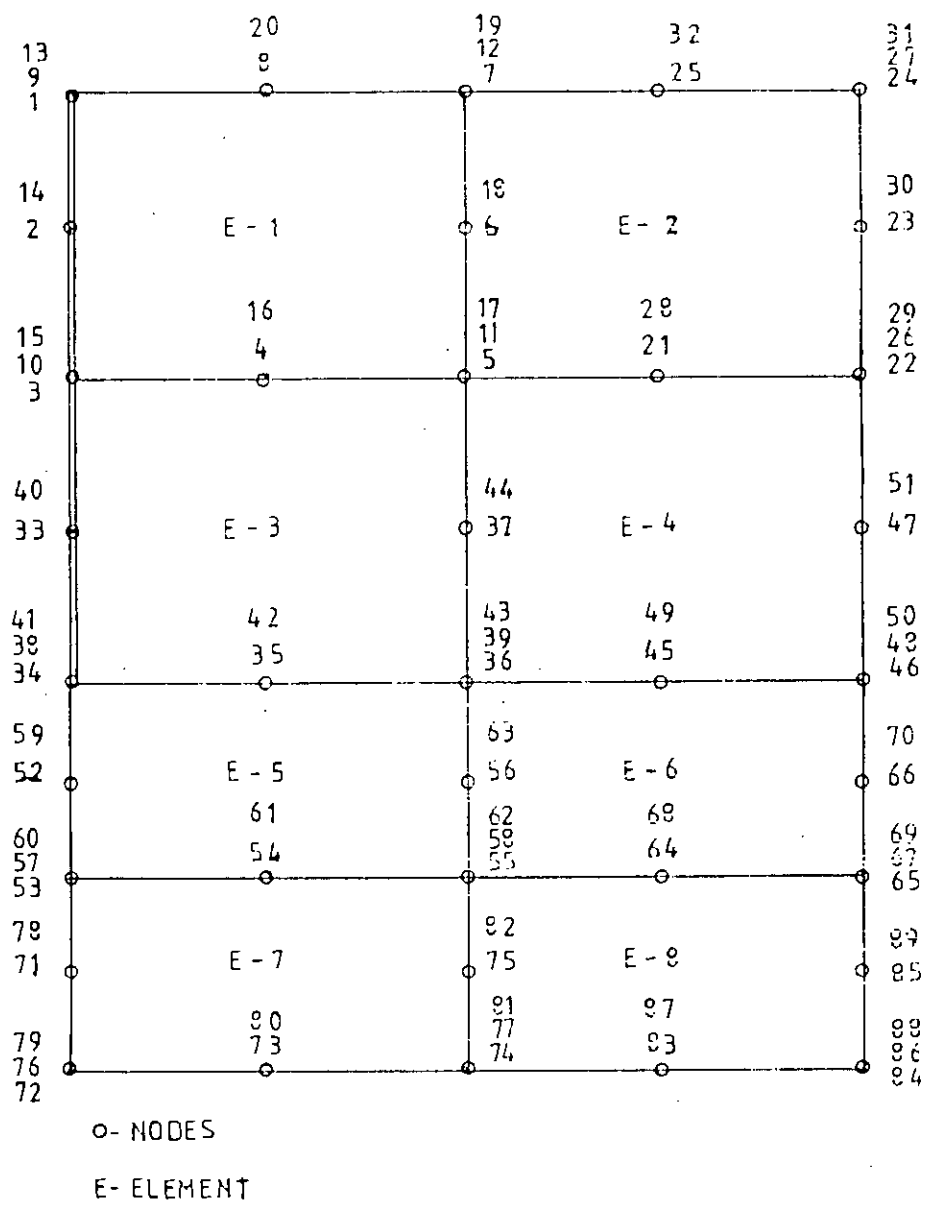


Fig. 5.5 : A Typical 8 - element Mesh

5.6 Parameter Study

The parameters affecting the numerical solution of nonlinear analysis are (a) Mesh size, (b) Tension stiffening, (c) Tensile strength of concrete, (d) Angle of crack (e) Shear retention factor of cracked concrete and (f) Norm of convergence tolerance. Influences of the some of the above parameters were studied by many authors which was discussed in article 2.5. In this study, influence of mesh size was studied only.

Effect of Mesh Refinement :

Model MOD42 was considered for this study. This model was studied by dividing it into a 4-element mesh and 8 eight element mesh. Refined model MOD42 was named as RTMOD42. The typical 8-element mesh is shown in Fig.5.5. Figs.5.6 shows the plan with reinforcements for the models. Fig.5.7 presents the idealised $M-\theta$ curves for the models. To facilitate a comparative study Table 5.3 is prepared and presented below.

TABLE 5.3

Model No.	Moments in kn-m			Stiffnesses			Effective width	
	M_{cr}	M_v	M_u	K_o	K_{cr}	K_p	Author $Y_{e.o}/Y$	Coull&Wong $Y_{e.o}/Y$
MOD42	47	296	338	36	8.0	3.9	0.34	0.36
RTMOD42	47	315	345	32	9.0	4.04	0.30	0.36

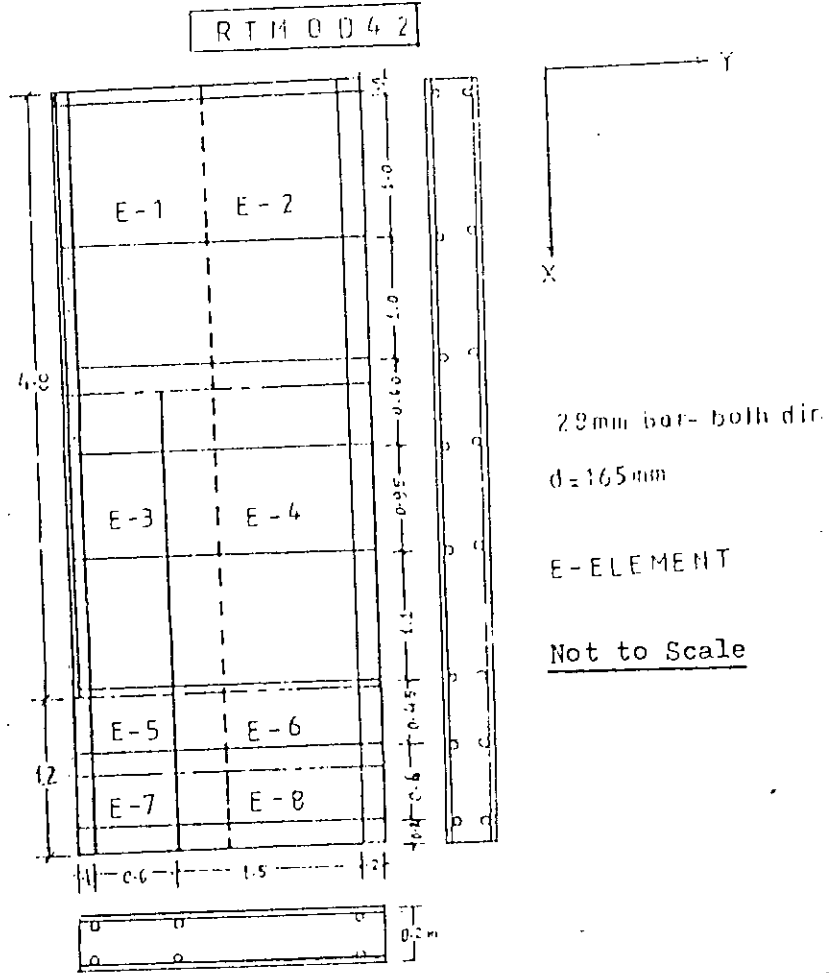


Fig. 5.6 : Plan with reinforcement for models MOD42 & RIMOD42

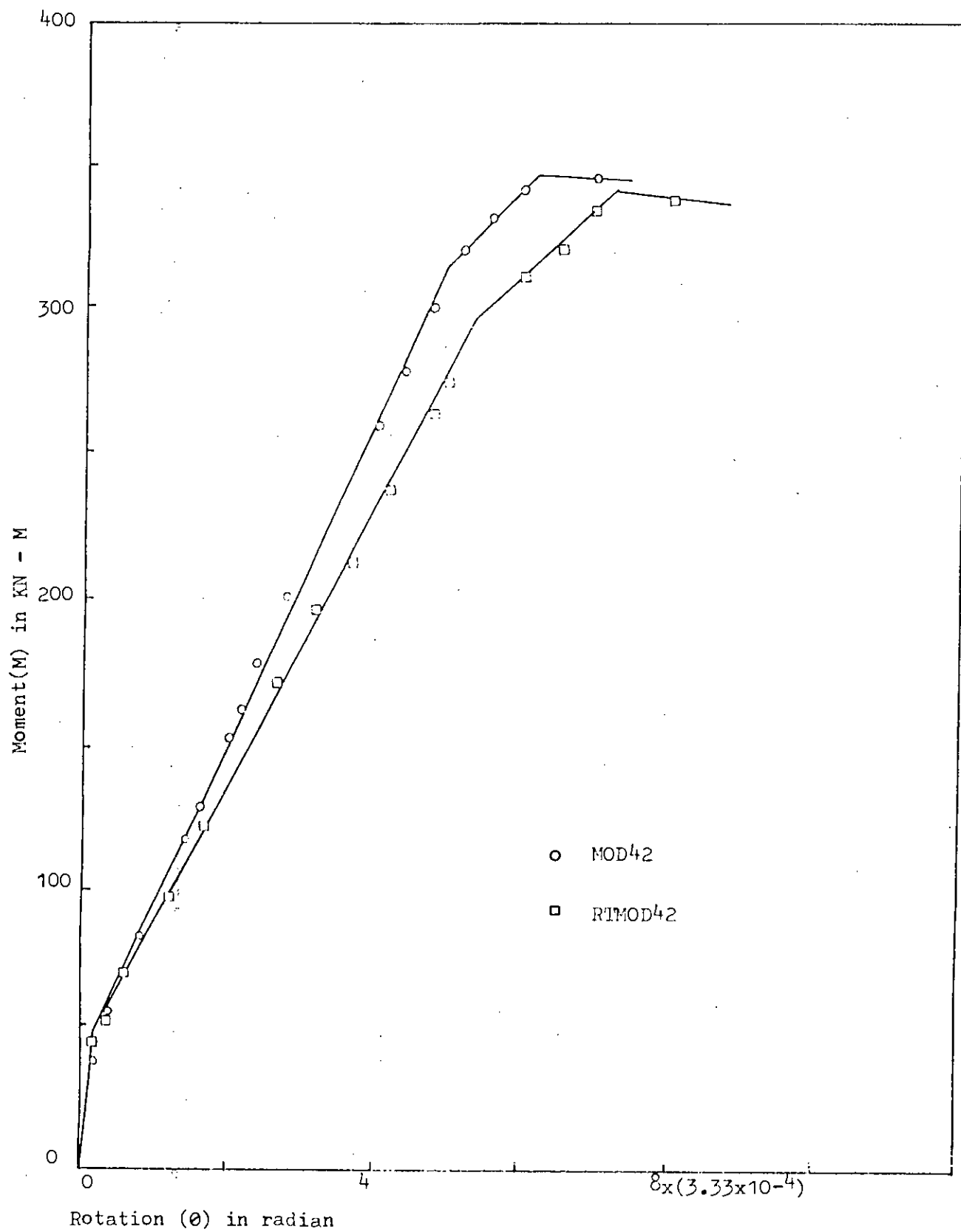
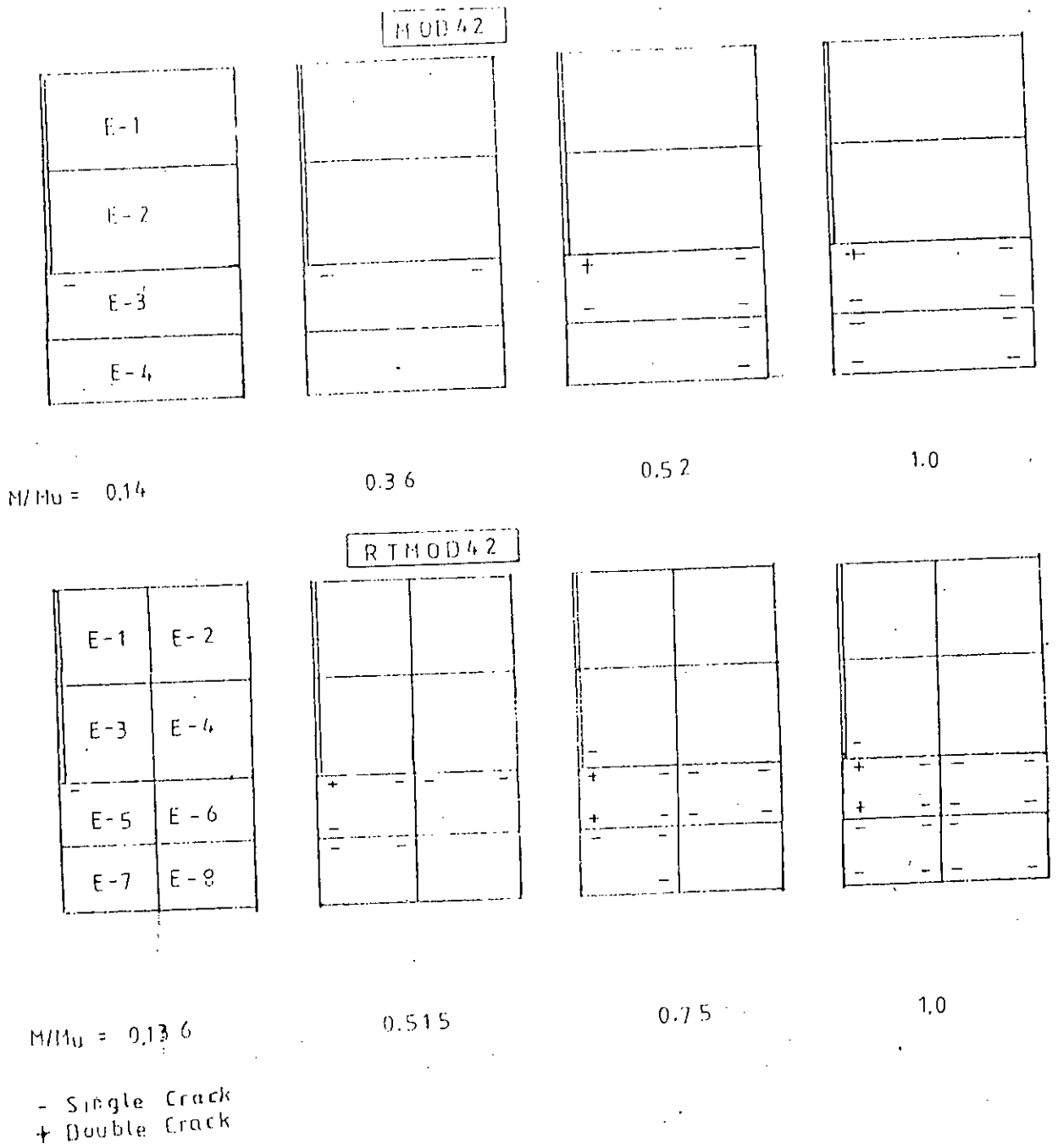


Fig. 5.7 : Comparison of M - θ curves for the models



Figs. 5. 8 : Effect of mesh refinement on crack pattern

It is found that the both models crack approximately at the same cracking moment although M_y and M_u for model RTMOD42 are 6% and 2% higher respectively. This deviations may be considered to be small. The value of K_o for model MOD42 is 11% higher than that of RTMOD42. But the values k_{cr} and K_p for model RTMOD42 are 11% and 3.46% higher respectively than those from MOD42. The value of K_o from MOD42 is closer to that from Coull & Wong.

Figs. 5.8 presents the propagation of cracks for the two models. Crack pattern for the two models are similar. Again sampling points near the interior edge of the shear wall cracked first and corridor slab cracked severely.

In this study, 4-element mesh was used throughout the investigations to save computer time as 8-element mesh required much more computer time.

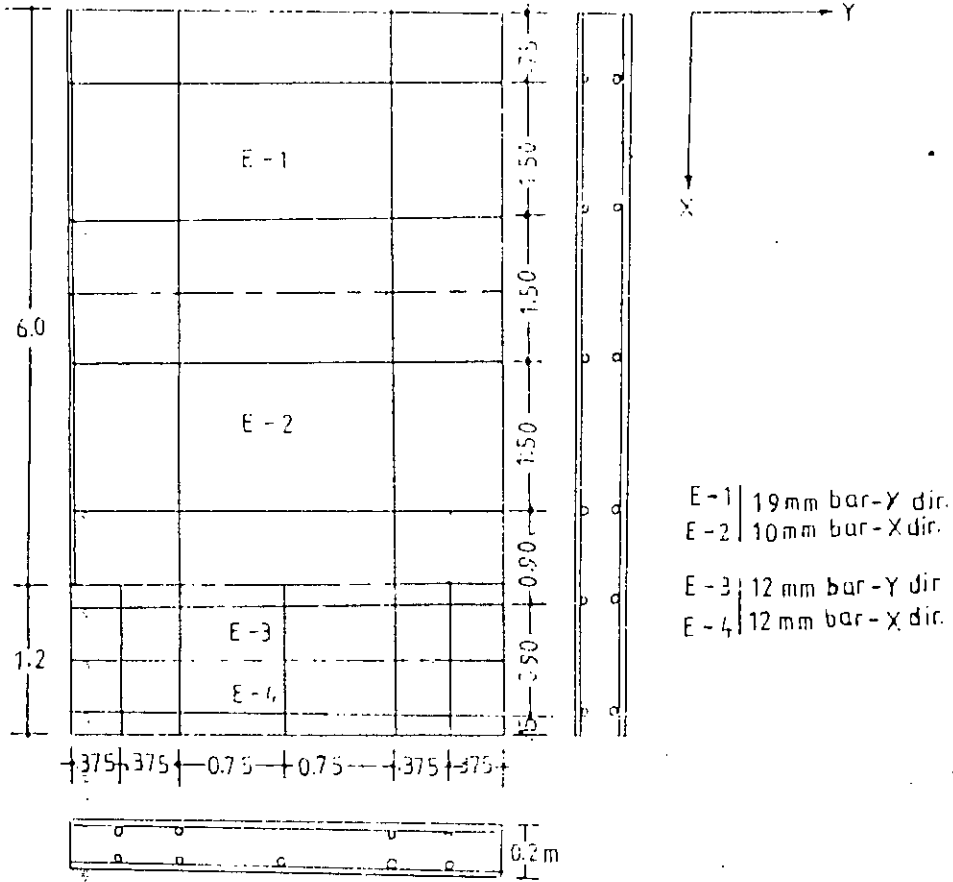
Considerations to Other Parameters :

Tension stiffening was ignored in this study. In order to minimize the number of elements, the wall was assumed to have zero thickness. Other parameters were included in numerical modelling as discussed in chapter 4.

5.7 Model Investigations on Effect of Reinforcement

In this stage several models named as TMOD1, TMOD2, TMOD3 and TMOD4 were studied. All the models had same geometric dimensions but different percentages of reinforcements. Plan with reinforcement arrangements are shown in Figs. 5.9.

TMOD 1



TMOD 2

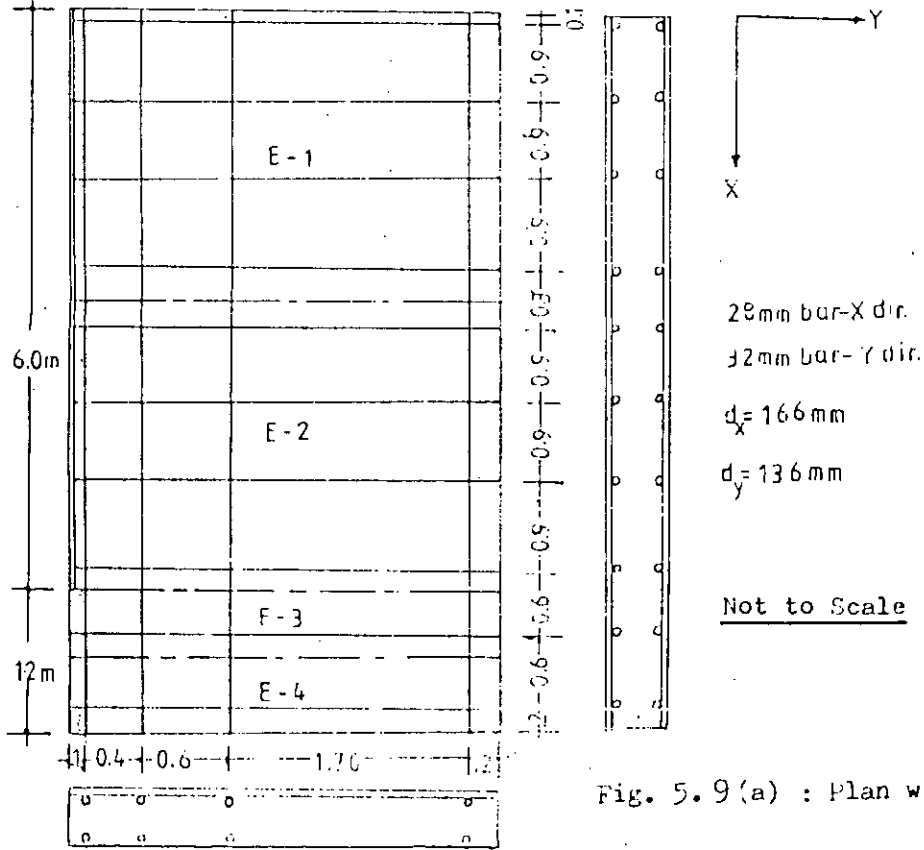


Fig. 5.9 (a) : Plan with reinforcement

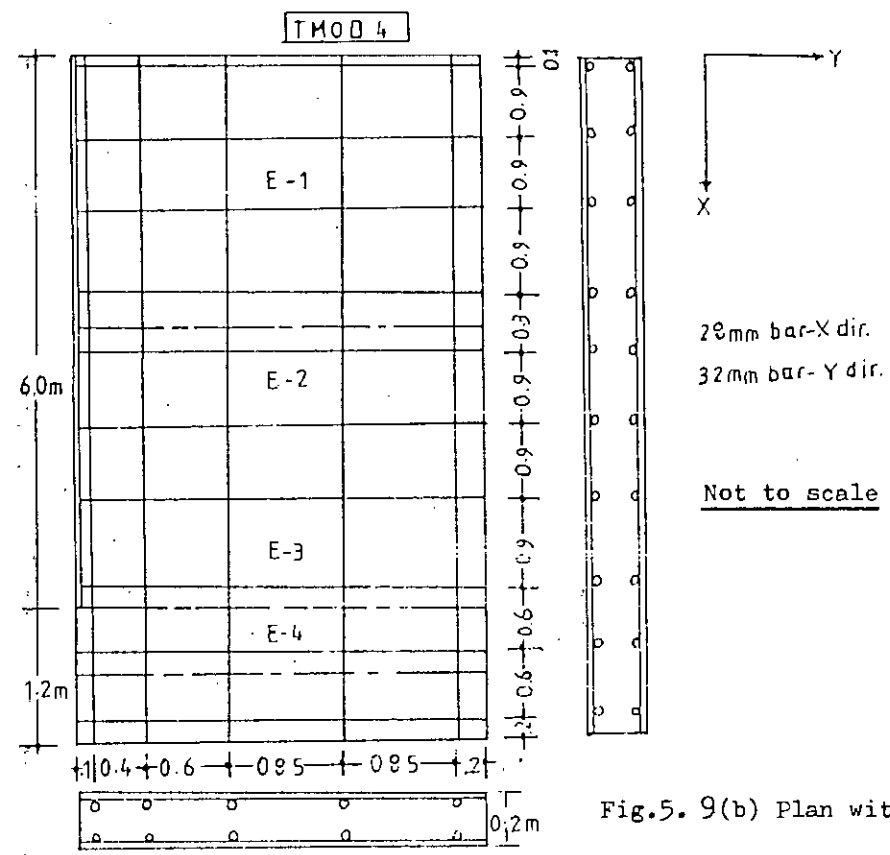
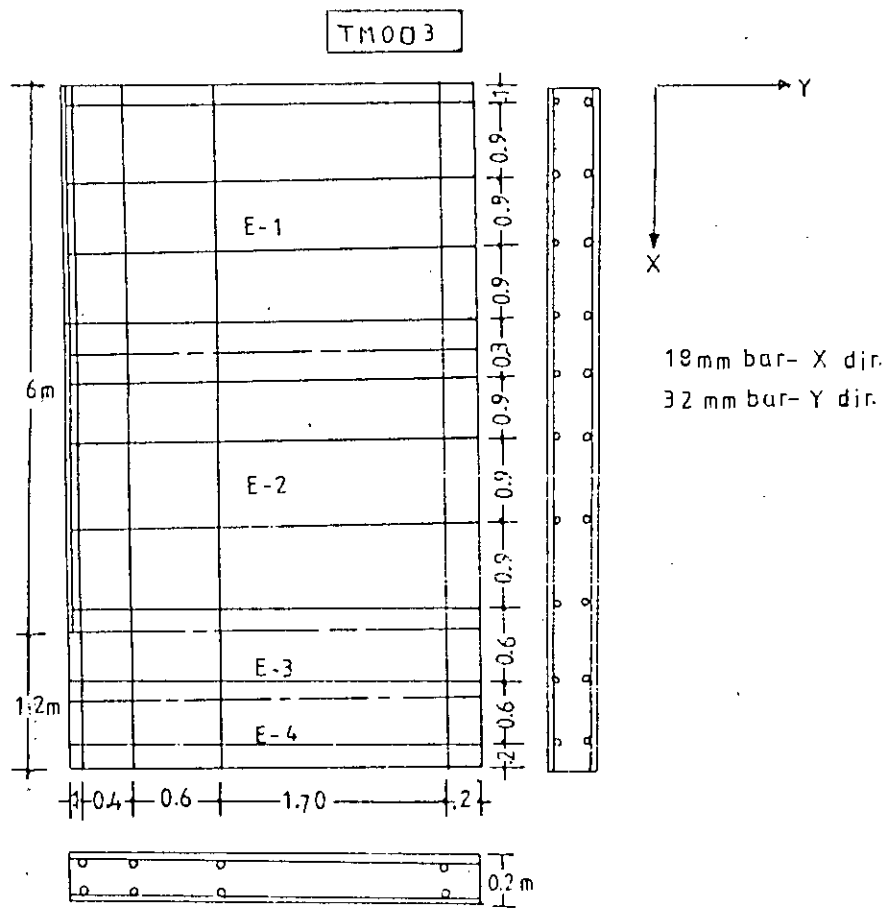


Fig.5. 9(b) Plan with reinforcement

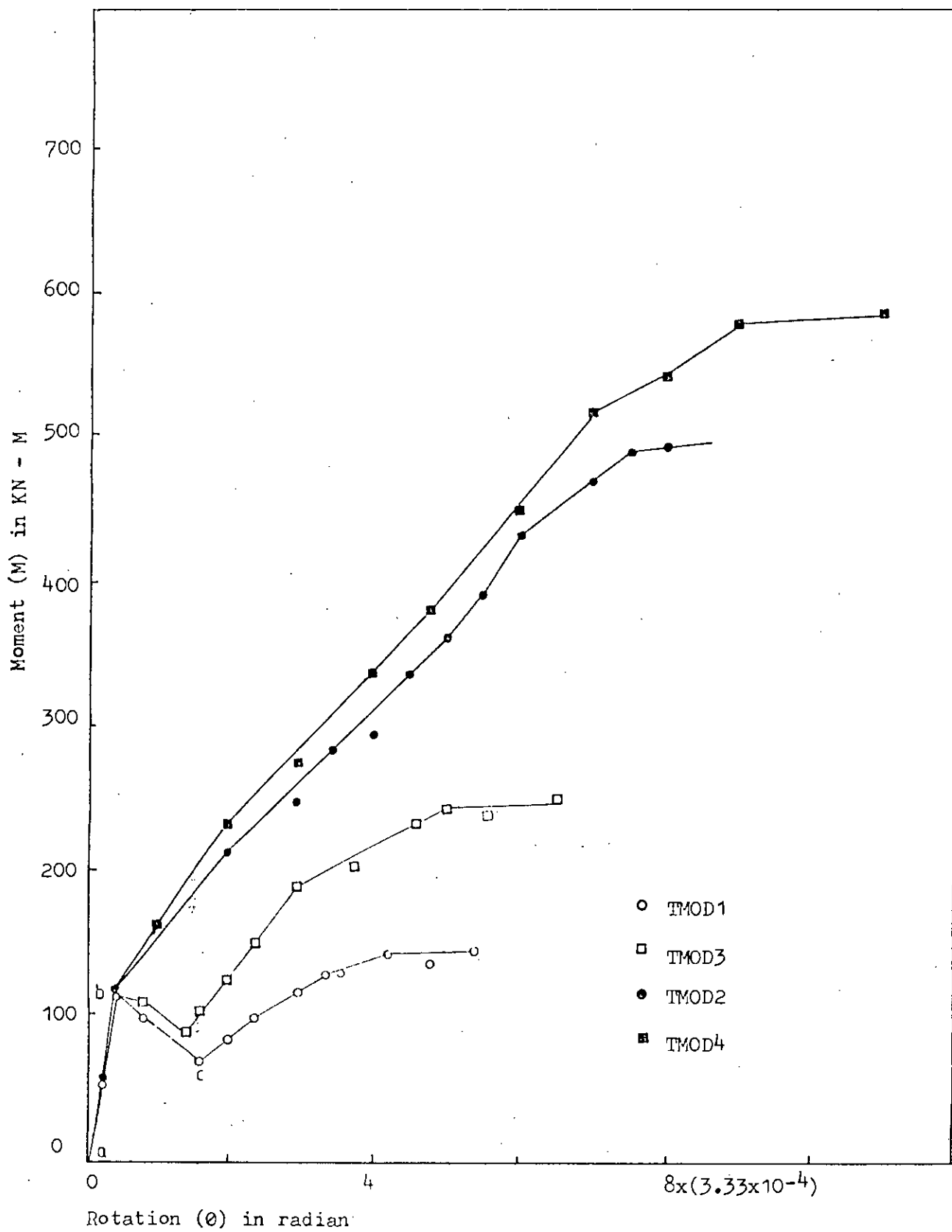


Fig. 5.10 : Comparison of M - θ relationships

Effect of Reinforcement on M- θ Relationships :

Figs. 5.10 presents M- θ relationships for the models TMOD1, TMOD2, TMOD3 and TMOD4. But the unusual shape of the M- θ graphs of models TMOD1 and TMOD3 draws the attention. The part ab of the graph represents precracking stage. As the imposed displacements are increased, cracks start forming and there is a sudden decrease in the moment as represented by the part bc of the curve. The moment M_b at point b represents the uncracked moment.

The reason for this type of behaviour is supposed to occur for providing very low steel in the slab. Steel provided in the model TMOD1 was $P_x(As/bd) = 0.074\%$, $P_y = 0.061\%$ and in the model TMOD3 was $P_x = 0.2\%$, $P_y = 0.784\%$. Those steels were much less than that prescribed by ACI Code ($P_{min} = 200/f_y = 0.4\%$). To analyze the M- θ graphs for the two models, Table 5.4 is prepared.

TABLE 5.4

Model	Moment at section at the interior edge of shear wall		Stiffness		Effective width	Analytical M_{veo} (kN-m)
	M_b	M_c	K_o	N_c	Y_{eo}/Y	
TMOD1	28	18.5	59		0.328	15
TMOD2	28.5	25.0	59		0.328	20

M_{veo} = ultimate moment of the slab section having effective width Y_{eo} .

The moment M_{veo} is evaluated following the procedure discussed in article (5.8.4).

Pre-cracking stiffness (K_o) for the two models are same. From the Table 5.4, it is found that the cracking moment M_b from $M-\theta$ curve is greater than the ultimate moment $M_{y..}$. Therefore, after cracking, the capacity of the slab section reduces as the steel provided in the slab is much less, resulting in a sudden decrease of moment.

Reinforcements were increased in models TMOD2 ($P_x = 0.52\%$, $P_y = 0.784\%$) and TMOD4 ($P_x = .65\%$, $P_y = .784\%$) and were investigated. Fig. 5.10 shows that as the reinforcement is increased, the point c is gradually shifted upward and finally the sudden drop in the graph disappears. The smooth curve of Model TMOD2 and TMOD4 is due to the fact that the steel provided is greater than that minimum steel specified by ACI Code. Therefore, percentages of steel has a remarkable influence on the shape of $M-\theta$ graphs and minimum steel specified by ACI code should be provided to have the normal behaviour of reinforced concrete.

Effect of reinforcement on stiffness :

Idealized $M-\theta$ curves for models TMOD2 and TMOD4 are presented in Fig. 5.11, to calculate the stiffnesses for the models. Table 5.5 is presented to compare the stiffnesses.

TABLE 5.5

Model	Stiffness			Effective width	Effective width
	K_o	K_{cr}	K_p	$Y_{e.o}/Y$	Coull & Wong
TMOD2	62	11.78	6.54	0.345	0.32
TMOD4	62	12.57	6.98	0.345	0.32

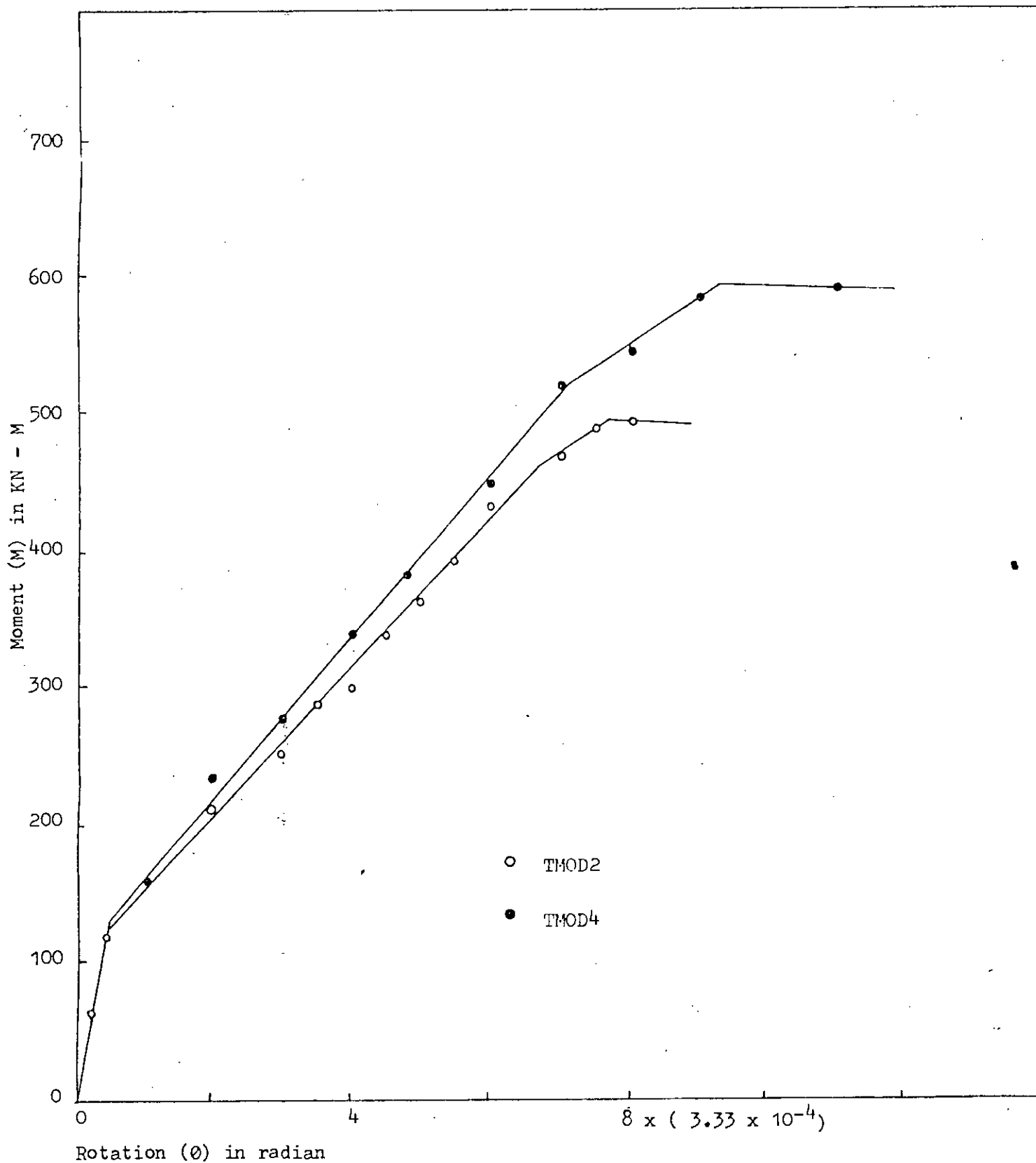


Fig. 5.11: Effect of reinforcement on M - θ relationships

Precracking stiffness for the two models are same although the amount of reinforcement in TMOD4 is 25% higher than that in TMOD2. Therefore, it may be concluded from the models analyzed that the amount of reinforcement has negligible influence on the precracking stiffness of slab.

Precracking effective width (Y_{e0}) for the models are only 6.5% higher than that from Coull & Wong linear analysis.

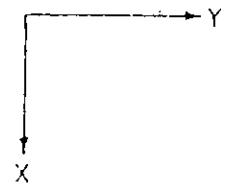
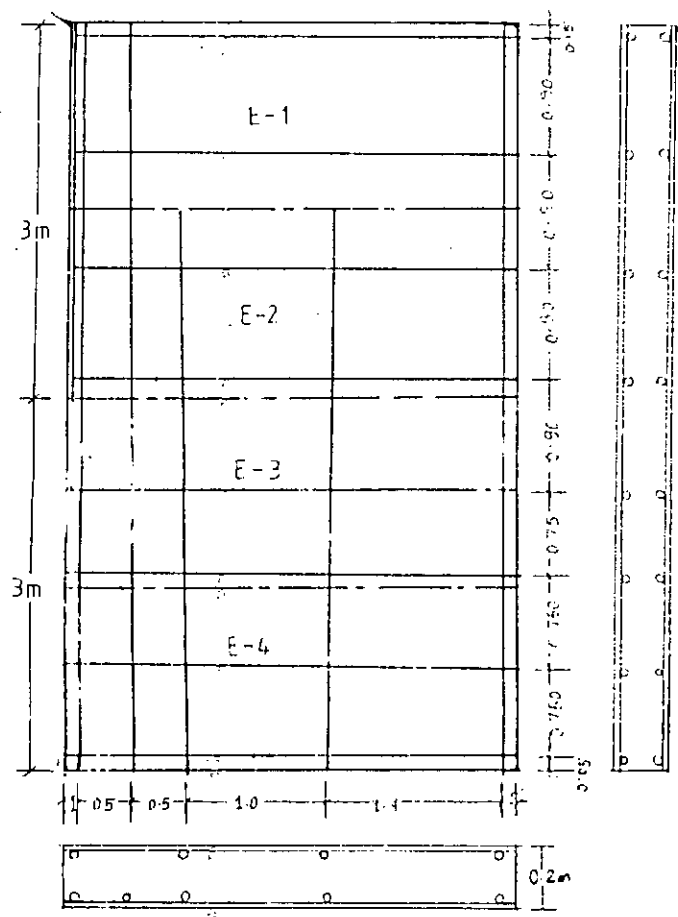
But cracking stiffness (K_{cr}) and post cracking stiffness (K_p) for model TMOD4 are approximately 6% higher than those for model TMOD2.

Cracking, yielding and ultimate moments increase with increase in percentages of reinforcement. Crack patterns are similar to the models described earlier. Corridor slab cracks severely as discussed in earlier models.

5.8. Model Investigations to Study the Effect of Geometric Parameters

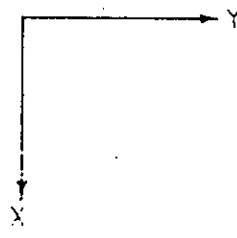
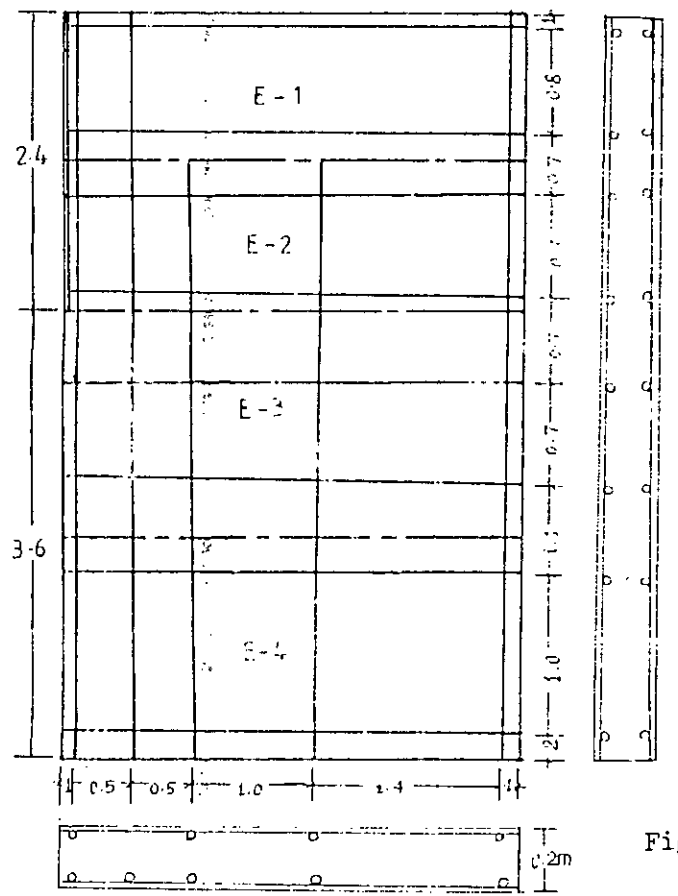
A systematic investigations was carried out with different slab-wall configurations with planar shear walls. In these investigations, the effect of geometrical parameters such as corridor width, L , spacing of shear wall, Y and slab width X on the behaviour of slab was studied. Most of the researchers conducted their research to relate the flexural stiffness and effective width with geometric parameters. Therefore, similar investigations were conducted so that the results could be compared with those established results. The models were divided into 4 groups having different ratio of Y/x and in each group the ratio L/x varied from 0.1 to 0.6.

MOD 65



28mm bar - Y direction
 32mm bar - X direction
 d = 164mm

MOD 66



28mm - Y dir.
 32mm - X dir.
 d = 164mm

Not to scale

Figs. 5.1 2: Plan with reinforcement

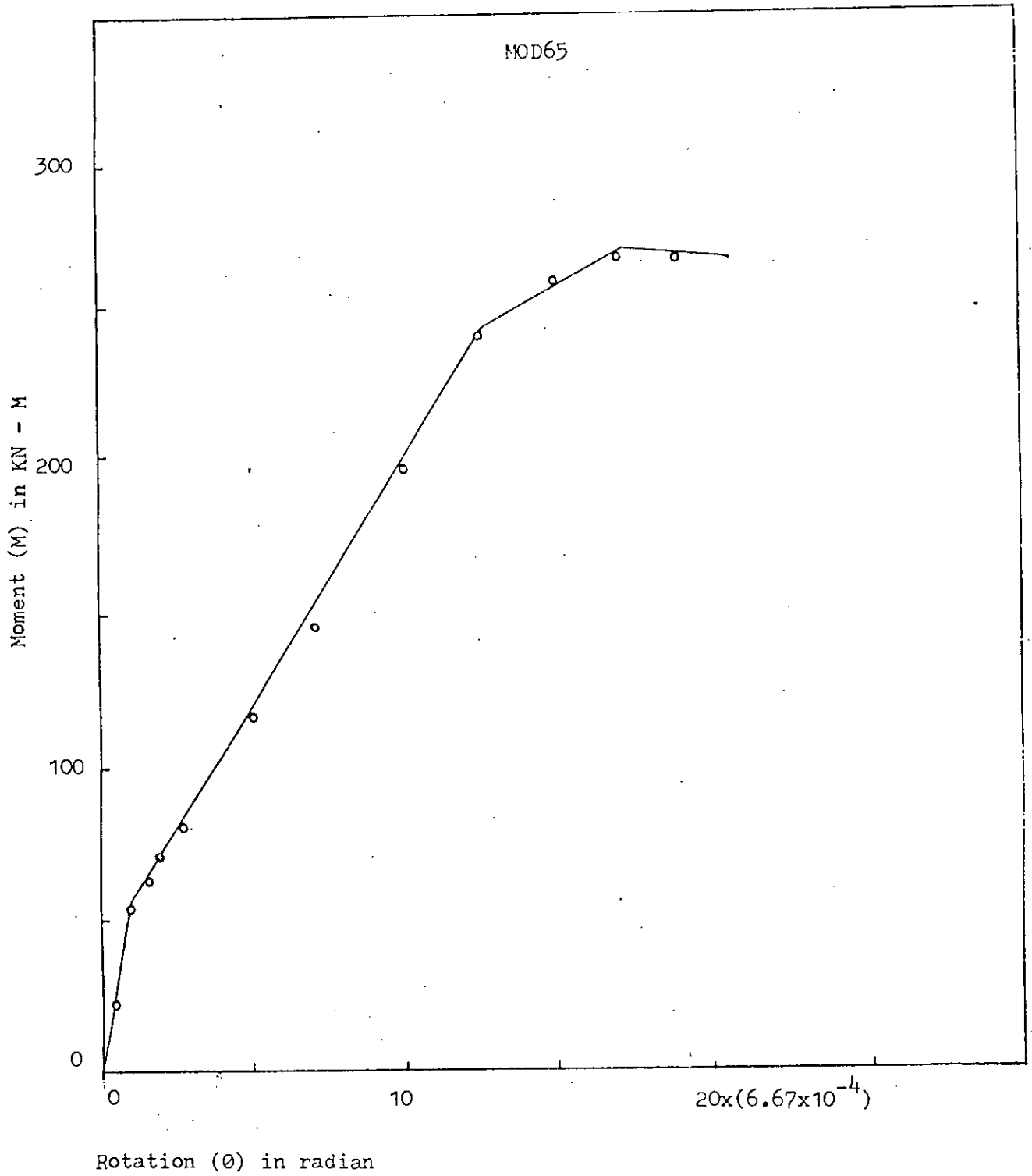


Fig. 5.13(a) M - θ relationship

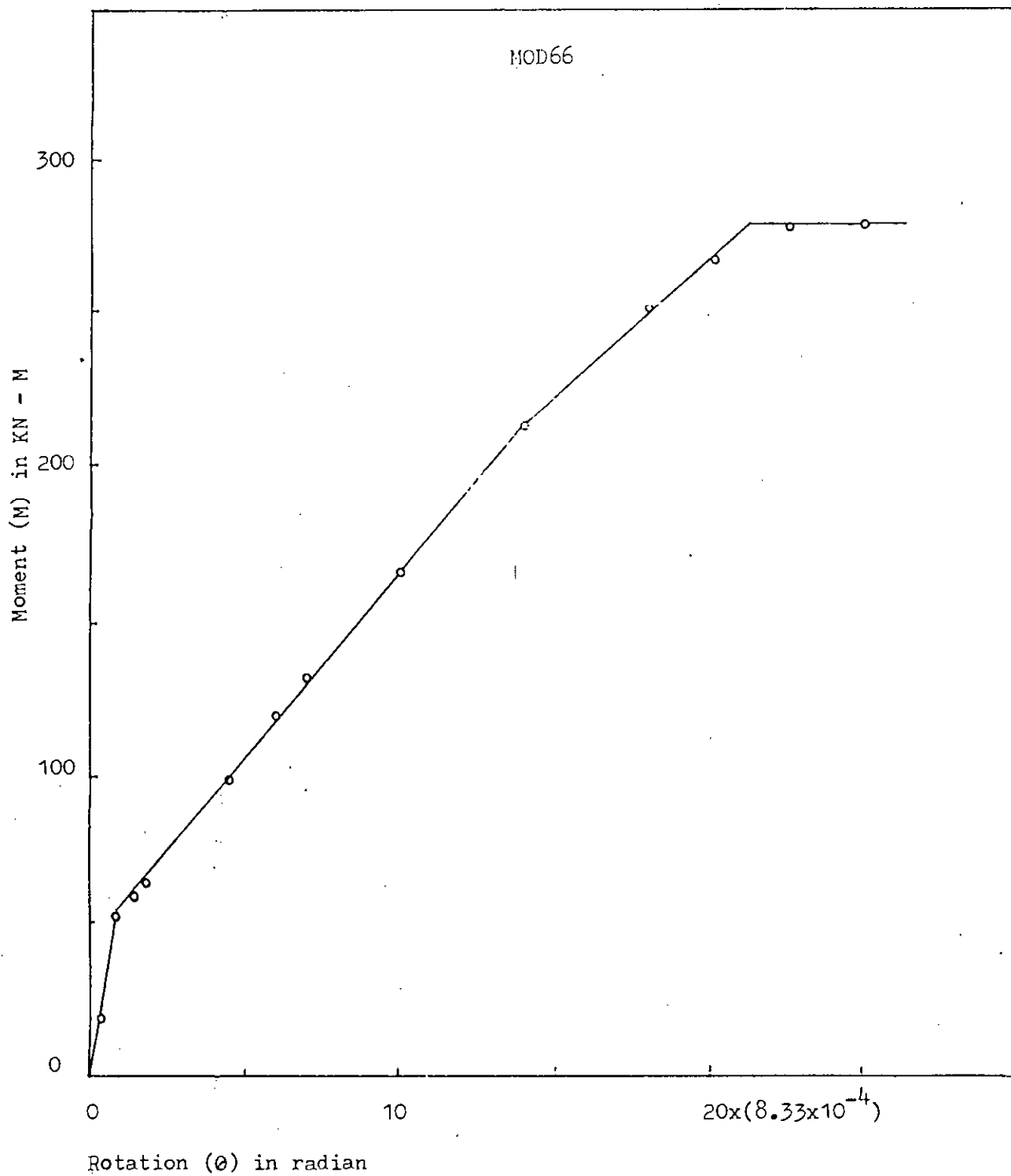
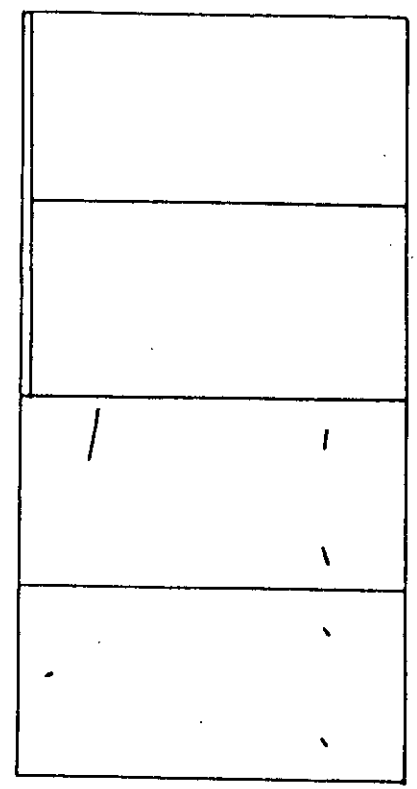
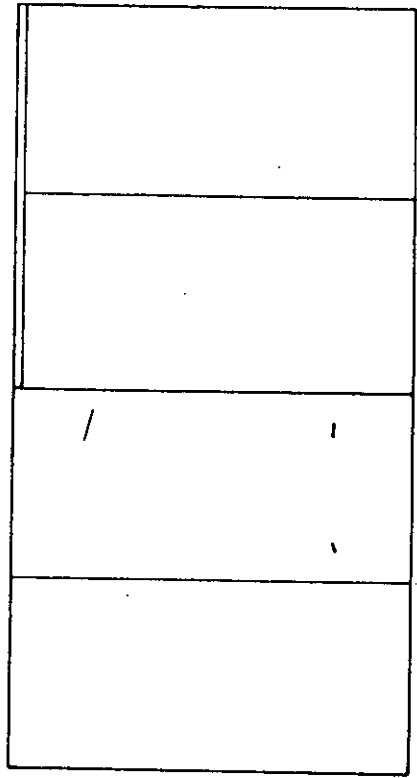
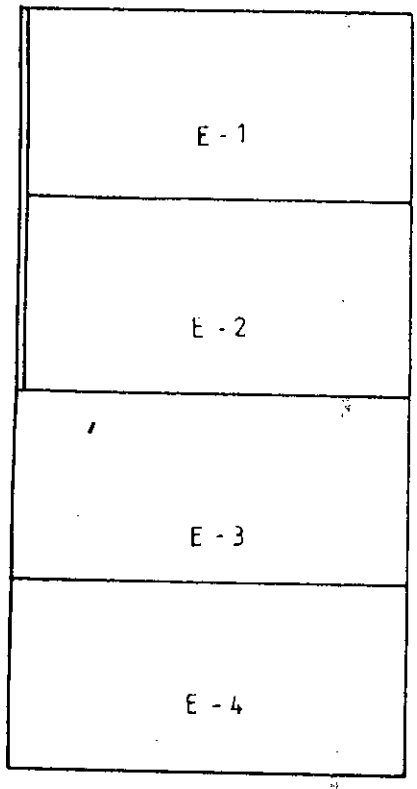


Fig. 5.13(b) : M - θ relationship

MOD62

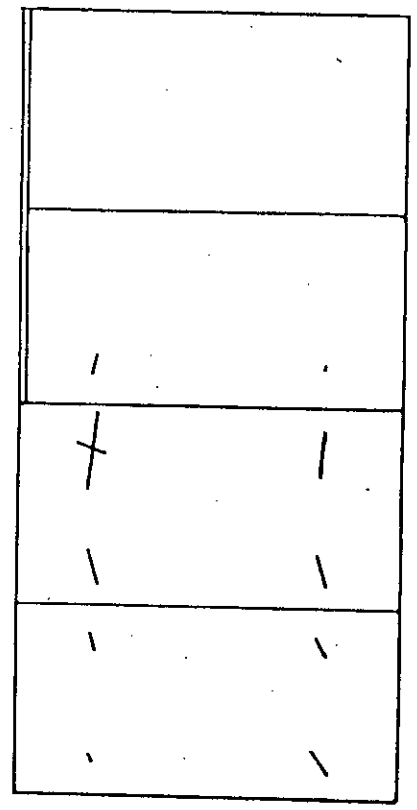
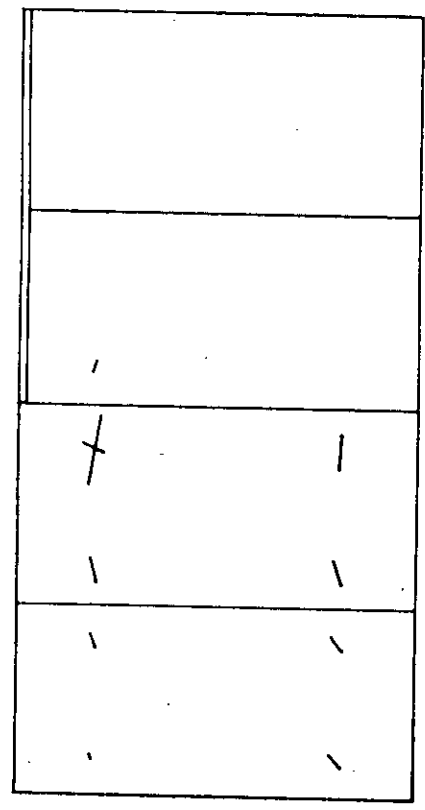
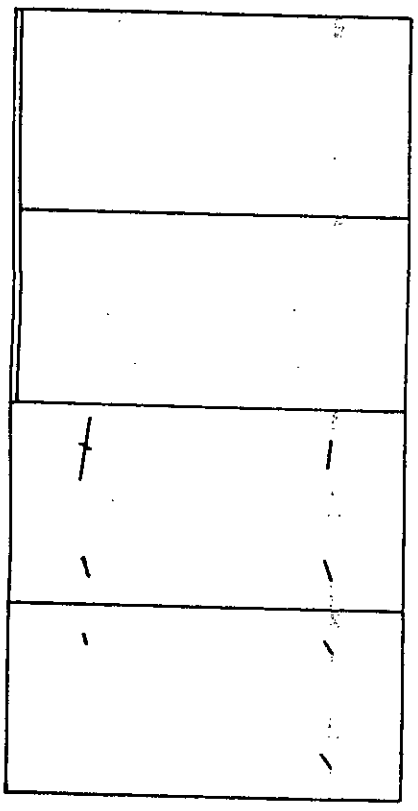


M/M_u = 0.238

0.32

0.42

STRAIN 0 .003 .006



M/M_u = 0.65

0.78

1.0

Fig. 5.14: Gradual propagation of cracks in model MOD62.

5.8.1 Description of Behaviour of Slabs in Theoretical Studies

a) Models with $Y/X = 0.6$

Models MOD61, MOD62, MOD63, MOD64, MOD65 and MOD66 having L/X 0.1, 0.2, 0.3, 0.4, 0.5 and 0.6 respectively were investigated in this group. Plan with reinforcement of models MOD61, MOD62, MOD63 and MOD64 were presented in Figs. 4 (Appendix). Idealized M- θ diagrams were also presented in Figs. 5 (Appendix). Plan with reinforcements of models MOD65 and MOD66 are shown in Fig. 5.12. Idealized M- θ diagrams for these models are presented in Figs. 5.13.

Cracking diagrams for the models MOD61, MOD62, MOD63 and MOD64 were also presented in Figs. 6 (Appendix). But those crack pattern merely shows the sampling points which are cracked. Cracking started in MOD61 at 25.3%, in MOD62 at 23.8%, in MOD63 at 22.5% and in MOD64 at 23% of ultimate load. In all the models cracks started from the interior edge of the shearwall and gradually propagated towards the edges of the slab. In all the models, corridor slab, that is Element 3 and Element 4 was cracked severely and failure was supposed to occur at the section passing through the interior edge of the shear wall. Similar cracking diagrams were also observed for models MOD65 and MOD66. In MOD65 cracks started at 21.3% and in MOD66 at 19.6% of ultimate load.

A particular model MOD62 is taken to study the actual direction of cracks. As it will be difficult to show the propagation of cracks in three dimension, crack patterns are shown in two dimensional (X-Y) plane. The direction of the cracks in the fig. represents the direction of principal stresses causing the crack and the length of the crack at a sampling point represents the magnitude of the corresponding principal strain.

TABLE 5.6

Model No.	Parameters		Moment from Idealised M- θ Curve in Kn-M			Ratios	
	Y/X	L/X	M_{cr}	M_y	M_u	M_{cr}/M_u	M_y/M_u
MOD61		0.1	100	467	560	0.179	0.830
MOD62		0.2	78	309	328	0.238	0.940
MOD63	0.6	0.3	63	235	280	0.225	0.800
MOD64		0.4	57	203	247	0.231	0.820
MOD65		0.5	57	240	268	0.213	0.896
MOD66		0.6	54	212	276	0.196	0.770
MOD41		0.1	98	319	412	0.238	0.774
MOD42		0.2	47	296	338	0.140	0.876
MOD43		0.3	38	245	308	0.125	0.795
MOD44	0.4	0.4	31	161	206	0.105	0.780
MOD45		0.5	30	261	287	0.105	0.910
MOD46		0.6	28	198	236	0.119	0.839
MOD21		0.1	68	312	364	0.187	0.850
MOD22		0.2	35	219	258	0.136	0.930
MOD23		0.3	30	193	262	0.115	0.740
MOD24	0.2	0.4	29	202	259	0.110	0.780
MOD25		0.5	17	157	181	0.100	0.870
MOD26		0.6	25	121	132	0.189	0.910
MOD11		0.1	54	237	293	0.184	0.810
MOD12		0.2	20	175	198	0.101	0.880
MOD13		0.3	21	105	198	0.190	0.950
MOD14	0.1	0.4	17	93	115	0.150	0.810
MOD15		0.5	15	87	108	0.139	0.805
MOD16		0.6	14	95	103	0.131	0.920

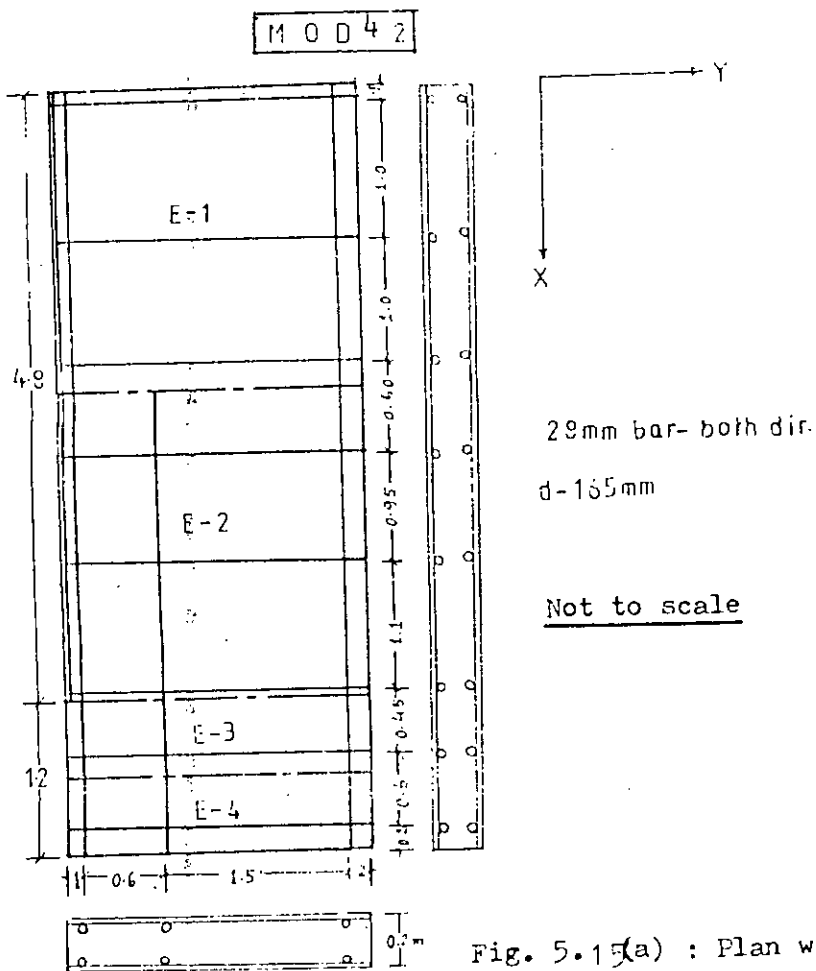
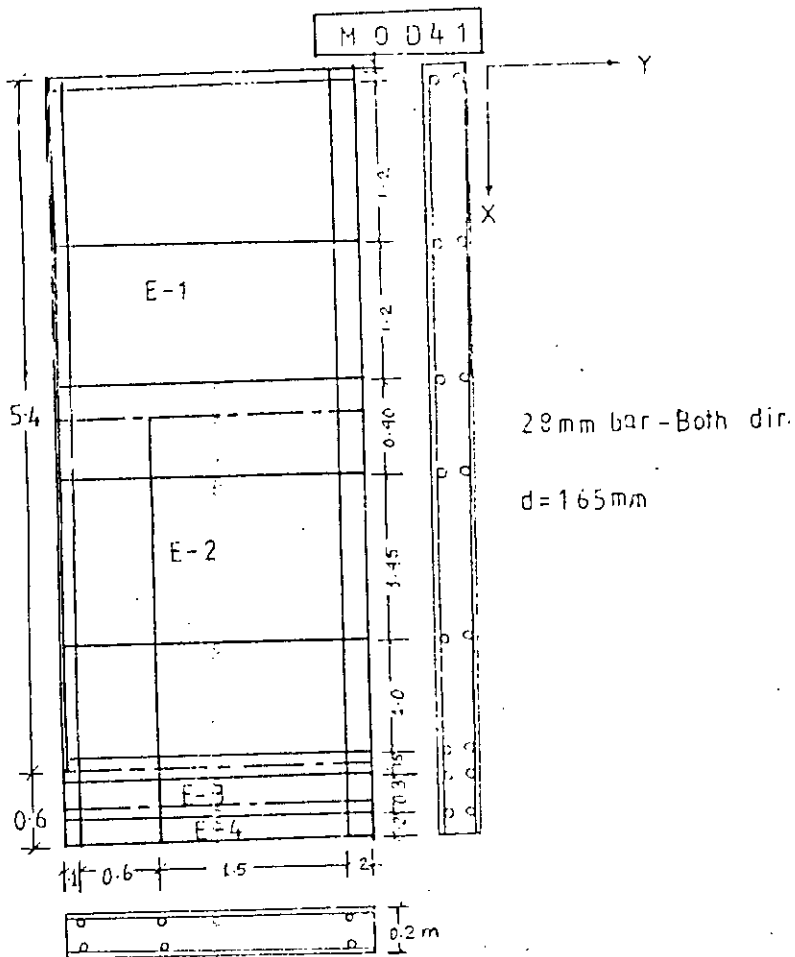
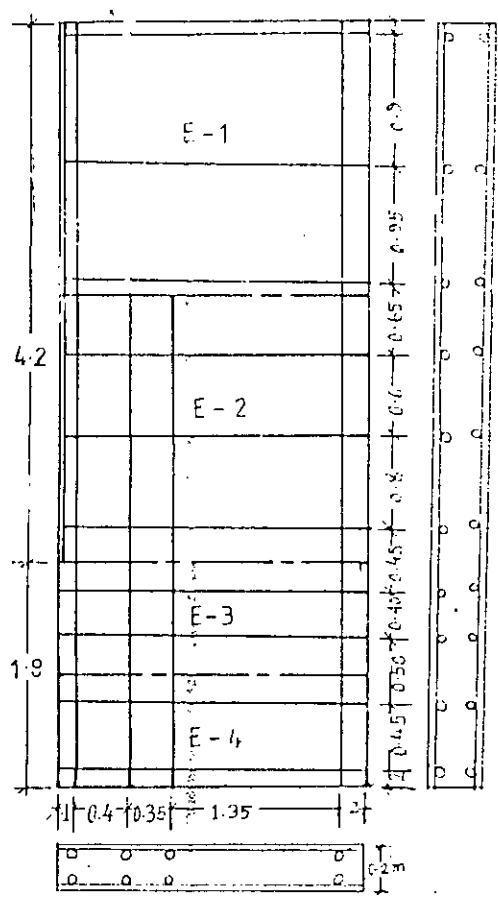


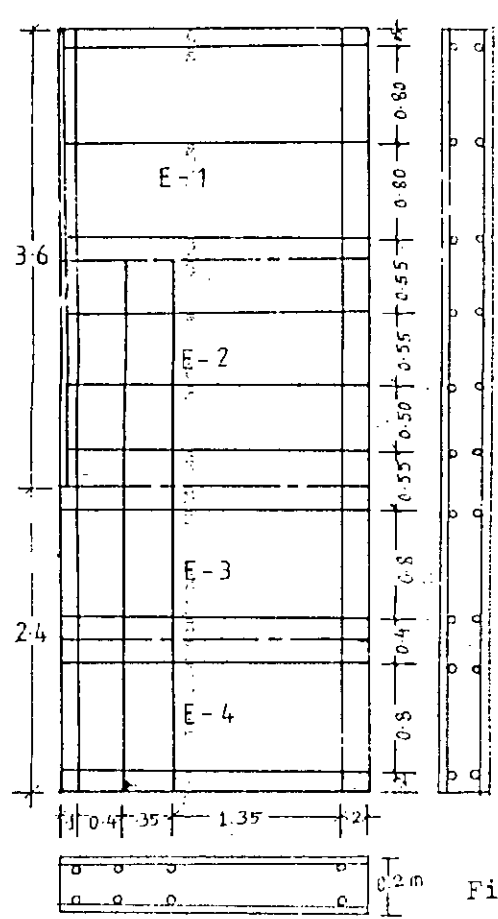
Fig. 5.15(a) : Plan with reinforcement



Y
X

25mm bar- both dir.

d=170mm



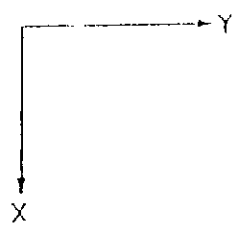
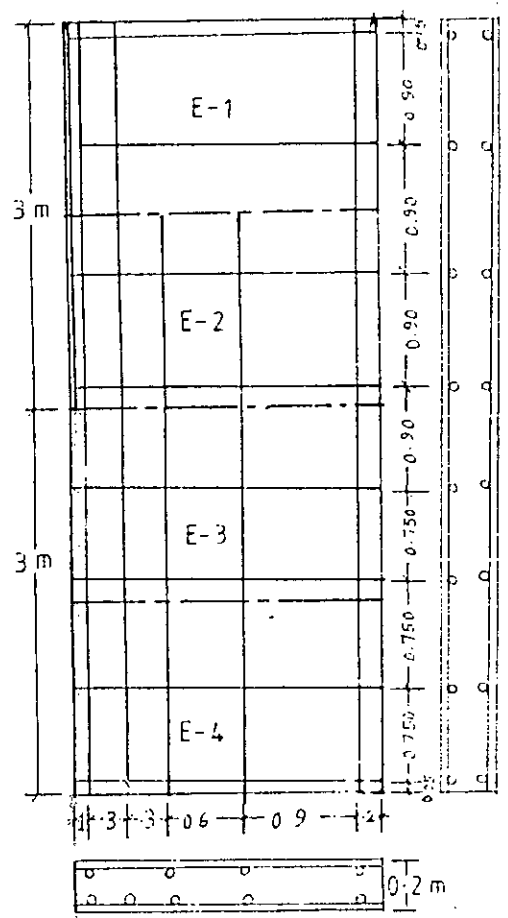
Y
X

25mm bar- both dir.

d=170mm

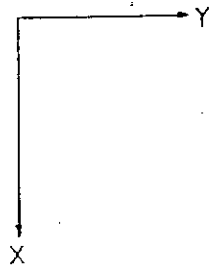
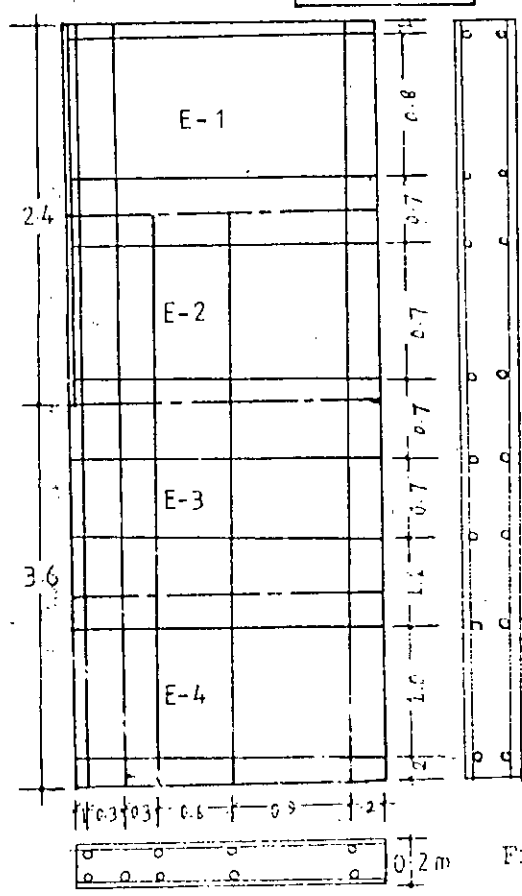
Not to scale

Fig. 5.15(b) : Plan with reinforcement



28 mm bar - Both dir.

d = 165 mm



28 mm bar - both dir.

d = 165 mm

Not to scale

Fig. 5.15 (c) : Plan with reinforcement

MOD41

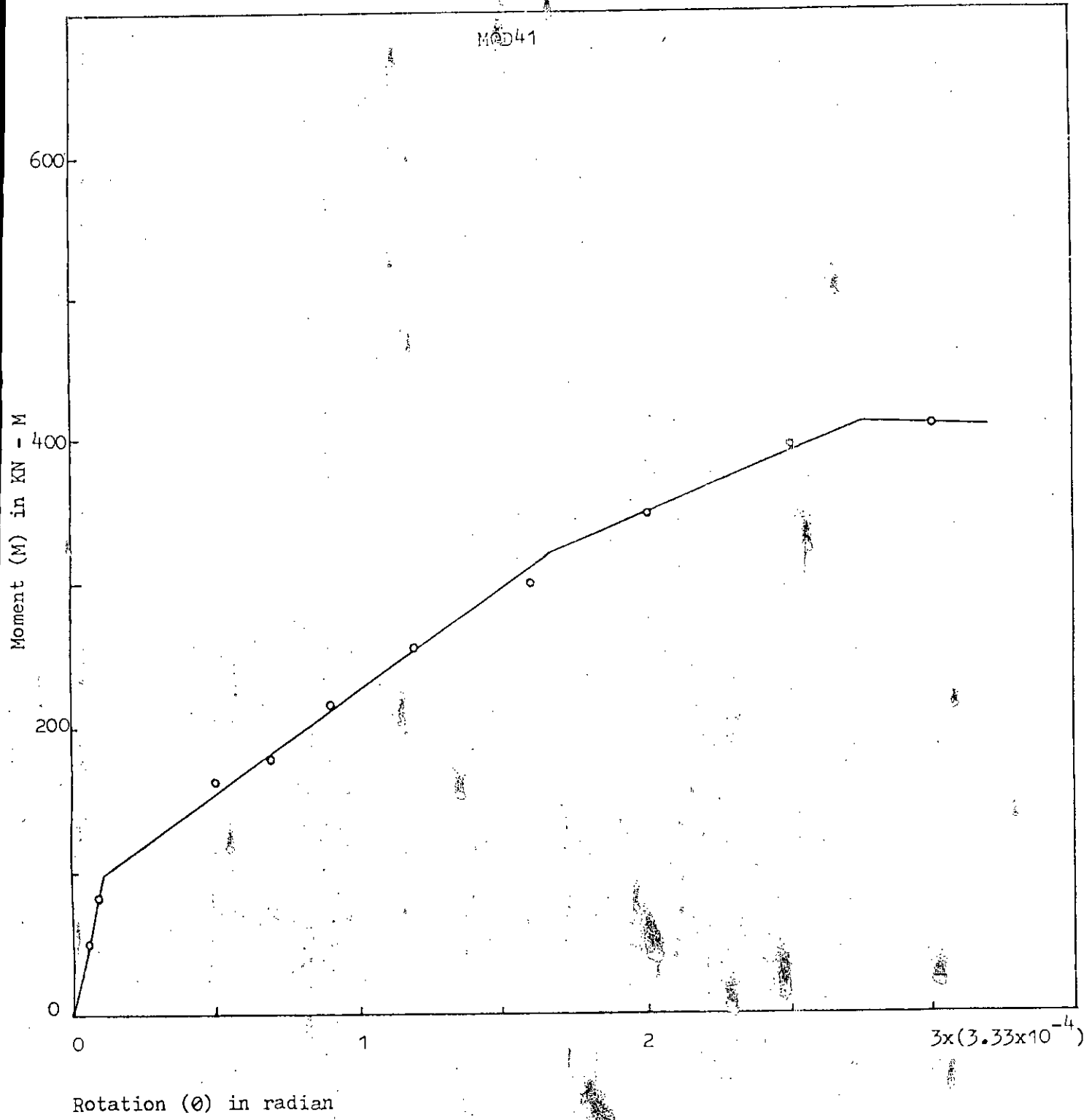


Fig. 5.16(a) : M - θ relationship

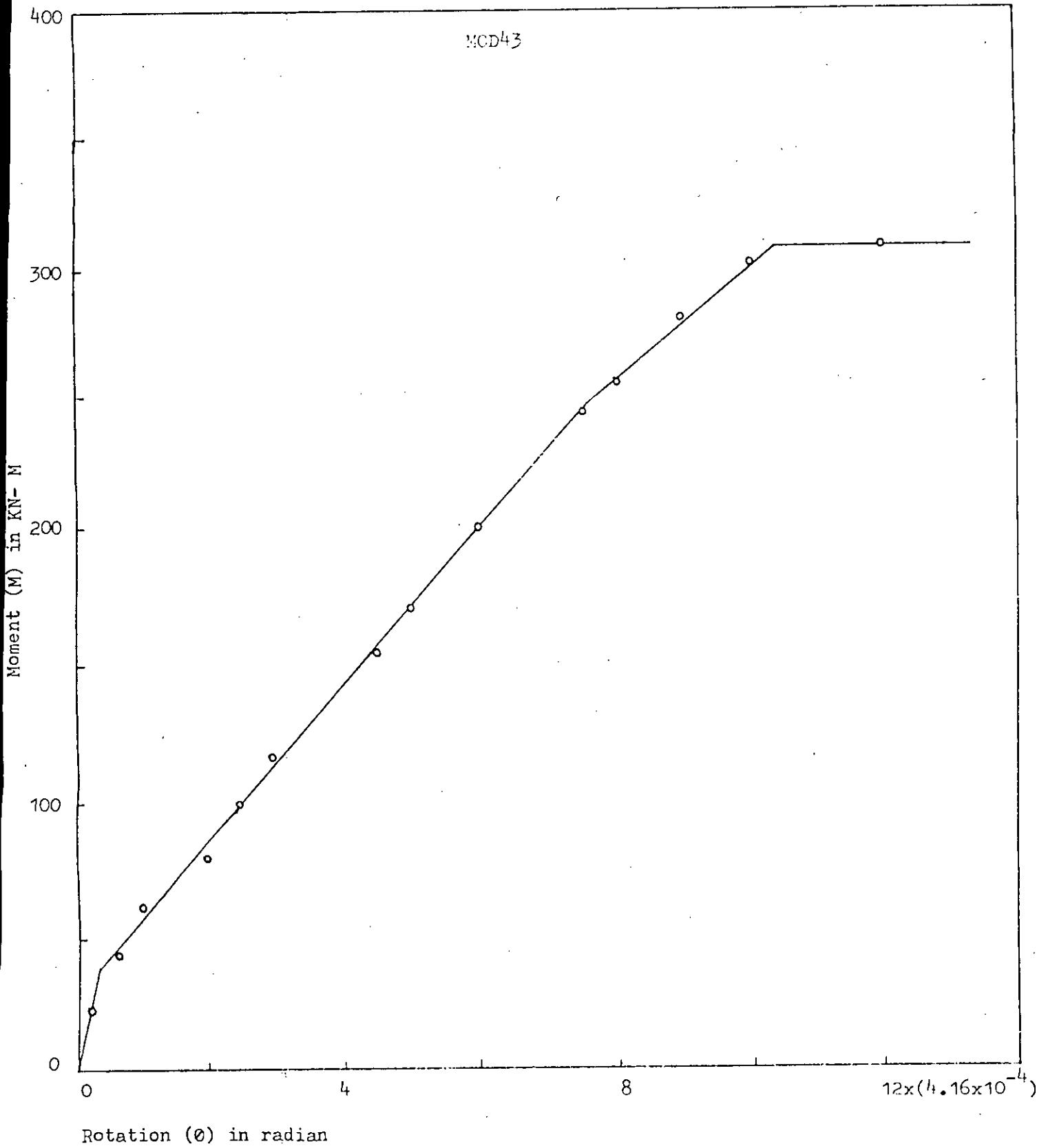


Fig. 5.16(c) : M - θ relationship

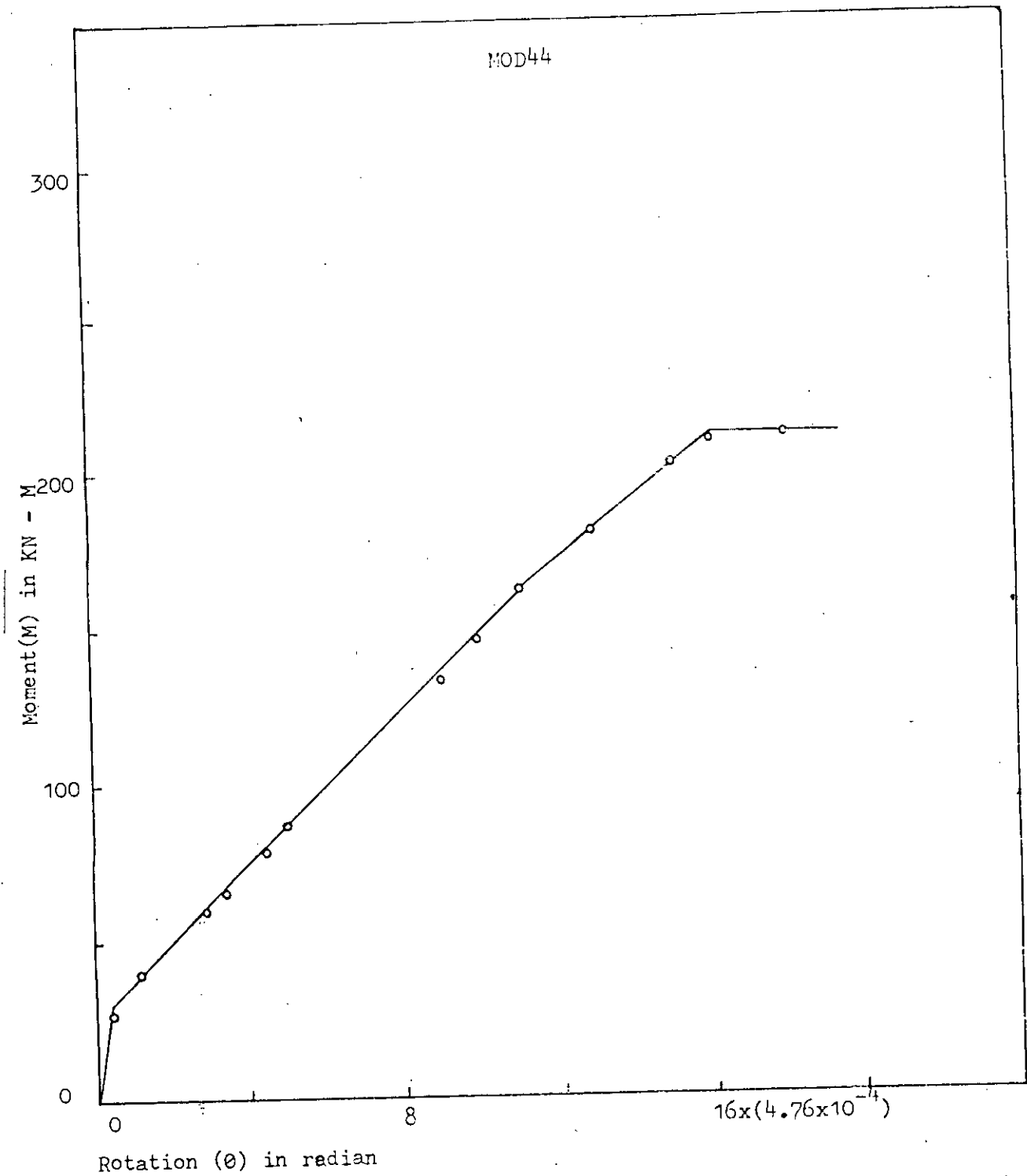


Fig. 5.16(d) : M - θ relationship

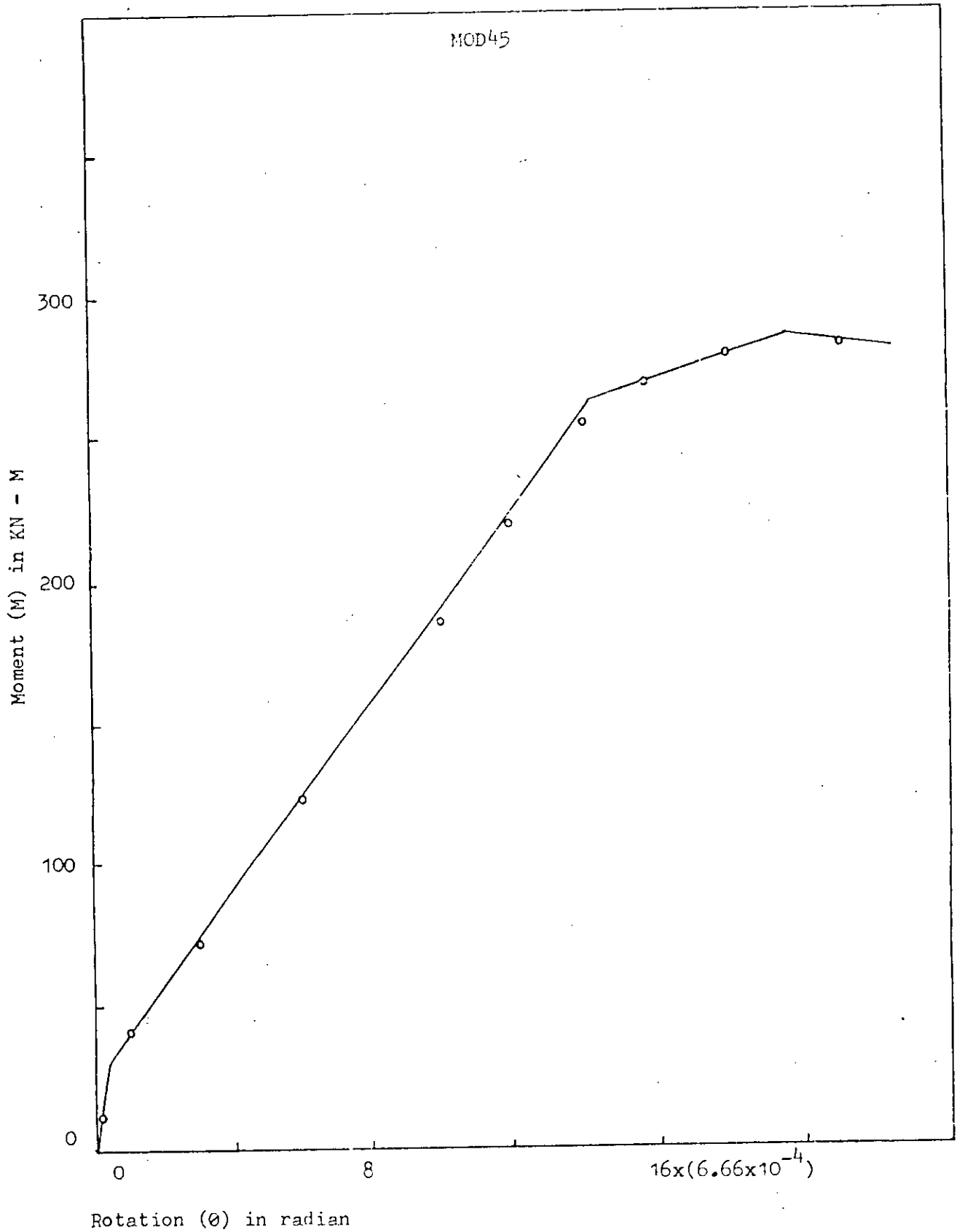


Fig. 5.16(e) : M - θ relationship

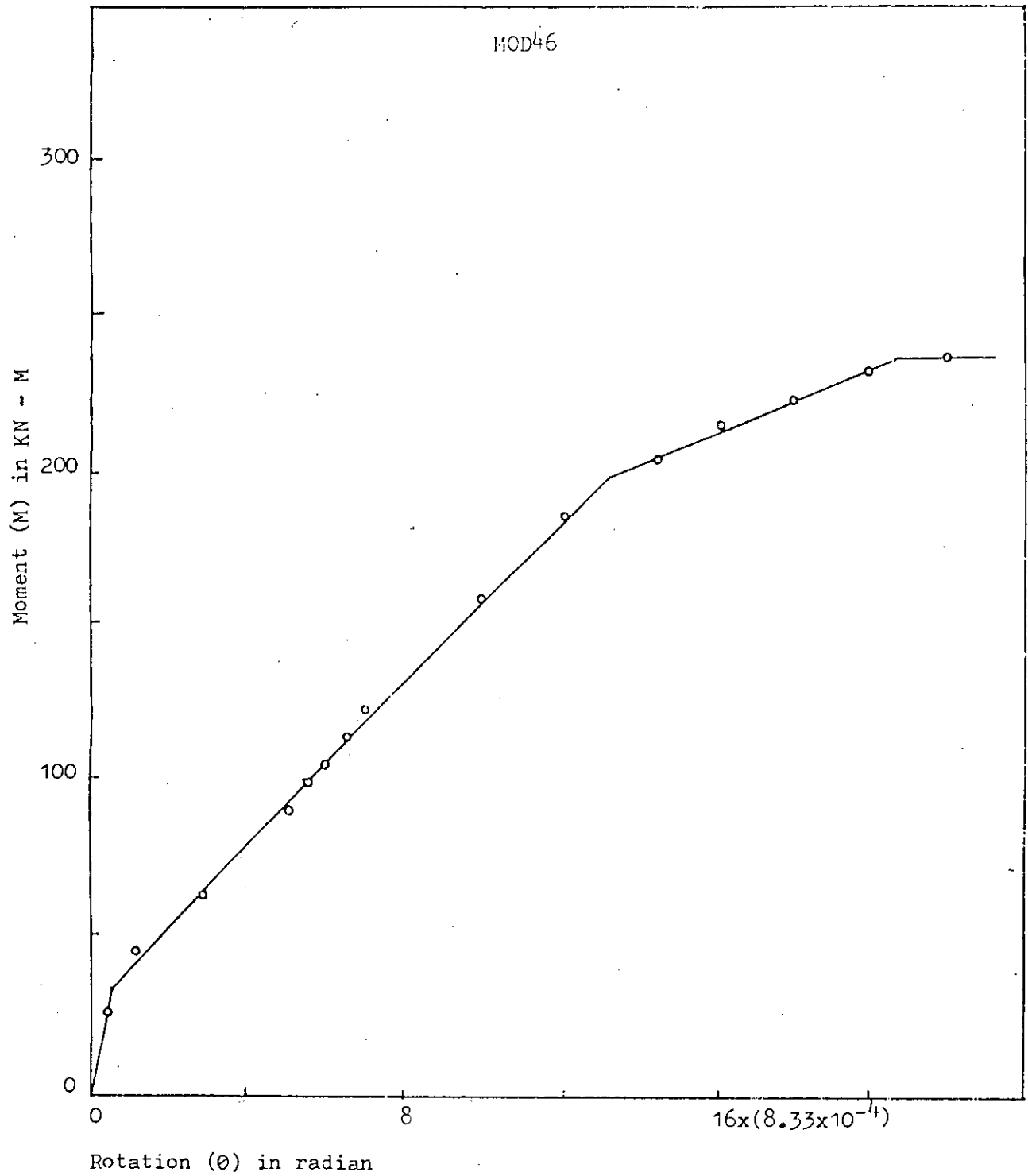
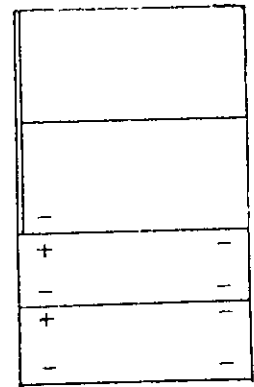
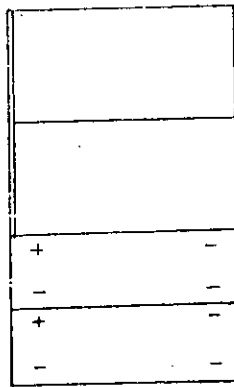
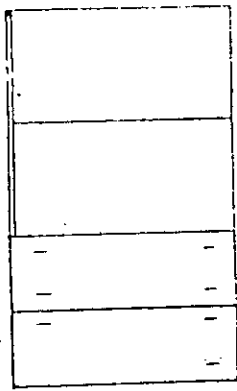
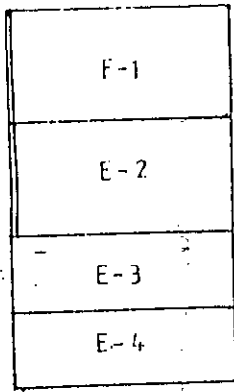


Fig. 5.16(f) : M - θ relationship

MOD 41



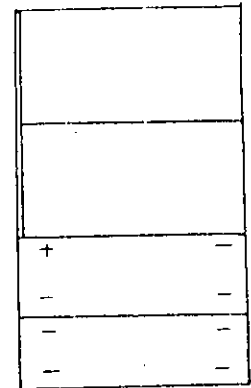
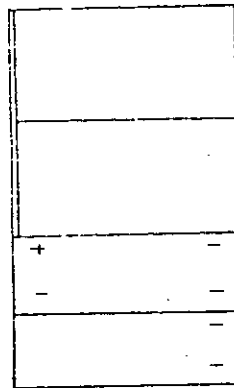
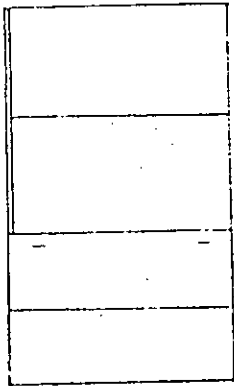
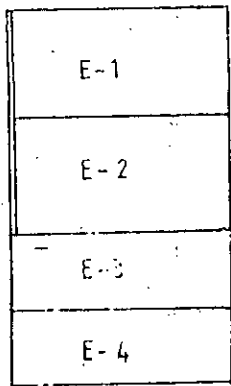
M/M₀ = 0.238

0.61

0.846

1.0

MOD 42



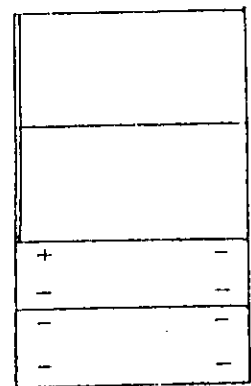
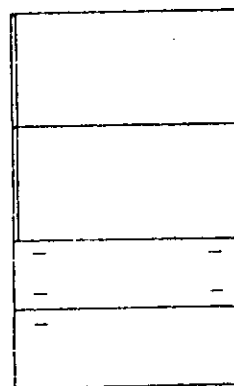
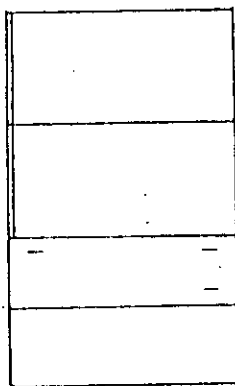
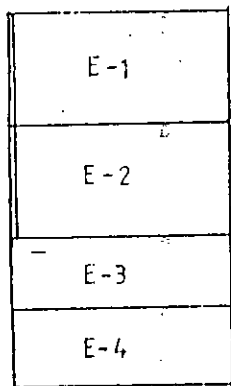
M/M₀ = 0.14

0.36

0.52

1.0

MOD 43



M/M₀ = 0.125

0.257

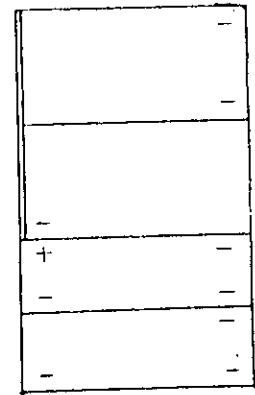
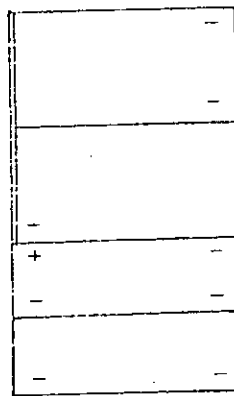
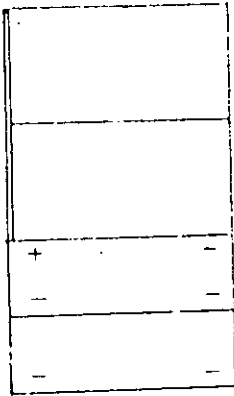
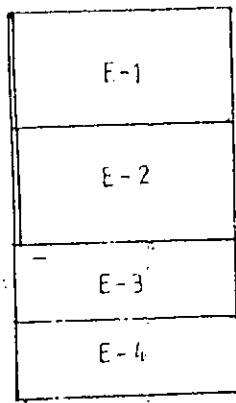
0.47

1.0

- Single Crack
 + Double Crack

Fig. 5.17 (a) : Crack propagation

MOD 44



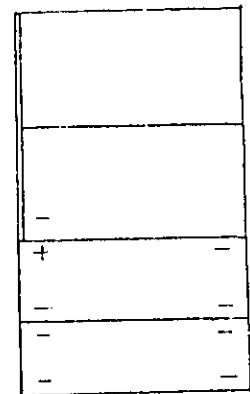
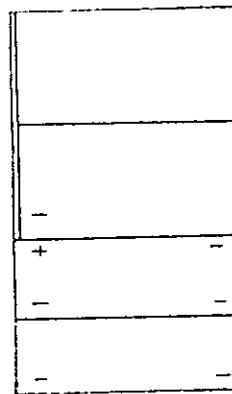
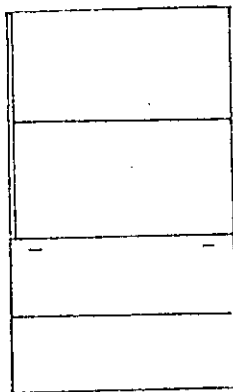
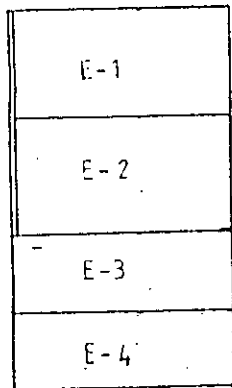
M/M_u = 0.105

0.66

0.973

1.0

MOD 45



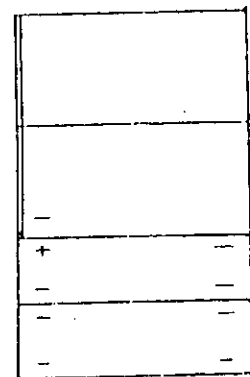
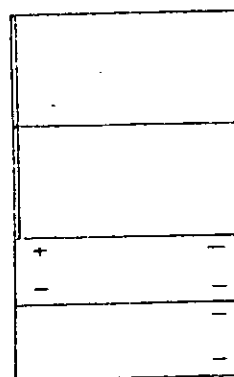
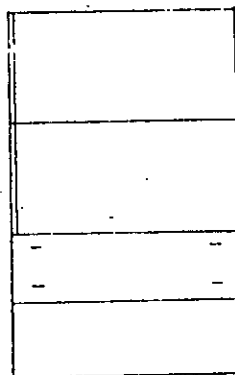
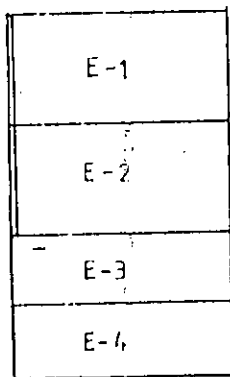
M/M_u = 0.105

0.25

0.76

1.0

MOD 46



M/M_u = 0.119

0.416

0.762

1.0

- Single Crack
+ Double Crack

Fig. 5.17(b) : Crack propagation

As there is a gradual increase in the magnitude of the principal strain due to increase in load the length of the crack in the figure is also gradually increased as shown in Fig.5.14.

Yielding of steel started in MOD61 at 83%, in MOD62 at 94%, in MOD63 at 84%, in MOD64 at 82% in MOD65 at 89.6% and in MOD66 at 77% of ultimate load.

Table 5.6 presents the values of M_{cr} , M_y and M_u from idealized M- θ curves for these models.

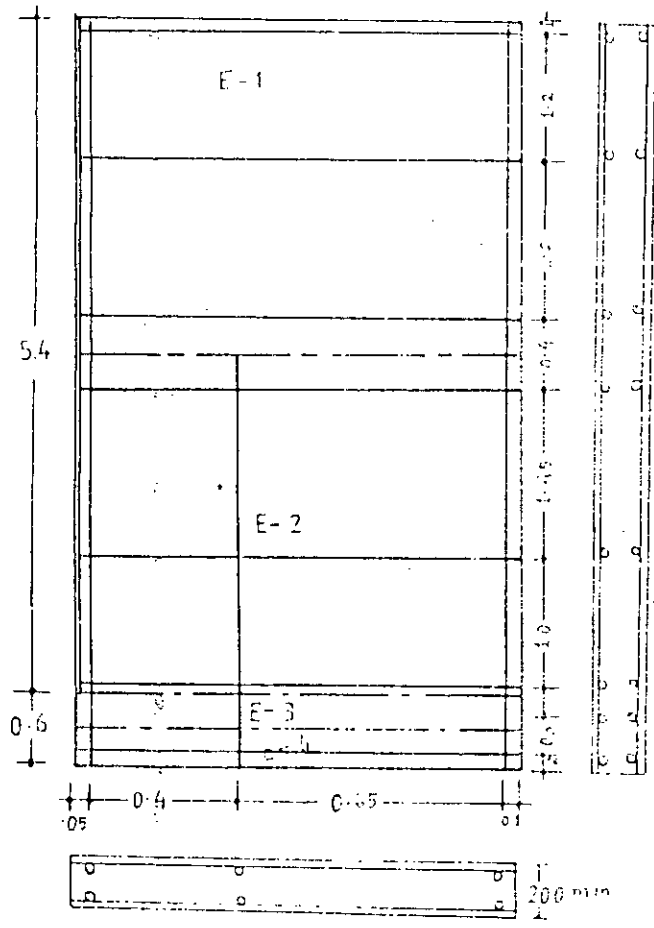
b) Models with $Y/X = 0.4$

Models MOD41, MOD42, MOD43, MOD44, MOD45 and MOD46 having L/x , 0.1 to 0.6 respectively were investigated. Figs. 5.15 show the plans with reinforcement of these models. Idealized M- θ curves for these models are presented in Fig. 5.16. the values of M_{cr} , M_y and M_u from idealized M- θ curves are presented in Table 5.6.

Figs. 5.17 show the gradual propagation of cracks in these models. Cracks started in MOD41 at 23.8%, in MOD42 at 14%, in MOD43 at 12.5%, in MOD44 at 12.5%, in MOD45 at 10.5% and in MOD46 at 11.9% of ultimate load. Similar crack pattern as previous models were observed. But crack started at a smaller percentages of ultimate load than the previous models.

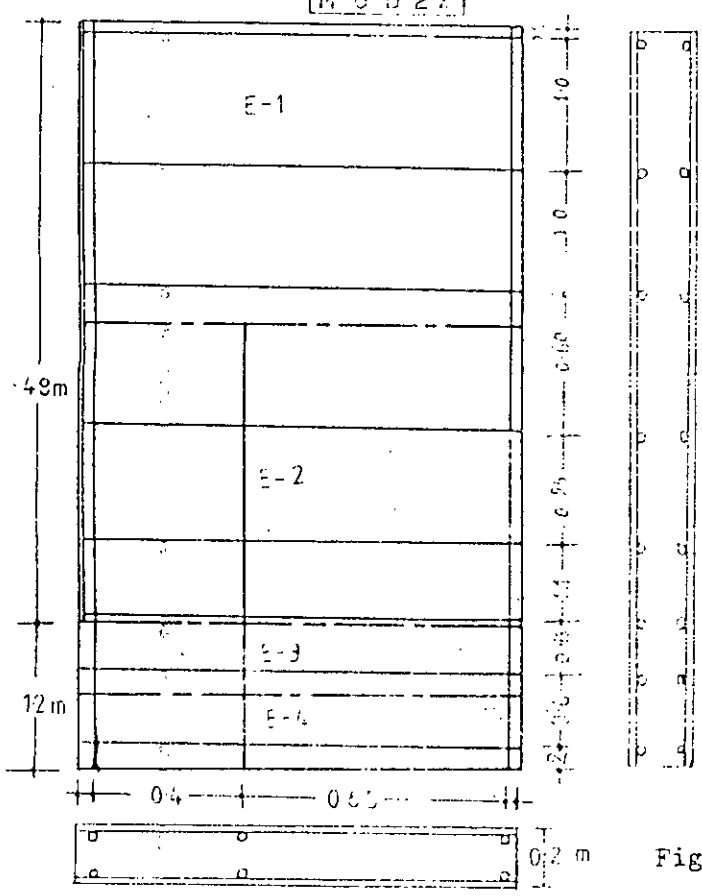
Yielding of steel started in MOD41 at 77.4%, in MOD42 at 87.6%, in MOD43 at 97.5%, in MOD44 at 78%, in MOD45 at 91% and in MOD46 at 83.9% of ultimate load.

M G D 21



25mm bar - Y direction
 22mm bar - X dir.
 $d = 170 \text{ mm}$

M G D 22

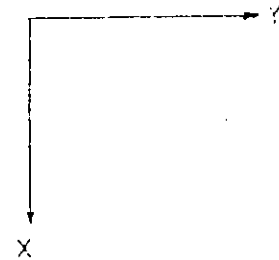
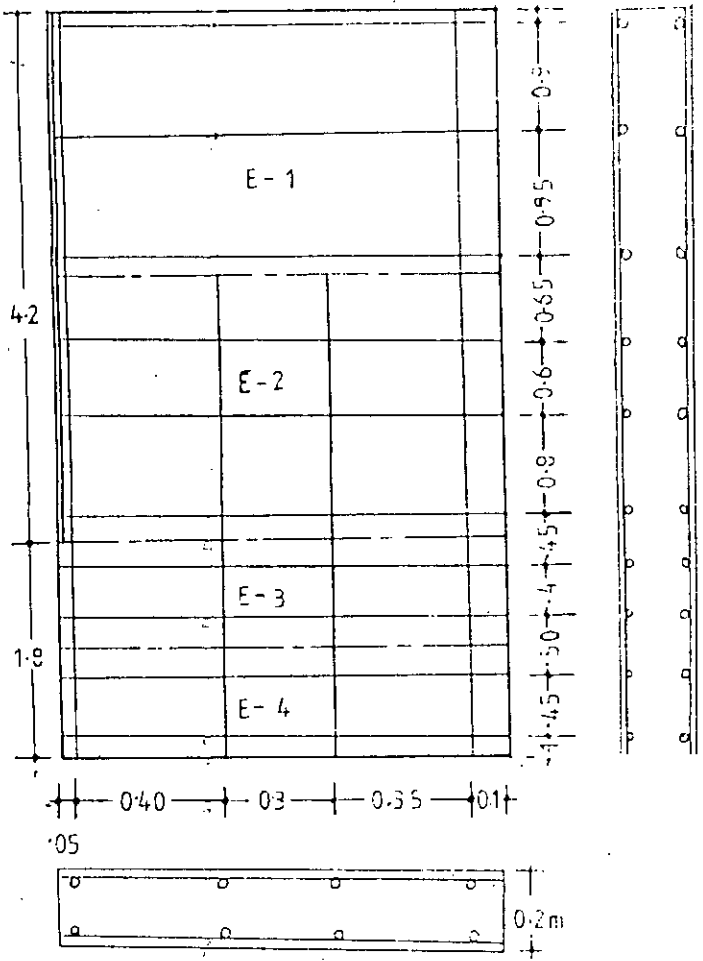


28mm bar - Y dir.
 22mm bar - X dir.
 $d = 170 \text{ mm}$

Not to scale

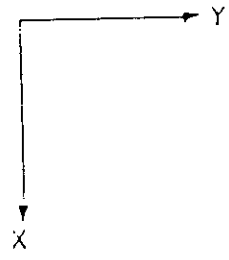
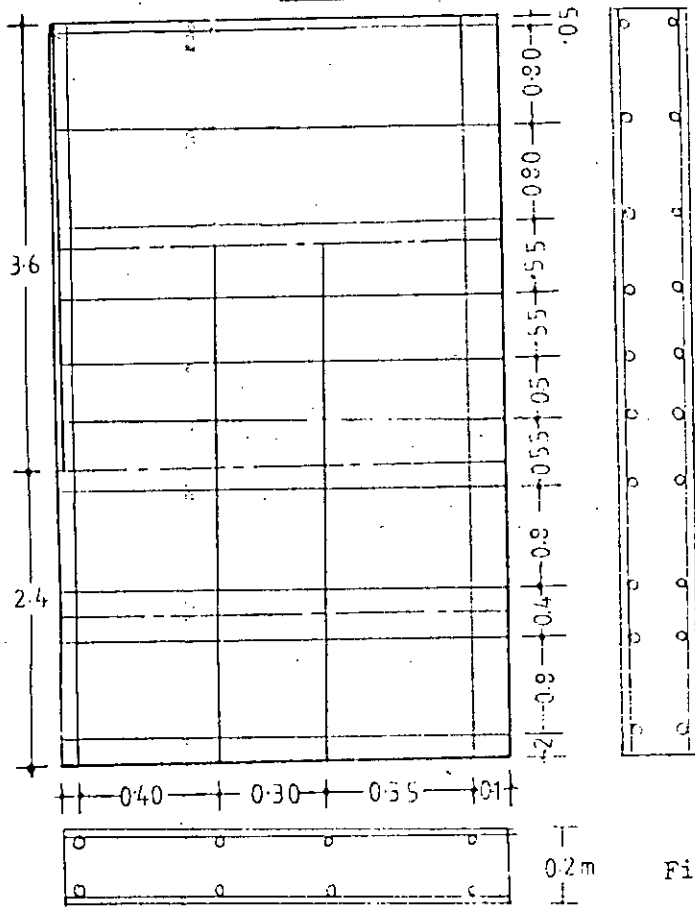
Fig. 5.18(a) Plan with reinforcement

MOD 23



25mm bar - Y - dir.
 22mm bar - X - dir.
 d = 170 mm

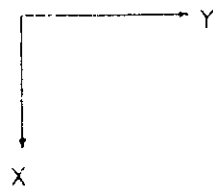
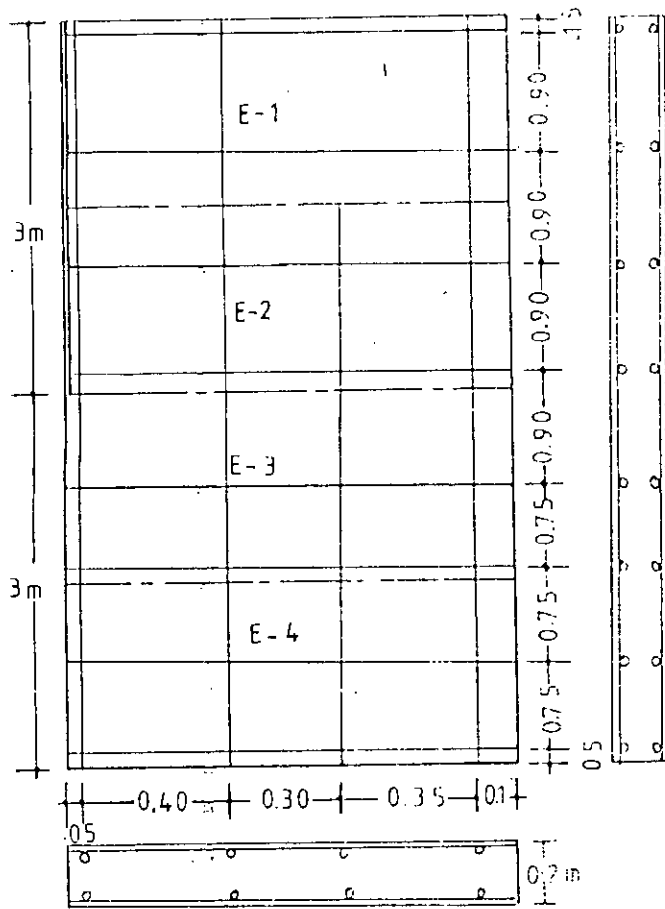
MOD 24



25mm bar - Y dir.
 22mm bar - X dir.
 d = 170 mm

Not to Scale

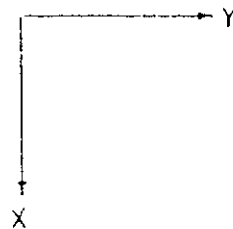
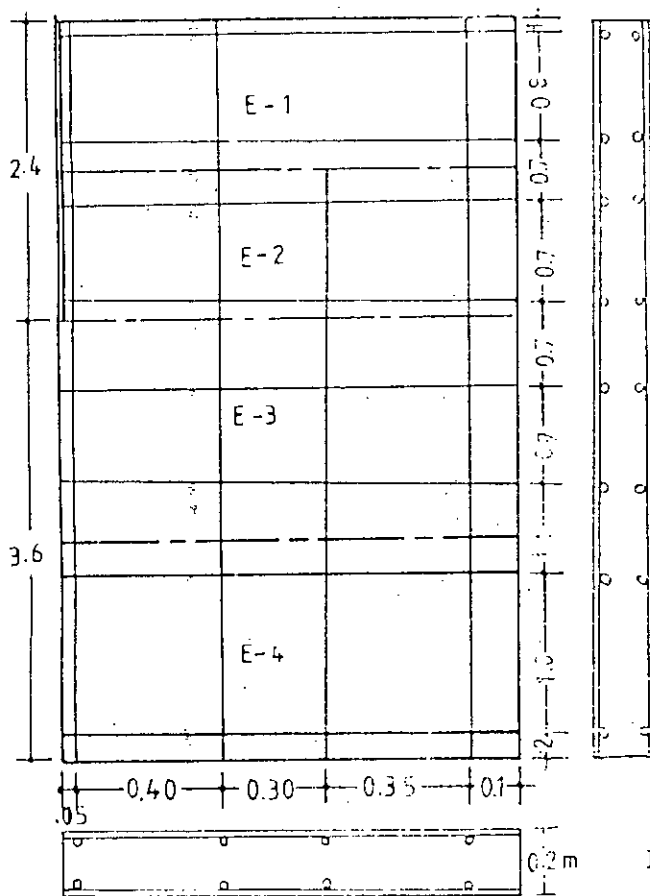
Fig. 5.18(b) Plan with reinforcement



28mm bar- Y dir.

25mm bar- X dir.

d=168mm



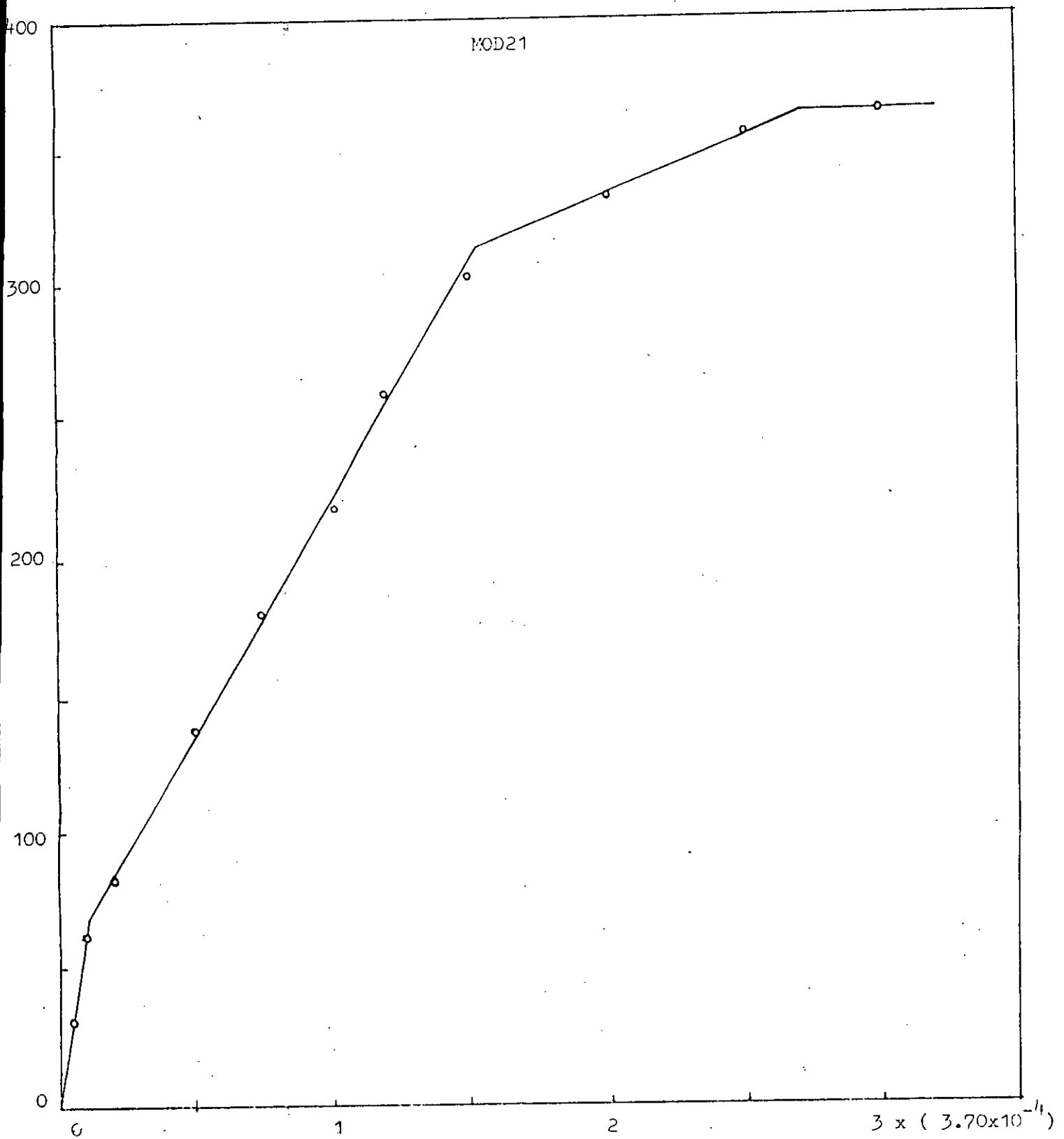
28mm bar- Y dir.

25mm bar- X dir.

d=168mm

Not to Scale

Fig. 5.18 (c) : Plan with reinforcement



Rotation (θ) in radian

Fig. 5.19(a) : M - θ relationship

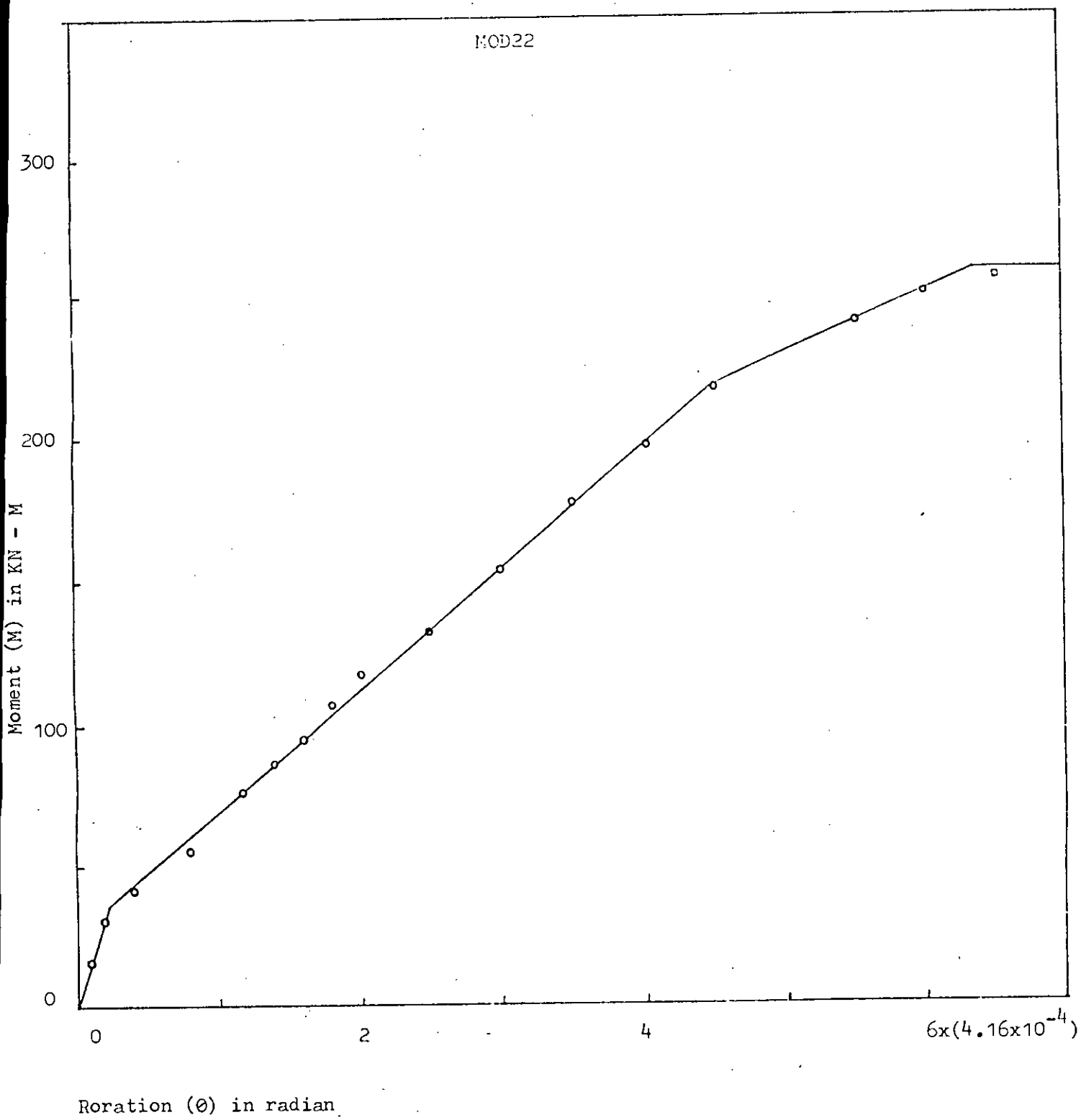


Fig. 5.19(b) : M - θ relationship

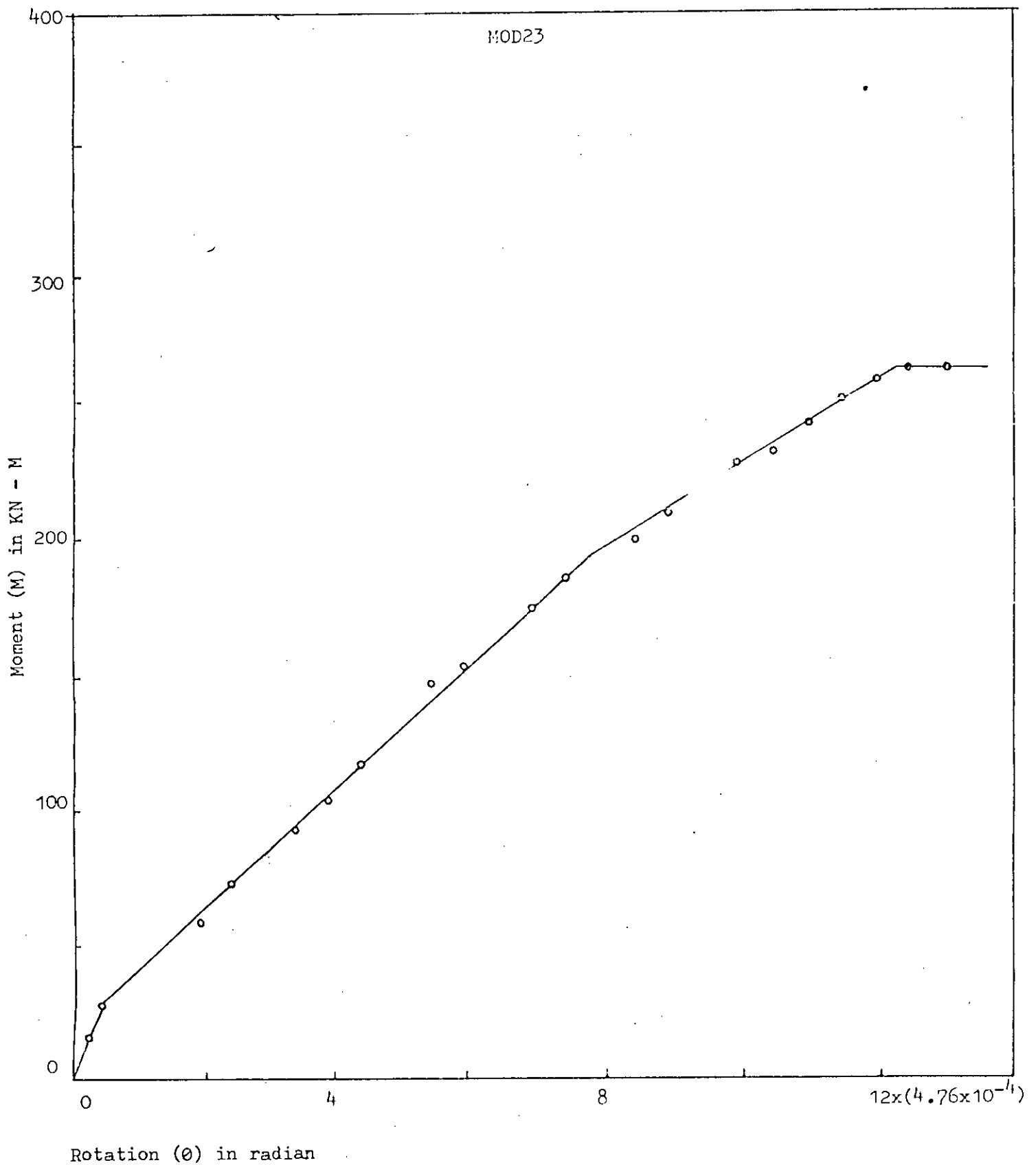


Fig. 5.19(c) : M - θ relationship

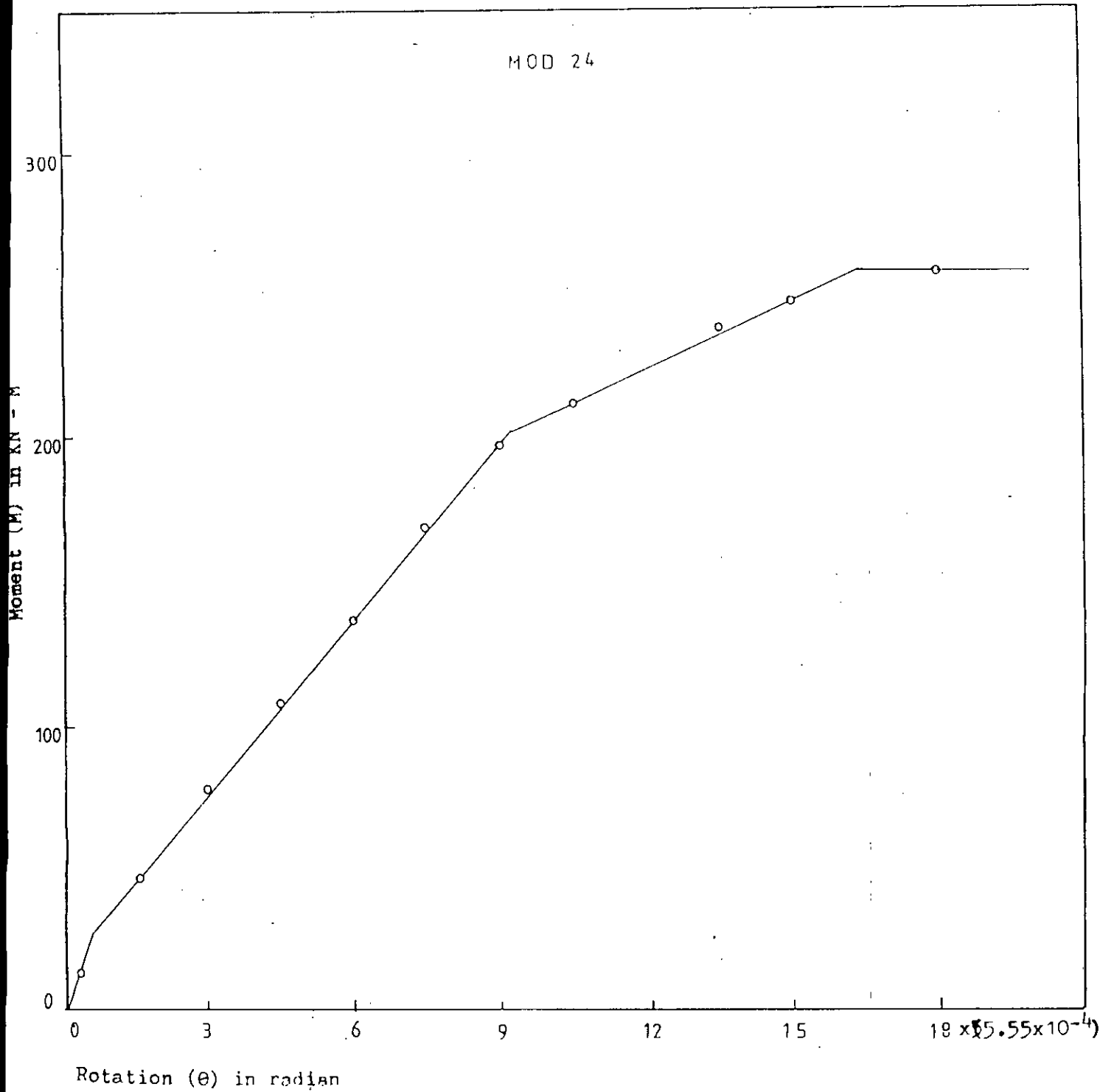


Fig. 5.19(d) : M - θ relationship

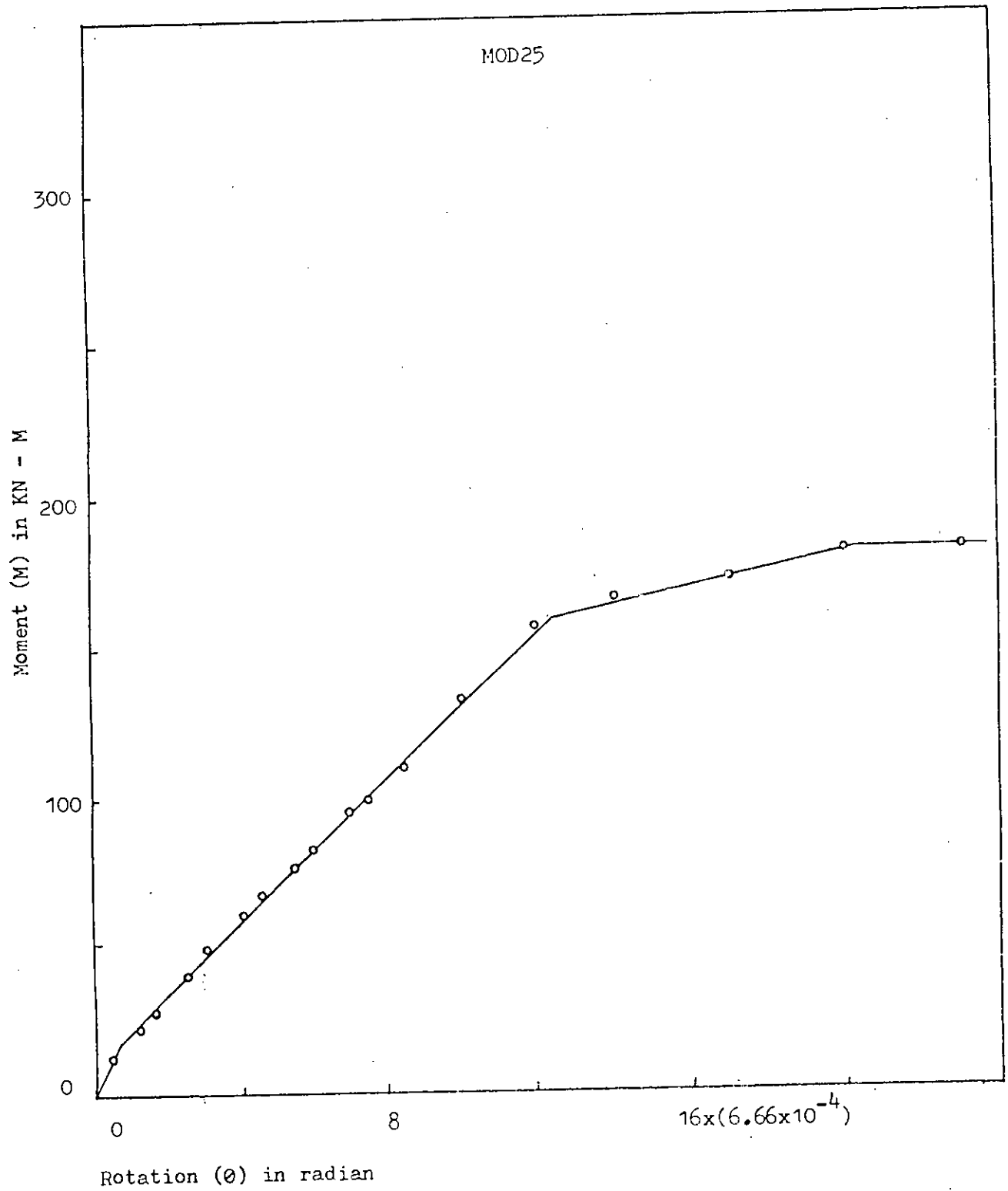


Fig. 5.19(e) : M - θ relationship

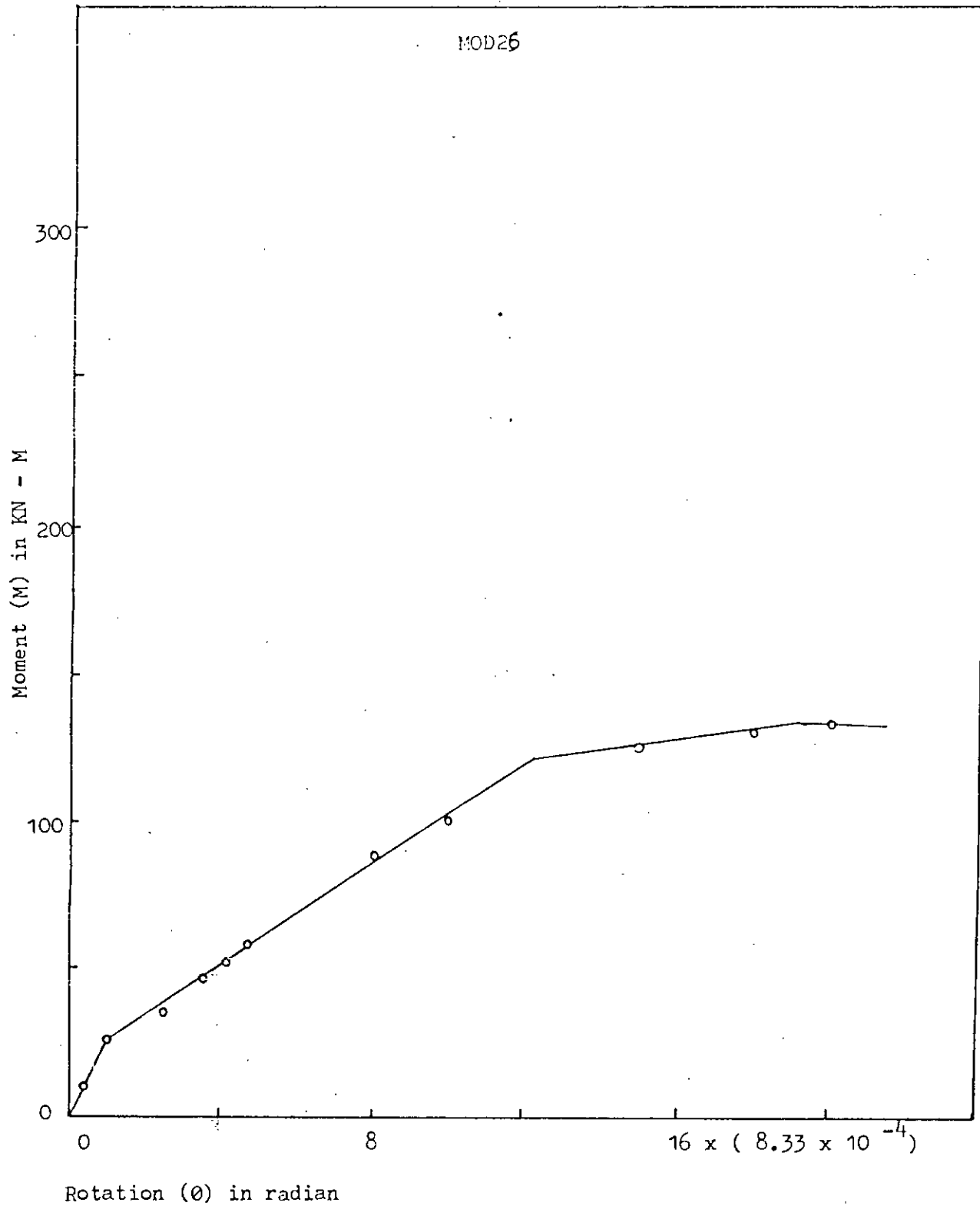
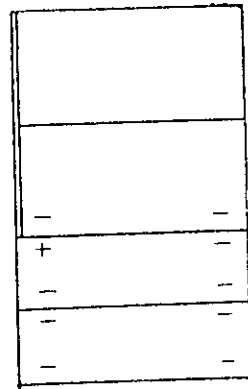
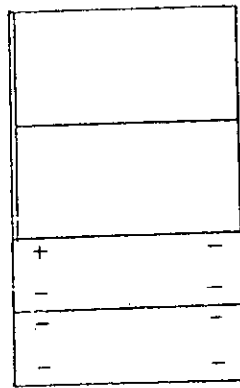
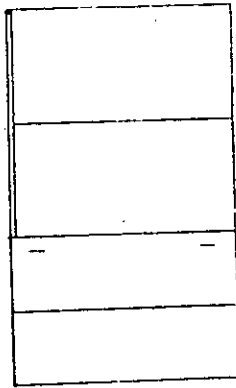
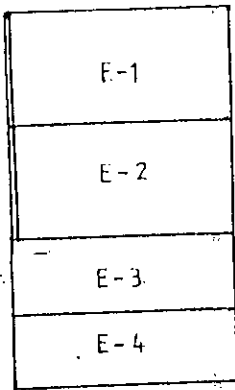


Fig. 5.19(f) : M - θ relationship

MOD 21



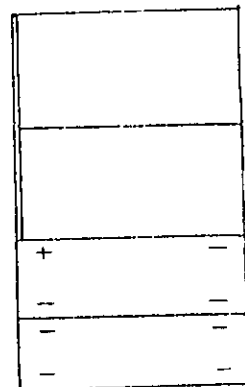
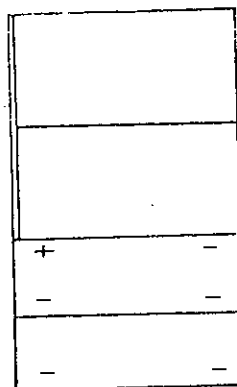
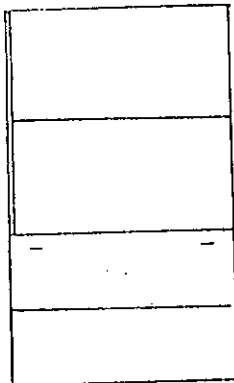
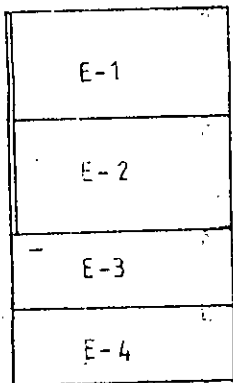
M/M_u = 0.187

0.21

0.71

1.0

MOD 22



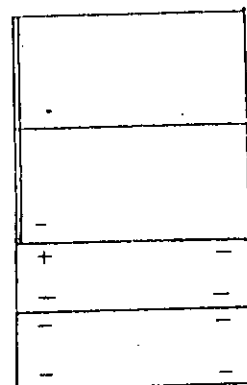
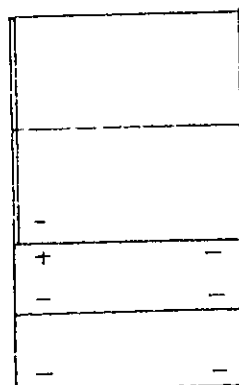
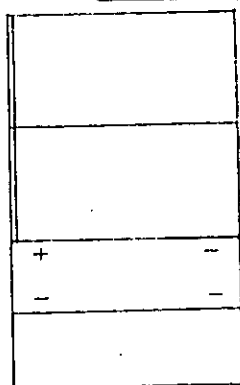
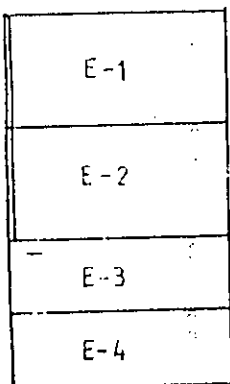
M/M_u = 0.136

0.232

0.686

1.0

MOD 23



M/M_u = 0.115

0.394

0.71

1.0

- Single Crack
+ Double Crack

Fig. 5.20(a) : Crack Propagation

MOD 24

E-1
E-2
E-3
E-4

+
-

+
-
-

-
+
-
-

M/M_u = 0.11

0.41

0.78

1.0

MOD 25

E-1
E-2
E-3
E-4

-

-
-

-
+
-
-

M/M_u = 0.10

0.25

0.414

1.0

MOD 26

E-1
E-2
E-3
E-4

-

-
-
-

-
+
-
-

M/M_u = 0.189

0.235

0.68

1.0

- Single Crack
+ Double Crack

Fig. 5.20(b) : Crack Propagation

c) Models with $Y/X = 0.2$

Models MOD21, MOD22, MOD23, MOD24, MOD25 and MOD26 having L/X 0.1 to 0.6 respectively were investigated in this group. Plan with reinforcements of models are shown in Figs. 5.18. Idealized $M-\theta$ curves for these models are presented in Figs. 5.19. The values of M_{cr} , M_y and M_u are presented in Table 5.6.

Figs. 5.20 show the gradual propagation of cracks in those models. Cracks started in MOD21 at 18.7%, in MOD22 at 13.6%, in MOD23 at 11.5%, in MOD24 at 11.0%, in MOD25 at 10% and in MOD26 at 18.9% of ultimate load. The crack patterns are similar to those described earlier.

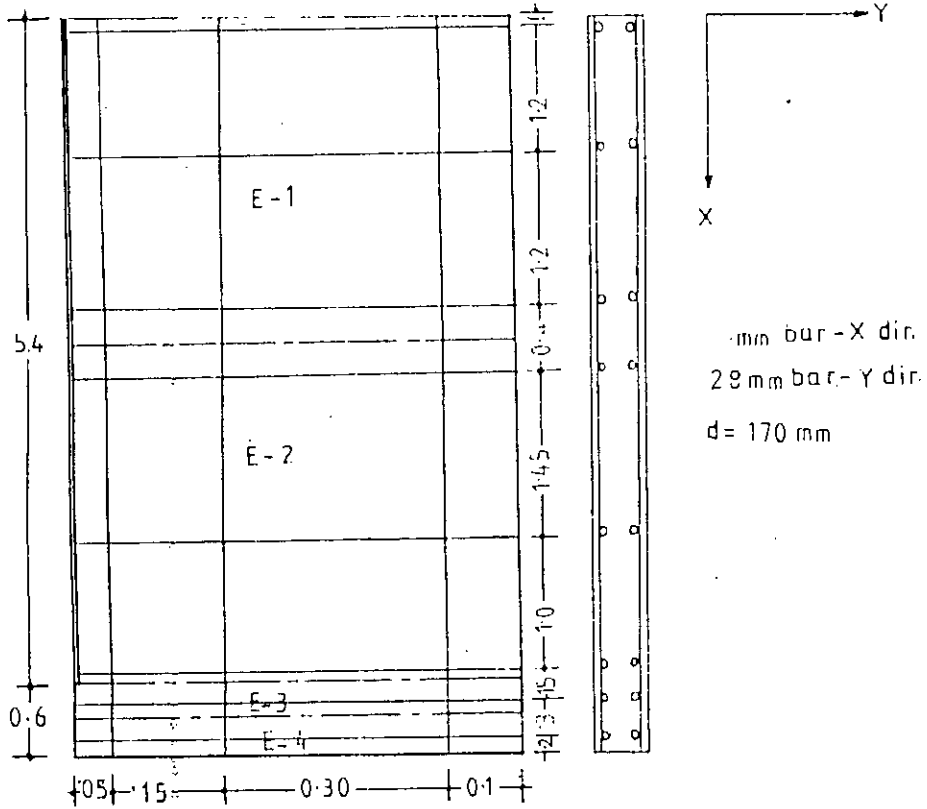
Yielding of steel started in MOD21 at 85%, in MOD22 at 93%, in MOD23 at 74%, in MOD24 at 78%, in MOD25 at 87% and in MOD26 at 91% of ultimate load.

d) Models with $Y/X = 0.1$

Models MOD11, MOD12, MOD13, MOD14, MOD15 and MOD16 having L/X 0.1 to 0.6 respectively were investigated in this group. Plan with reinforcements of models are shown in Figs. 5.21. Idealized $M-\theta$ curves for these models are presented in Figs. 5.22. The values of moments from idealized curves are presented in Table 5.6.

As the crack patterns are similar to those described earlier, they are not plotted. Cracks started in MOD11 at 18.4%, in MOD12 at 10.1%, in MOD13 at 19%, in MOD14 at 15%, in MOD15 at 13.9% and MOD16 at 13.1 of ultimate load.

MOD 11



MOD 12

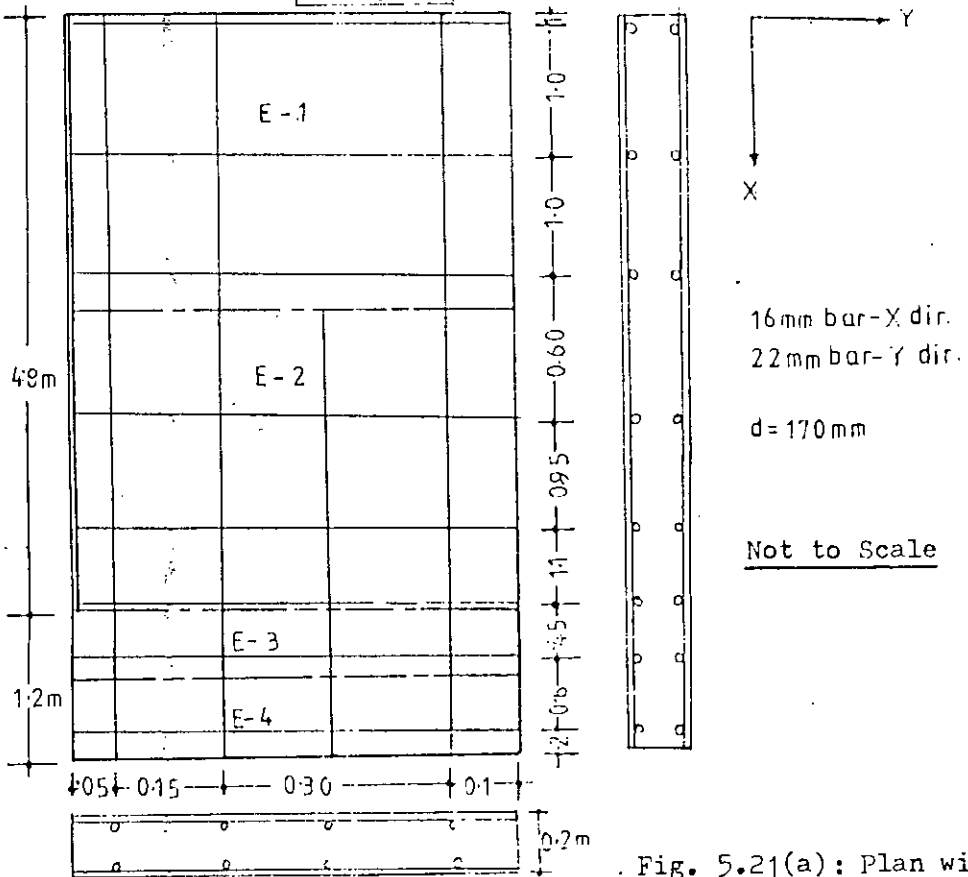


Fig. 5.21(a): Plan with reinforcement

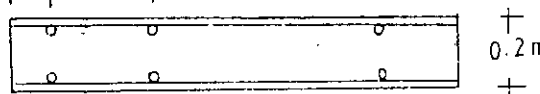
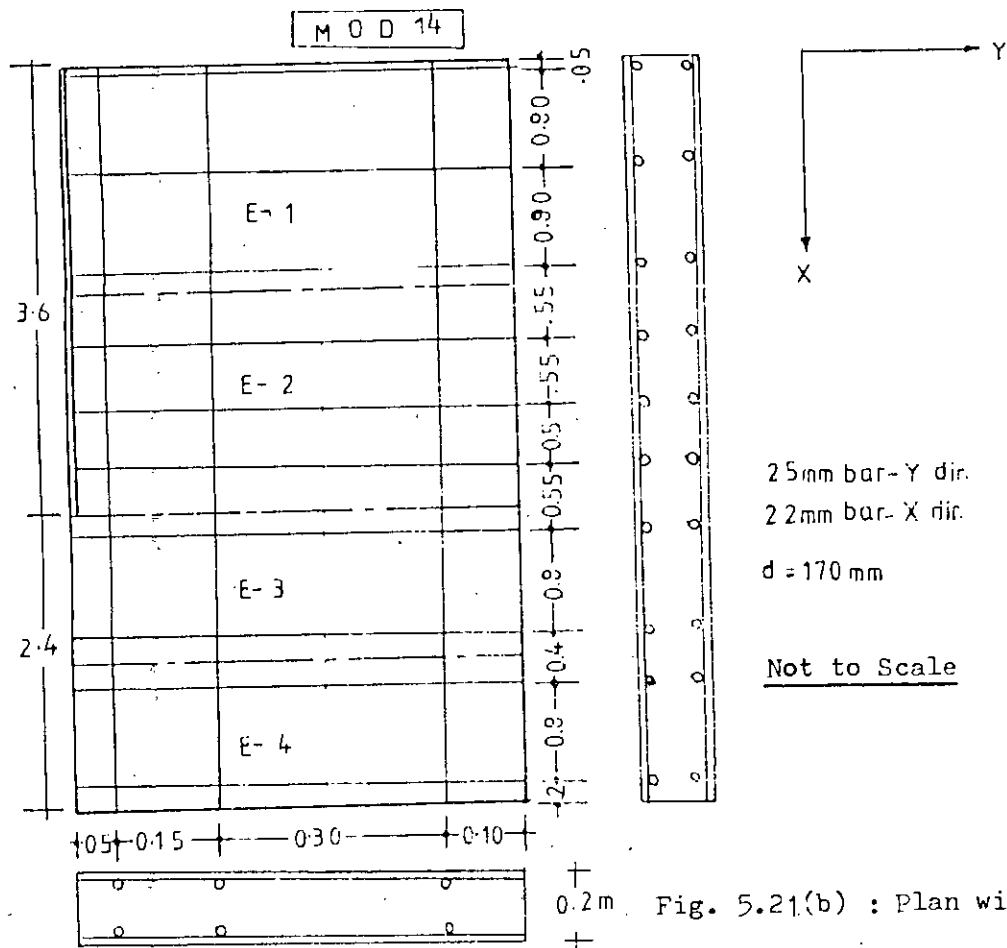
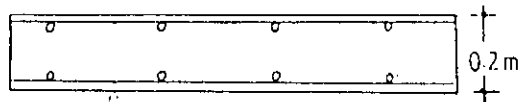
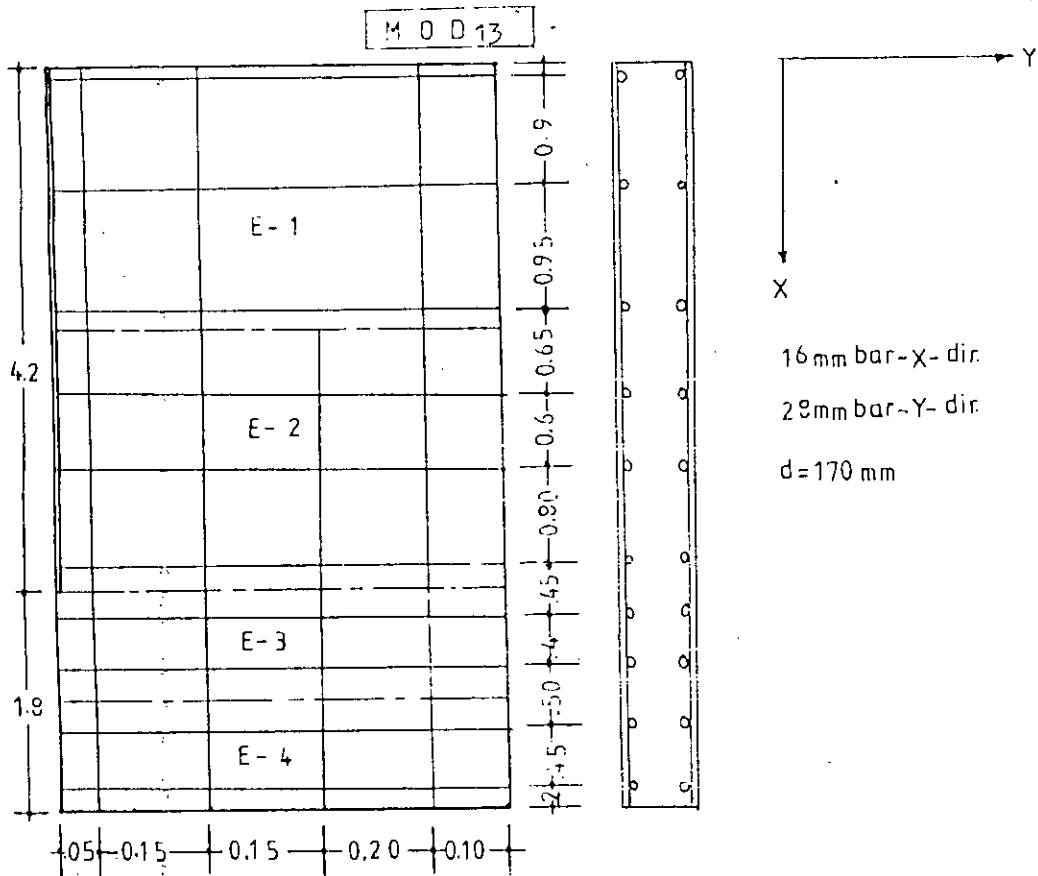
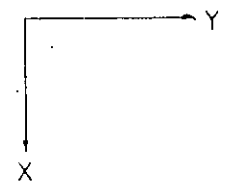
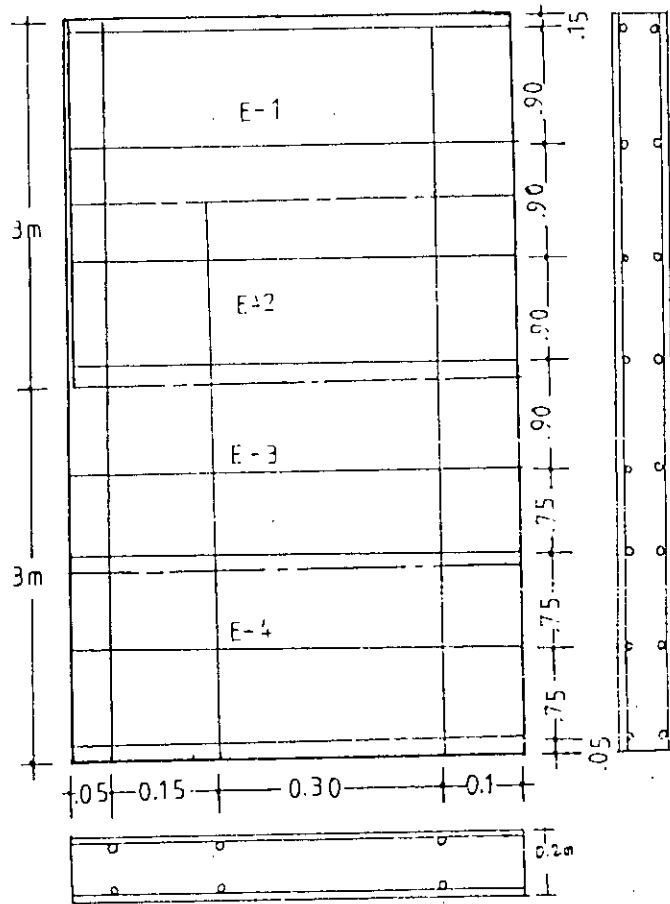
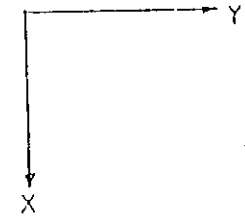
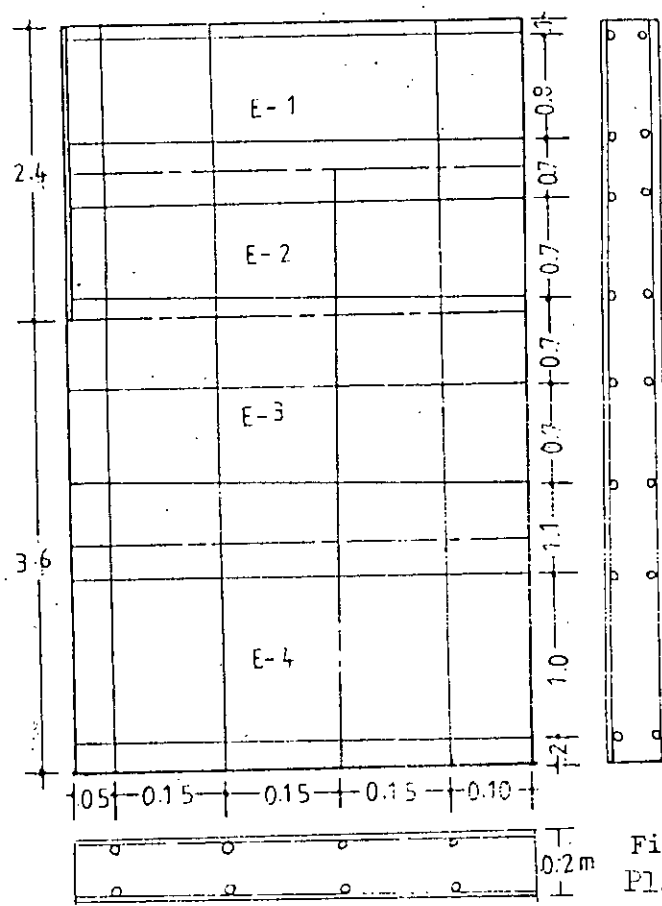


Fig. 5.21(b) : Plan with reinforcement



28mm bar - Y dir
 25mm bar - X dir
 d = 168mm



28mm - Y dir
 22mm - X dir
 d = 170mm

Not to Scale

Fig. 5.21(c):
 Plan with reinforcement

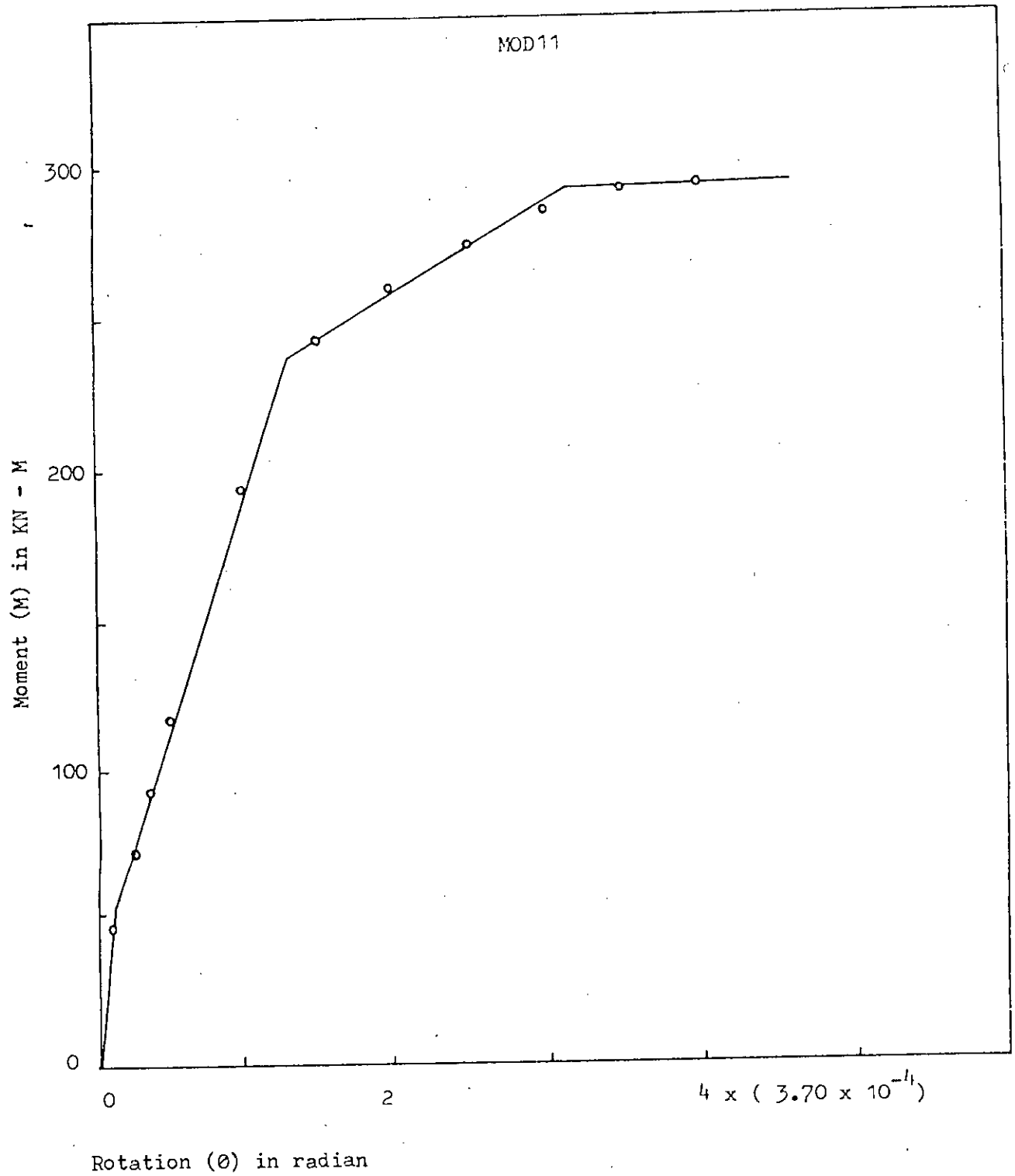


Fig. 5.22(a) : M - θ relationship

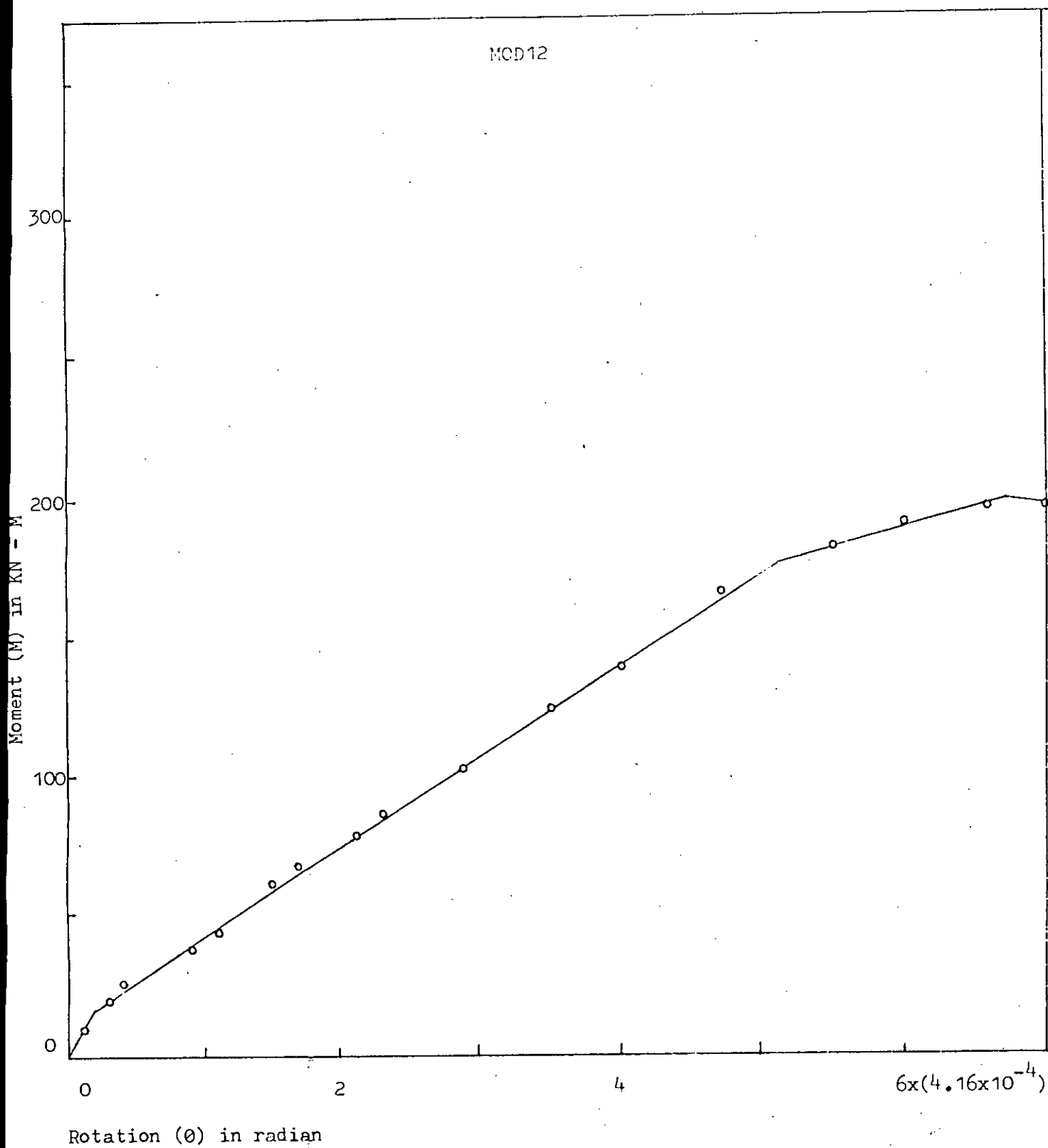


Fig. 5.22(b) : M - θ relationship

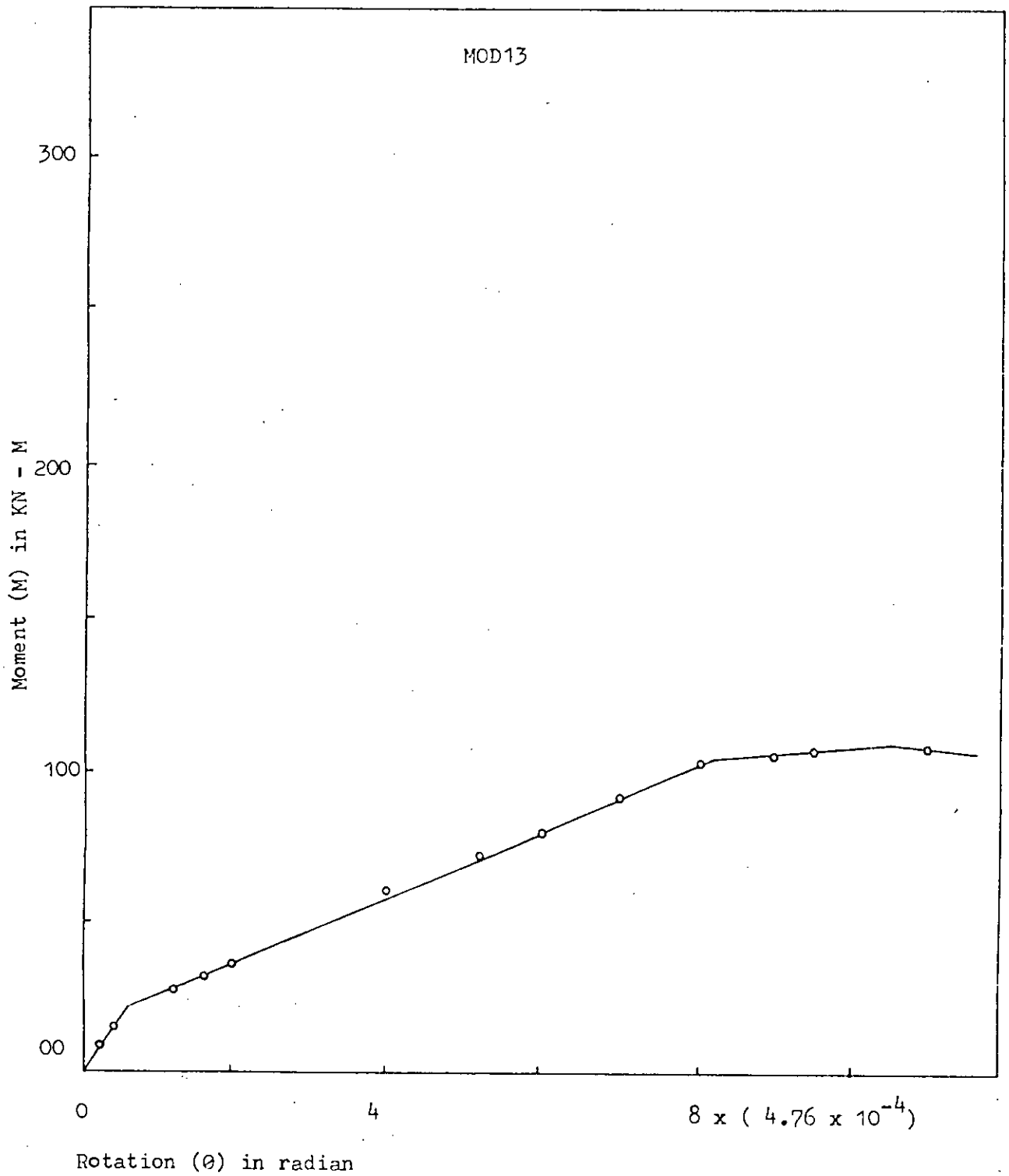


Fig. 5.22(c) : M - θ relationship

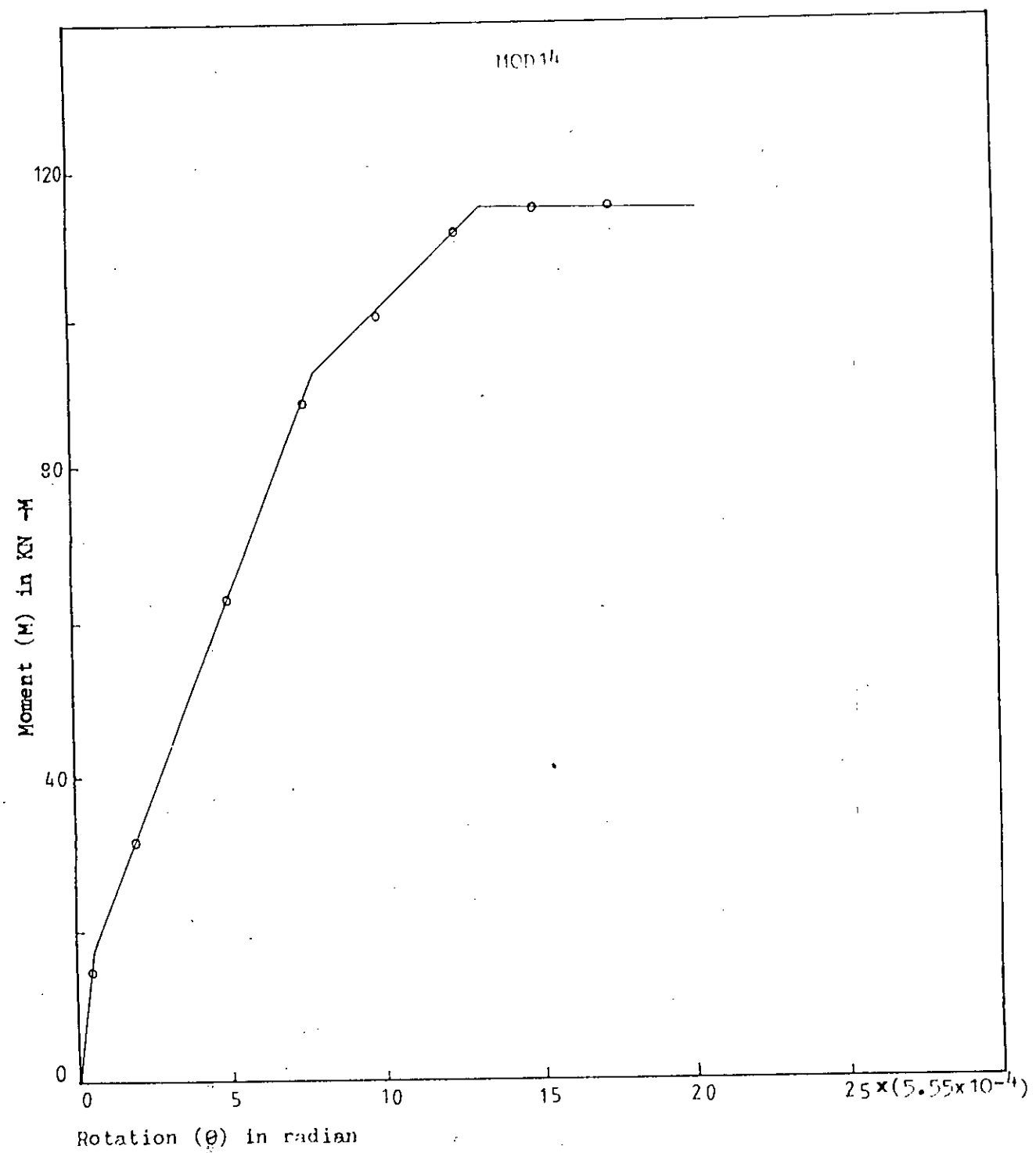


Fig. 5.22(d) : M - θ relationship

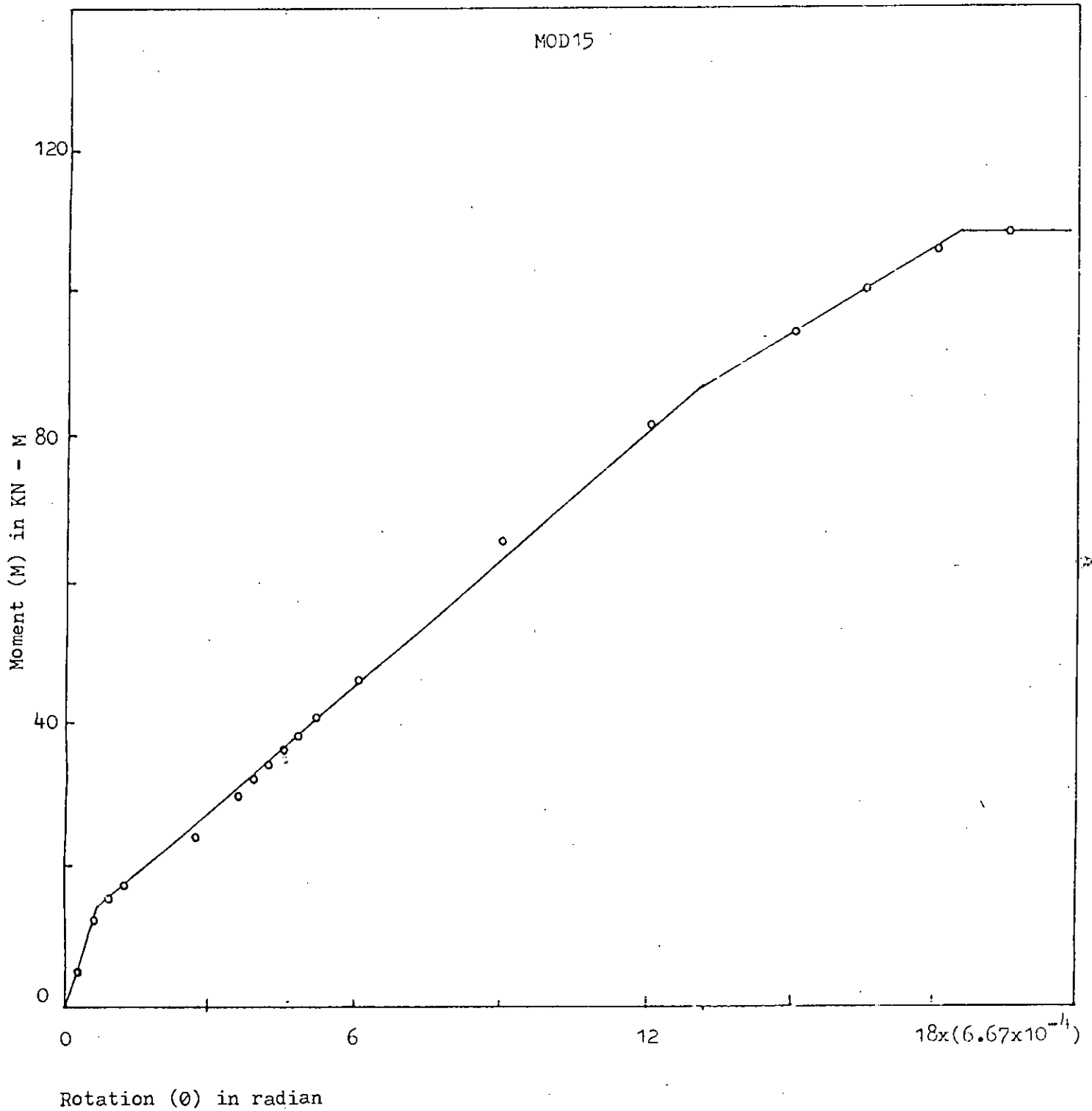


Fig. 5.22(e) : M - θ relationship

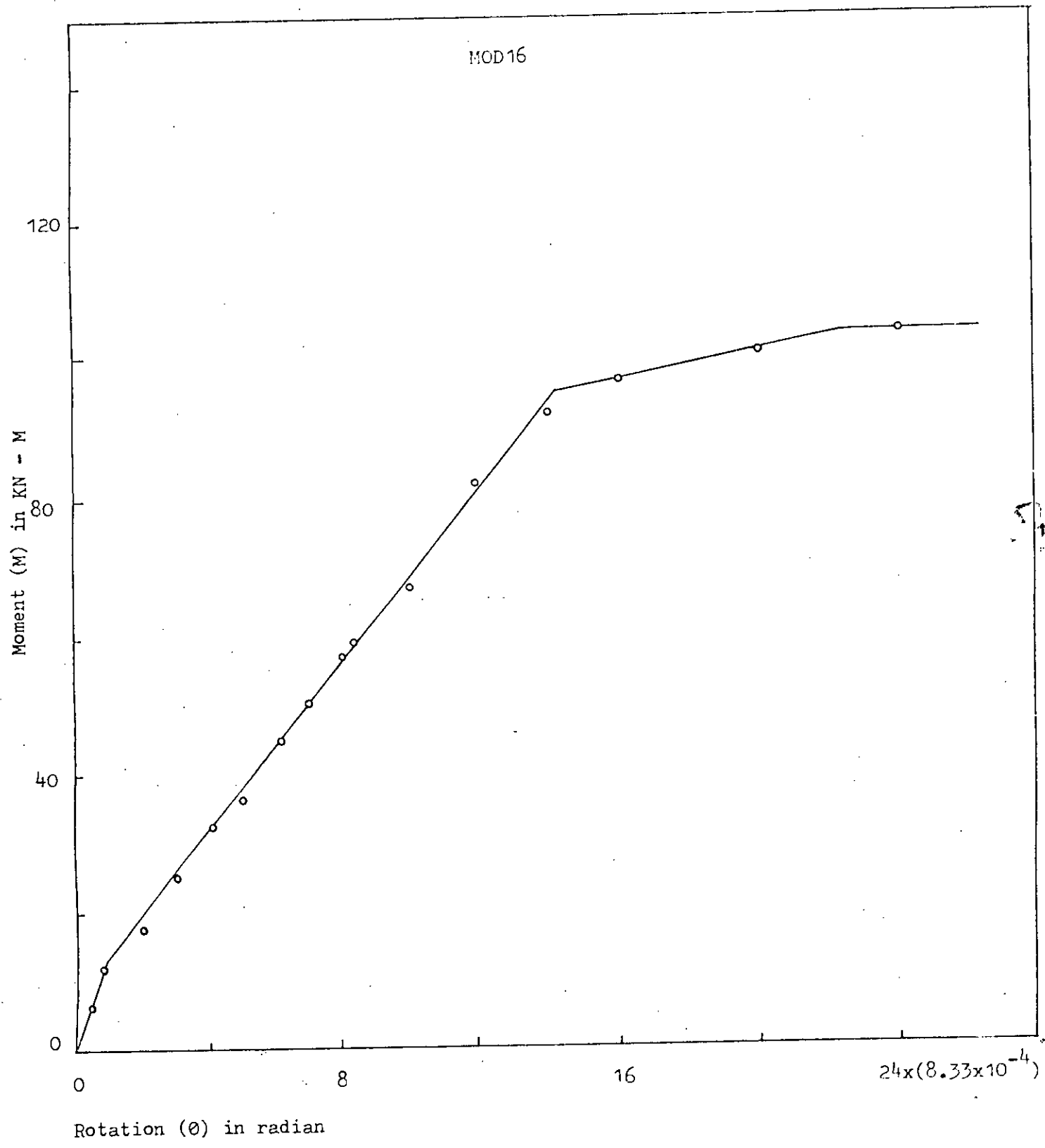


Fig. 5.22(f) : M - θ relationship

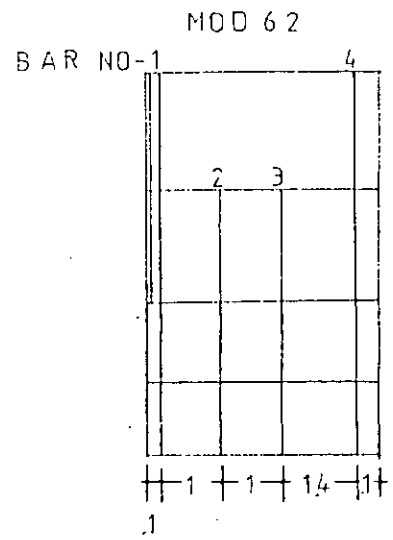
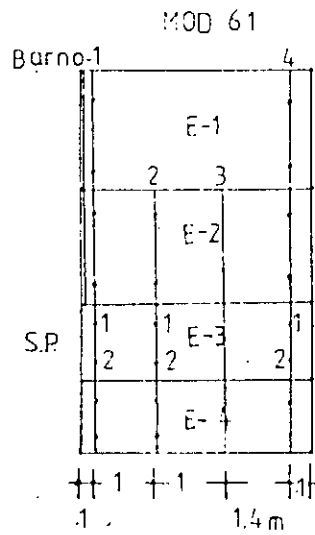
Yielding of steel started in MOD11 at 81%, in MOD12 at 88%, in MOD13 at 95%, in MOD14 at 81%, in MOD15 at 80.5% and in MOD16 at 92% of ultimate load.

Discussion on Crack Pattern

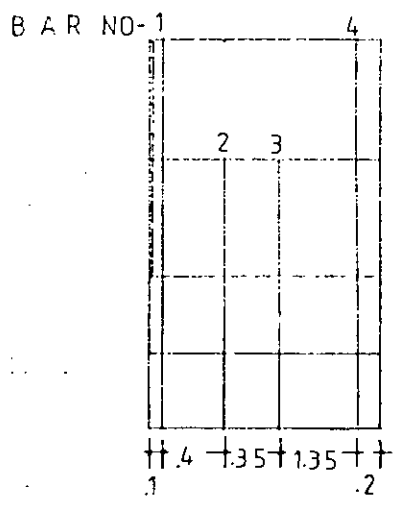
In this study, cracking means the cracking of sampling points in an element. A sampling point can crack in three directions. Cracking of sampling points located on the tension side (bottom layer) of the slab are shown in the cracking diagrams, only four elements were used in the study, so the number of stress sampling points in the tensile region is not large. Therefore, the resulting crack pattern is crude. A model was also studied with 8-element having more stress sampling points in the tension side, giving approximately the similar crack pattern. For all the models, it is found from the crack pattern that the cracks originate from the interior edge of the wall and in element near the interior edge of the wall (corridor slab) cracks are more pronounced as almost all the sampling points are cracked.

So, it may be concluded that the corridor slab is more highly stressed particularly the section passing through the interior edge of the shearwall.

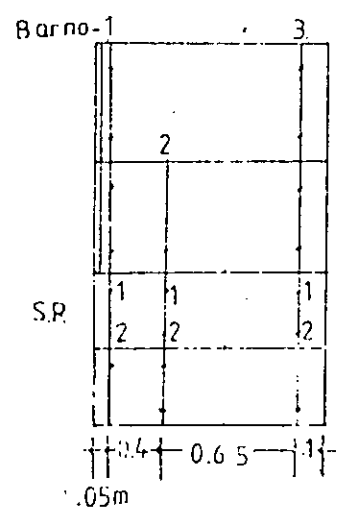
Although cracking of sampling points in the tension side of the slab are plotted, the sampling points in the top layer of the slab are also cracked. Some top layer sampling points in Element 2, Element 3 and Element 4 are found to crack.



MOD 44



MOD 22



MOD 23

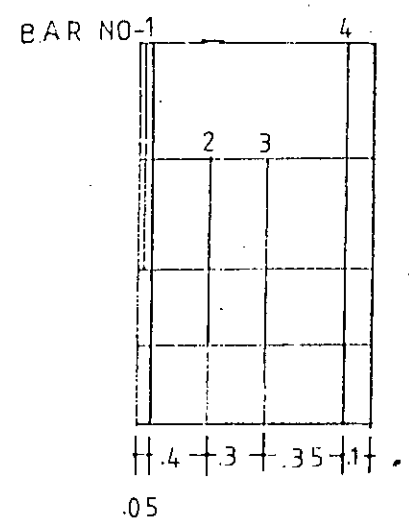


Fig. 5.23: Numbering of bars in the models

5.8.2 Study on Behaviour of steel in Slab

Bottom reinforcements in x-direction are considered for study as these reinforcements play important rule in resisting flexure. Each bar has two sampling points in each element. For the convenience of description, the bars are named as shown in Fig. 5.28, although they were addressed in a different manner during computer analysis.

In this article, 5-models will be discussed to study the behaviour of steel throughout the slab.

5.8.2.1 Model Descriptions

a) Study of Model MOD61

Fig. 5.23 presents the bottom reinforcements in x-direction with their numbering. Table 5.7 presents the stresses in reinforcement at the sampling points throughout the loading history to compare the stresses in the reinforcements.

Figs. 5.24 shows the variation and development of stresses in a bar at different elements throughout the entire loading stages. From the figures it is clear that the sampling points of the element 3 are stressed much higher than those of other elements. Bar (1) close to the shear wall is under compressive stresses at sampling points in element 4. The sampling point (1) of all the bars except bar (4) in element 3 are yielded. Bar (4) is under compression at element 3 and 4. The sampling points of all the bars at element 1 and Element 2 are stressed negligibly in comparison to those sampling points at element 3. This is very clear, when Figs. 5.24 are examined.

TABLE 5.7

STRESSES IN STEEL IN N /MM ² for model MOD61									
M/M _u	Bar No.	Element-1		Element-2		Element-3		Element-4	
		S.P.		S.P.		S.P.		S.P.	
		1	2	1	2	1	2	1	2
0.18	1	0.003	0.006	0.0012	0.021	9.9	6.6	4.3	1.16
0.60	1	0.06	0.108	-0.079	0.012	205.0	91.0	-34.0	-42.00
0.98	1	0.143	0.205	-0.37	0.284	345.0	162.0	41.7	-154
0.18	2			0.096	0.198	5.9	3.96	2.6	0.704
0.60	2			-0.241	0.744	190	129	20	14
0.98	2			-2.40	0.479	345	259	184	60.2
0.18	3			0.109	0.305	1.82	1.29	0.84	0.23
0.60	3			0.716	2.60	109	101	40.2	36.6
0.98	3			-1.360	12.3	345	202	189	137
0.18	4	0.124	0.236	0.013	0.339	-0.04	-0.025	-1.65	-0.463
0.60	4	1.08	2.79	3.93	7.06	-116	-50	-12.2	11.8
0.98	4	3.56	5.68	5.20	28	-133	-133	-32	16.6

S.P. -- Sampling point of bar in an element

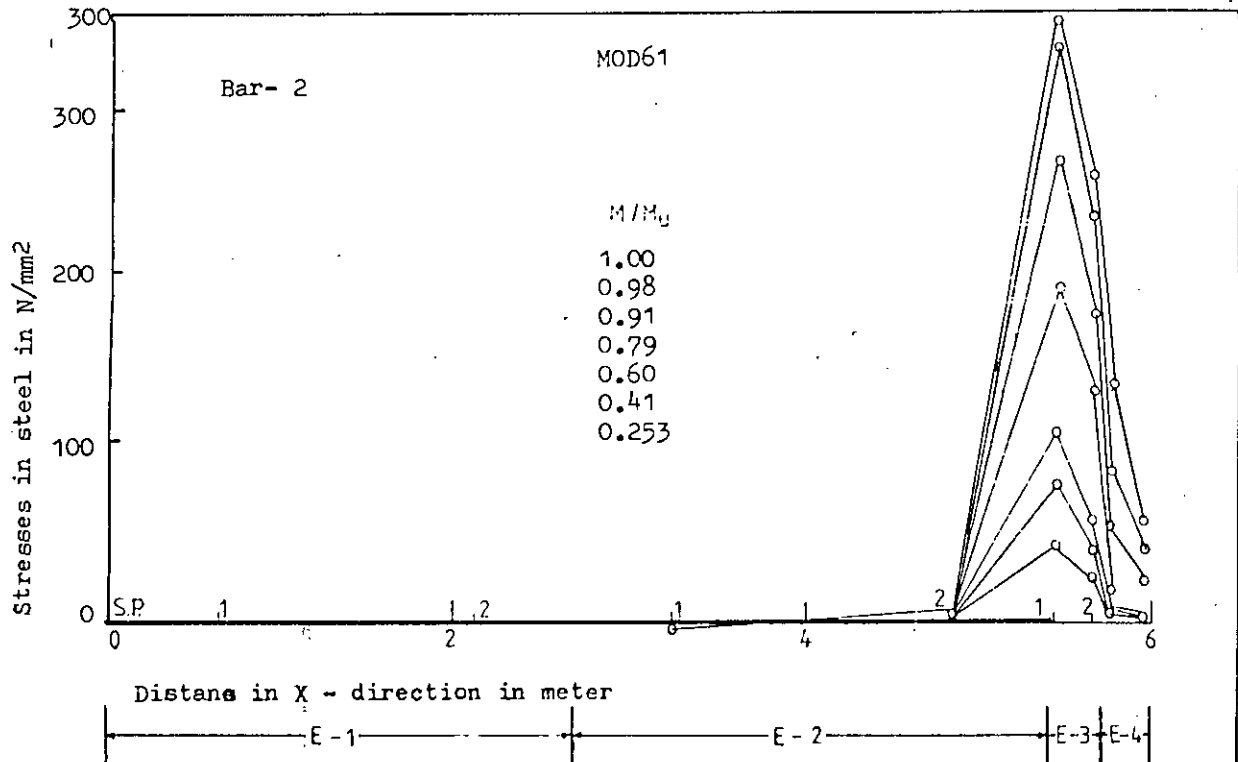


Fig.5.24(b) : Development of stress in bar-2

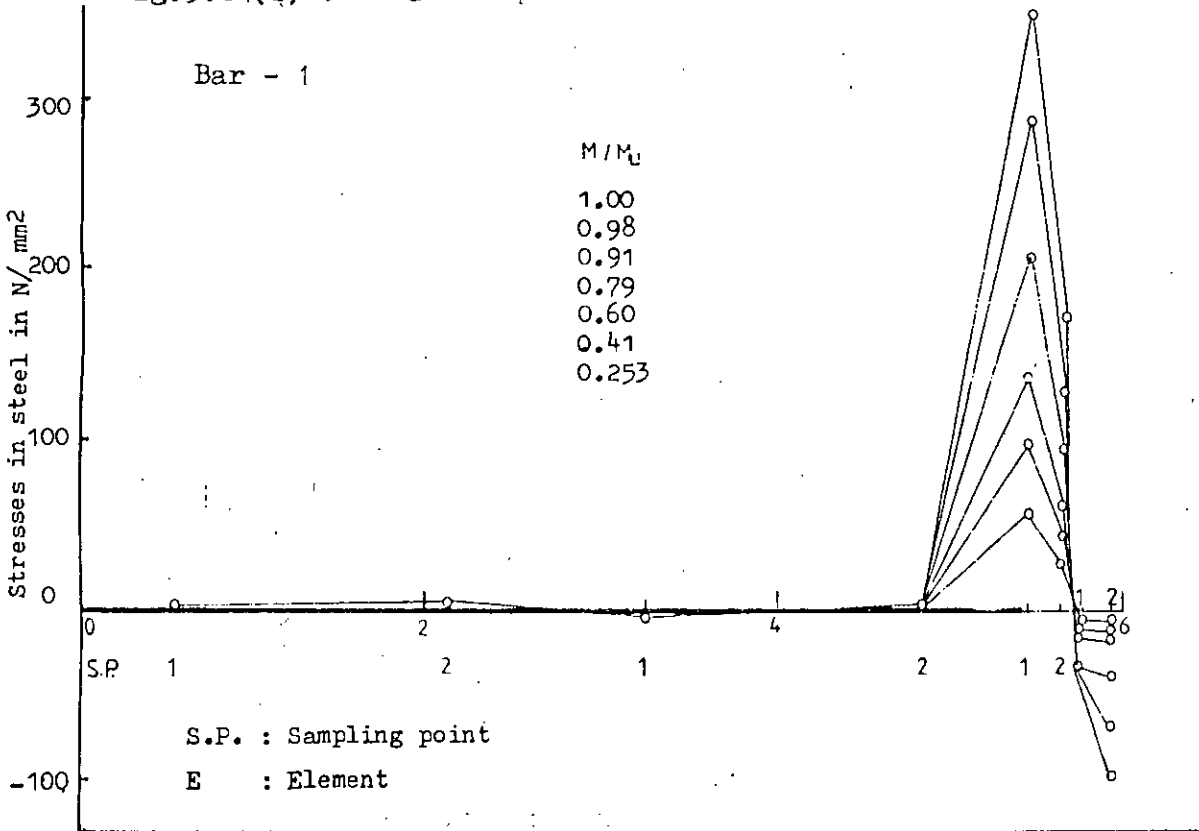


Fig. 5.24(a) : Gradual development of stress in bar -1

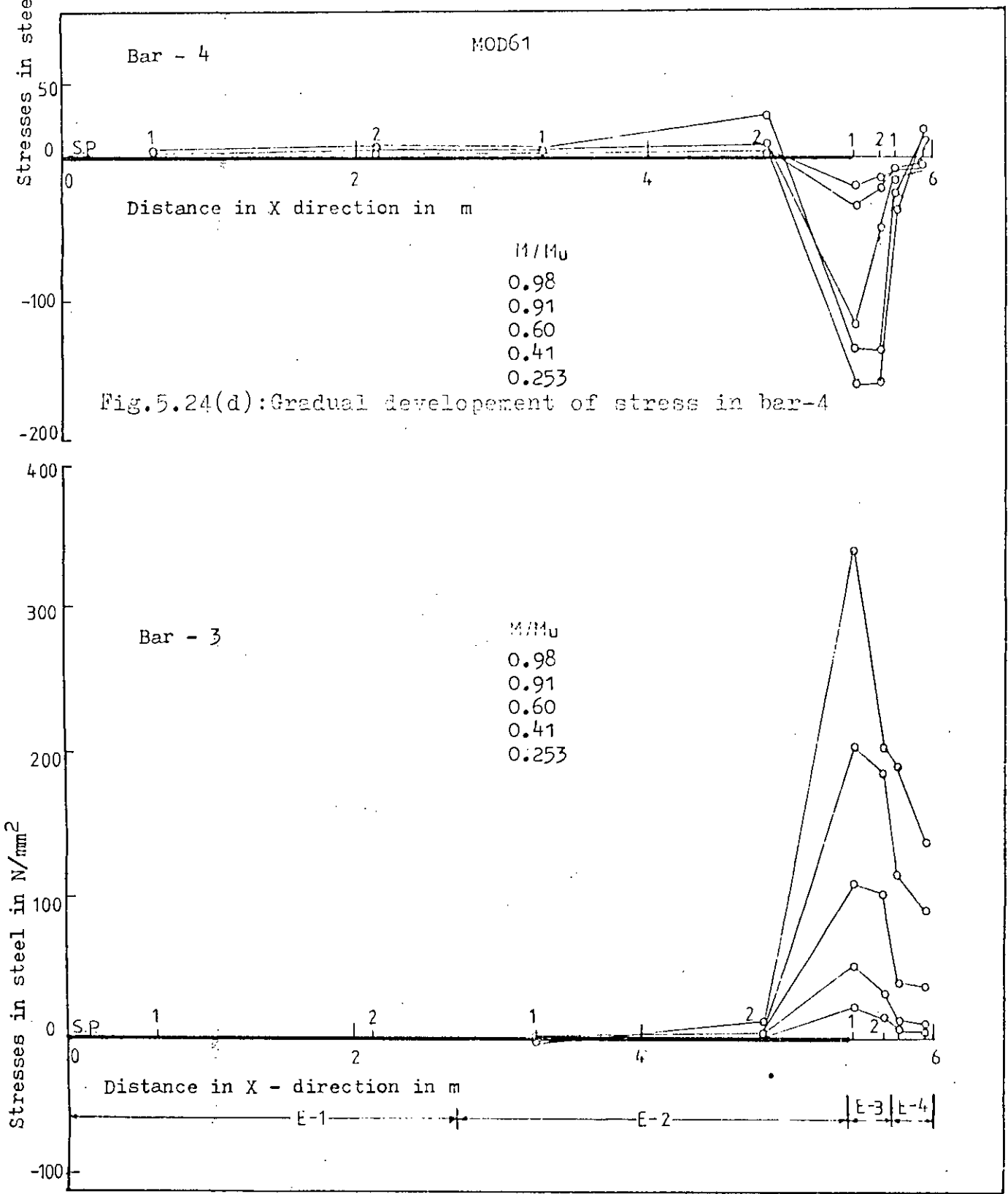
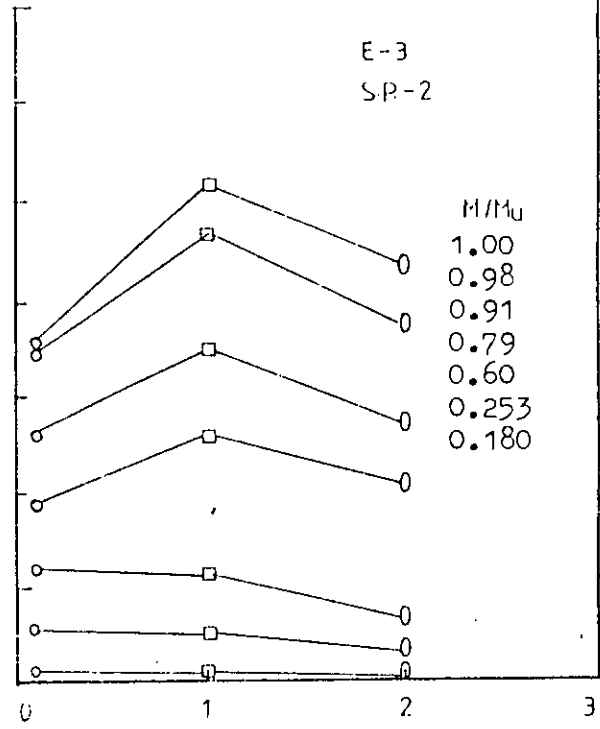
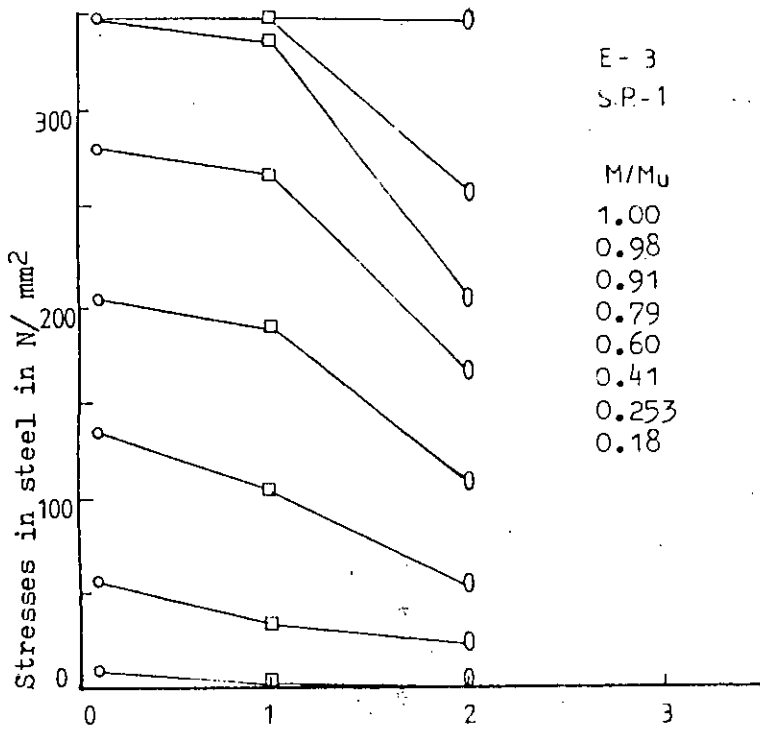
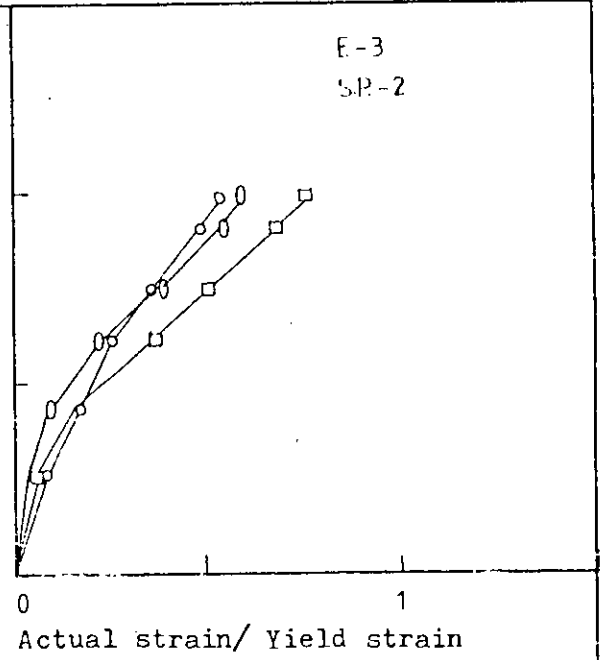
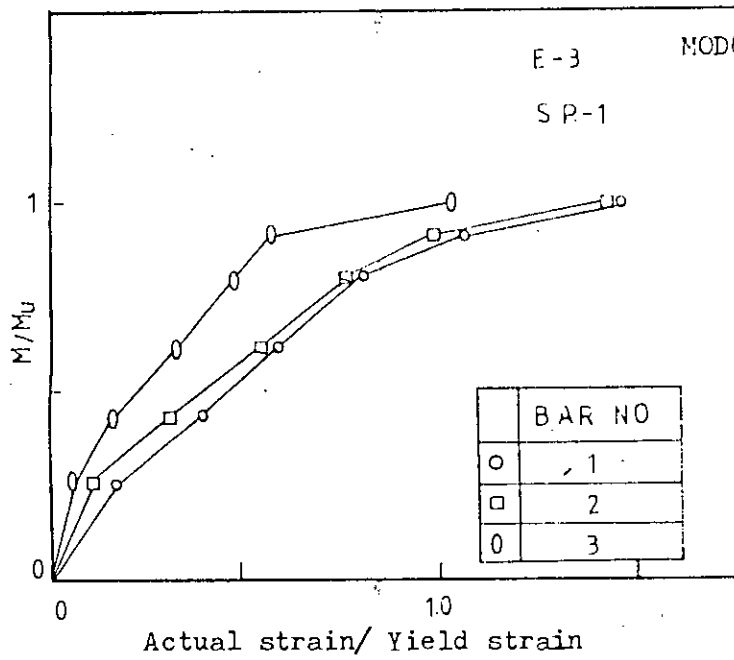


Fig. 5.24(c) : Gradual development of stress in a bar -3



Transverse distance from shearwall in m

Transverse distance from shearwall in m

M : Actual moment
M_u: Ultimate moment

Fig. 5.25: Stresses and strains in steel

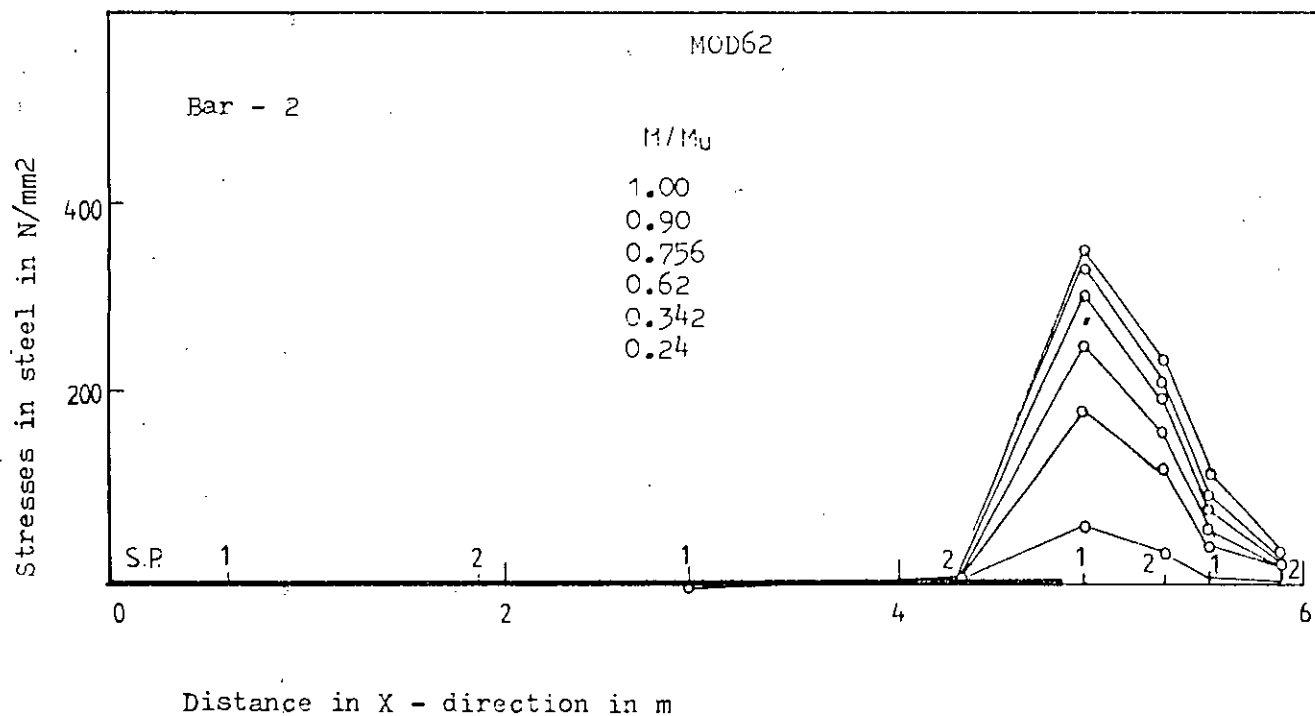


Fig.5.26(b): Gradual development of stress in bar-2

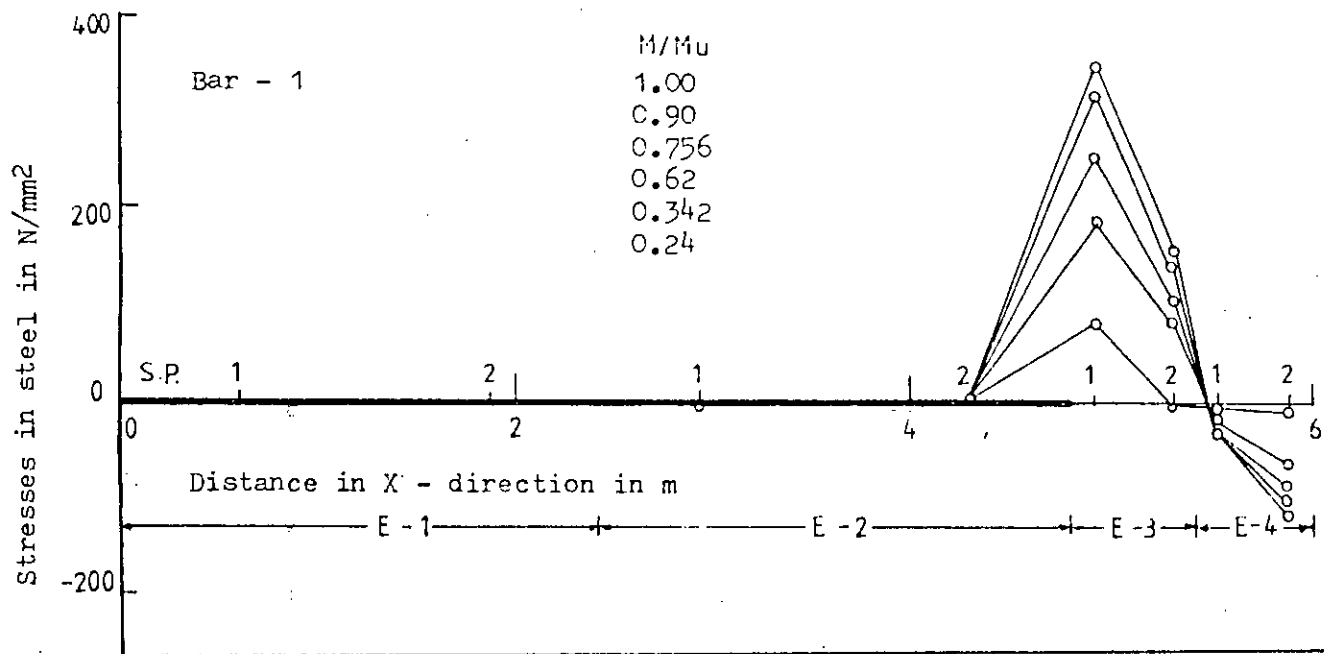


Fig. 5.26(a) : Gradual development of stress in bar-1

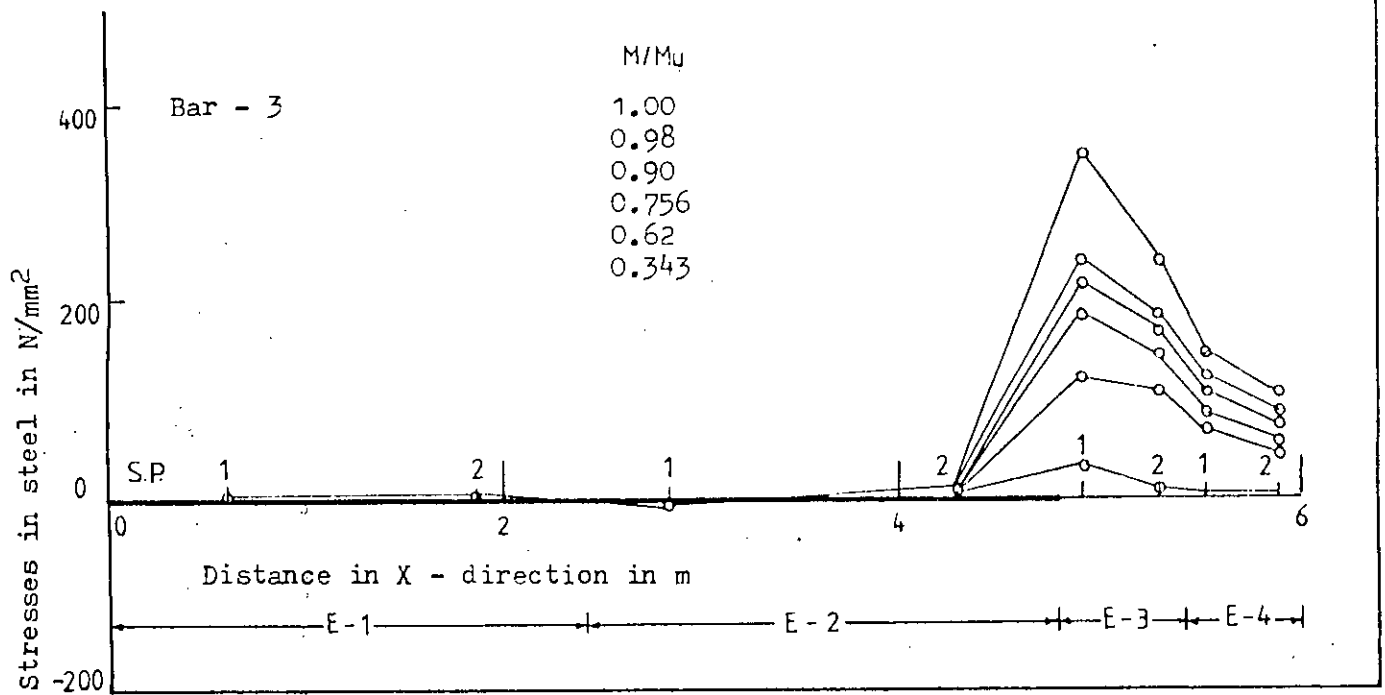
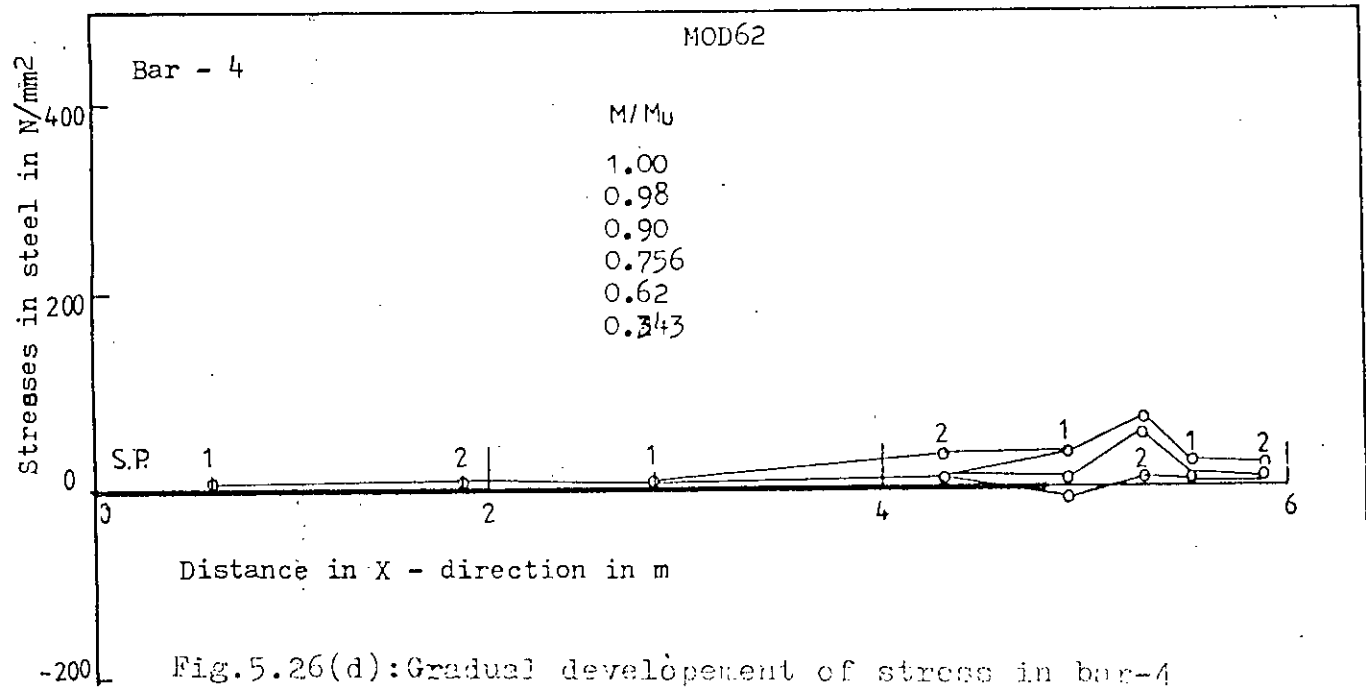


Fig. 5.26(c) : Gradual development of stresses in a bar-3

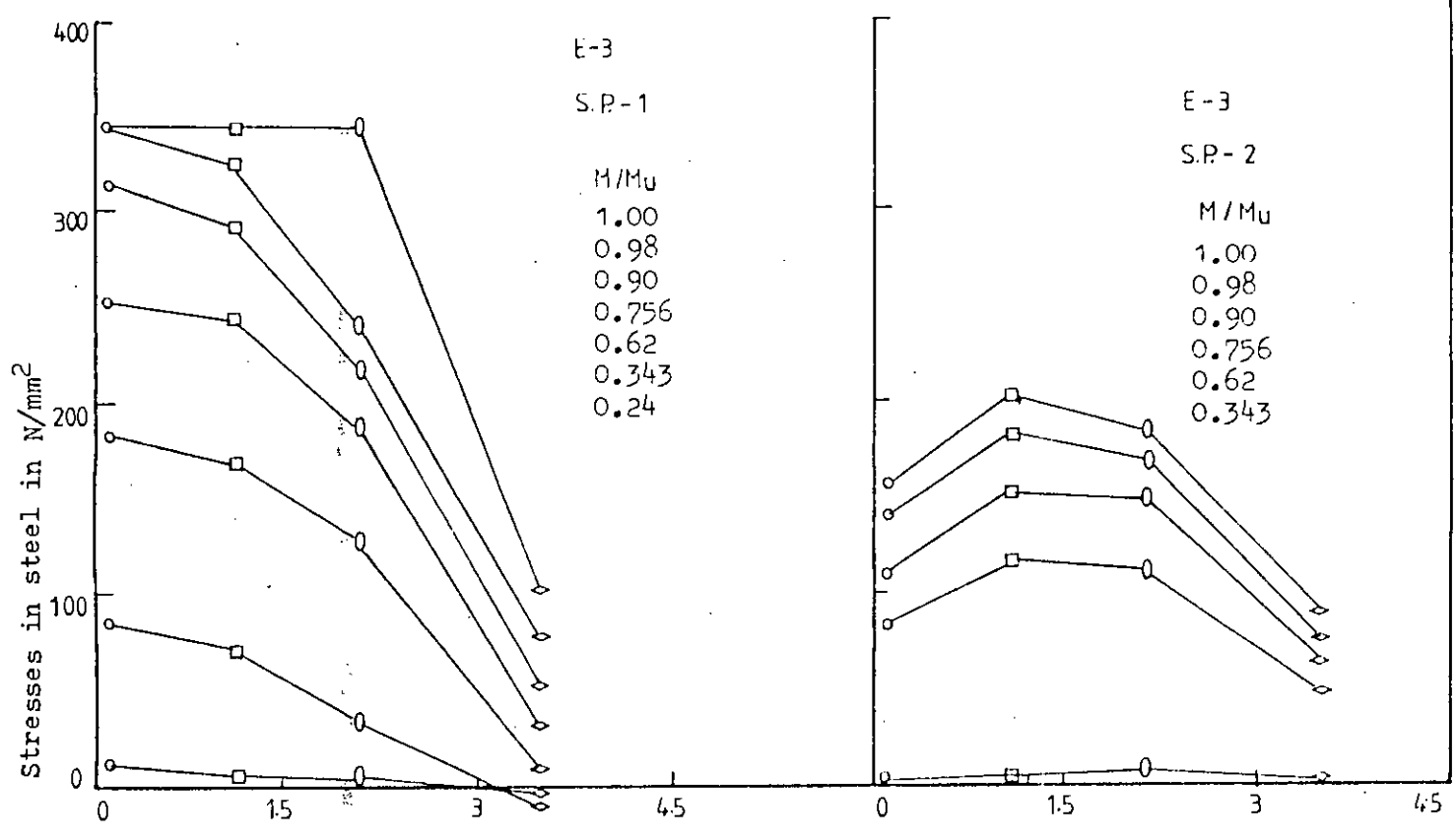
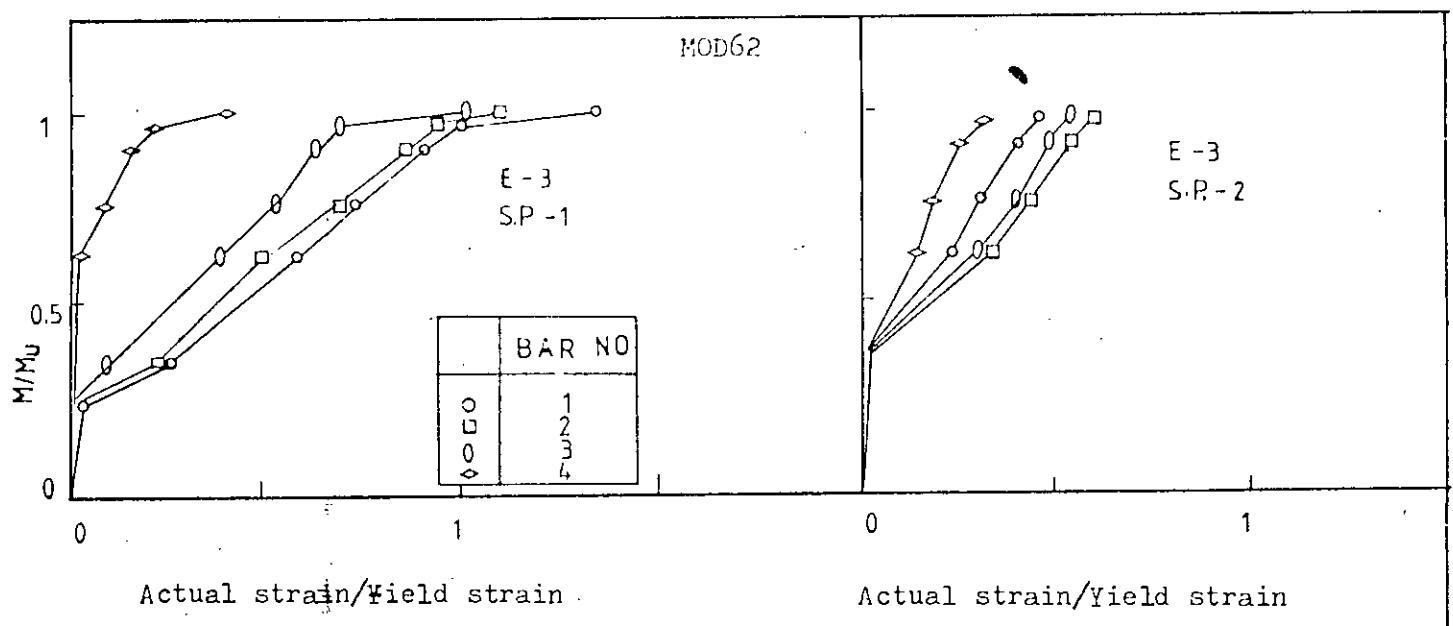


Fig. 5.27 : Stresses and strain in steel

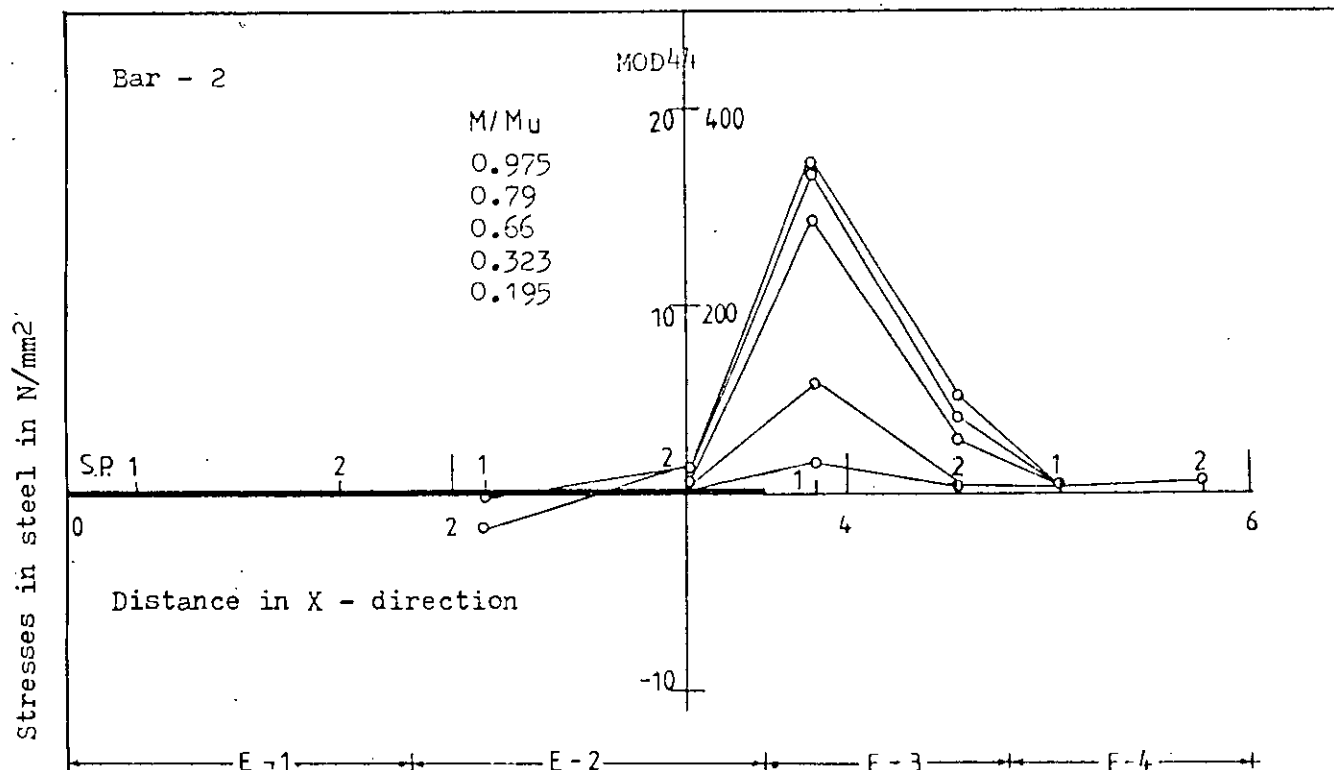


Fig. 5.28(b): Gradual development of stress in bar-2

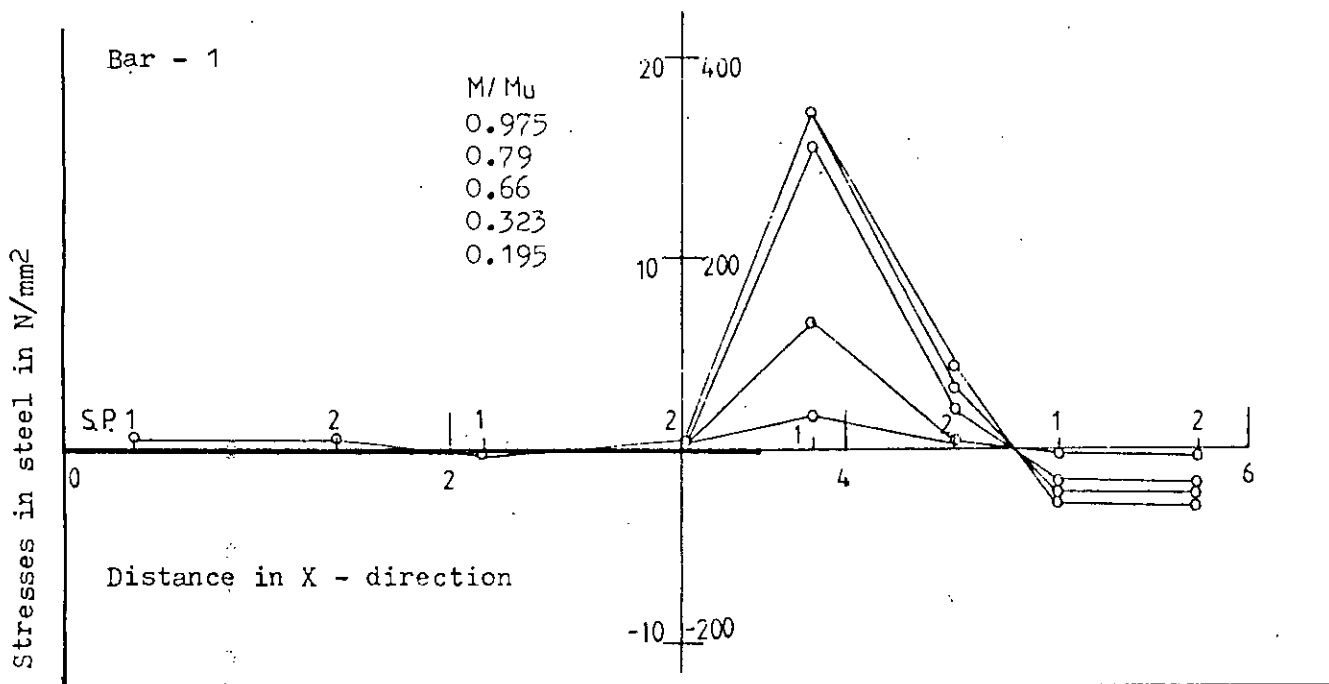


Fig. 5.28(a) : Gradual development of stresses in bar-1

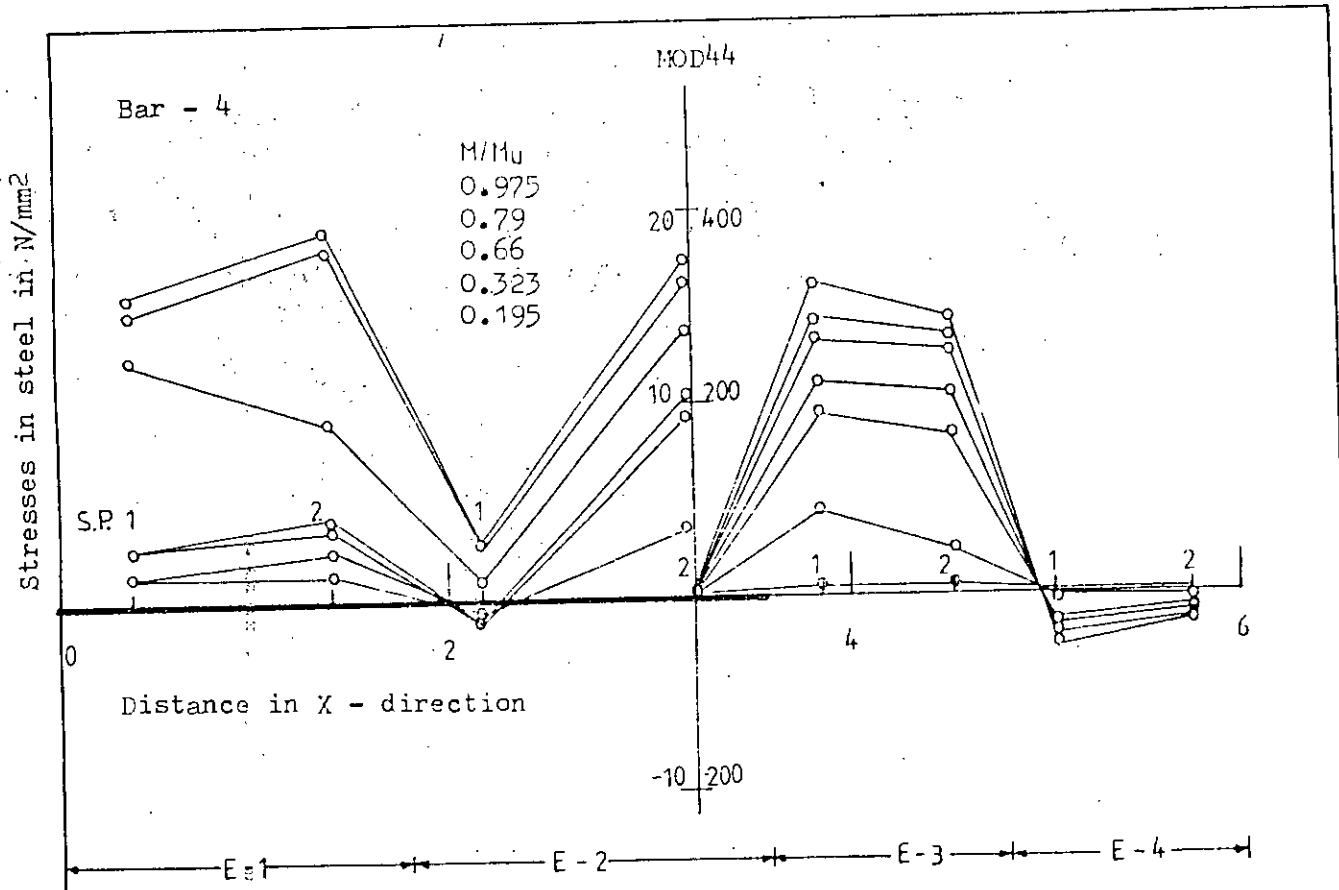


Fig.5.28(d): Gradual development of stress in bar-4

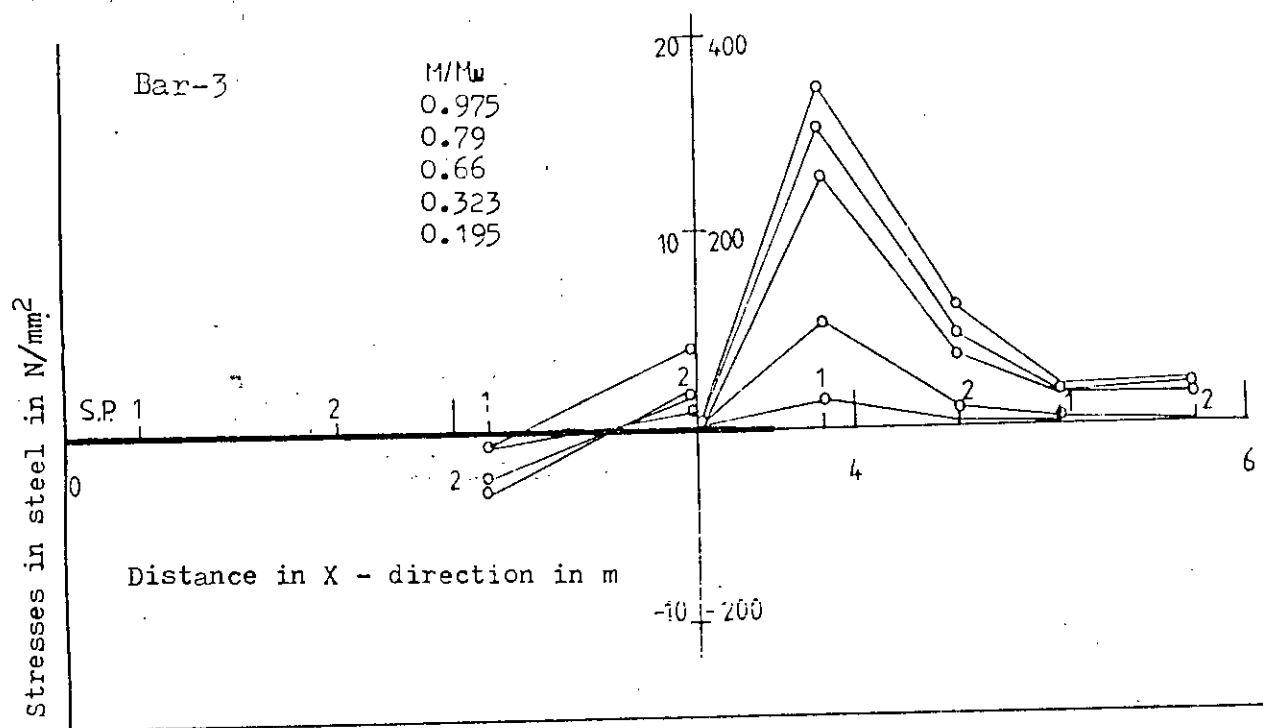


Fig. 5.28(e) : Gradual development of stresses in bar-3

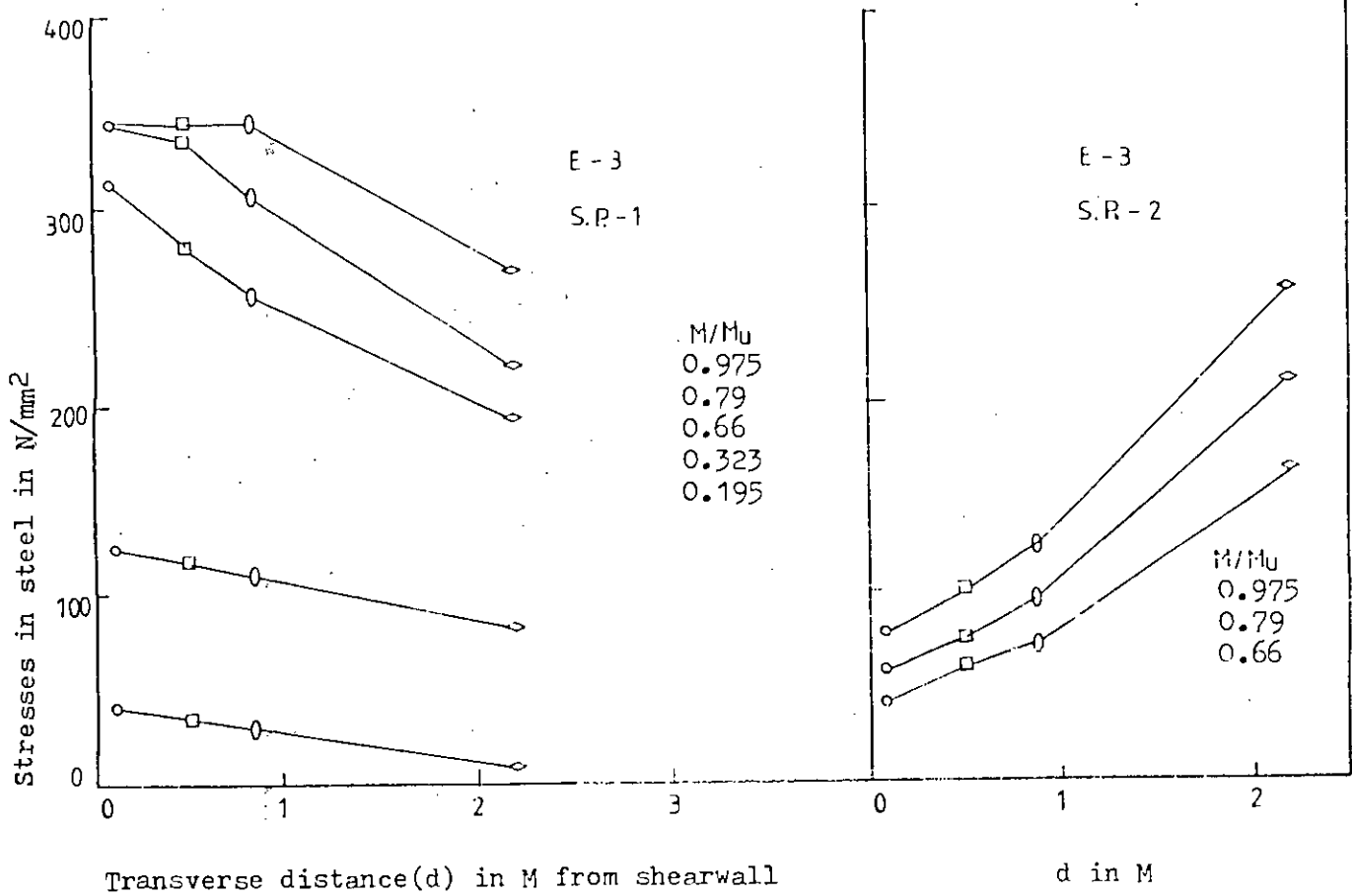
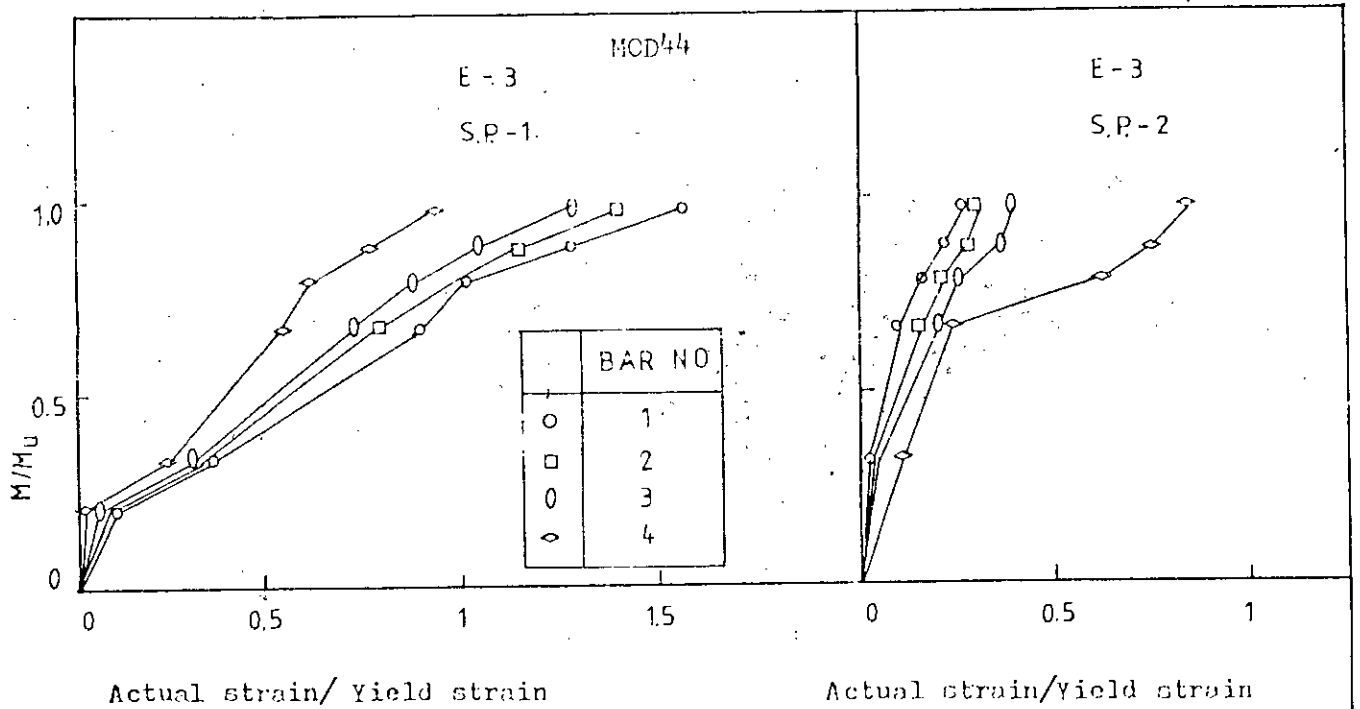


Fig. 5. 29 : Stresses and strains in steel

Fig. 5.25 shows the stresses and strains in steel at element 3. As the Element 3 is highly stressed, this element is closely studied. From the stress diagram, it is seen that the bars close to the shear wall are stressed higher and as the load increases the bars close to the shear wall yield first. Steel at sampling point 1 are stressed higher than that at sampling point 2. This is also evident from the strain diagram of steel. Therefore, a stress concentration occurs at a section passing through the interior edge of the shear wall.

b) Study of Model MOD62

Figs. 5.23 shows the bottom reinforcements in x-direction with their numbering. Figs. 5.26 show the variation of stresses in a bar at different elements, which presents the similar behaviour of steel like previous model. But bar 4 is under tensile stresses at element 3 and 4.

Figs. 5.27 shows the stresses and strain in steel at element 3 representing the same behaviour of steel as in previous model.

c) Study of Model MOD44

Figs. 5.23 shows the bottom reinforcements in x-direction. Figs. 5.28 showing variation of stresses in a bar at different elements represents similar behaviour as before. Figs. 5.29 shows the stresses and strains in steel at element-3.

d) Study of Model MOD22

Fig. 5.23 presents the bottom reinforcements in x-direction.

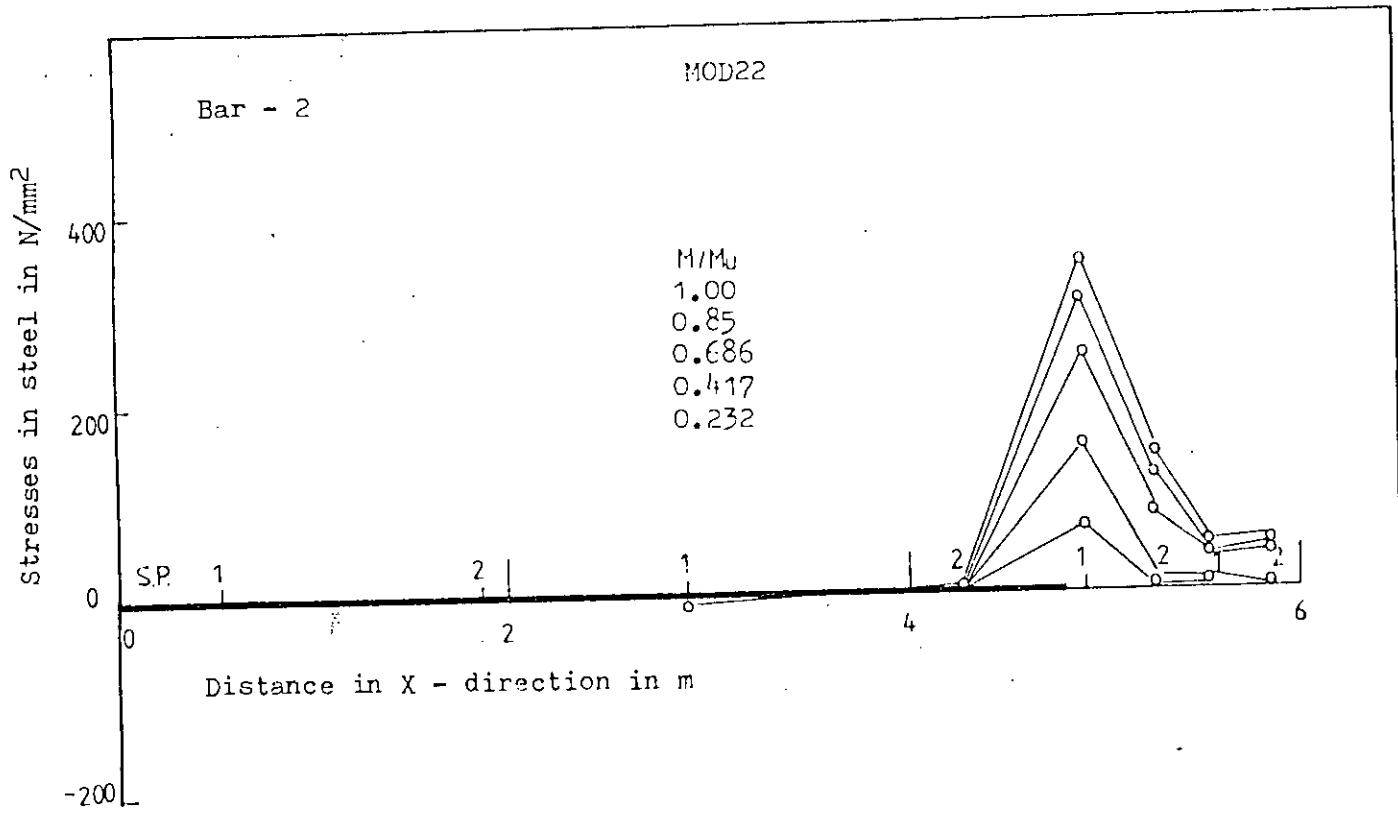


Fig. 5.30(b): Gradual development of stress in bar-2

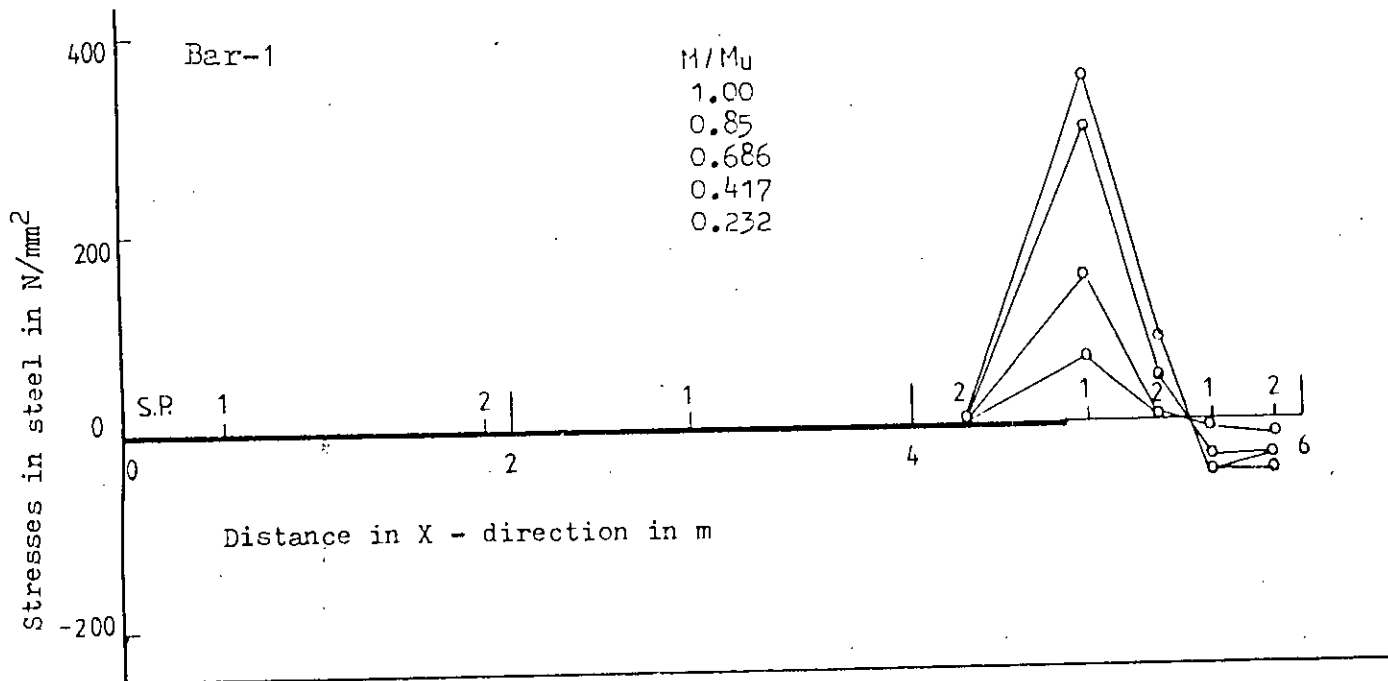


Fig. 5.30(a) Gradual development of stresses in bar-1

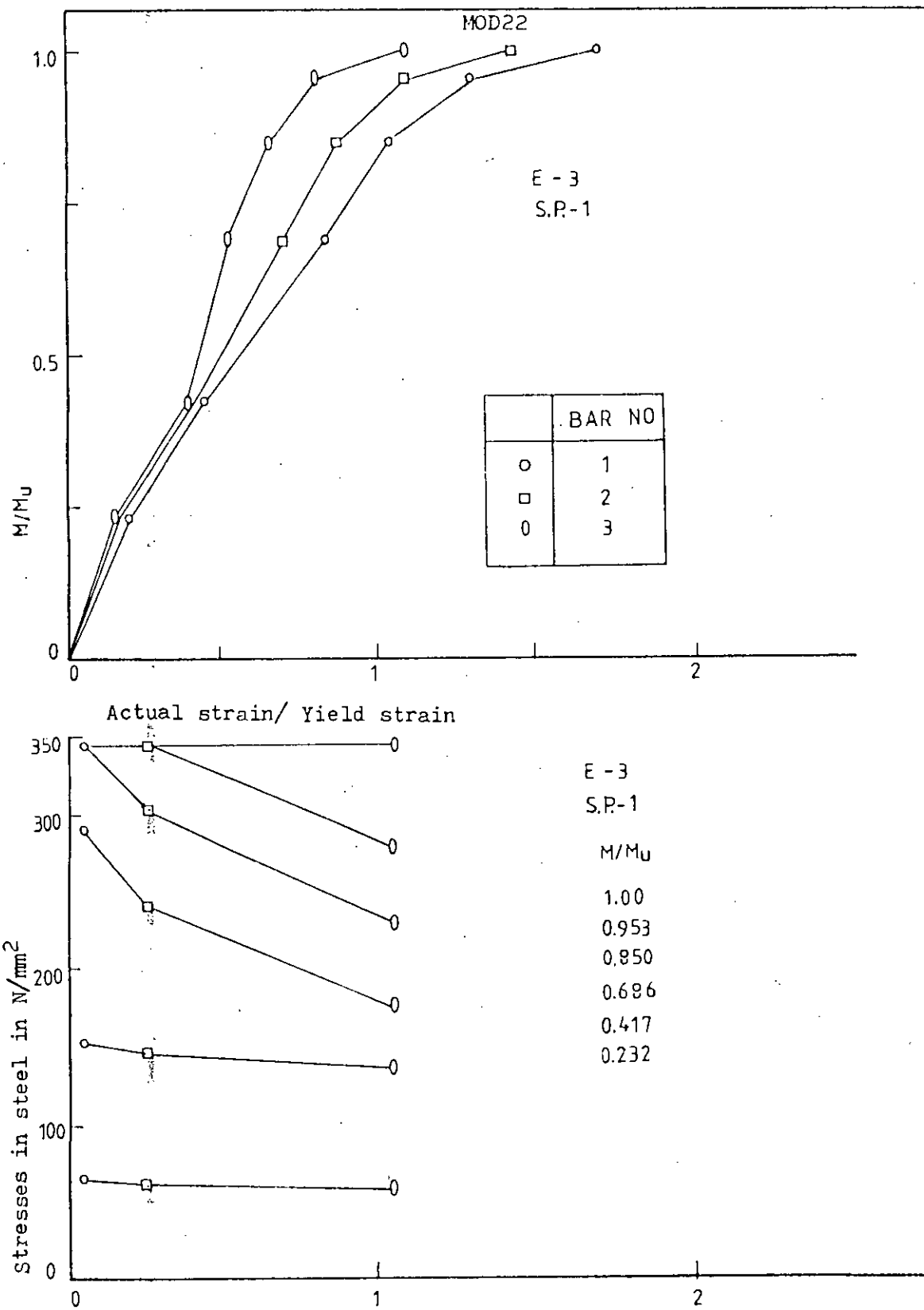


Fig. 5.31 : Stresses and strain in steel

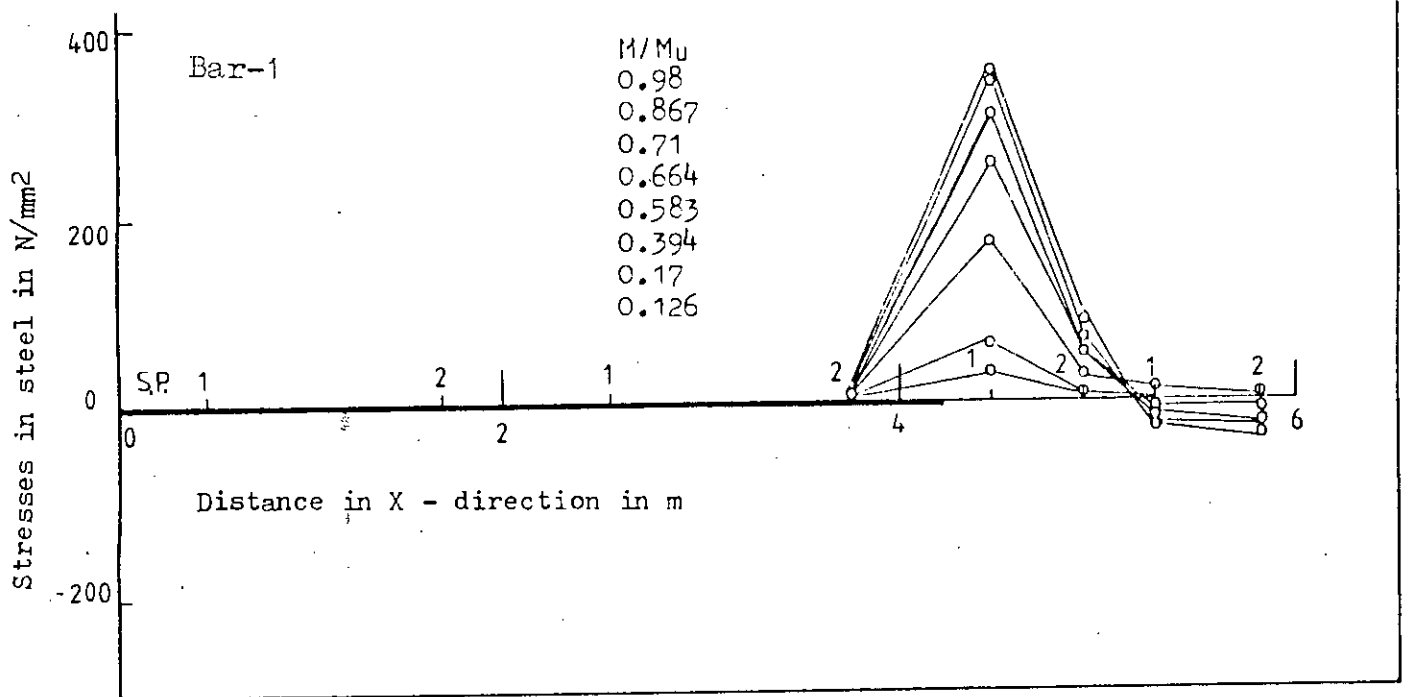
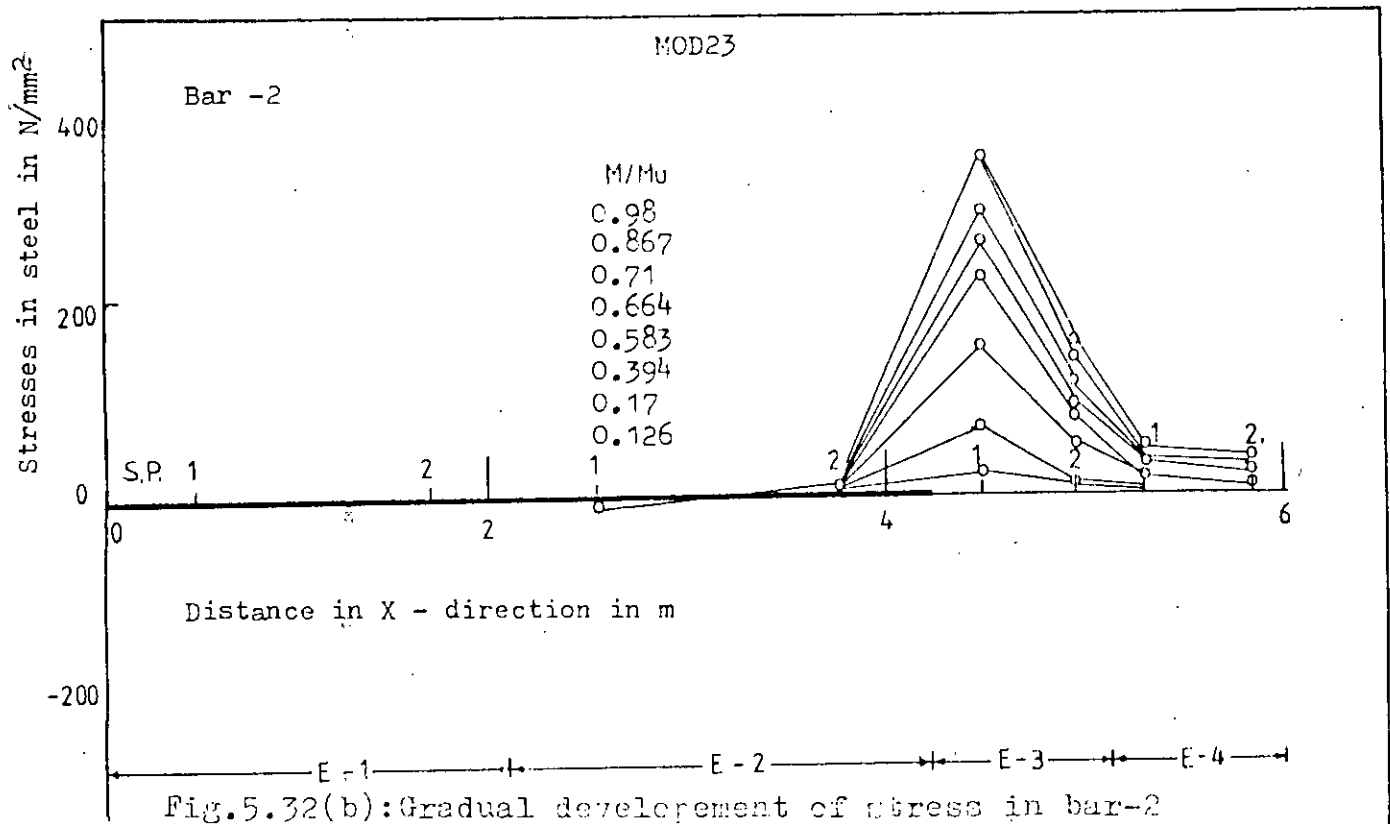


Fig. 5.32(a) : Gradual development of stresses in bar-1

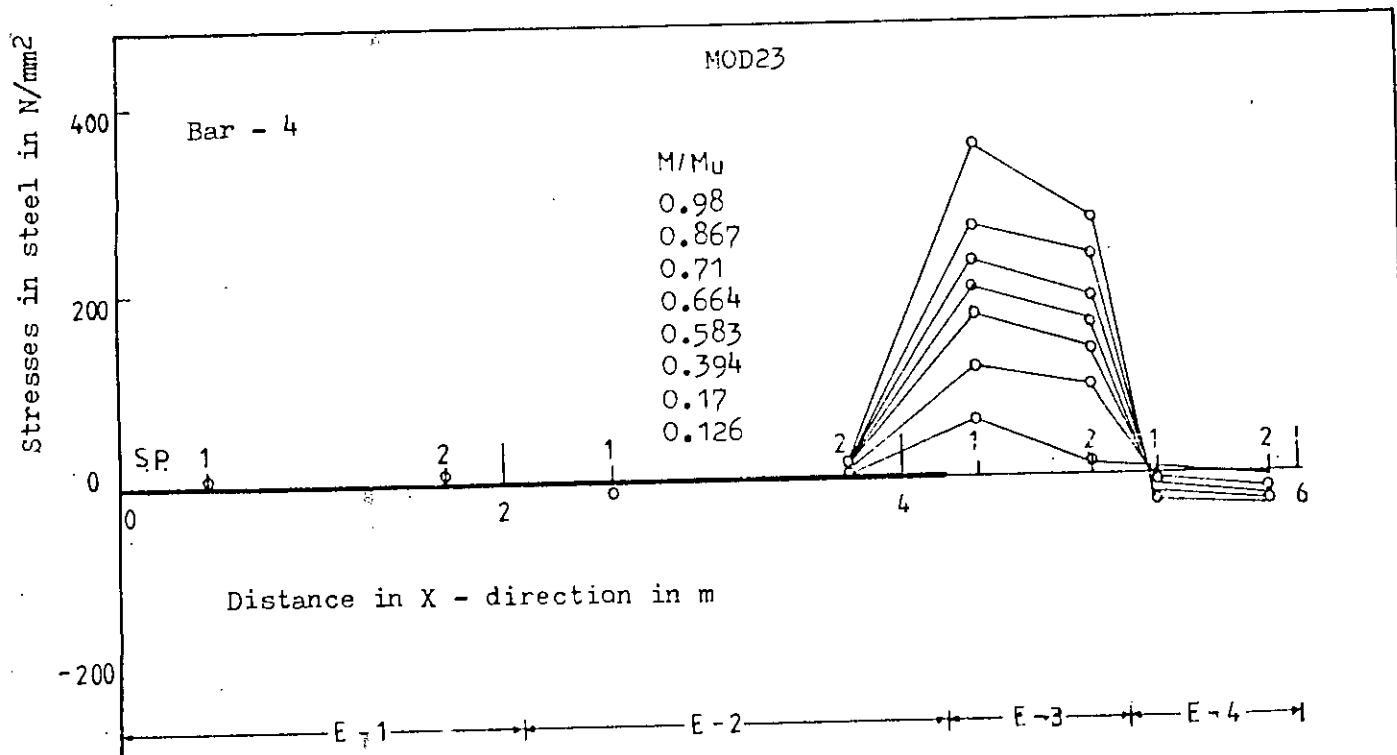


Fig.5.32(d): Gradual developement of stress in bar-4

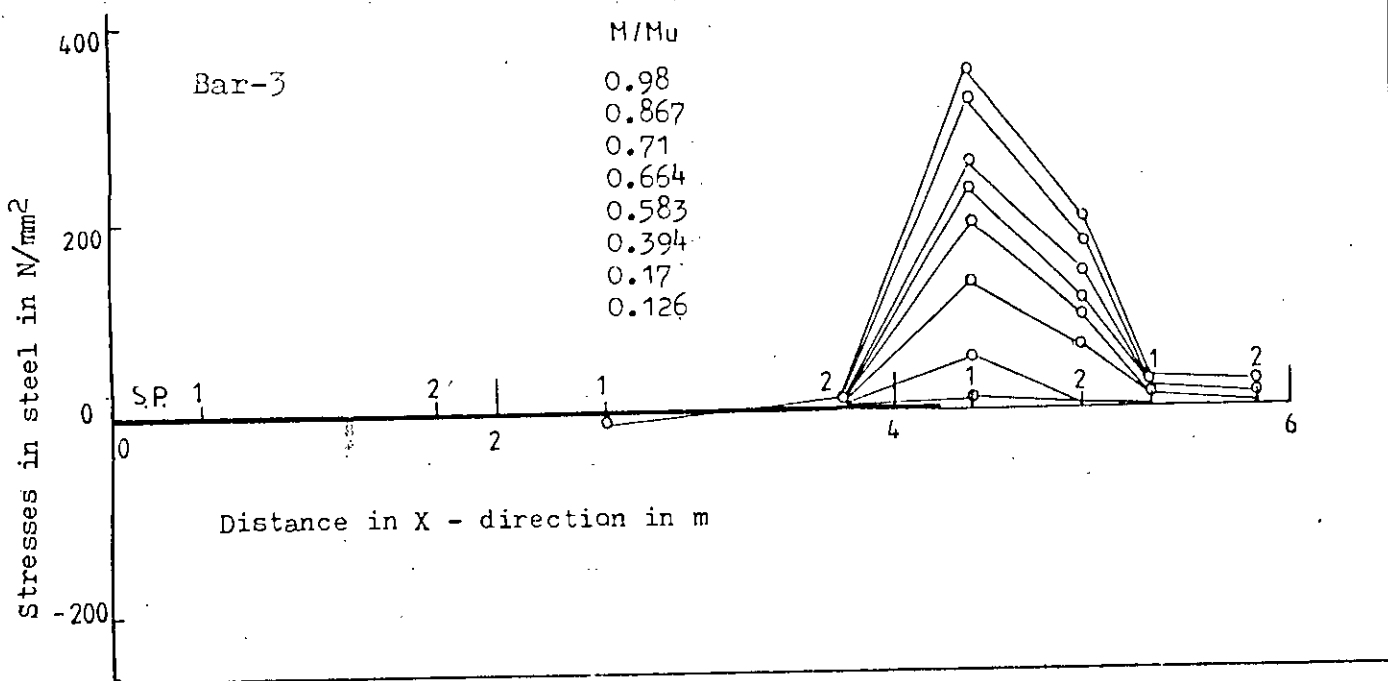


Fig. 5.32(c) : Gradual development of stresses in bar-3

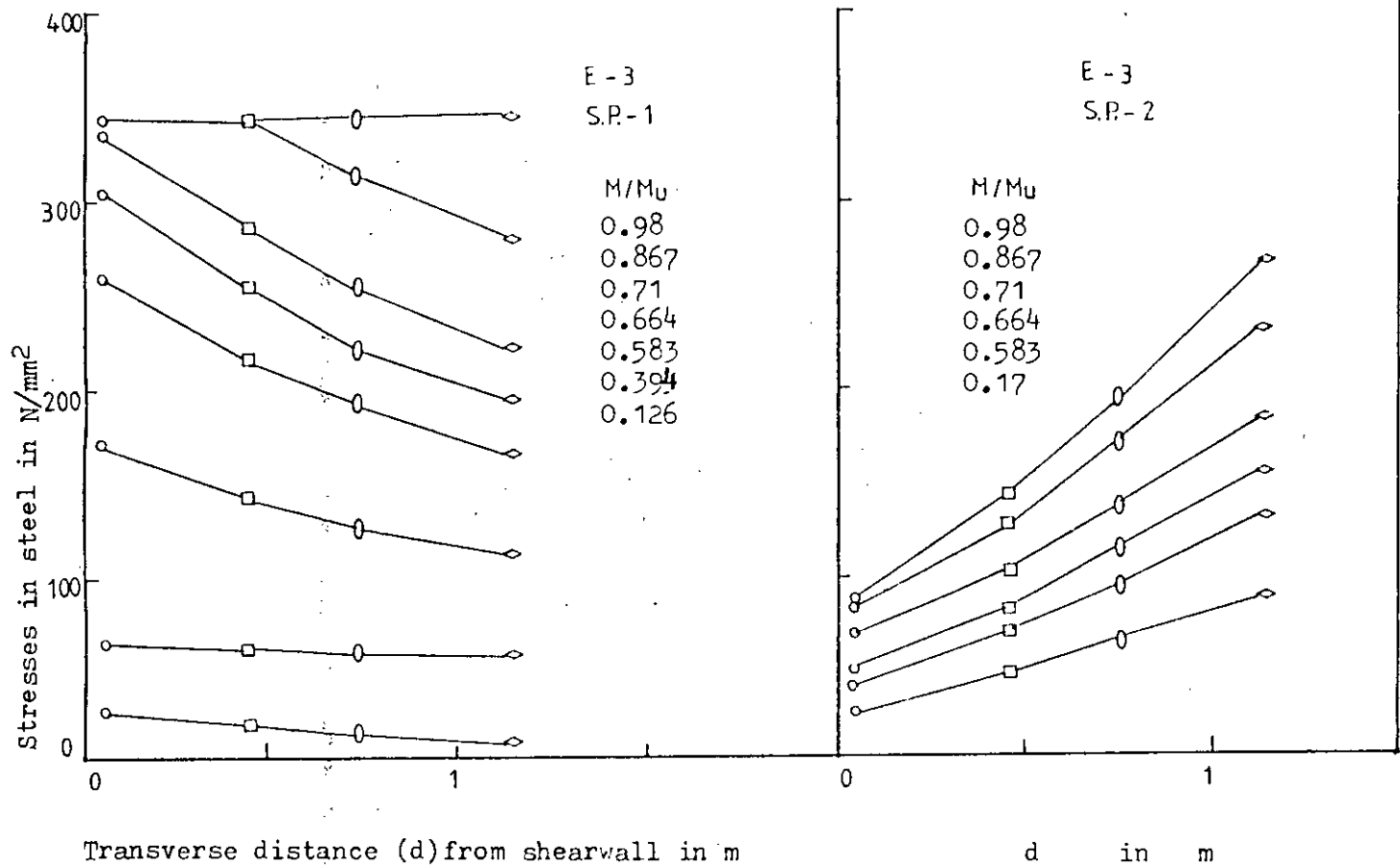
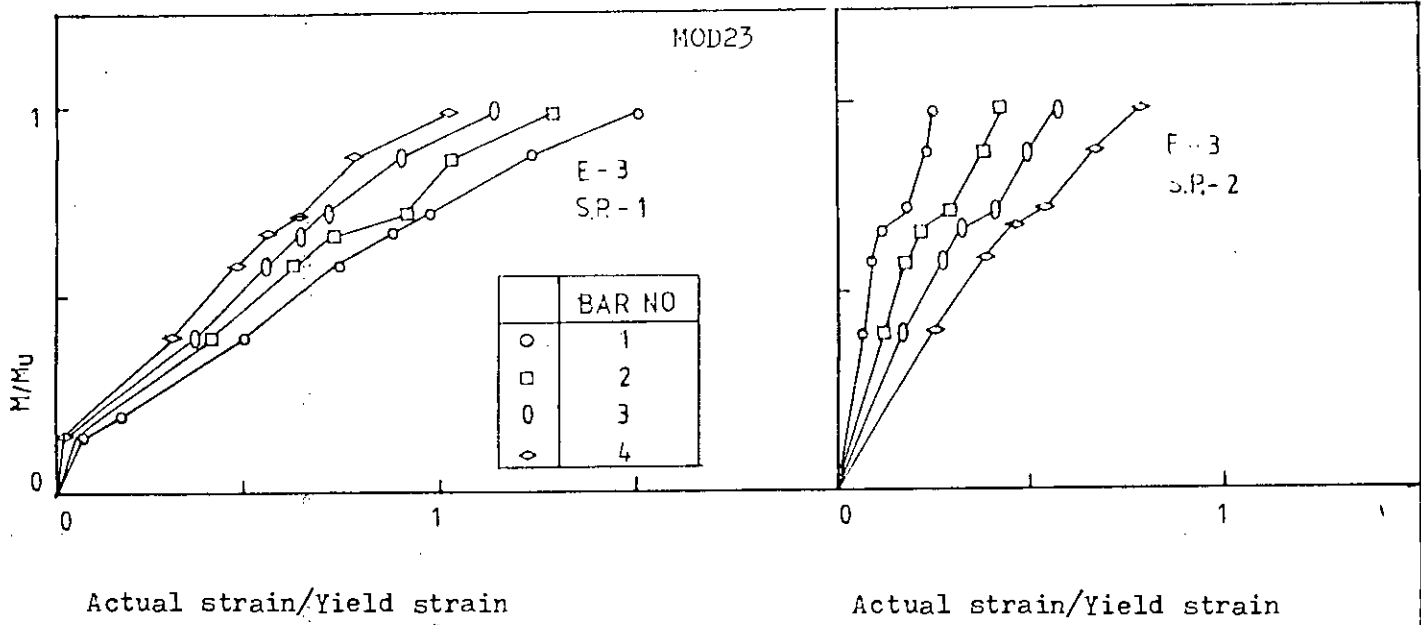


Fig.5.33: Stresses and strains in steel

Figs. 5.30 shows the variation of stresses in a bar at different elements representing similar behaviour. Fig. 5.31 shows the stresses and strain in steel at element-3.

e) Study of Model MOD23

Fig. 5.23 shows the bottom reinforcement in x-direction, Figs. 5.32 show the variation of stresses in a bar at different elements representing similar type of behaviour. Bar 4 furthest from the shear wall is subjected to tensile stress at element-3 and compressive stresses at element-4. Fig. 5.33 shows the stresses and strains in steel at element-3 for the model.

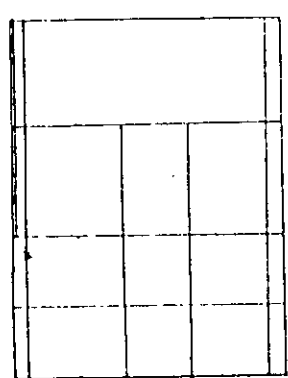
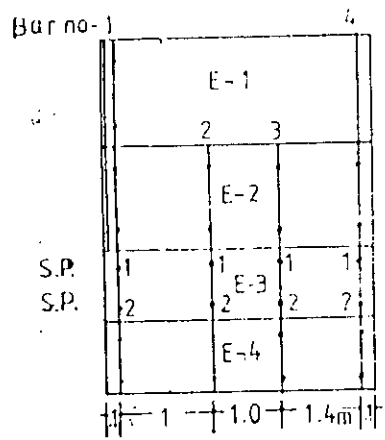
5.8.2.2 Yielding Pattern of Steel for the Models

Fig. 5.34 shows the yield pattern of steel for the models. Yield pattern for all the models revealed that the steel close to the interior edge of the shear wall yielded first. Steels far from the shear wall in transverse direction are yielded later. Only the steels in element-3 are yielded. Almost all the steels in element-3 are yielded at sampling point 1, before failure of the slab. All the models are designed according to direct design method which requires yielding of sufficient number points with minimum redistribution of stresses to convert the slab into a mechanism for failure. This consideration is supposed to be fulfilled by the models.

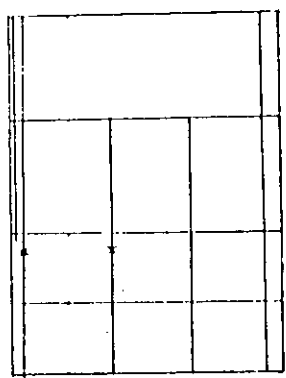
5.8.2.3 Discussion on Behaviour Steel

Steel stress diagrams shows that the stresses in steel nearest to the shearwall increases at a much higher rate than those furthest from the shearwall. That is stress concentration occurs near the shear wall as load increases. It represents that the effective width of the slab gradually decreases with increase

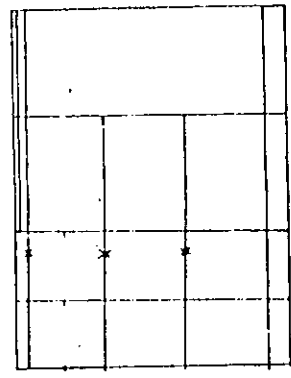
M O D 61



$M/M_u = 0.93$

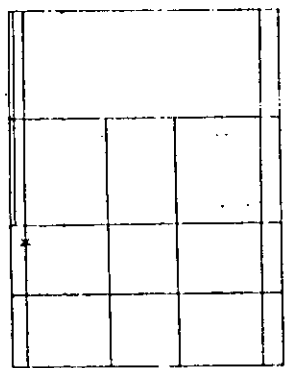
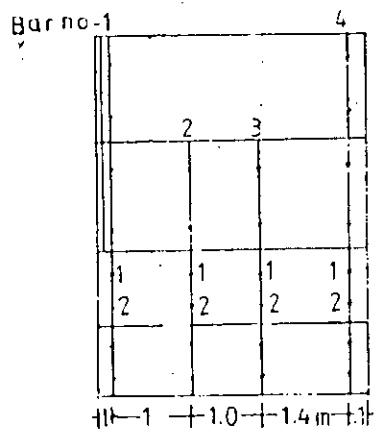


0.91

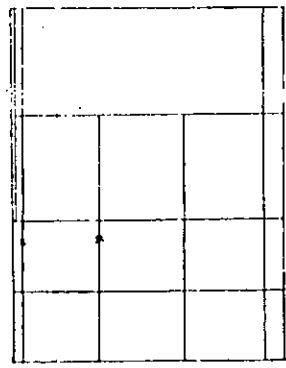


1.0

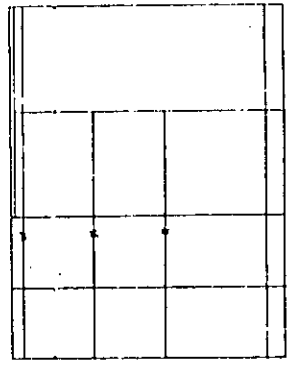
M O D 62



$M/M_u = 0.94$



0.97



1.0

Fig. 5.34(a) : Yield pattern of steel

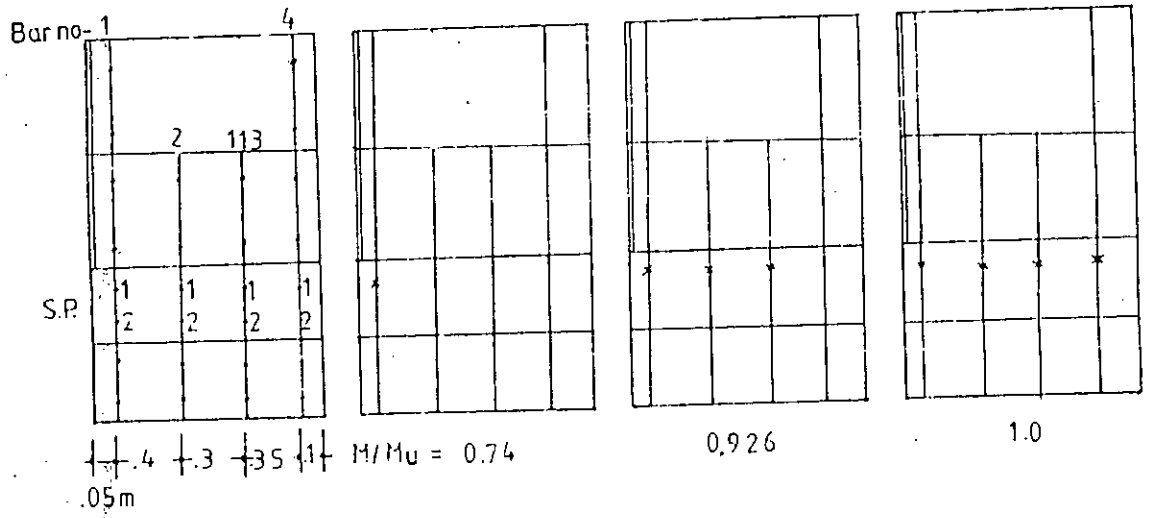
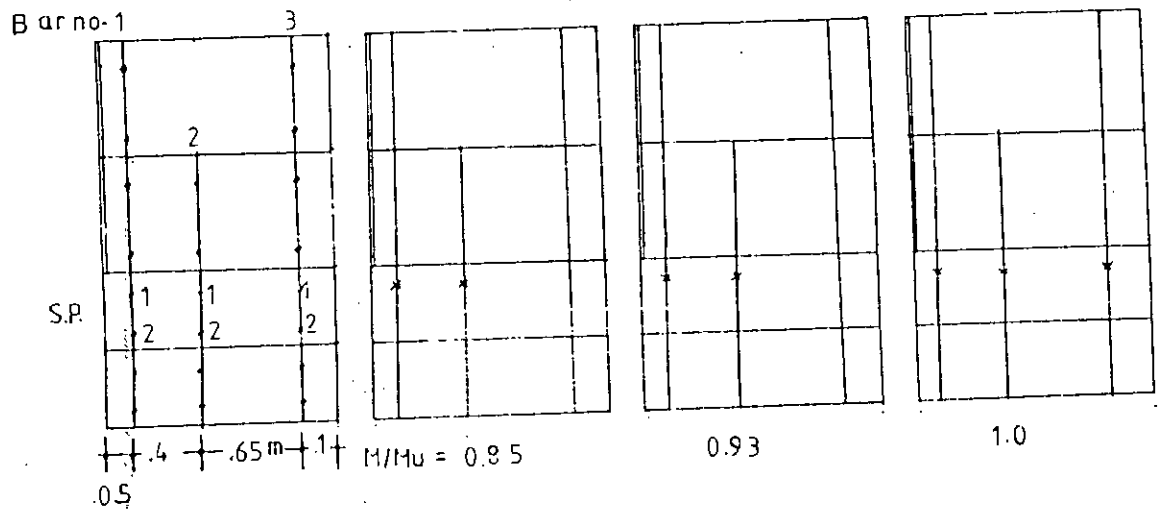
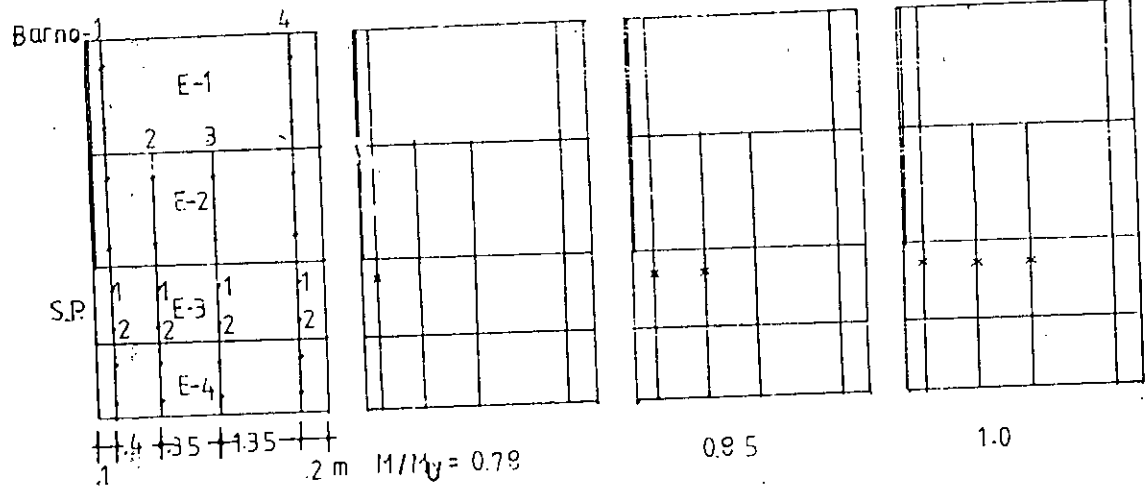


Fig. 5.34(b) : Yield pattern of steel

in load.

The general steel behaviour can be described as trilinear⁴ consisting of behaviour before cracking, after cracking and after yielding of steel. Before the development of first cracks, very little strain exists in the reinforcing steel and the load-strain relationship can be taken as linear. At this stage, applied load is resisted mainly by concrete, hence the steel is inactive. After cracking, a gradual increase in strain occurs in the steel and curves may be taken as linear until yield. After yielding, a rapid increase in strain with little increase in load occurs giving a nonlinear and almost flat curve.

5.8.3 Interpretation Results

M- θ diagrams are idealized for simplicity in determining the flexural stiffnesses of slab. Idealized curves for all the models are used to study the effect of various geometric parameters on bending stiffness and effective width of the slab. Using equations 2.5 and 2.6, the bending stiffnesses K_0 , K_{cr} , K_p and corresponding Y_{e0}/Y , Y_{ecr}/Y and Y_{ep}/Y are evaluated where Y_{e0} is precracking, Y_{ecr} is cracking and Y_{ep} is post cracking effective widths. Table 5.8 is prepared to include all the necessary items for interpretation of results.

a) Comparison of Nonlinear Results to those of Coull & Wong (12) and Qadeer & Stafford Smith (7)

The results from nonlinear analysis are compared with those of Coull & Wong and Qadeer Smith as their results were experimentally verified. As the researcher's adopted linear analysis, the linear part of the nonlinear analysis (precracking part) should agree with each other. Fig. 5.35 shows the variation of Y_{e0}/Y with L/X for different values of Y/X from nonlinear analysis and those from Coull and Wong. Comparative study shows a close agreement with each other as the variation are only 1.0% to 8%.

Fig. 5.36 and Table 5.9 compare the precracking stiffness (K_0) of nonlinear analysis to those of Qadeer & Smith.

TABLE 5.8

Model No.	Parameters			Bending Stiffness				Effective width			Ratios	
	Y/X	L/X	L/Y	K _o	K _{cr}	K _p	Y _{e.o} /Y	Y _{cr} /Y	Y _{ep} /Y	Y _o /Y	K _{cr} /K _o	K _p /K _o
MCD61	0.1	0.17	0.17	187.77	48.70	19.00	0.16	0.046	0.019	0.15	0.26	0.100
MCD62	0.2	0.33	0.33	44.68	9.80	4.19	0.29	0.062	0.021	0.28	0.22	0.076
MCD63	0.3	0.50	0.50	20.61	5.90	1.83	0.38	0.109	0.033	0.38	0.29	0.089
MCD64	0.4	0.67	0.67	12.56	2.93	1.14	0.47	0.108	0.043	0.47	0.24	0.091
MCD65	0.5	0.83	0.83	7.52	2.06	0.60	0.48	0.130	0.038	0.52	0.27	0.080
MCD66	0.6	1.00	1.00	6.05	1.51	0.75	0.58	0.145	0.073	0.58	0.25	0.126
MCD41	0.1	0.25	0.25	152.00	37.62	15.08	0.21	0.053	0.021	0.21	0.25	0.099
MCD42	0.2	0.50	0.50	36.00	8.00	4.00	0.34	0.075	0.038	0.36	0.23	0.111
MCD43	0.3	0.75	0.75	17.00	5.44	2.98	0.46	0.145	0.081	0.50	0.32	0.175
MCD44	0.4	1.00	1.00	9.00	1.982	1.26	0.52	0.115	0.070	0.58	0.22	0.140
MCD45	0.5	1.25	1.25	6.33	2.010	0.54	0.60	0.191	0.051	0.64	0.32	0.086
MCD46	0.6	1.50	1.50	4.67	1.40	0.51	0.67	0.201	0.073	0.71	0.30	0.109
MCD21	0.1	0.50	0.50	121.00	33.00	12.76	0.34	0.093	0.036	0.29	0.27	0.109
MCD22	0.2	1.00	1.00	26.00	7.28	3.59	0.51	0.140	0.070	0.56	0.28	0.140
MCD23	0.3	1.50	1.50	12.50	4.79	2.75	0.68	0.260	0.150	0.72	0.38	0.220
MCD24	0.4	2.00	2.00	6.82	2.52	1.01	0.76	0.281	0.114	0.79	0.37	0.150
MCD25	0.5	2.50	2.50	4.11	1.61	0.45	0.78	0.304	0.084	0.83	0.39	0.110
MCD26	0.6	3.00	3.00	2.78	0.89	0.42	0.81	0.255	0.120	0.85	0.32	0.150
MCD11	0.1	1.00	1.00	89.50	30.15	6.70	0.51	0.170	0.038	0.57	0.34	0.075
MCD12	0.2	2.00	2.00	18.00	6.59	2.58	0.68	0.250	0.098	0.75	0.37	0.144
MCD13	0.3	3.00	3.00	7.25	2.26	0.69	0.79	0.250	0.075	0.85	0.32	0.095
MCD14	0.4	4.00	4.00	3.74	1.31	0.52	0.83	0.290	0.116	0.88	0.35	0.140
MCD15	0.5	5.00	5.00	2.23	0.90	0.45	0.85	0.340	0.170	0.92	0.40	0.200
MCD16	0.6	6.00	6.00	1.48	0.67	0.18	0.87	0.384	0.105	0.93	0.45	0.120

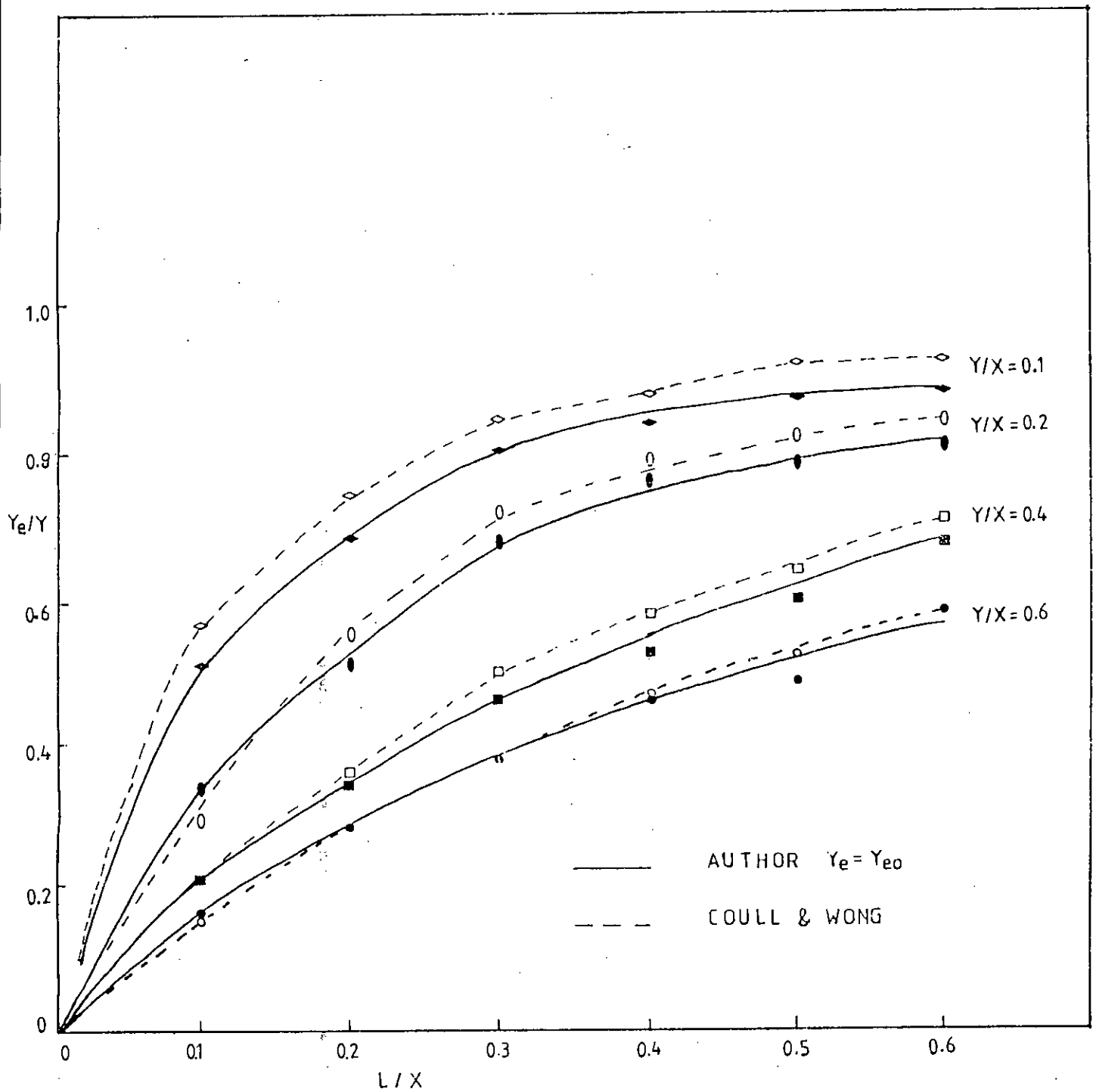


Fig. 5.35 : Comparative study of Effective width

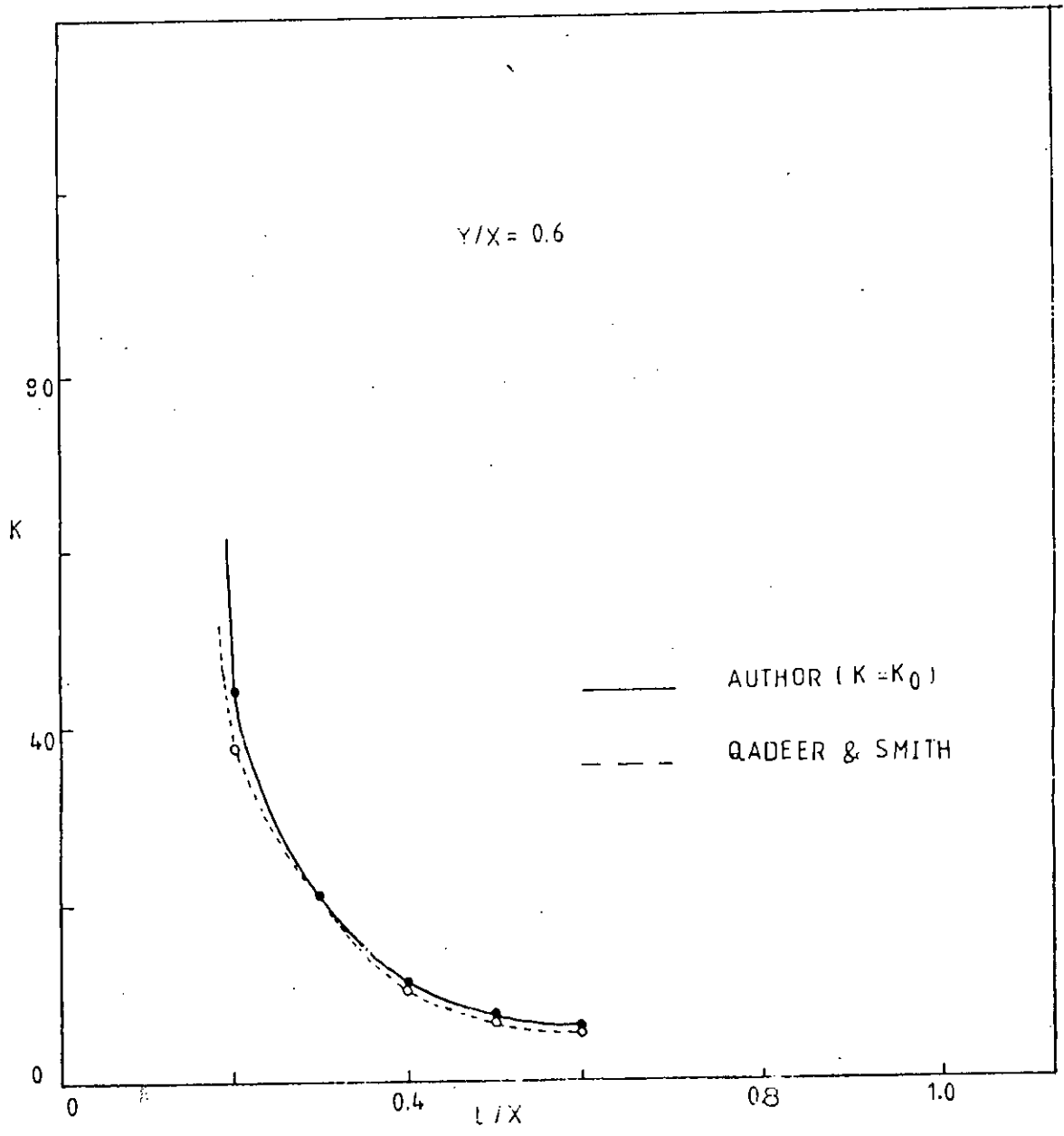


Fig. 5.36 : Comparison of Stiffness

TABLE 5.9

Parameters		K_0	K
Y/X	L/X	Author	Qadeer & Smith
	0.2	44.60	38.0
	0.3	21.00	21.5
0.6	0.4	12.56	10.6
	0.5	7.52	7.2
	0.6	6.05	5.4

Results from nonlinear analysis are 2 to 15% higher than those from Qadeer and Smith showing a good agreement.

b) Effective width as a function L/X

Figs. 5.37 shows the variation of Y_{e0}/Y , Y_{ecr}/Y and Y_{ep}/Y with L/X for different values of Y/X. Effective width gradually increases with the increase of L/X, but the rate of increase decreases as the value of L/X becomes larger. From the graphs, it can be said that the effective width of the slab gradually decreases with increase in load. The ratio of cracking to precracking effective width ranges between 0.25 to 0.45 and the ratio of postcracking to precracking effective width ranges between 0.08 to 0.22 for the models studied.

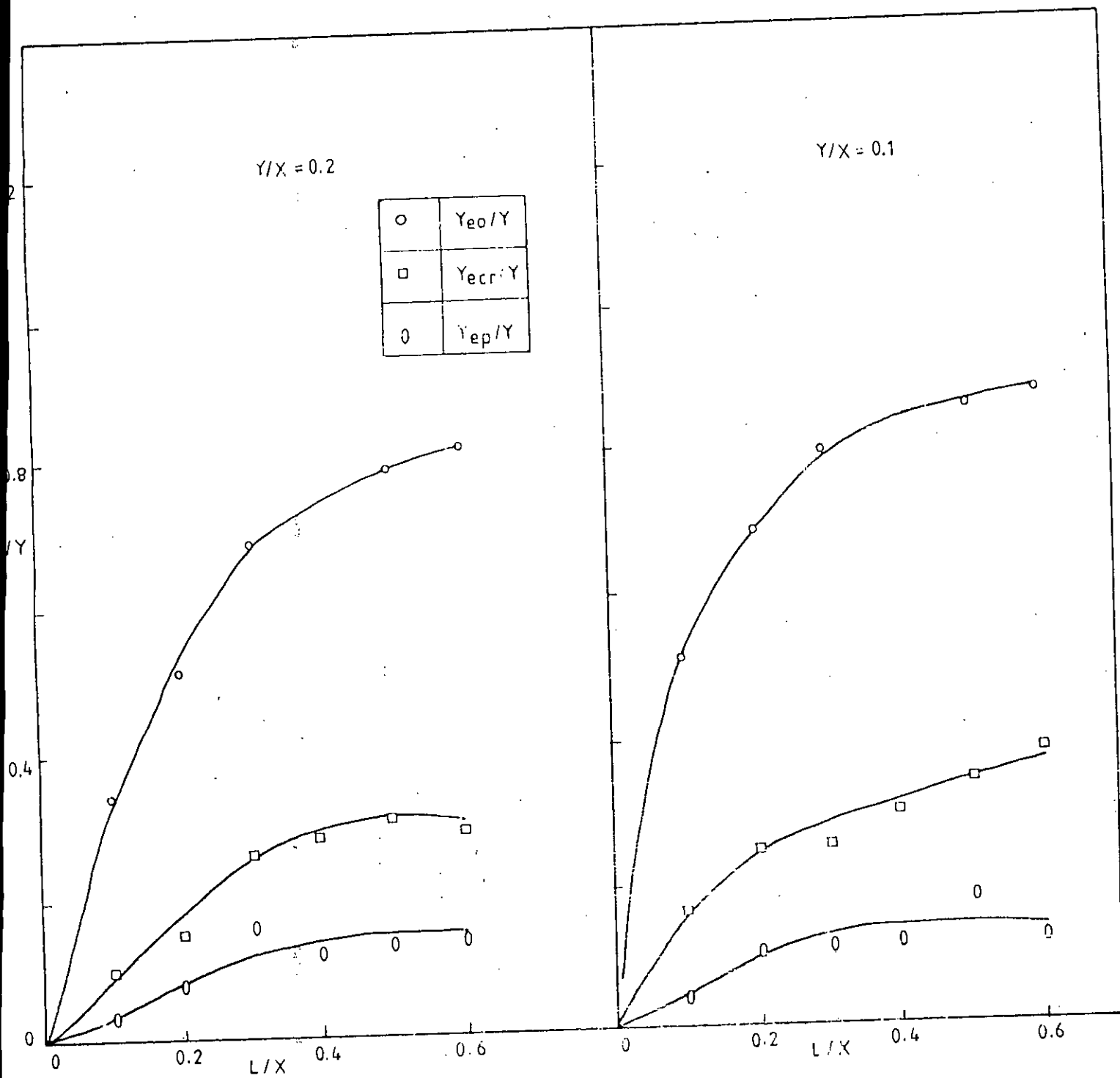


Fig. 5.37(a) : Effective width as a function of L/X

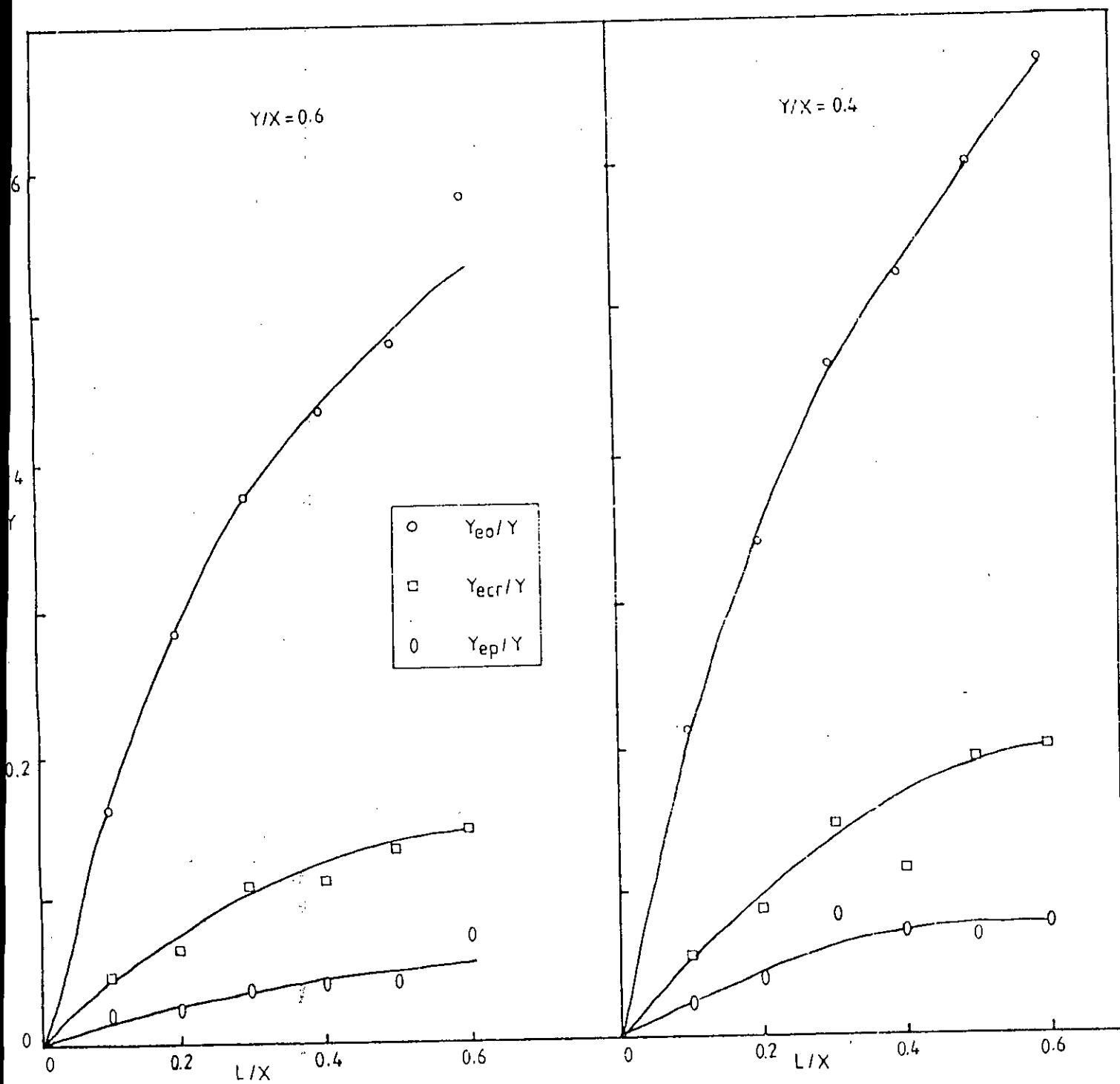


Fig. 5.37(b) : Effective width as a function of L/X

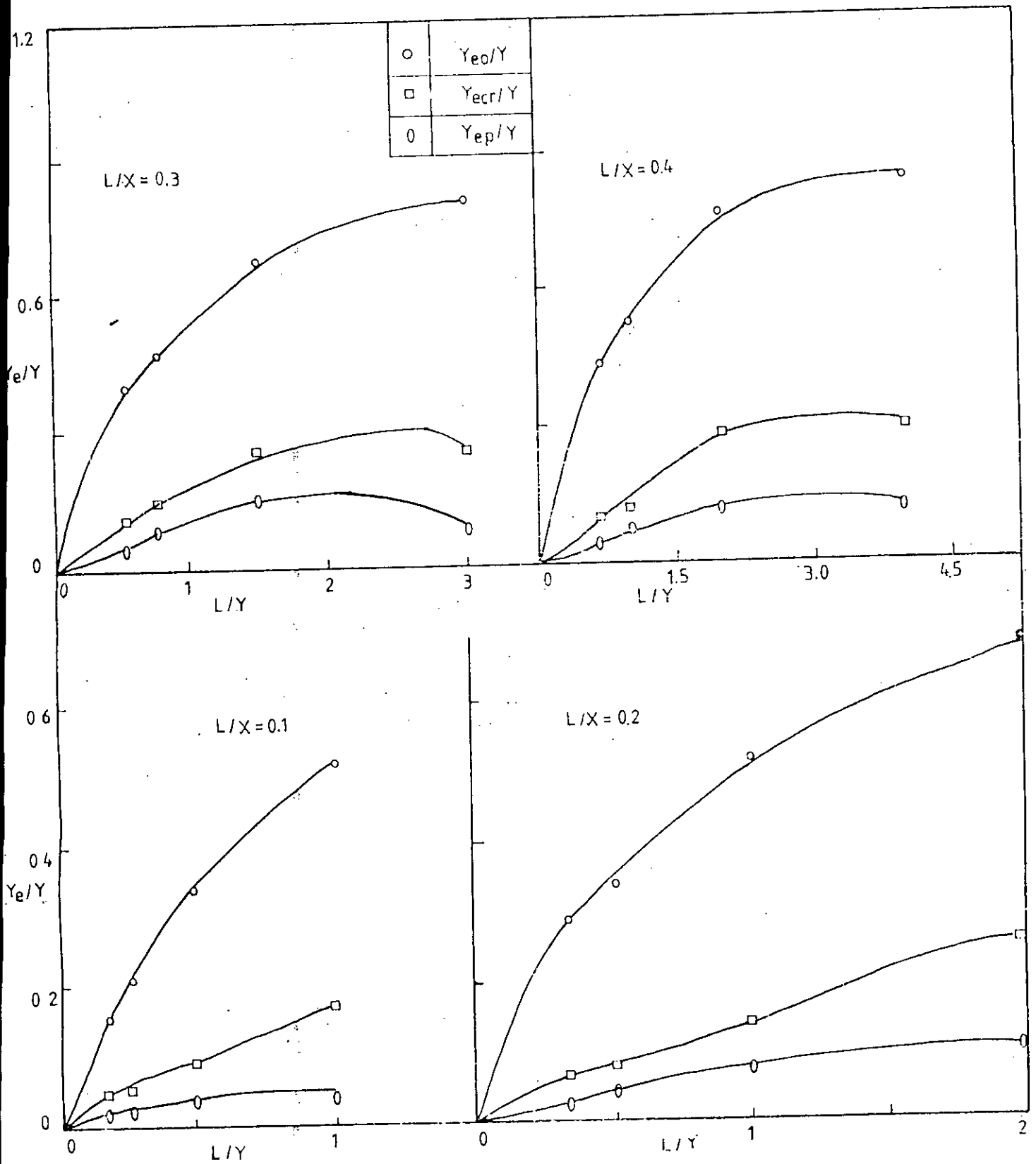


Fig. 5.38(a) : Effective width as a function of L/Y

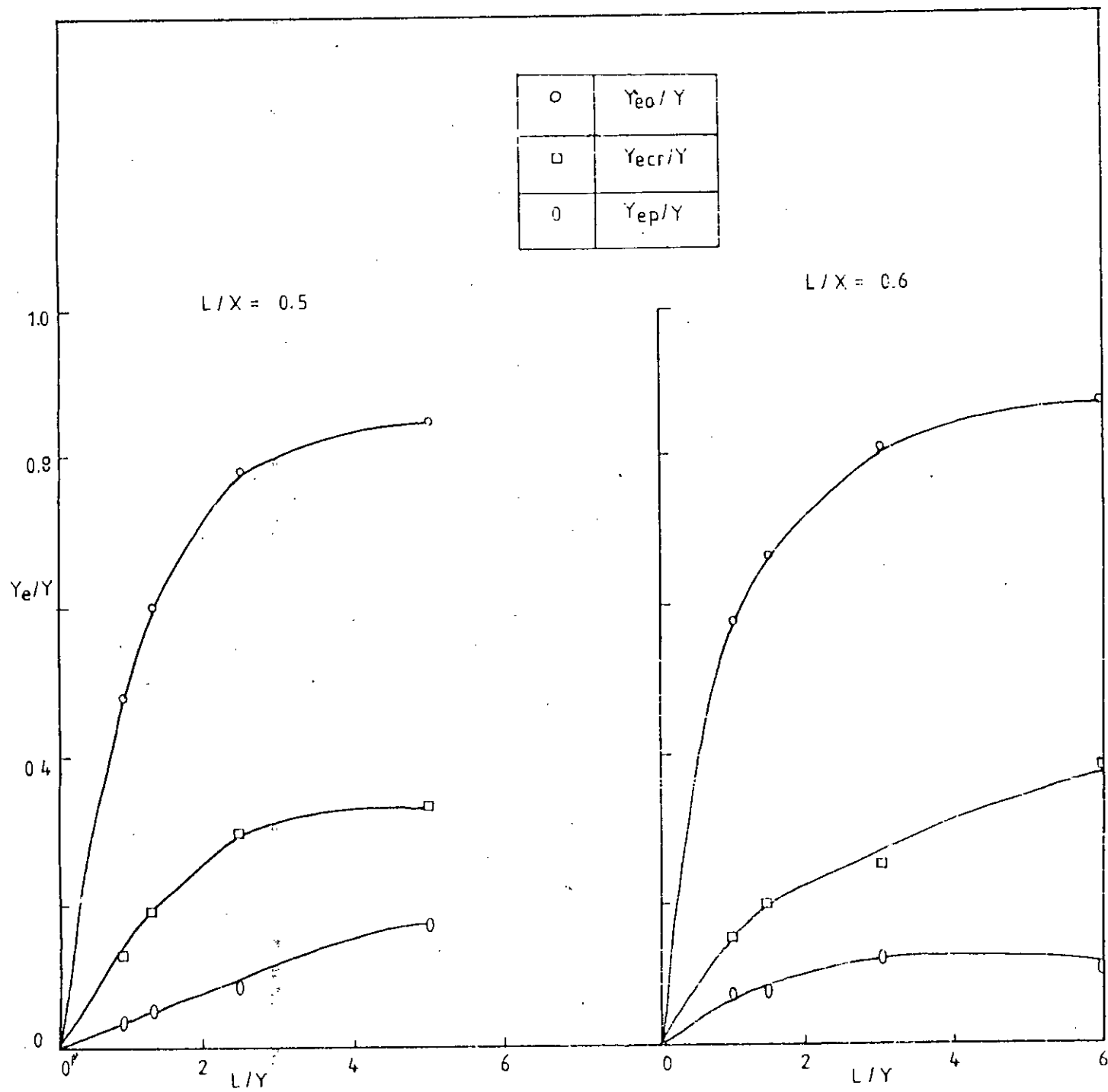
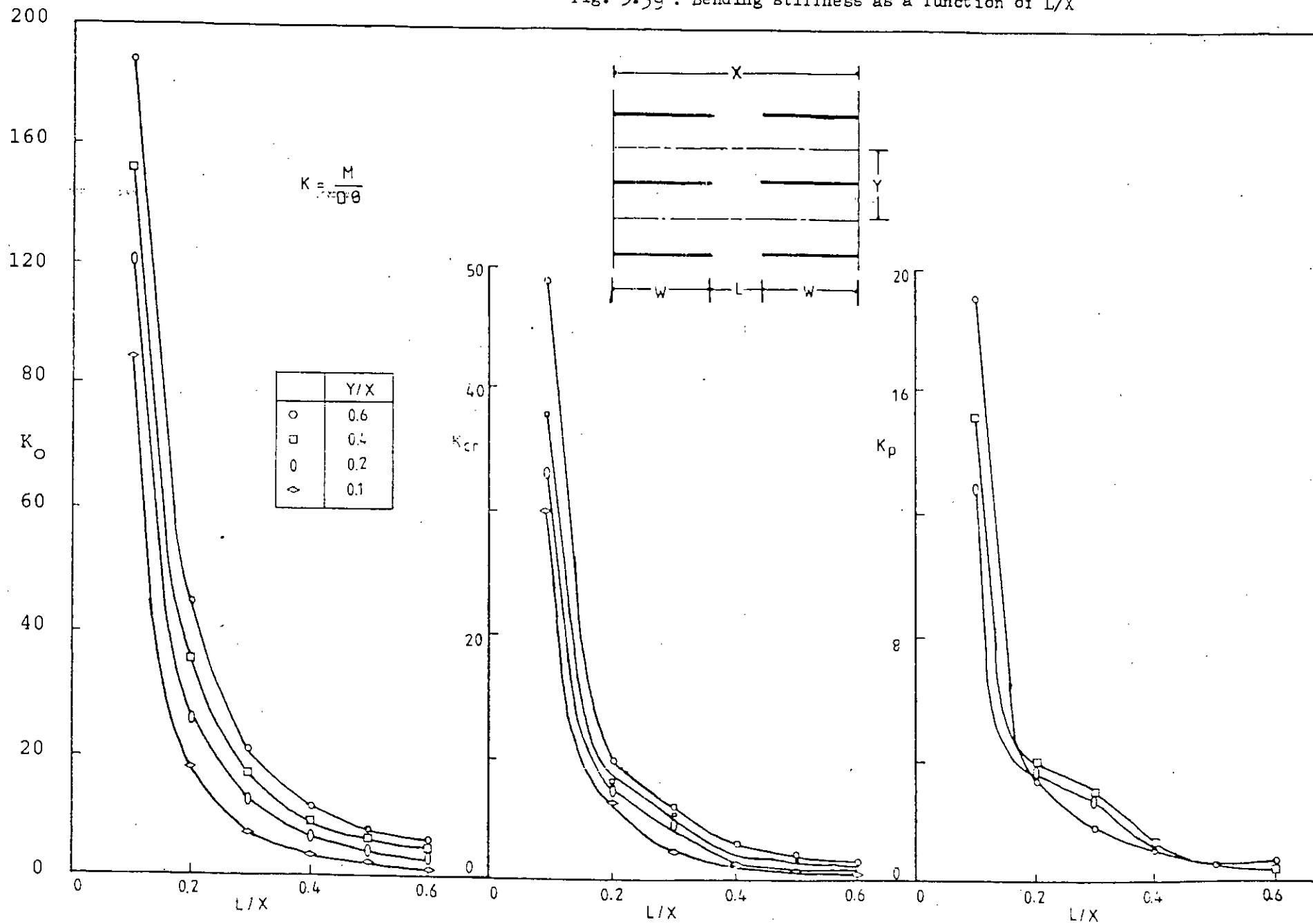


Fig. 5.38.b) : Effective width as a function of L/Y

Fig. 5.39 : Bending stiffness as a function of L/X



c) Effective width as a function L/Y

Figs. 5.38 show the variation of Y_{e0}/Y , Y_{ecr}/Y and Y_{ep}/Y with L/Y for different values Y/X . The graphs show that the effective width increases with the increase of L/Y .

d) Bending Stiffness as a Function L/X

Fig. 5.39 shows the variation of K_0 , K_{cr} and K_p with L/X for different values of Y/X . The graphs show that the stiffness decreases with increase of L/X and for a particular value of L/X stiffness increases with the increase of Y/X . Stiffness decreases as load increases. This is also evident from the Table 5.8, where the ratio of K_{cr} to K_0 and K_p to K_0 are evaluated. It can be inferred from the models analyzed that the ratio of cracking to precracking stiffness ranges between 0.25 to 0.45 and the ratio postcracking to precracking stiffness ranges between 0.08 to 0.22.

5.8.4 Analytical Interpretation of Nonlinear Results

Idealized M- θ curves presented previously approximate the behaviour of the slab. Flexural stiffnesses and effective widths derived from idealized curves were discussed with graphs in previous article. In this article, effort will be made to correlate the cracked moment M_{cr} and ultimate moment M_u derived from idealized curves with analytical results considering the slab as a beam of some effective width.

As discussed earlier, the transverse section passing through the interior edge of the shearwall is critical. It was evident from both crack diagrams and yielding diagrams. Analytical results will be derived on the basis of the capacity of this section.

a) Analytical determination of cracked moment.

Simple beam theory is used to determine the cracked moment of the slab section subjected to flexure. Fig. 5.40 clearly shows the procedure.

The following equation can be used to find cracked moment analytically.

$$f_r = M_{cra} \cdot c / I \quad (5.1)$$

where M_{cra} = Analytical cracked moment

$$c = t / 2$$

$$I = Y_{eo} \cdot t^3 / 12 + (n - 1) A_s \cdot d_1^2$$

Therefore for a particular value of modulus of rupture (f_r) M_{cra} can be found using equation 5.1.

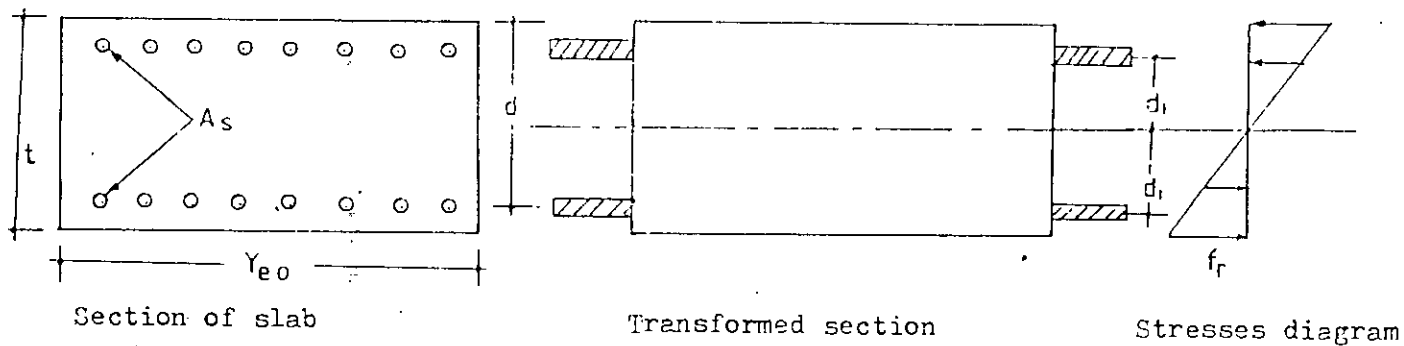


Fig. 5.40 : Determination of cracking moment

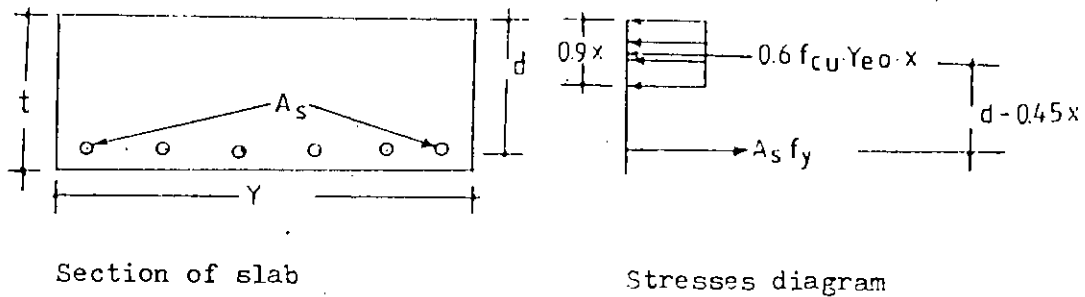


Fig. 5.41 : Determination of ultimate moment

b) Analytical determination of ultimate moment

Fig. 5.41 shows the stress diagram for determining the ultimate moment. According to diagram:

Y = Width of the section

d = Effective depth of tension reinforcement

f_{cu} = Cube crushing strength of concrete

f_y = Yield strength of steel

A_s = total area of tension reinforcement

x = Depth of concrete rectangular stress block

M_{ua} = ultimate moment of slab section having width Y .

The following equation can be written:

$$A_s \cdot f_y = 0.67 \cdot f_{cu} \cdot Y(0.9x) \quad (5.2)$$

$$\text{and } M_{ua} = A_s f_y (d - 0.45x) \quad (5.3)$$

Using equation 5.2, x can be found, then from equation 5.3. M_{ua} can be determined.

c) Relation between Analytical and Nonlinear Results

Table 5.10 presents the nonlinear and analytical results. In this study, effort will be made to correlate and establish relations between them. The basic idea in determining the behaviour of slab is that the slab acts as a wide coupling beam in resisting external loads. Simple beam theory was adopted in formulating the expressions (eqns. 2.5 & 2.6) to calculate the effective width of coupling beam. These equations are used to

TABLE 5.10

Model No.	Parameters		Results from Idealized M-θ Curves Moments in kn-m at section at the interior edge of the shear wall				Analytical Moments in kn-m			Ratios	
	Y/X	L/X	M _{cr}	M _y	M _u	M _{cr a}	M _{tr a}	M _{cr a} /M _{cr}	M _{tr a} /M _u		
MOD61		0.1	18.20	84.50	102.00	15.10	127.70	0.82	1.25		
MOD62		0.2	26.00	103.00	109.33	23.32	128.10	0.90	1.17		
MOD63	0.6	0.3	29.10	108.50	129.20	26.38	174.30	0.91	1.35		
MOD64		0.4	32.57	116.00	141.15	29.94	174.30	0.92	1.24		
MOD65		0.5	38.00	160.00	179.00	33.75	212.00	0.89	1.18		
MOD66		0.6	40.72	159.00	207.00	40.86	212.00	1.00	1.03		
MOD41		0.1	17.50	58.00	74.90	14.00	105.00	0.80	1.40		
MOD42		0.2	15.67	98.67	112.00	15.70	115.00	1.00	1.03		
MOD43	0.4	0.3	17.54	113.00	140.00	20.92	126.00	1.19	0.90		
MOD44		0.4	17.70	92.00	117.00	21.89	126.00	1.23	1.08		
MOD45		0.5	20.00	174.00	191.33	26.15	182.00	1.30	0.95		
MOD46		0.6	21.00	149.00	177.00	29.00	183.00	1.38	1.04		
MOD21		0.1	12.00	56.70	66.20	10.96	90.70	0.89	1.37		
MOD22		0.2	11.67	73.00	80.67	11.76	92.00	1.01	1.14		
MOD23	0.2	0.3	13.85	89.10	120.90	16.40	109.00	1.18	0.91		
MOD24		0.4	16.30	115.00	140.00	17.53	110.00	1.08	0.80		
MOD25		0.5	12.33	103.00	120.00	18.50	112.00	1.50	0.94		
MOD26		0.6	18.75	91.00	99.00	19.54	113.00	1.04	1.14		
MOD11		0.1	9.82	43.10	53.30	7.70	73.40	0.78	1.38		
MOD12		0.2	6.70	58.00	66.00	8.14	68.00	1.21	1.03		
MOD13	0.1	0.3	9.69	48.50	51.00	9.47	60.00	0.98	1.18		
MOD14		0.4	9.85	53.10	65.70	9.80	76.00	0.99	1.16		
MOD15		0.5	10.00	58.00	72.00	10.59	82.00	1.06	1.13		
MOD16		0.6	10.12	71.25	78.00	11.24	86.00	1.11	1.20		

calculate the effective width in precracking, cracking and postcracking stages of idealized curves. Using the precracking effective width as width of the slab and considering the slab as a beam, the cracked moment M_{crs} is calculated using equation 5.1

In this article M_{crs} are calculated for all the models and presented in the Table 5.10. It is found from the table that the ratio M_{crs}/M_{cr} for the models MOD61, MOD62, MOD63, MOD64, MOD65 and MOD66 ranges between 0.824 to 1.003, that is M_{cr} is slightly higher. For other models sometimes M_{cr} is larger and sometimes M_{crs} is larger. The maximum range lies between 0.80 to 1.30. But in most cases, the ratio are close to unity. M_{cr} may be taken as approximately equal to M_{crs} , as the deviation from unity is about 15%. Therefore, the concept of designing the slab as coupling beam of some effective width is supported from the investigation.

Considering the bay width Y of the slab as width of the beam, the ultimate moment M_{ua} is calculated for all the models. From the Table 5.10 the ratio. M_{ua}/M_u ranges between 0.90 to 1.40.

In most of the models M_{ua} is larger than M_u . So it may be concluded that the ultimate moment determined analytically are higher than the ultimate moment found from nonlinear analysis.

CHAPTER 6

CONCLUSIONS AND SUGGESTIONS FOR FURTHER STUDY

6.1 Conclusions

The behaviour of slabs in coupled shear wall structures has been investigated by finite element method considering nonlinear behaviour of reinforced concrete. A modified nonlinear 3-D finite element program is developed for analysis of coupled shear wall structures based on available finite element program. From the theoretical analysis, the following conclusions can be drawn:

i) For the models studied it may be concluded that Flexural stiffness of slab in precracking stage is not affected by the amount of reinforcement but stiffness in cracking stages are increased by 6% when reinforcements are 25% higher. Minimum reinforcement suggested by ACI Code should be provided to have normal behaviour of a reinforced concrete slab.

ii) The stiffness of slab gradually decreases with the increase of loads which is evident from the idealized $M-\theta$ curves. It is concluded from the study that the ratio of the cracking to precracking stiffness ranges between 0.25 and 0.45 and the ratio of post cracking to precracking stiffness ranges between 0.08 and 0.22 for the models studied.

iii) Precracking effective width Y_e from nonlinear analysis is found to be in good agreement with those from linear analysis as the variation ranges between 1.0% and 8%. Also precracking stiffness K_e from nonlinear analysis are only 2 to 15% higher than those from linear analysis showing good agreement. Therefore, the values of Y_e and K_e from nonlinear analysis can be used in working strength design.

iv) Effective width of the slab gradually decreases with increase in load similar to the stiffness of slabs. Therefore the values

of $Y_{e,cr}$ and $Y_{e,p}$ presented in this study can be used by designers using ultimate strength design. Values of stiffness in the post-cracking range may be used in the collapse load analysis of the structures.

v) It is concluded that the transverse section passing through the interior edge of the shear wall is critical for model failure which is evident from the cracking and yielding diagrams discussed in this study.

vi) Cracking moments determined analytically are found to be in agreement with those found from nonlinear analysis as the ratios of the two moments in most of the models are close to unity. Ultimate moments determined analytically are higher than those from nonlinear analysis.

6.2 Suggestions for Further Study

More investigations should be done with various types of shearwalls as in this study only planar shear wall was used.

To verify the results experimental investigations should be made.

Investigations can be done with multiple bands of opening in the shearwall as in this study only one band of opening was studied.

This program can be modified to study the behaviour of slab in coupled shearwall structures under reverse cyclic loading.

This program can also be modified to account for the provision of closing and opening of cracks in reinforced concrete during loading history.

REFERENCES

1. Rosman, R., 'Approximate Analysis of Shear Walls Subjected to Lateral Loads', Journal of the ACI , proceedings, Vol. 61, No.6, June 1964, pp. 717-754.
2. Barnard, P.R., 'Interaction of Shearwalls Connected Solely through Slabs', Proceedings, Symposium on tall buildings , Pergamon press , Newyork, 1967, pp. 157-173.
3. Choudhury, J.R. Discussions, Ref. 2.
4. Qadeer, A., Discussions, Ref.2.
5. Michael, D. Discussions, Ref. 2.
6. Choudhury, J.R. 'Analysis of plane and spatial systems of Interconnected Shear walls " , Ph.D. Thesis, University of Southampton, 1968.
7. Qadeer, A., 'The bending Stiffness of Slabs connecting Smith, B. S. Shearwalls", Title no.66-37, Journal of the ACI, June-1969, pp.464-473.
8. Michael, D. Discussions, ACI Journal No.12, Proc.Vol.66, December, 1969.
9. Coull, A. Discussions, Ref. 2.
10. Tso, W.K., 'Effective Width of Coupling Slabs Mahmoud, M.A. in Shear Wall Buildings, Journal Struct. Div. Am. Soc. Civ. Engrs., 1977, 103, ST3, March, 573-586.

11. Huq, M.M. 'Flexural Stiffness of Floor slabs in Shear Wall Structures', M.Sc. Thesis, BUET, 1974.
12. Coull, A., Wong, Y.C. 'Bending Stiffness of Floor Slabs in Cross-Wall Structures", Proc. Instn. Civil, Engrs, Vol.71, Part-2, London, March 1981.
13. Kotsovos, M.D., Newman, J.B. 'A Mathematical Description of the the Deformational Behaviour of Concrete Under Complex Loadings', Magazine of Concrete Research, Vol.31, No.107, June, 1979, pp.77-90.
14. Kotsovos, M.D., 'A Mathematical Description of the Strength Properties of Concrete under Jeneralised Stress", Magazine of Concrete Research, Vol. 31, No.108, September, 1979, pp. 151-158.
15. Kotsovos, M.D., Newman, J. B. 'Behaviour of Concrete Under Multiaxial Stress', Journal of the ACI, September, 1977, pp.443-446.
16. Kotsovos, M.D. 'Concrete. A Brittle Fracturing Material' Materials and Structures, RILEM, Vol.17, No.98, pp. 107-115, 1984.
17. Elnounu, G.F.R. 'Design of Shear Wall floor Slab Connections', Ph.D. Thesis, University of Glasgow, 1985.
18. Bari, M.S. 'Design of Shear Wall Floor Slab Connections Using Shear Reinforcement', Ph.D. thesis, University of Glasgow, 1987.

19. Kabir, A. 'Nonlinear Analysis of Reinforced Concrete Structural Slabs', Ph.D. thesis, University of Strathclyde, Glasgow, U.K., March, 1986.
20. Wood, R.H. 'The Reinforcement of Slabs in Accordance with Pre-determined Field of Moments', Concrete, Feb, 1968, pp. 69-76.
21. Armar, G.S.T. 'Correspondence on 'The Reinforcement of Slabs in Accordance with a Pre-Determined Field of Moments, Concrete, Aug. 1968, pp. 319-320.
22. Zeinkiewicz, O.C. 'The Finite Element Method' , McGraw Hill, 3rd Edition, 1977.
23. Owen, D. R.J., Hinton, E., 'Finite Element in Plasticity - Theory and Practice" . Pineridge press , Swansea , 1980.
24. Irons , B.M., 'A Frontal Solution Program for Finite Element Analysis " , International Journal for Numerical Methods in Engineering, vol.2, , 1970 , pp-5-32.
25. Hinton , E. , Owen, D.R.J. 'Finite Element Programming " Academic Press, 1977.

APPENDIX

Investigation on Boundary Conditions

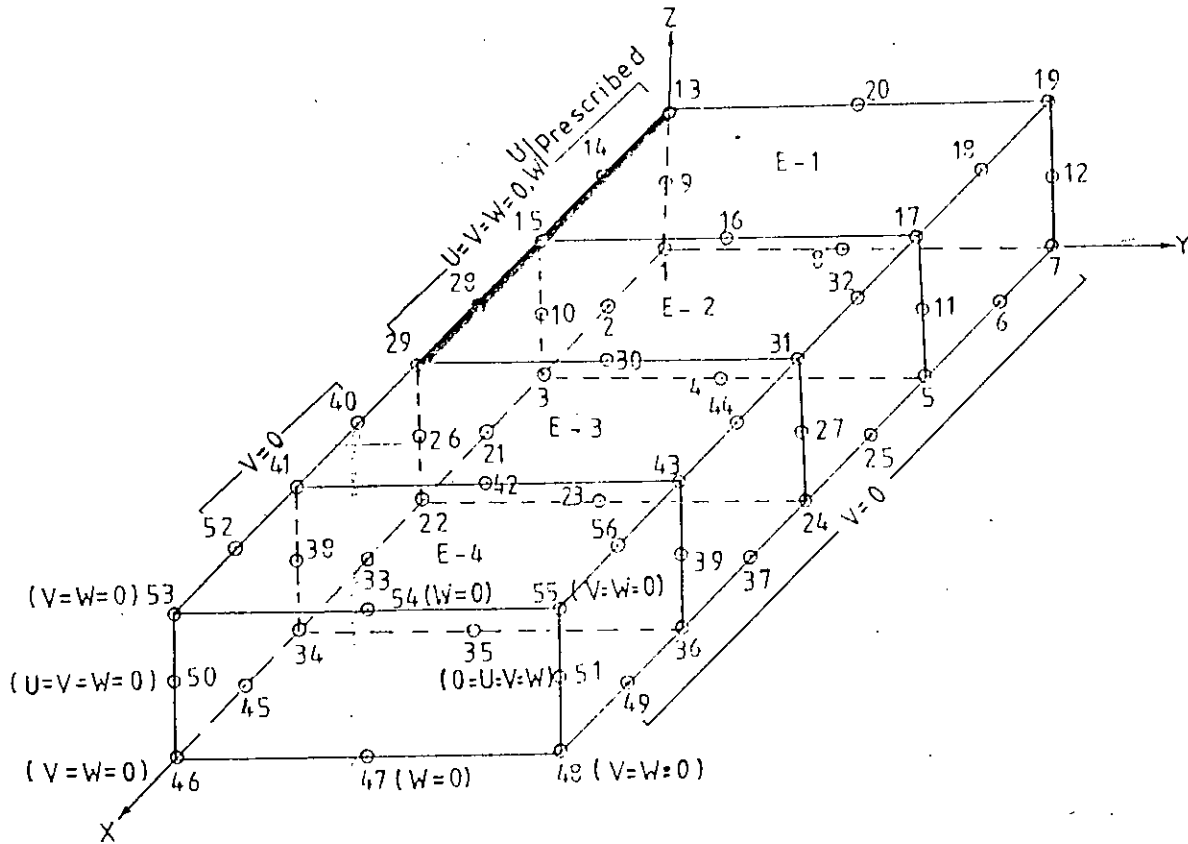
Investigation on Boundary Condition I (Case I) :

Fig. 1(a) shows the 4 element mesh with node numbering. Boundary conditions are shown on the figure. Prescribed displacements were imposed at the nodes on the shear wall forcing the shear wall to rotate as shown in the Fig. 1(b). Midlayer nodes (9,10,26) were prescribed with only z-displacement(w) so that they remained in the vertical plane v-v. Top layer nodes (13,14,15,28,29) and bottom layer nodes (1,2,3,21,22) were prescribed with x and z displacements (u,w) so that the line ab could be forced to rotate with the same angle (θ) as the shear wall. X-displacement were equal to $\theta.t/2$ where t was the thickness of the slab.

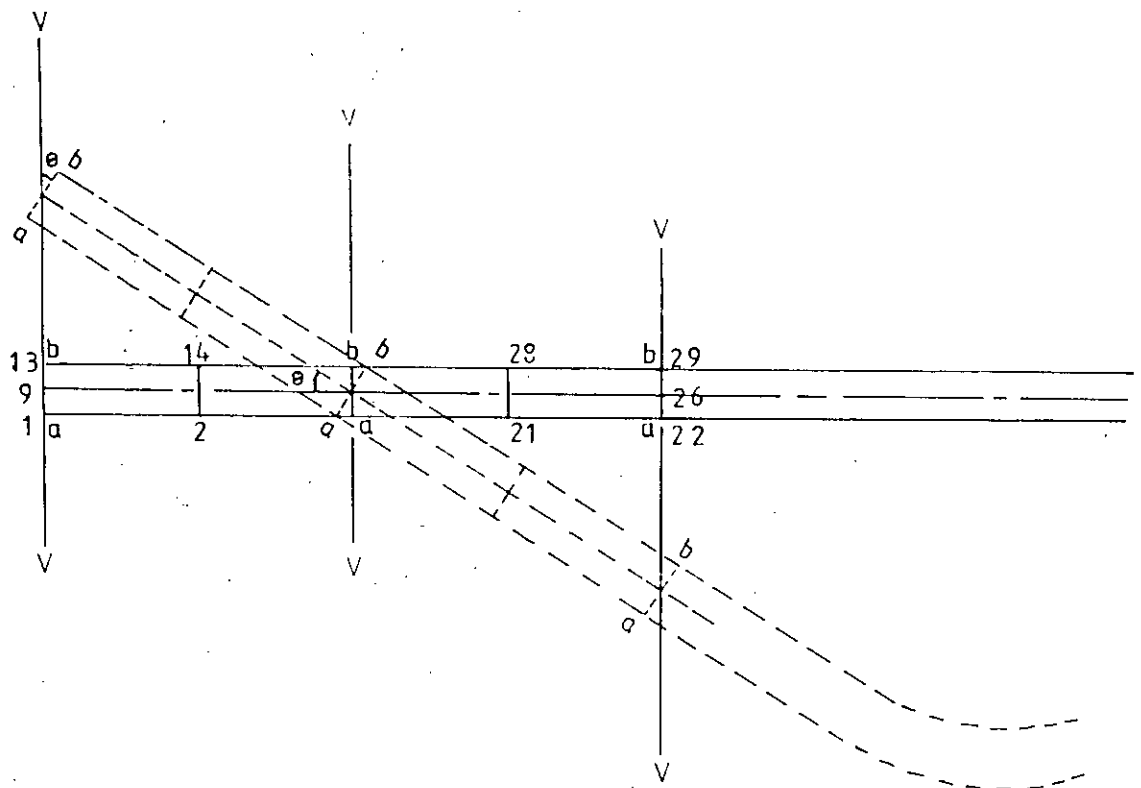
Model TMOD1 was studied with this boundary condition. For a particular rotation θ (0.4/3000) radian, the z-displacements produced in the slab nodes are shown in Table 1. The deflected shape of the slab is shown in Fig. 1(c) with resultant z-forces at the restrained nodes. But downward resultant z-forces at nodes (2,14) and upward resultant z-forces at nodes (21,28) were in opposite direction to those of prescribed displacements at these nodes. This was considered to be a unusual behaviour, so to had the answer. Model TMOD1 was investigated with boundary condition II.

Investigation on Boundary Condition II (Case II) :

Fig. 2(a) shows the 4 element mesh with node, numbering. Boundary conditions were applied only on nodes at middle layer (Fig.2(b)) whereas nodes at top and bottom layers were allowed



(a) Finite element mesh with boundary condition



(b) Slab deformation

Fig. 1 : Boundary Condition I (CASE I)

TABLE I

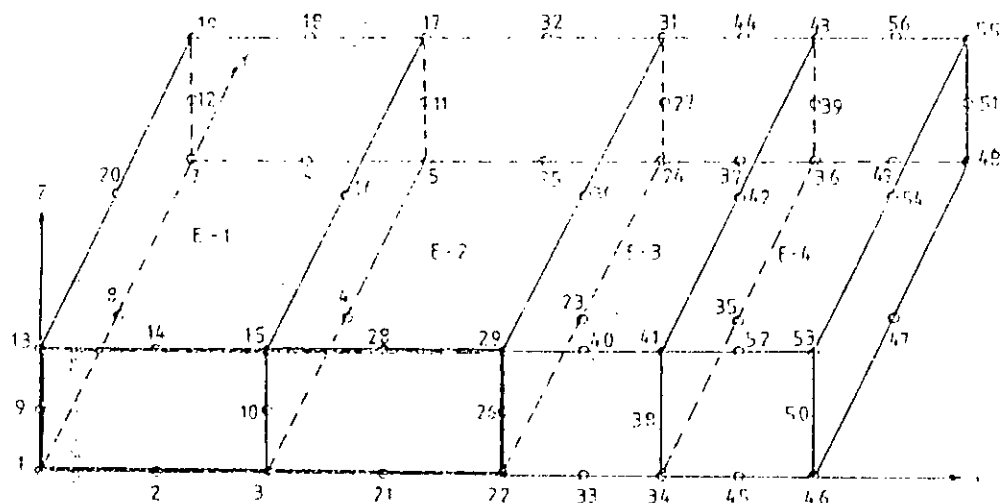
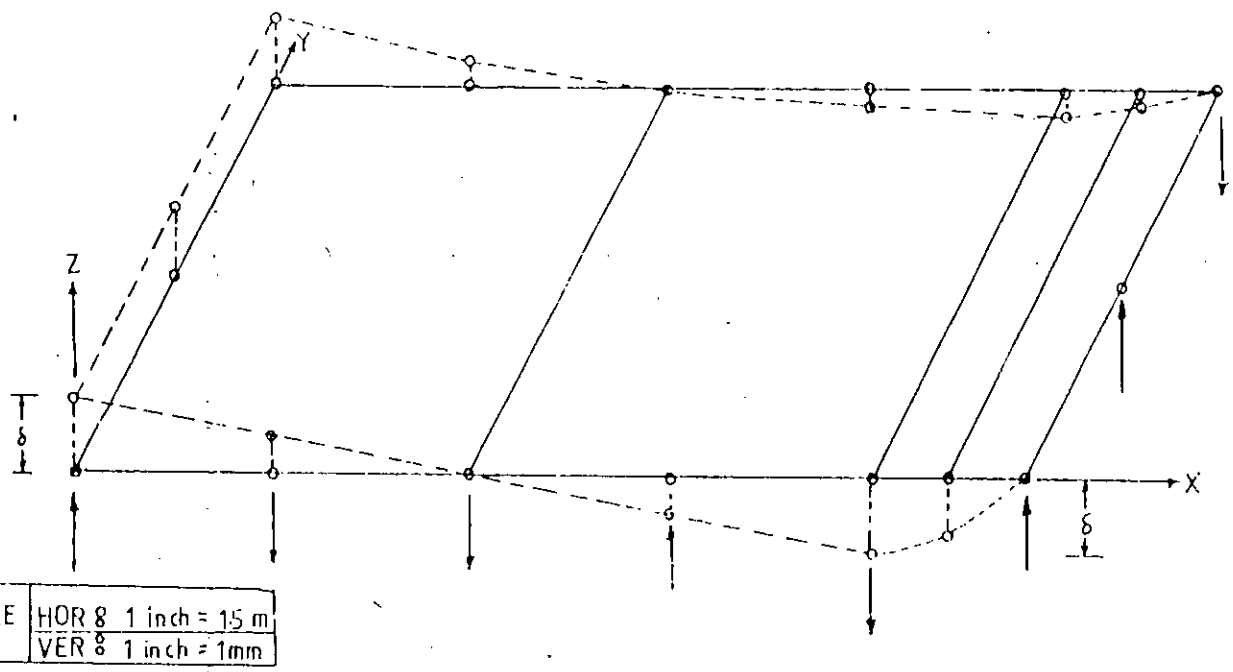
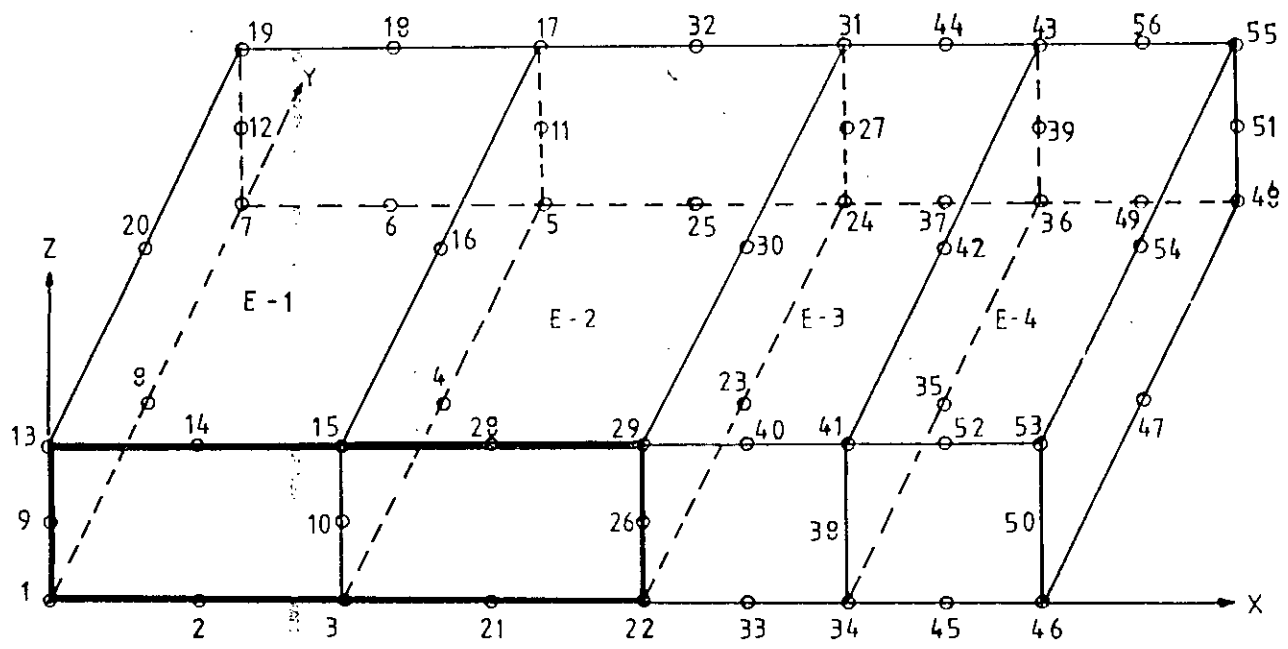


Table for comparative study

Rotation(θ) = 0.4/3000 radian

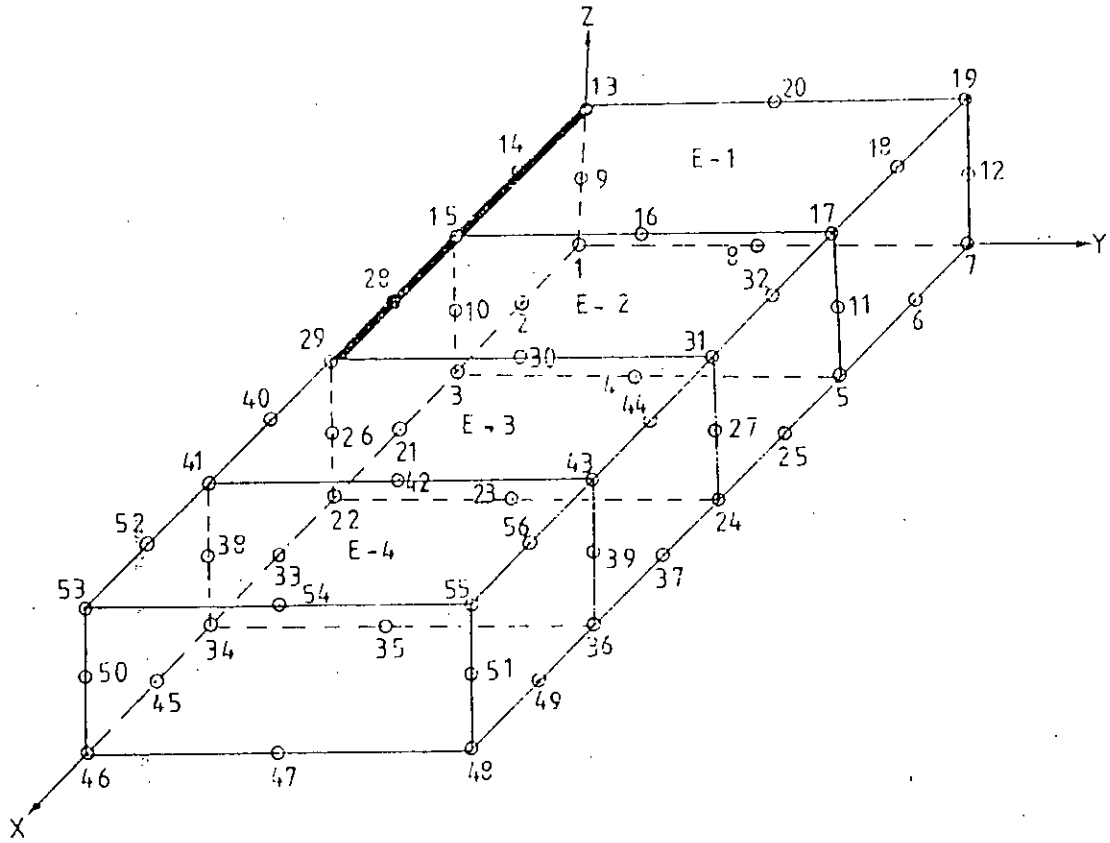
CASE I				CASE II			
Node no.	z-disp. in mm.	Node no.	z-disp. in mm.	Node no.	z-disp. in mm.	Node no.	z-disp. in mm.
1	0.400*	24	-0.110	1	0.399	24	-0.254
2	0.200*	26	-0.400*	2	0.200	26	-0.400*
3	0.000*	27	-0.110	3	-0.007	27	-0.254
5	-0.016	28	-0.200*	5	-0.046	28	-0.273
6	0.113	29	-0.400*	6	0.130	29	-0.400
7	0.350	31	-0.110	7	0.340	31	-0.254
8	0.375	34	-0.290	8	0.386	34	-0.302
9	0.400	36	-0.0524	9	0.400*	36	-0.215
10	0.000	38	-0.290	10	0.000*	38	-0.302
11	-0.016	39	-0.0524	11	-0.035	39	-0.215
12	0.350	41	-0.290	12	0.340	41	-0.302
13	0.400*	43	-0.0524	13	0.401	43	-0.215
14	0.200*	46	0.000*	14	0.202	46	0.002
15	0.000*	47	0.000*	15	0.007	47	-0.294
17	-0.016	48	0.000*	17	0.032	48	0.0026
18	0.113	50	0.000*	18	0.160	50	0.000*
19	0.350	51	0.000*	19	0.340	51	0.000*
20	0.375	53	0.000*	20	0.386	53	0.001
21	-0.200*	54	0.000*	21	-0.273	54	-0.294
22	-0.400*	55	0.000*	22	-0.400	55	0.0013

* Prescribed displacement

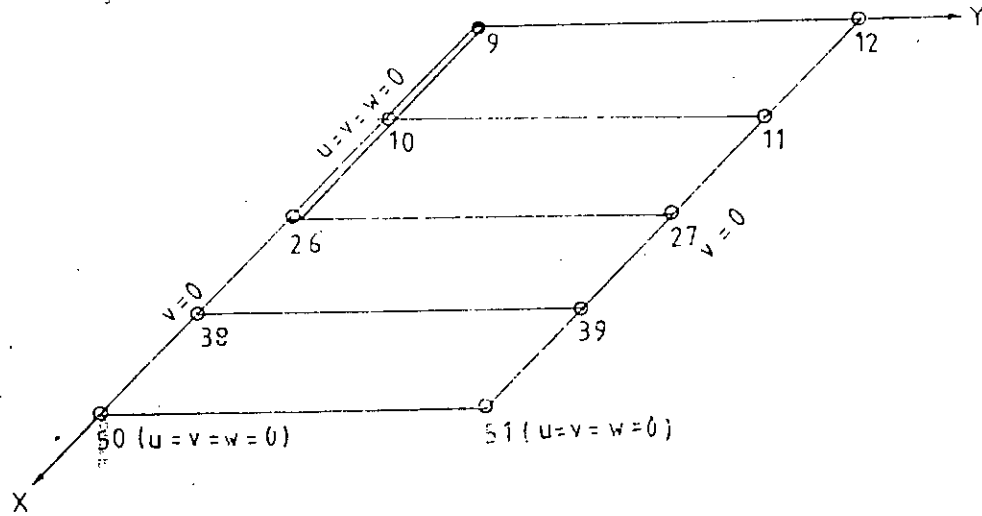


(c) Deflected shape for Case I

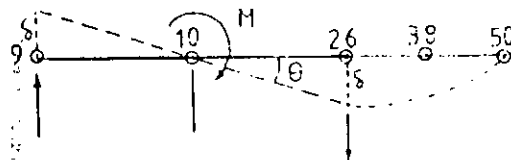
Fig. 1 : Investigation on Case I



(a) Mesh with Node Numbering



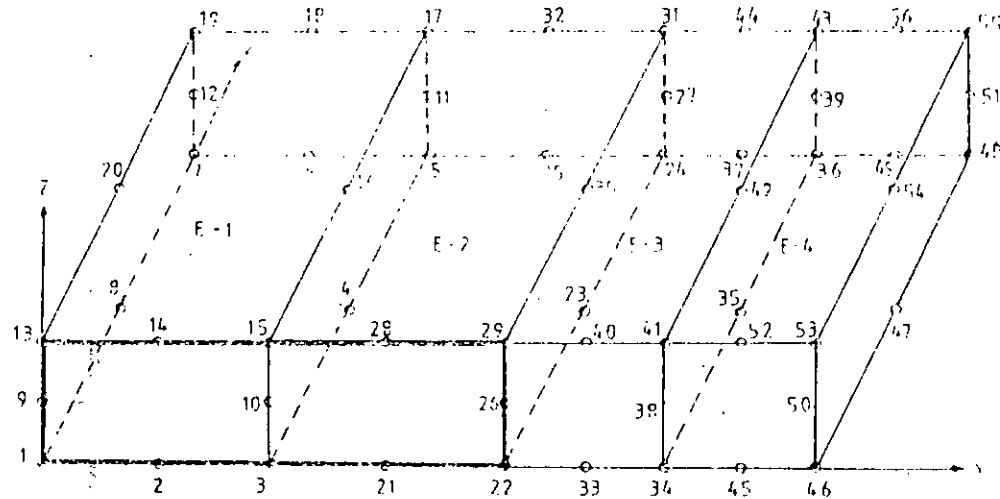
(b) Midlayer showing nodes with boundary conditions



(c) Slab deformation due to wall rotation

Fig. 2 : Investigation on Case II

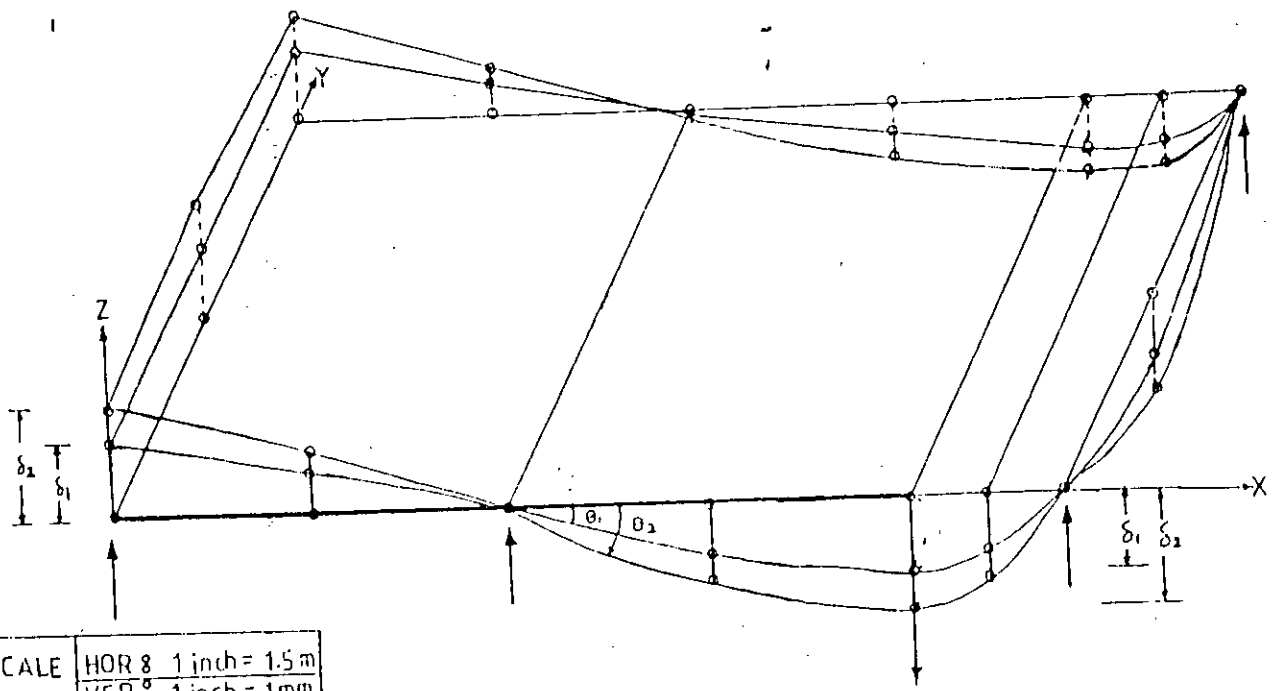
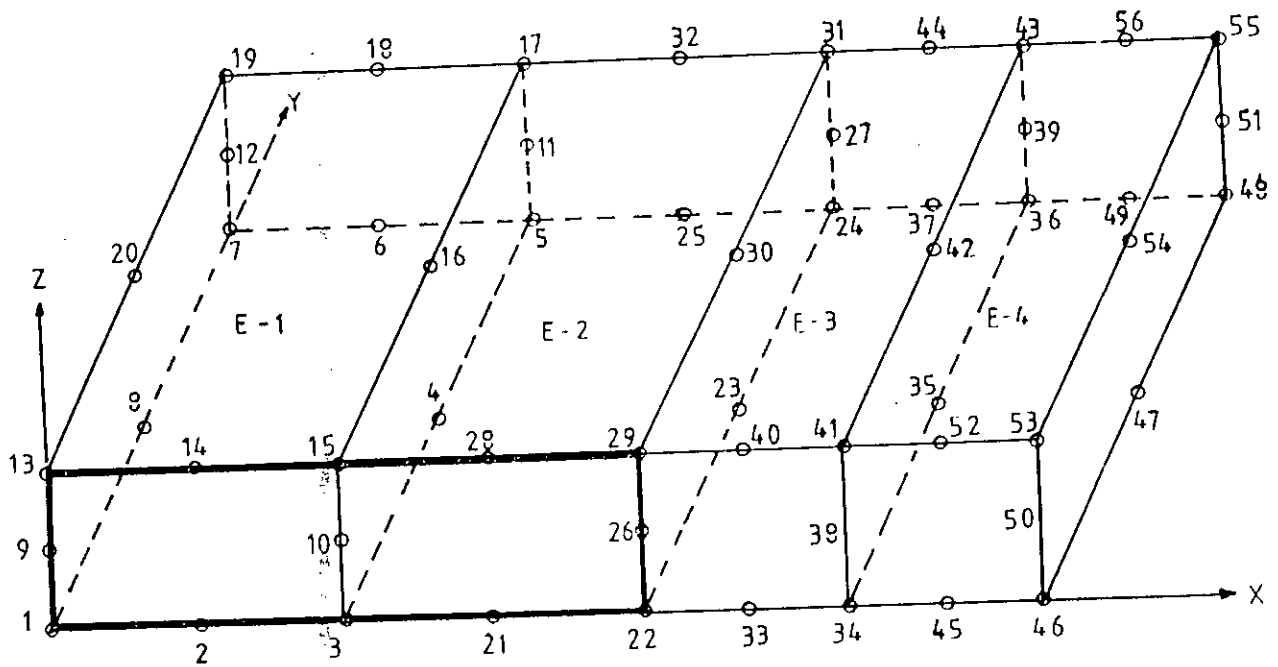
TABLE 2



Nodal z-displacements for CASE II

Rotation(θ_2) = 0.6/3000 radian				Rotation (θ_1)=0.4/3000 radian			
Node no.	z-disp. in mm.	Node no.	z-disp. in mm.	Node no.	z-disp. in mm.	Node no.	z-disp. in mm.
1	0.598	24	-0.379	1	0.399	24	-0.254
2	0.300*	26	-0.600*	2	0.200	26	-0.400*
3	0.009	27	-0.379	3	-0.007	27	-0.254
5	-0.038	28	-0.038	5	-0.046	28	-0.273
6	0.195	29	-0.600	6	0.130	29	-0.400
7	0.530	31	-0.379	7	0.340	31	-0.254
8	0.580	34	-0.452	8	0.386	34	-0.302
9	0.600*	36	-0.215	9	0.400*	36	-0.215
10	0.000*	38	-0.452	10	0.000*	38	-0.302
11	-0.046	39	-0.215	11	-0.035	39	-0.215
12	0.530	41	-0.452	12	0.340	41	-0.302
13	0.602	43	-0.320	13	0.401	43	-0.215
14	0.304	46	0.003	14	0.202	46	0.002
15	0.009	47	-0.440	15	0.007	47	-0.294
17	-0.050	48	0.000	17	0.032	48	0.0026
18	0.240	50	0.000*	18	0.160	50	0.000*
19	0.530	51	0.000*	19	0.340	51	0.000*
20	0.580	53	0.003	20	0.386	53	0.001
21	-0.409	54	0.440	21	-0.273	54	-0.294
22	-0.600	55	0.000	22	-0.400	55	0.0013

* Prescribed displacements



SCALE	HOR 8 1 inch = 1.5 m
	VER 8 1 inch = 1 mm

(d) Deflected Shape of Model TMOD1

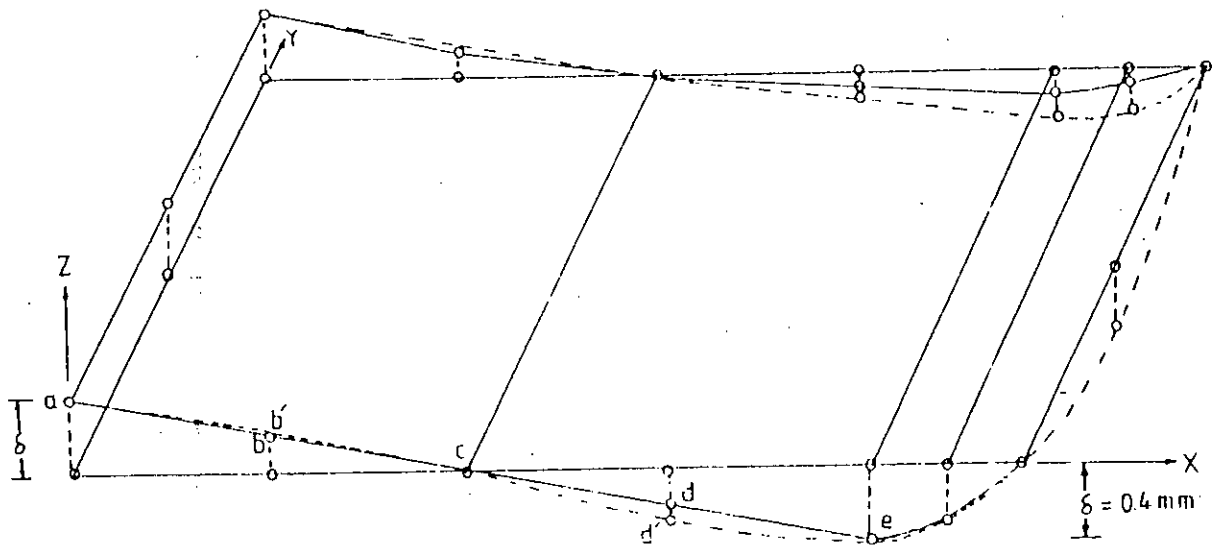
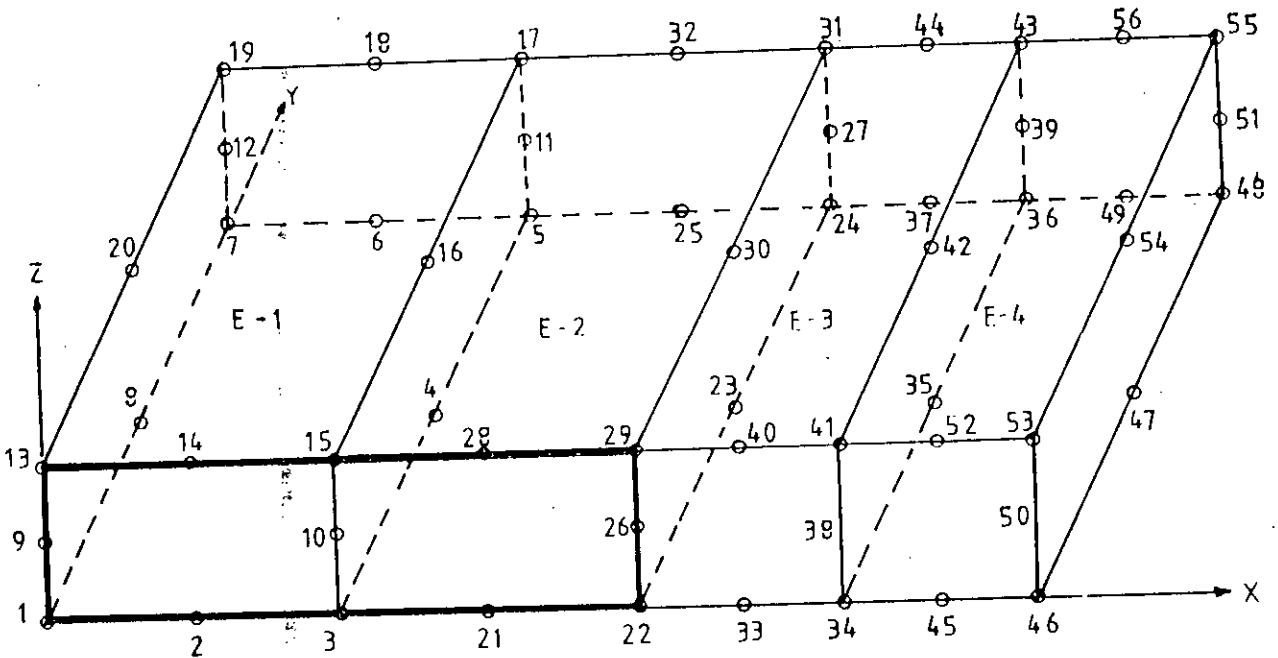
Fig. 2 : Investigation on Case II

to move freely. Equal and opposite z-displacements were prescribed at wall nodes 9 and 26 to produce rotation θ of wall as shown in Fig. 2(c).

Model TMOD1 was studied with this boundary condition. Table 2 shows the z-displacements at nodes of the slab for rotations (θ) (0.4/3000) and (0.6/3000) radian. The deflected shape of the slab is shown in Fig. 2(d) with resultant z-forces at the restrained nodes 9, 10 and 26.

Comparative Study of Deflected Shapes of Model TMOD1 :

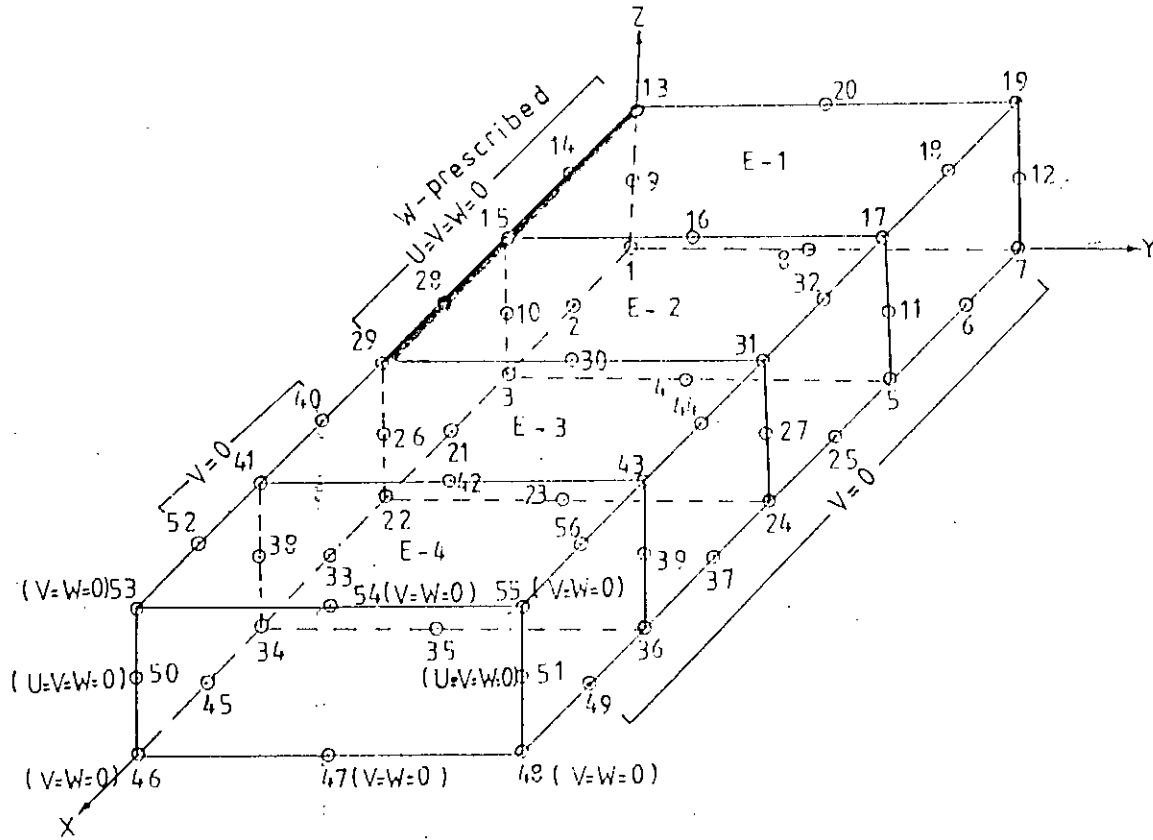
Table 1 compares the z-displacements of two cases due to a particular rotation (0.4/3000) radian of the wall. Deflected shapes of Model TMOD1 from two different boundary conditions are superimposed on each other for a particular rotation (0.4/3000) radian in Fig. 2(e) for comparison. In boundary condition I, shear wall was forced to remain straight line as shown by straight line abcde. But when shear wall was allowed to behave freely as in boundary condition II, the deflected shape of the shear wall assumed the curved dashed line ab'cd'e. Curve ab'c was convex upward and curve cd'e was convex downward. Therefore, in boundary condition I, the points b' and d' were forced to remain at points b and d respectively. For this reason a downward resultant z-force at nodes (b) and upward resultant z-force at nodes (d) were found. Convexity of curve cd'e was increased more rapidly than that of curve ab'c as rotation θ was increased which is evident from Fig. 2(d).



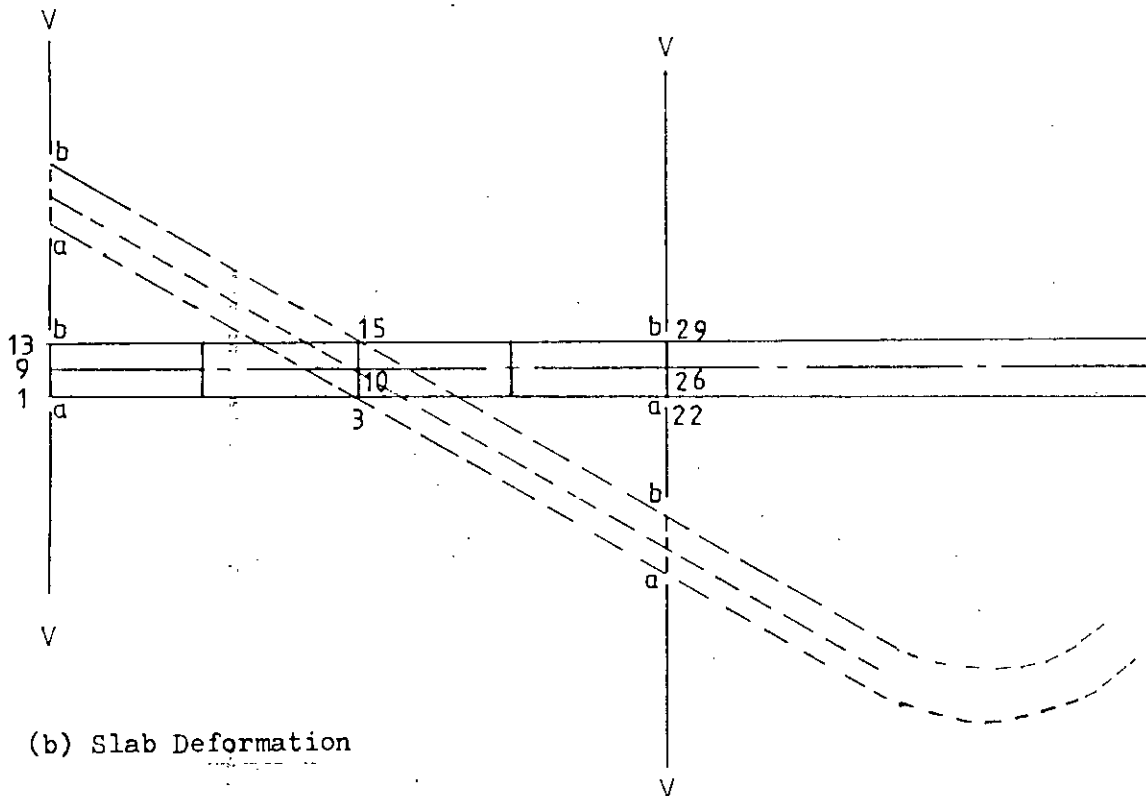
SCALE HOR 8 : 1 inch = 15m
VER 8 : 1 inch = 1mm

— case 1
- - - case a

Fig. 2 (e) : Comparative study of deflected shapes of model TMOD1



(a) Mesh with Boundary Conditions



(b) Slab Deformation

Fig. 3 : Investigation on Case III

Investigation on Boundary Condition III (Case III) :

Fig. 3(a) shows the 4 element mesh with node numbering. Boundary conditions are shown on the Fig. In this condition, the shear wall was forced to rotate in such a way that the line ab was always remained on same vertical line v-v as in Fig. 3(b). That is , rotation of line ab was not allowed. Only z-displacements were prescribed at nodes on shear wall. Resultant z-forces at the restrained nodes had the same directions as in boundary condition I.

Discussion on three Cases of Boundary Conditions :

Boundary condition II gives more flexibility in the behaviour of slab. It reduces the rigidity of the shearwall and does not maintain the continuity at the line of symmetry. Therefore, it does not maintain condition discussed in article 2.3 to determine the flexural stiffness.

Boundary condition III gives a more rigid structure as nodes on the shear wall remain in the same vertical line throughout the entire loading. This may produce lengthening of the shear wall which is evident from Fig. 3(b).

Boundary Condition I, maintains the rigidity of the slab as well as allows the rotation of the vertical nodal lines. It also maintains the continuity of the slab at line of symmetry. Before conducting the main investigations with this boundary condition, several models were studied with boundary condition III and I for a comparative study.

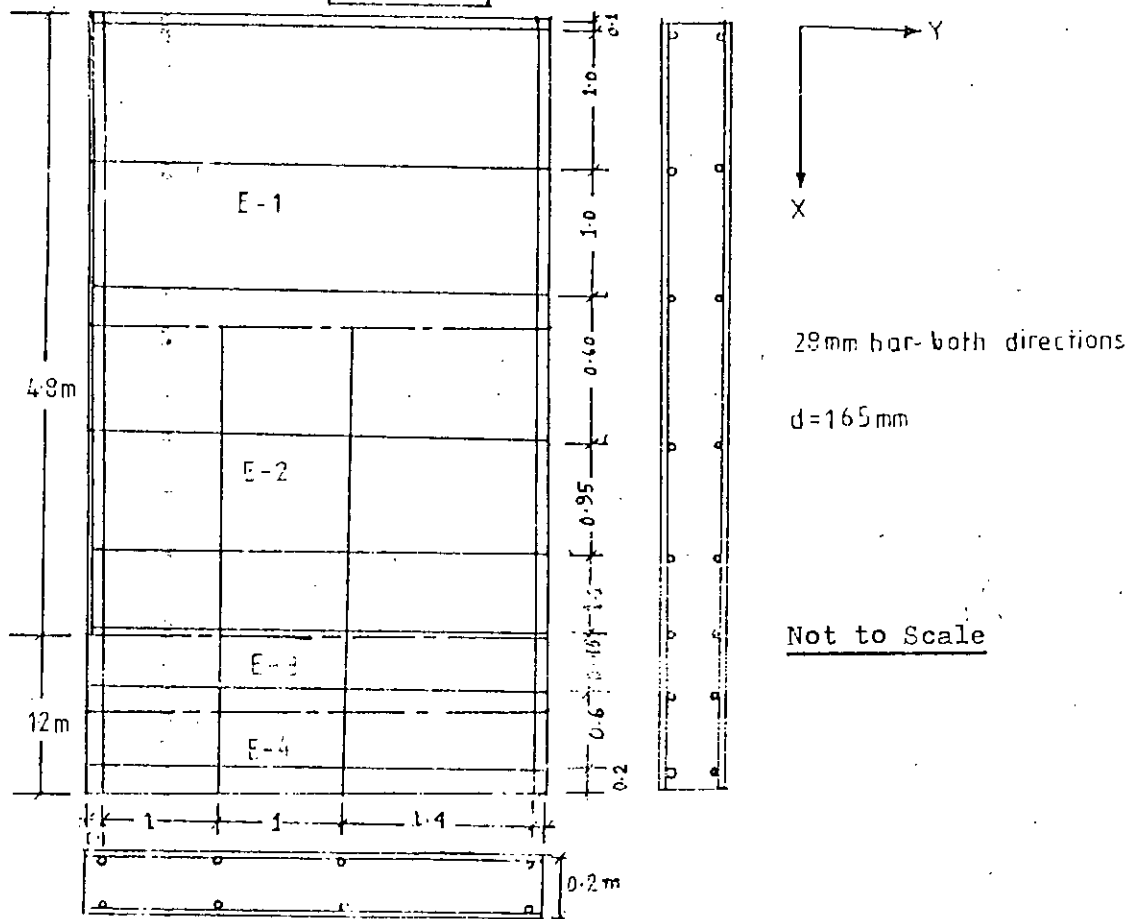
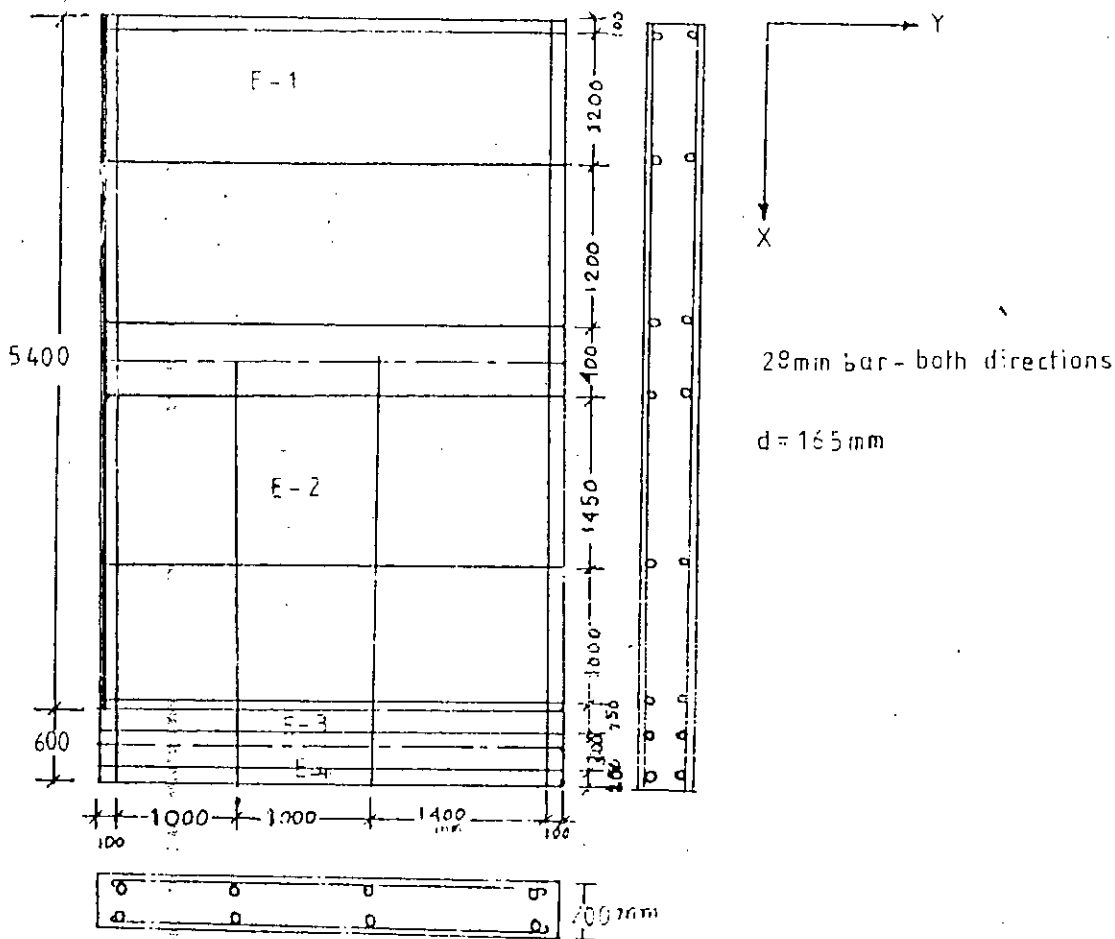
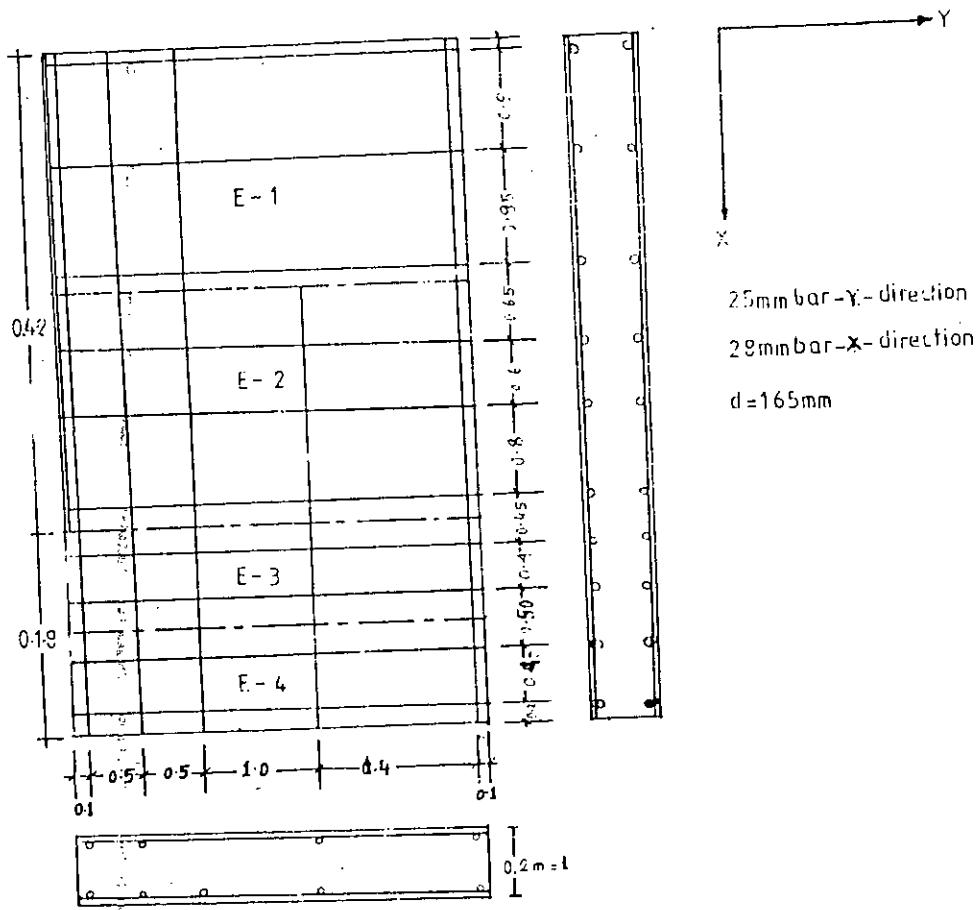


Fig. 4(a): Plan with Reinforcement

MOD 63



205

MOD 64

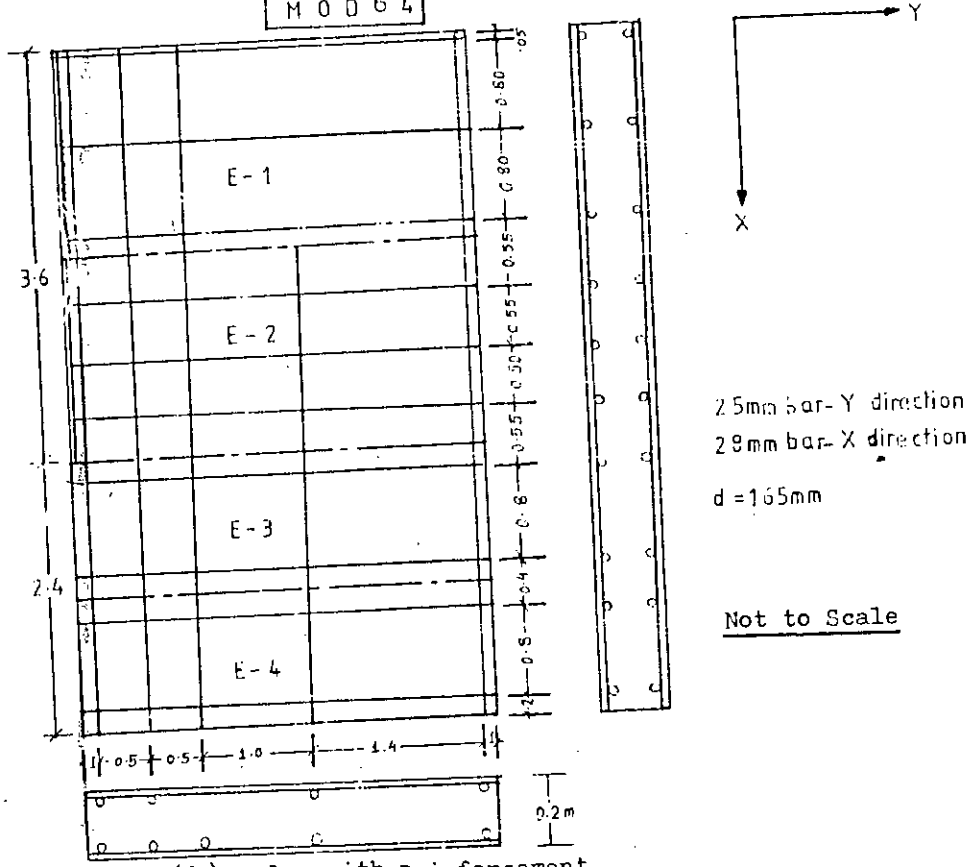


Fig.4(b): Plan with Reinforcement

Effect of Boundary Condition on Bending Stiffness of Slabs

Boundary conditions I and III were imposed on models MOD61, MOD62, MOD63 and MOD64 to study the behaviour of slab such as bending stiffness, crack propagation and yielding of steel. Plan with reinforcements for the above models are shown in Fig. 4. Idealized $M-\theta$ diagrams for models MOD61, MOD62 and MOD64 are presented in Fig. 5. Procedure for idealization of $M-\theta$ curve is presented in article 5.3. From the $M-\theta$ curves it is clear that the boundary condition III makes the structure stiffer than the boundary condition I. The values of K_o , K_{cr} and K_p are evaluated from the idealized curves for the two cases are presented in Table 3.

Comparison of Stiffness :

Comparing the values of K_o , K_{cr} and K_p from Table 3, it is clear that the values obtained from boundary condition III are higher than those from boundary condition I. For the models investigated, the values K_o from Case I are 71% to 94% of those from Case III, the values K_{cr} from Case I are 54% to 74% of those from Case III and the values K_p from Case I are 34% to 50% of those from Case III. Therefore, the Case III gives much higher stiffness than Case I.

Comparison of $M-\theta$ Curves :

It is evident from $M-\theta$ curves that the cracking moments (M_{cr}), yield moments (M_y) and ultimate moments (M_u) for Case III are higher than those for case I. For comparison Table 4 are presented.

TABLE 3 (a)

Model No	CASE I					CASE III				
	K_o	K_{cr}	K_p	K_{cr}/K_o	K_p/K_o	K_o	K_{cr}	K_p	K_{cr}/K_o	K_p/K_o
MOD61	187.7	48.7	19	0.26	0.101	200.7	66.2	37.7	0.33	0.19
MOD62	44.7	9.8	4.2	0.22	0.094	52.5	15.2	6.98	0.29	0.13
MOD63	20.6	5.9	1.8	0.29	0.090	28.5	11.0	5.50	0.39	0.19
MOD64	12.6	2.9	1.14	0.24	0.091	17.6	5.58	2.69	0.32	0.15

TABLE 3 (b)

Model No.	$K_o(I)/K_o(III)$	$K_{cr}(I)/K_{cr}(III)$	$K_p(I)/K_p(III)$
MOD61	93.5%	73.56%	50.4%
MOD62	85.0%	64.34%	60.0%
MOD63	72.3%	53.60%	34.0%
MOD64	71.4%	52.45%	42.3%

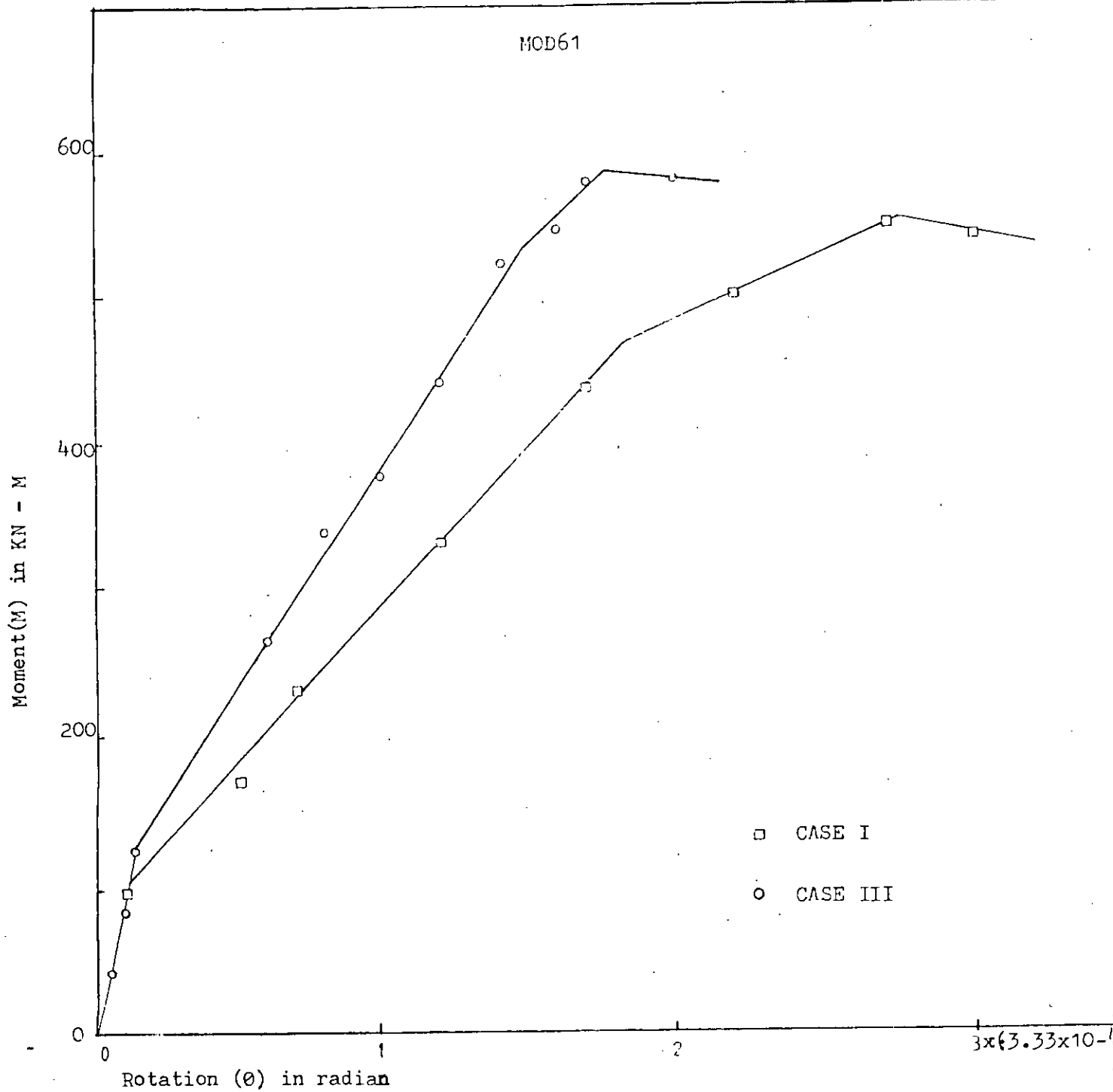


Fig. 5 (a) M - θ curves for Case I and Case III

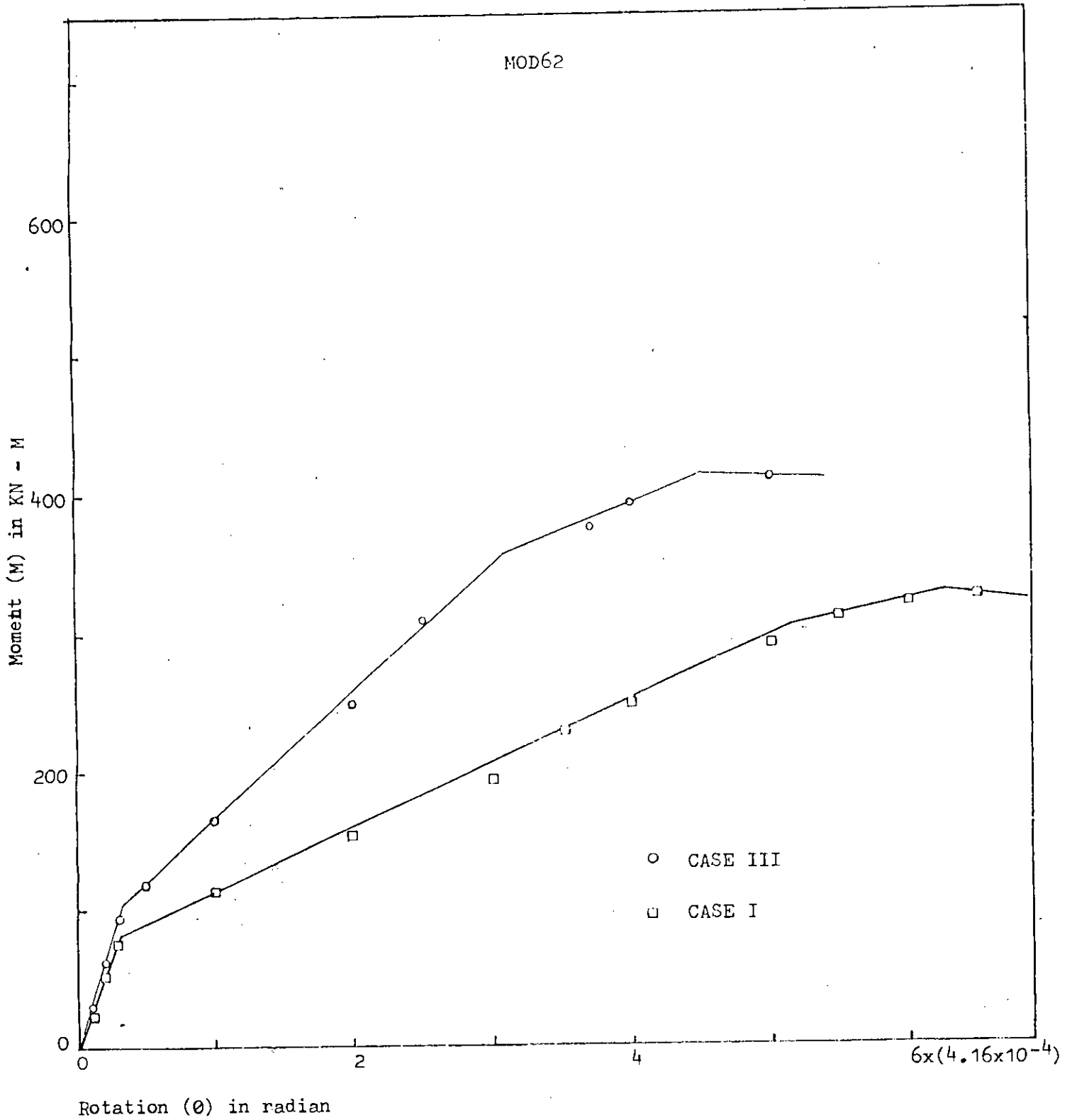


Fig. 5 (b) : Comparison of M - θ curves for Case I and Case III

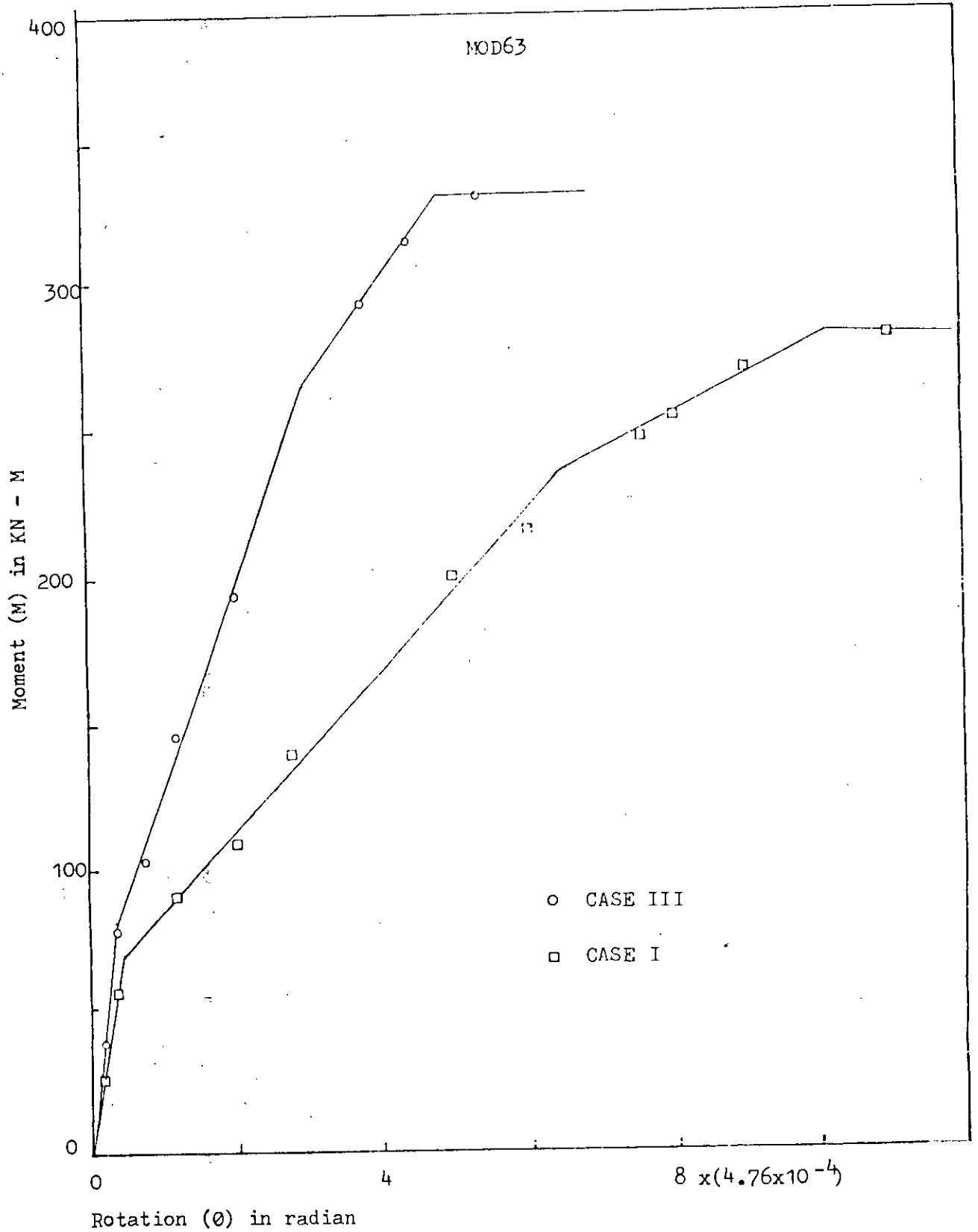


Fig. 5 (c) : Comparison of M - θ curves for Case I and Case III

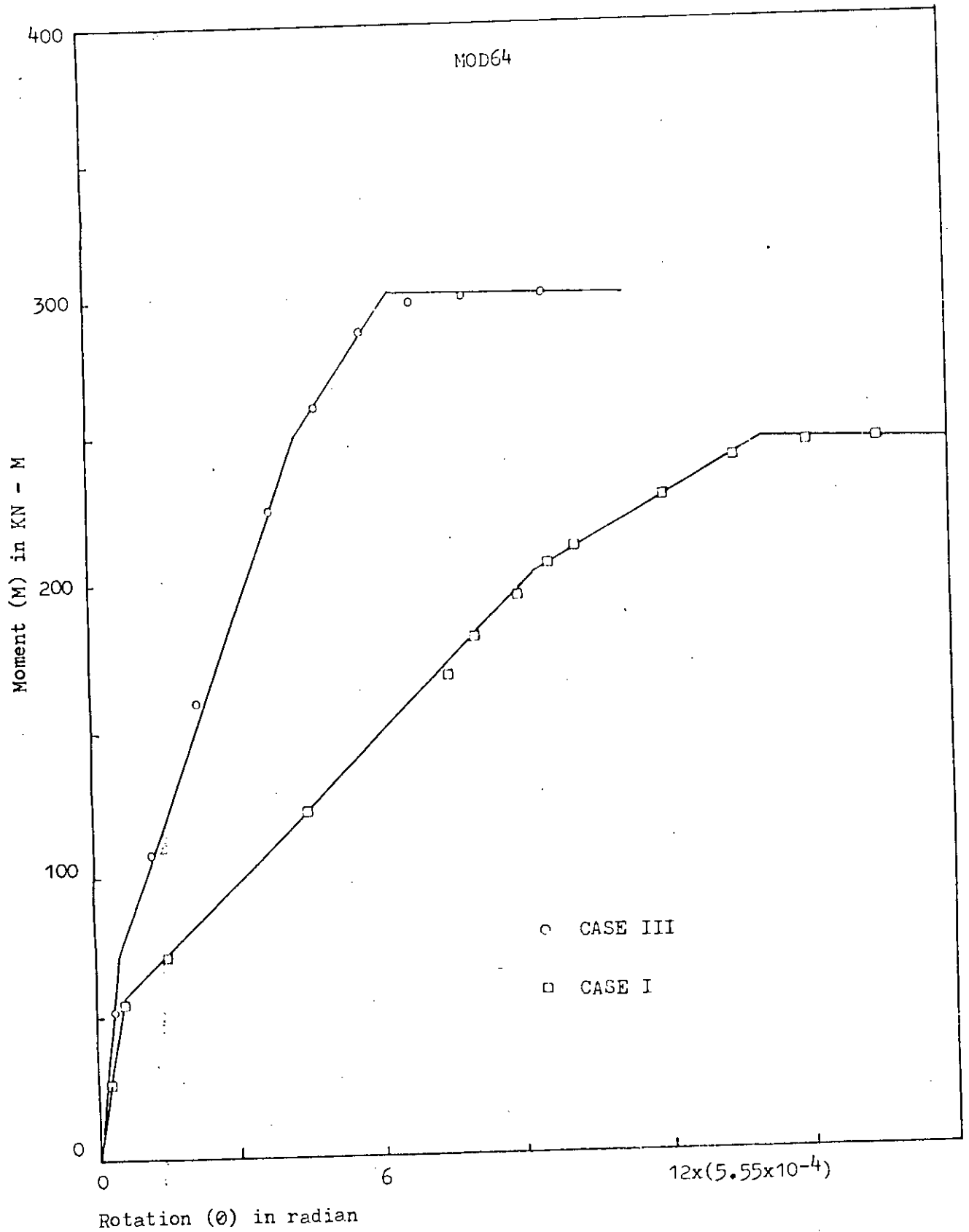


Fig. 5 (d) : Comparison of M - θ curves for Case I and Case III

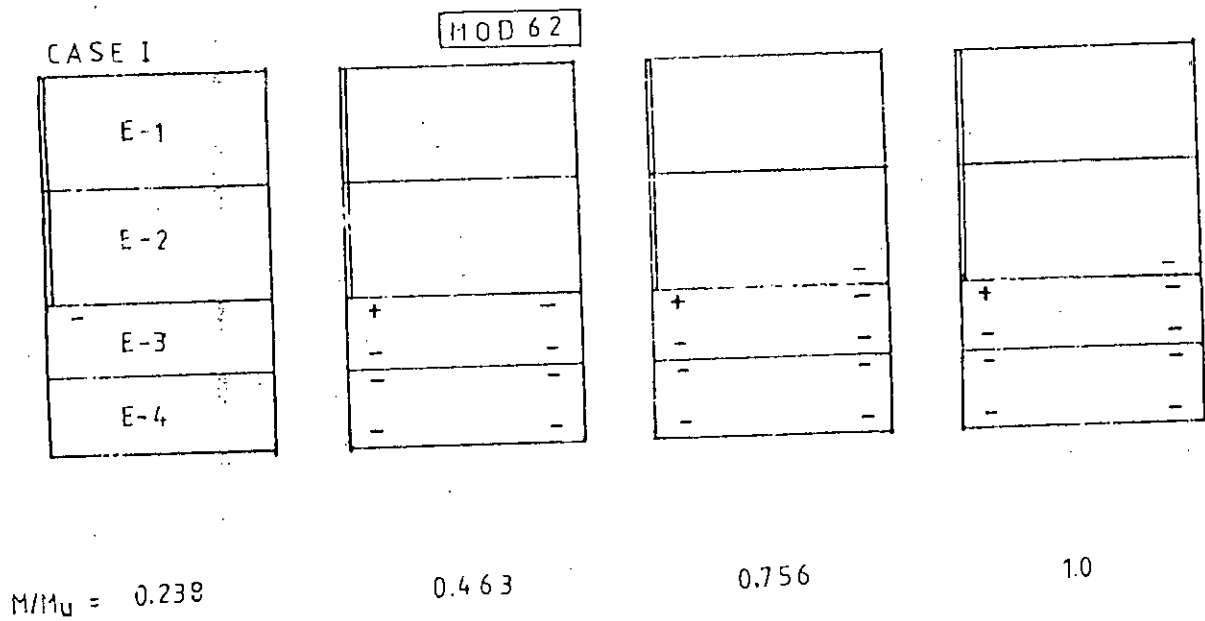
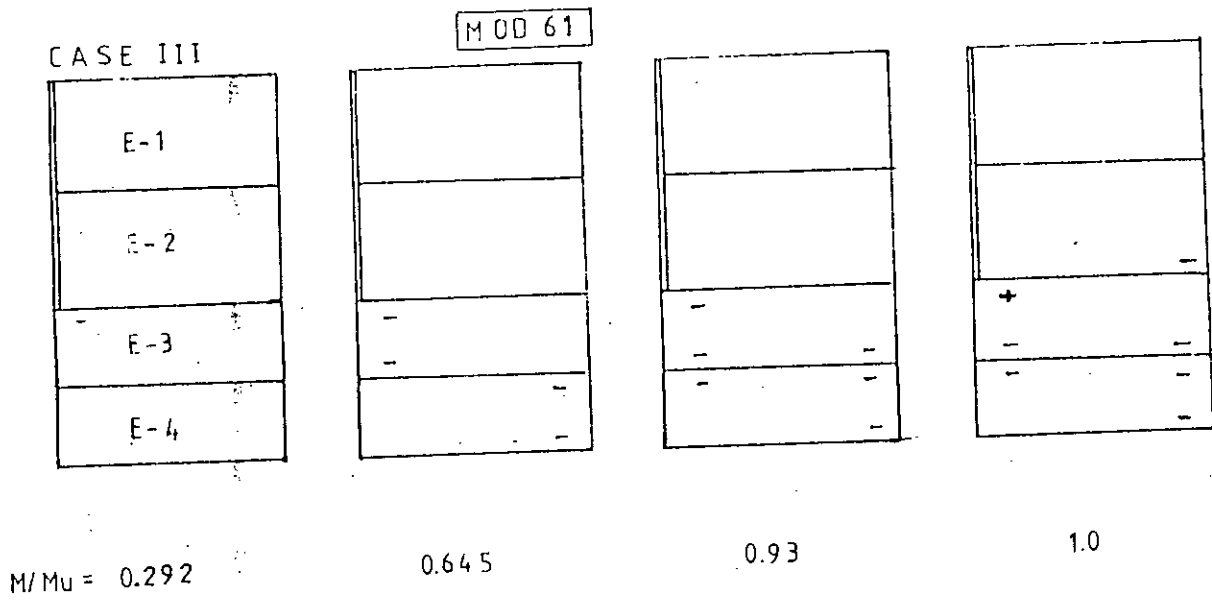
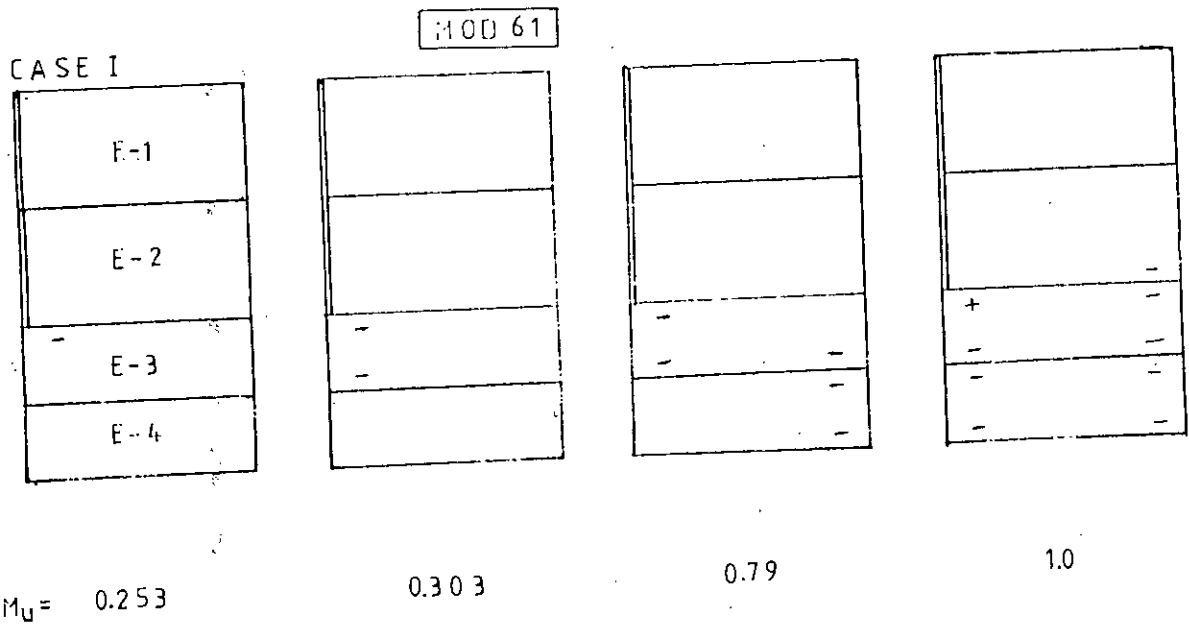
TABLE 4

Model No.	Case I			Case III		
	M_{cr}	M_y	M_u	M_{cr}	M_y	M_u
	Values are in kn-m			Values are in kn-m		
MOD61	100	467	560	126	530	585
MOD62	78	309	330	104	356	400
MOD63	66	235	280	79	263	330
MOD64	57	203	247	70	248	302

For the models studied, M_{cr} of case I ranges between 75% to 83% of Case III and M_u ranges between 82% to 96% of Case III. Therefore, from the investigation it may be said that Case III yielded higher cracking moments and ultimate moments.

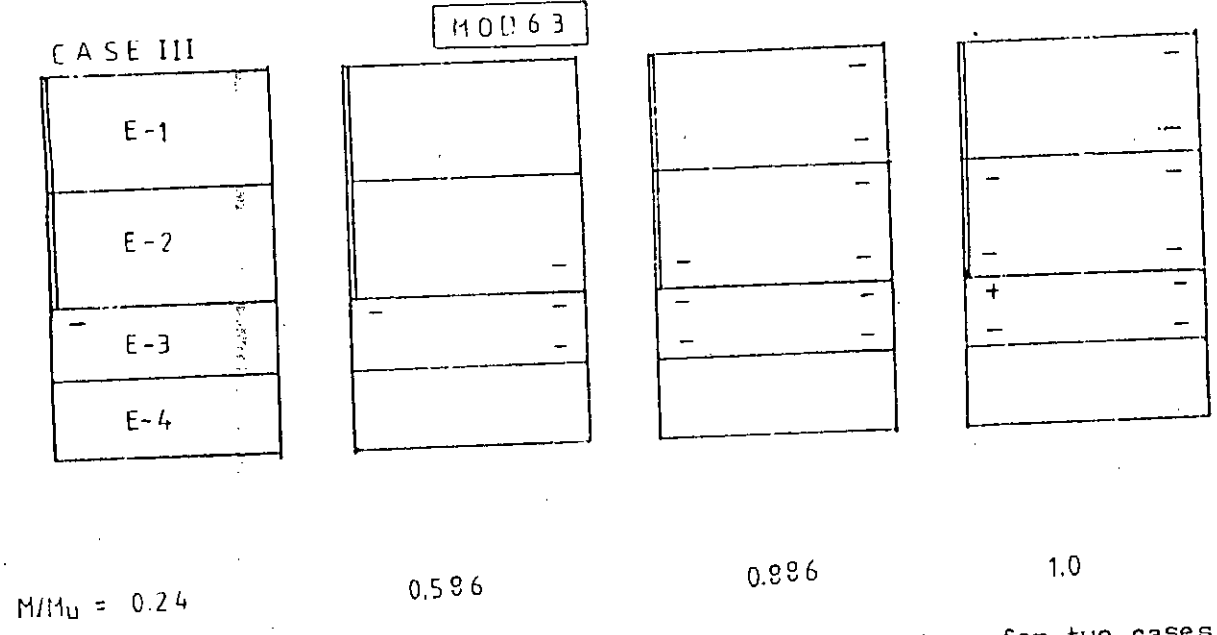
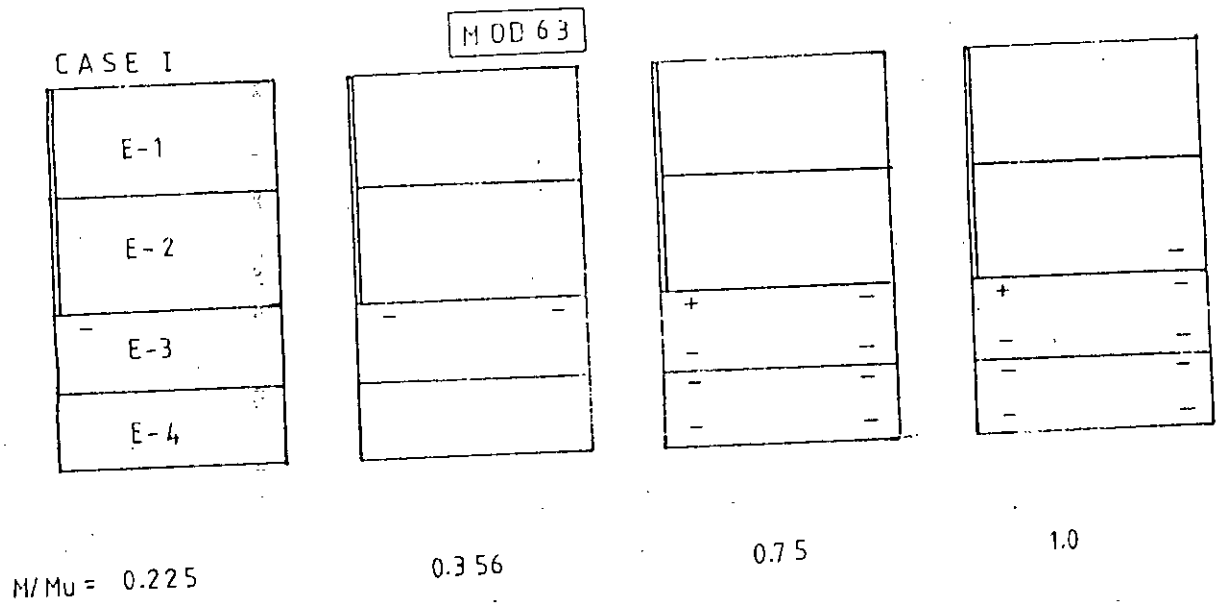
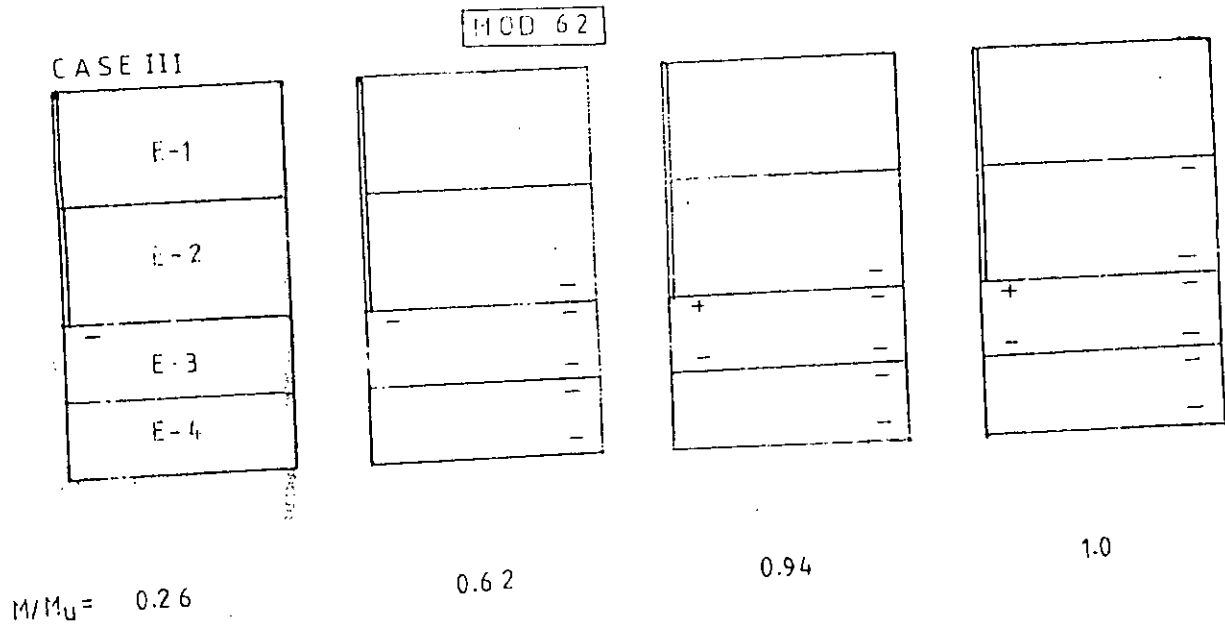
Comparison of Crack Pattern

Figs. 6 show the propagation of cracks in models for Case I and Case III. There are eight sampling points in an element and are equally distributed to the top and bottom layer. Their x,y,z distances from the boundary (surface nearest to the sampling points considered) of the element are 21.13% of x,y and z dimensions of the element (Fig.4.3). In the cracking diagram, gradual cracking of sampling points (1,3,5,7) of an element (Fig.4.3) on the tension side (bottom layer) of the slab are shown. From the crack pattern, it is clear that the cracks



- Single Crack
+ Double Crack

Fig. 6 (a): Comparison of crack pattern for two Cases



- Single Crack
+ Double Crack

Fig. 6 (b) : Comparison of crack pattern for two cases

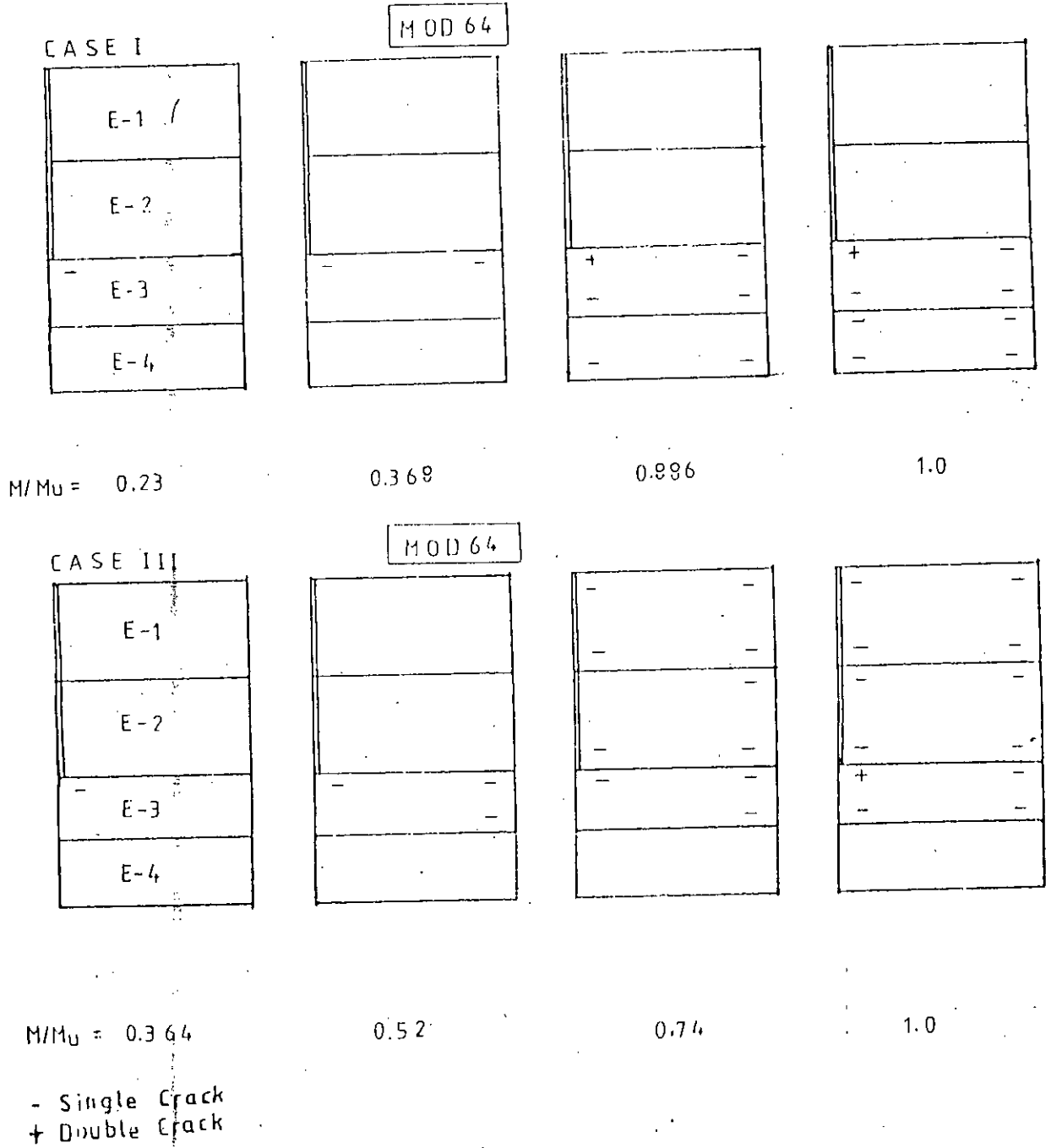
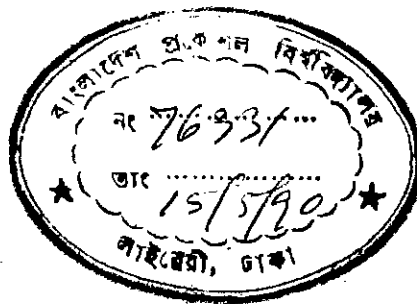


Fig. 6 (c) : Comparison of crack pattern for two cases

originate from the interior edge of the shearwall at element-3, for both cases. Cracks propagate from the interior edge of the shear wall towards the periphery of the slab. It may be said that element-3 is cracked earlier and then element-4. For the Case I, element 3 and element 4, that is, corridor slab, cracks severely than the elements, 1 and 2. But for Case III, Element-3 cracks severely and also the element 1 and element-2 are found to crack while for case I, little cracks are observed in element-1 and element 2. So, for Case III, elements containing the shear wall are cracked more than those for Case I. The reason may be due to the fact that in case III, rotation of the vertical nodal lines are not allowed and nodal lines are always remain on the same vertical line. This definitely causes the lengthening of the shear wall as the shear wall undergoes rotation. But in Case I, simultaneous z-translation and rotation of vertical nodal lines are allowed which minimizes the lengthening effect.

From the crack pattern it may be concluded that the critical section is the section which passes through the interior edge of the shear wall.



48. Smith, D G E and Johnson, R P, "The Interaction of Masonry Panels, Beams and Columns", B/20/5 Sub-Committee, Technical Paper 218, University of Warwick, March 1976.
49. Smith, D G E and Johnson, R P, "Derivation of the Design Method for Beams on Walls Presented in Technical Paper 47", B/20/5 Sub-Committee, Technical Paper 219, University of Warwick, March 1976.
50. Smith, D G E and Johnson, R P, "Walls on Beams, A Simplified Approach", B/20/5 Sub-Committee, Technical Paper 220, University of Warwick, March 1976.
51. CP 117: Part I, "Draft Standard for the Use of Structural Steel in Buildings Part 3 : Composite Construction", British Standard Institution, August 1976.
52. CP 111 : Part 2 : 1970, British Standard Code of Practice, Structural Recommendations for Loadbearing Walls, Part 2, British Standard Institution.
53. Bennet, E W, "Structural Concrete Elements", Chapman and Hall.

